INVESTIGATING SMALL SCALE PARTICLE ACCELERATION EVENTS AT THE SUN AND ITS IMPLICATIONS FOR CORONAL HEATING.

A thesis

Submitted in partial fulfillment of the requirements

Of the degree of

Doctor of Philosophy

By

Tomin K James

20122039

INDIAN INSTITUTE OF SCIENCE EDUCATION AND RESEARCH (IISER) PUNE

where tomorrow's science begins today

October,2019

Certificate

Certified that the work incorporated in the thesis entitled *'Investigating small scale particle acceleration events at the Sun and its implications for coronal heating.'*, submitted by *Tomin K James* was carried out by the candidate, under my supervision. The work presented here or any part of it has not been included in any other thesis submitted previously for the award of any degree or diploma from any other University or institution.

Date

Prof Prasad Subramanian

Declaration

I declare that this written submission represents my ideas in my own words and where others' ideas have been included, I have adequately cited and referenced the original sources. I also declare that I have adhered to all principles of academic honesty and integrity and have not misrepresented or fabricated or falsified any idea/data/fact/source in my submission. I understand that violation of the above will be cause for disciplinary action by the Institute and can also evoke penal action from the sources which have thus not been properly cited or from whom proper permission has not been taken when needed.

Date

Tomin K James
Roll No - 20122039

For,

Amma & Pappa

Teenakutty and Unnikuttan

(...and my lovely friends who’ve kept my soul sane over these years)

Acknowledgements

It has been a long, arduous and yet a very rewarding journey. Over these past few years, I have learnt a lot, travelled a lot, met some fantastic people and collected good memories that'll stay with me forever. There were highs and lows, excitement and disappointments, deadends and new insights. But what remained constant was the love and support I received from people near and far. Without them, this thesis would not have been possible.

Firstly, I express my heartfelt gratitude to my thesis supervisor, Prof Prasad Subramanian. He encouraged me, understood my strengths and weakness and helped me strive towards my research goals. His meticulousness in research related matters is something that I'll take as a life lesson in my budding young scientist. His ability to candidly express the research problems added a lot of finesse and value to this thesis. He was always there to hear my grievances and give solutions to my questions. More than a PhD supervisor, he is an amazing kind-hearted human being. His gentle behaviour whenever I faltered lifted my spirits and gave me renewed vigour to try harder. I will very fondly remember the discussions we had on research and many other things. Dear Sir, I shall never be able to pay back in kind for the support and help that you've provided me, but I think I'll take that as an inspiration to work harder to be a good scientist and make you proud.

I can never thank my institute IISER Pune enough for all the support - both financially and for my research. I saw this institute grow in front of my eyes and forever will have a special place in my heart. The superb facilities, ready access to amenities and exposure to an excellent academic environment played a crucial role in the completion of my thesis. The administrative staff always went over the way to help me get financial grants, approvals and documentation done. I would specifically like to give a shoutout to, Mr Tushar Kurulker, who is part of the academic staff, Mr.Prabhabhkar and Mrs.Dhanashree, of the Physics administrative office, who helped me a lot during my time here. I would also like to thank the Library, security and house-keeping services.

I express my gratitude for suggestions and feedback from Prof Divya Oberoi and Dr Rejish Nath, who are part of my Research Advisory Committee. Their inputs and suggestions bought better clarity to my work.

I would like to express my sincere gratitude to my collaborator, Dr Eduard Kontar of the University of Glasgow. I learned a lot about instrumental data analysis from him. Later I was fortunate enough to visit the University of Glasgow under the ERASMUS MUNDUS programme to work with him. His hospitality made my visit extremely comfortable. I also thank relatives and acquaintances who've helped me a lot during my visit to the UK.

I share lot's of beautiful memories with my fellow groupmates at the Plasma Astrophysics Group. I thank the senior members, Dr Arun, Dr Madhushuhan, Dr Nishtha and Dr Sasi, who all have helped in one way or another in my life as a PhD student. I happily remember all the late-night discussions I had on almost anything under the Sun with Nishtha. Her cheerful personality has lifted my mood more than once. I learned a lot from Sasi, and we have lots of fun experiences together - the adventurous yet gratifying Callisto antenna setup mission, trip to Kashmir and setting up of workstation for the group. I would also like to thank the present members Mayur and Debesh for their excellent company.

Next, I want to mention all my dear friends that I had the fortune to meet during my IISER life. Mukul, Jerrin, Ankita, Anjusha, Hridya and Aditi, who are my fellow batchmates, for the warmth and love they have showered on me. Mehak,Aditi(Audi), Sandip, Neeladri, Bharat, Ron, Anish, Shivani, Amar, Akhila, Jay, Kashyap and Divya who all belong to my junior batch but without hesitation adopted me as one of their own and gave me some beautiful memories and friendship that will last for a lifetime. I am indebted to them. I would like to give a shoutout to Mehak, for her loving personality and for all the late night coffee meets. She was a constant source of encouragement for me in this journey.

Now, I want to give my unwavering love and gratitude to the most beautiful human being I have ever met - my best friend Dhriti. She is witty, caring, kind, brilliant and has this fantastic ability to being a source of joy. She had lifted me up when I was down, comforted me during trying times and believed in me when nothing was working out. I am privileged to have you in my life and everyday with you is a blessing.

Lastly, I would like to humbly say thanks to my family for their sacrifices, unconditional love and steadfast support. Without them and their constant encouragement, this endeavour would not have been possible. My mother was a constant source of hope and is an inspiration to look up to. She staunchily supported me when I was confused about enrolling for a PhD. Thank you Amma for everything. You're a gem. My father, for his support. My loving sister and brother for their love. I can never say enough thanks to my family. I hope I have made you guys proud.

For the sake of brevity I have to cut it short here but this is in no-way an exhaustive list of people that have helped me during these years. You all have a special place in my heart. Thank you!

Abstract

Particle acceleration in the Solar atmosphere is an ill-understood problem. This lack of understanding creates impediments in our knowledge about how energy is generated and transported in the solar atmosphere. Studies show that the majority of energy released in transient events are used in the acceleration of particles. A proper understanding of this process is then vital to understand how the solar corona is heated. Since most of the coronal heating is carried out by small transient events, in this thesis, we lay particular emphasis on understanding the particle acceleration dynamics in them.

With the current sensitivity levels of space instruments, it is challenging to directly observe and quantify extremely small energy release events on the scale of nanoflares. Hence we turned our attention on very small flaring events which had both HXR and a SEP correspondence, but which did not have any big flares or CMEs associated with it. The simultaneous occurrence of HXR radiation and SEP particles makes sure that the selected events for the study had significant amounts of particle acceleration. From our study, we found that these small events accelerations almost similar amounts of electrons at the HXR, producing electrons and SEP electrons. This number for bigger events are much smaller, i.e. the number of SEP electrons that escape towards Earth as SEP is only a small fraction of the HXR producing electron. We observe that the ratio of number of escaping electrons to that of HXR electrons range from 6% to over 100%. By comparison this ratio is only $\sim 0.2\%$ for large flares. The total energy in the HXR producing electrons is $\sim 10^{24}$˘10^{26} while the same for electron population that escaped into the interplanetary medium is $\sim 10^{23}$ to 10^{25} erg (James et al., 2017).

In another study, we used high temporal resolution type I noise storm data from the NRH to investigate the energetics. Type I noise storm bursts represents some of the smallest examples of particle acceleration. We employed a model-independent particle acceleration framework developed by Subramanian et al to calculate the energy in a representative burst and the amount of non-thermal energy contained in them. We find that non-thermal electrons are only a small fraction of the thermal population. The power input by a representative burst was in the range of 10^{20} to 10^{23} ergs/s. Thus these bursts are likely contributors to active region coronal heating (James and Subramanian, 2018).

Lastly, we tried to decouple the effects of source acceleration effects and transport effects on the SEP particles. SEP particles are the only means by which we can directly sample particles accelerated in the Sun. Hence to properly understand the actual source information carried by these particles, it is essential first to know how transport through interplanetary space changes their characteristics. We observe that SEPs can be divided into symmetric and non-symmetric based on their time-intensity profile shape. We use this distinction to find any possible correlation between other physical quantities such as spectral indices, flare intensities, low energy electrons etc. Understanding transport effects is also essential to understand why certain SEP events show a delay in arrival eventhough simultaneous injection happened at the flare site. We also show initial results from a focussed transport model based Monte-Carlo simulations. The power law of the magnetic field fluctuations in the interplanetary magnetic field line seems to play a significant role in deciding the symmetricity of the SEP events.

Publications

1. **Tomin James, Prasad Subramanian, Eduard P Kontar**; Small electron acceleration episodes in the solar corona, Monthly Notices of the Royal Astronomical Society, Volume 471, Issue 1, 11 October 2017, Pages 89–99, DOI:10.1093/mnras/stx1460.

2. **Tomin James, Prasad Subramanian**; Energetics of small electron acceleration episodes in the solar corona from radio noise storm observations, Monthly Notices of the Royal Astronomical Society, Volume 479, Issue 2, 11 September 2018, Pages 1603–1611, DOI:10.1093/mnras/sty1216.

Table of contents

List of figures

List of tables

Chapter 1

Introduction

1.1 The Sun

1.1.1 Historical Perspective

The Sun is our closest star and sustainer of life on Earth. The light and heat from the Sun, warmed Earth, thus providing favourable conditions for life to emerge, evolve and thrive. The Sun is the most prominent astronomical body during the daytime, has long fascinated our ancestors regarding its origins and its influence on life. The Sun was venerated and mystified in most of the ancient cultures with elaborate folklores created around it. In Hindu culture, the Sun deity is known as Surya(Sanskrit word for the Sun). One other popular synonym for the Sun in Sanskrit is Aditya. The Adityas are important deities in the Vedas with several hymns dedicated to them. Surya Namaskar(Sun salutes) is an elaborate sequence of poses, thought to have originated from yogic traditions, honouring the Sun as the source of life on Earth. Another indicator of the veneration parted to the Sun is the existence of numerous Surya temples across India. The most famous one of them being the Konark Surya Temple, a world heritage site, located in the present Indian state of Odisha. The temple which was constructed during the 13th century majestically depicts a grand chariot with twelve wheels pulled by seven horses, which is the vehicle of the Sun god. These instances show us that the astronomical body of the Sun commanded an essential role in the lives of our ancestors.

1.1.2 Scientific Perspective

The earliest systematic observations of the Sun dates back to the Babylonians in 1300 BC, containing detailed Solar eclipse sightings. Ancient Indian astronomers like Aryabhata, Bhaskara I and Bhaskara II made detailed observations on the motion of the Sun in different

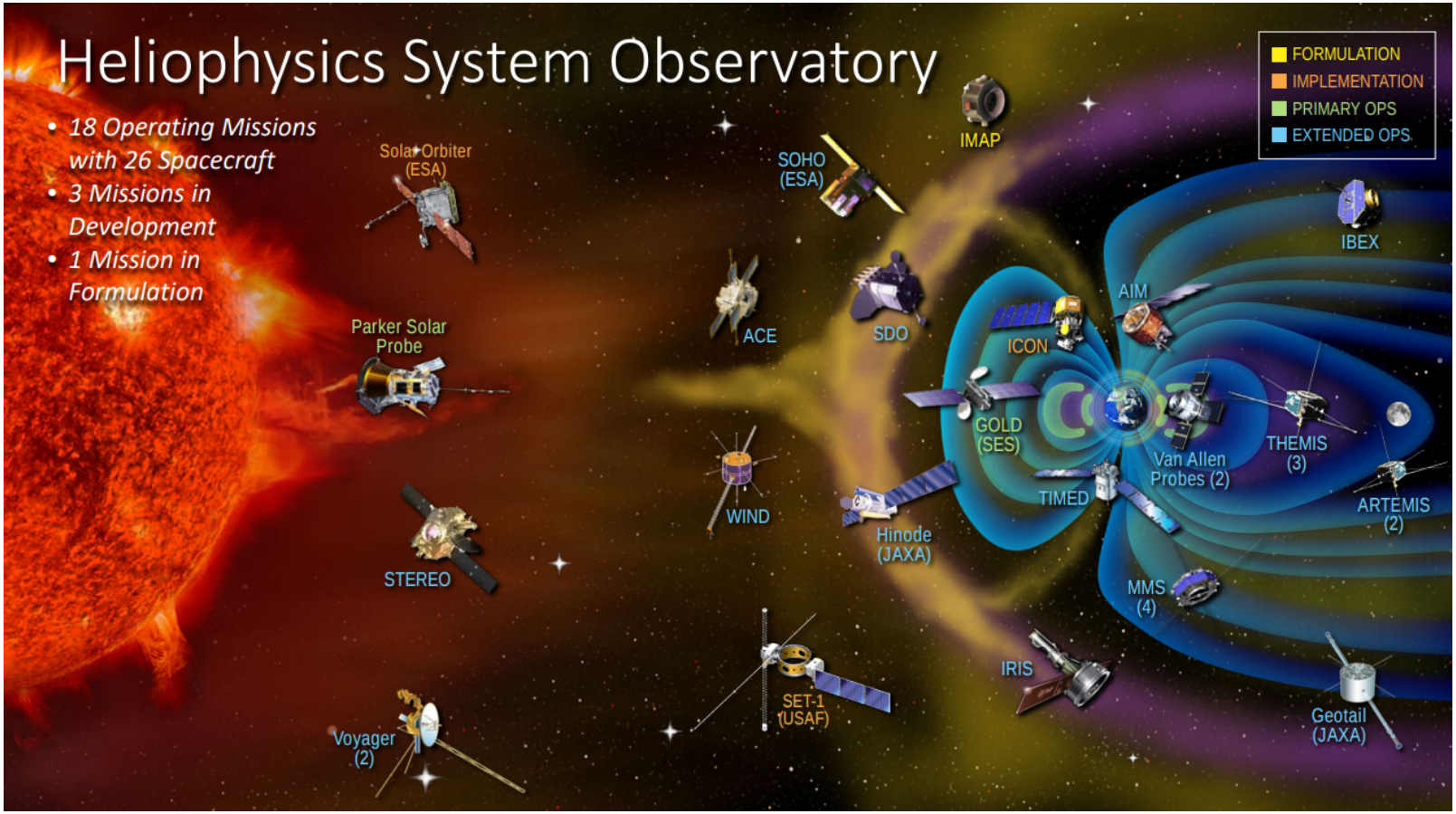

Fig. 1.1 Current family of Heliophysics spacecrafts with their approximate location in reference to Sun-Earth distance. Parker Solar Probe launched in July 2018 is the latest to join this list of every growing assets. Upcoming Indian mission, Aditya L1 would be placed near ACE. Credit: NASA/Heliophysics Division

seasons and its effect on life on Earth. These detailed observations enabled ancient Indian astronomers to make accurate sundials which were used to determine time from the Sun's altitude. With the dawn of the Renaissance period, the Sun got more attention in regards to Earth and our place in this universe. Copernicus proposed the heliocentric view of the world in 1517, attracting much wrath from the Church. Galileo in 1610 started observing the Sun using his new telescope, documenting the features on it, especially the Sunspots(Mason, 2002). Galileo's detailed observations further strengthened the case for the heliocentric model.

In the present era, the study of the Sun is conducted using a host of space-borne and ground-based instruments. Powerful computers today enable us to do detailed simulations regarding various processes at the Sun. The Sun is studied not only just as an astronomical body but also as the producer of energy which drives processes throughout the entire solar system and in particular to the immediate environment surrounding the Earth and the effects it can cause on life on Earth. The Sun is also our closest star, and this gives helio-physicists unprecedented opportunities compared to other branches of astrophysics. Getting a detailed understanding about the processes that happen at the Sun and its near environment(called the Heliosphere), is a precursor to understanding other stellar systems which are orders of magnitude farther than the Sun. Study of heliophysics has attained newfound importance in the past few decades from a space-weather perspective as well. The explosive events that happen in the solar atmosphere have a direct bearing on life on the Earth. Currently, many space agencies operate multiple spacecrafts studying the Sun and its immediate environment, ranging up to the Earth (Fig 1.1). India is sending a mission on its own to study the Sun named Aditya-L1, which would be located around the L1 point. Aditya-L1 is scheduled to be launched in early 2021 (Fig 1.2).

1.2 Sun as a star

The Sun is located at the centre of the Solar System and comprises 99.86% of its weight. The barycenter of the solar system in its most distant configuration lies at around 2 $R_{\odot}$ from the centre of the Sun. Even though the Sun is the most massive object in the Solar System, compared to the hundreds of billion stars present in the Milky Way, it is a very ordinary star. For example, Betelgeuse, a red giant, is 700 times bigger and 14000 times brighter than the Sun. We list a few important physical properties of the Sun below (Zombeck, 2007):

1. **Spectral Type**: The Sun is a G2V spectral class star according to the Morgan-Keenan (MK) system for stellar classification. In the MK system, letters O,B,A,F,G,K and M denotes different classes, with O being the hottest and M being the coolest. The Arabic

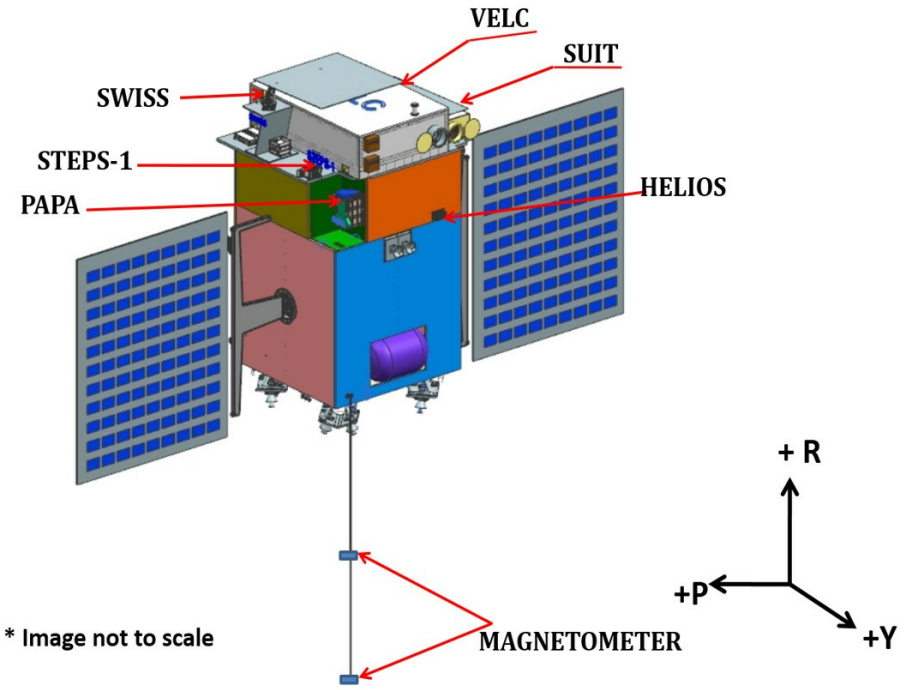

Fig. 1.2 Spacecraft for the proposed Aditya L1 mission, with instruments marked. The mission will be able to provide simultaneous coverage of the corona(visible chronograph and NIR), Photosphere(soft and hard X-ray) and Chromosphere(UV). The spacecraft will also carry particle detectors to measure in-situ energetic particle flux. The current scheduled launch date is early 2021. Credit: ISRO

numeral succeeding the class letter denotes a further subdivision of the temperature of the star(with 0 being hottest and nine being coolest). The roman numeral denotes the luminosity class, based on the fact that the stellar spectrum is uniform along the different evolution stages of a star (Morgan et al., 1943). Thus the Sun is a main-sequence star with temperature $\sim$ 5800 K.

2. **Radius**: The Sun is almost a perfect sphere of plasma with radius $(6.96 \pm 0.001) \times 10^5$ km. The difference between solar equatorial radius and polar radius is less than 10 km. The solar radius is about 109 times that of the Earth, resulting in a surface area about 12000 times that of the Earth. The volume of the Sun is $1.41 \times 10^{18} km^3$, and hence can accommodate 1.3 million Earth-sized objects inside it.

3. **Mass**: The solar mass (computed using the orbital period of the Earth) is determined to be $1.988 \pm 0.00007) \times 10^{30}$ kg, which is about 333,000 times that of Earth and 1500 times that of Jupiter. The average density of the Sun is around 1.41 g/cm^3. However, this is only an average value. The density can range from 160 g/cm^3 from the centre of the Sun to $10^{-16} g/cm^3$ to the outer layer of the Sun.

4. **Composition**: Since the Sun is in the main-sequence stage, it is still in the process of converting Hydrogen(H) into Helium (He) using a proton-proton(pp) chain reaction which uses four protons to form a Helium nucleus. This reaction chain which is known as PP1 is the dominant form of converting Hydrogen to Helium in Sun-like stars(in bigger stars this process proceeds via CNO cycle). The current composition of the Sun, is thus mainly Hydrogen($\sim$ 73%) while the rest is Helium($\sim$ 25%). Less than 2% is composed of heavier elements like oxygen, carbon etc. This nucleosynthesis cycle also determines the remaining time it can remain in the main-sequence stage. Currently, the Sun is fusing $\sim$ 500 million tons of Hydrogen to Helium, which means it will have enough fuel to burn stably for another 5 billion years.

1.2.1 Structure of the Sun

The Sun is very nearly in equilibrium with force of gravity being counteracted by gas pressure, thereby maintaining hydrostatic equilibrium. However, due to differences in the composition and conditions for energy transport, the Sun could be thought of as composed of different layers. Here we give a brief description of these different layers with emphasis given to the solar atmosphere where most of the problems addressed in this thesis occur.

The **solar interior** consists of all the layers below the visible part of the Sun called the photosphere. The innermost layer of the Sun is the **core** which extends from the centre

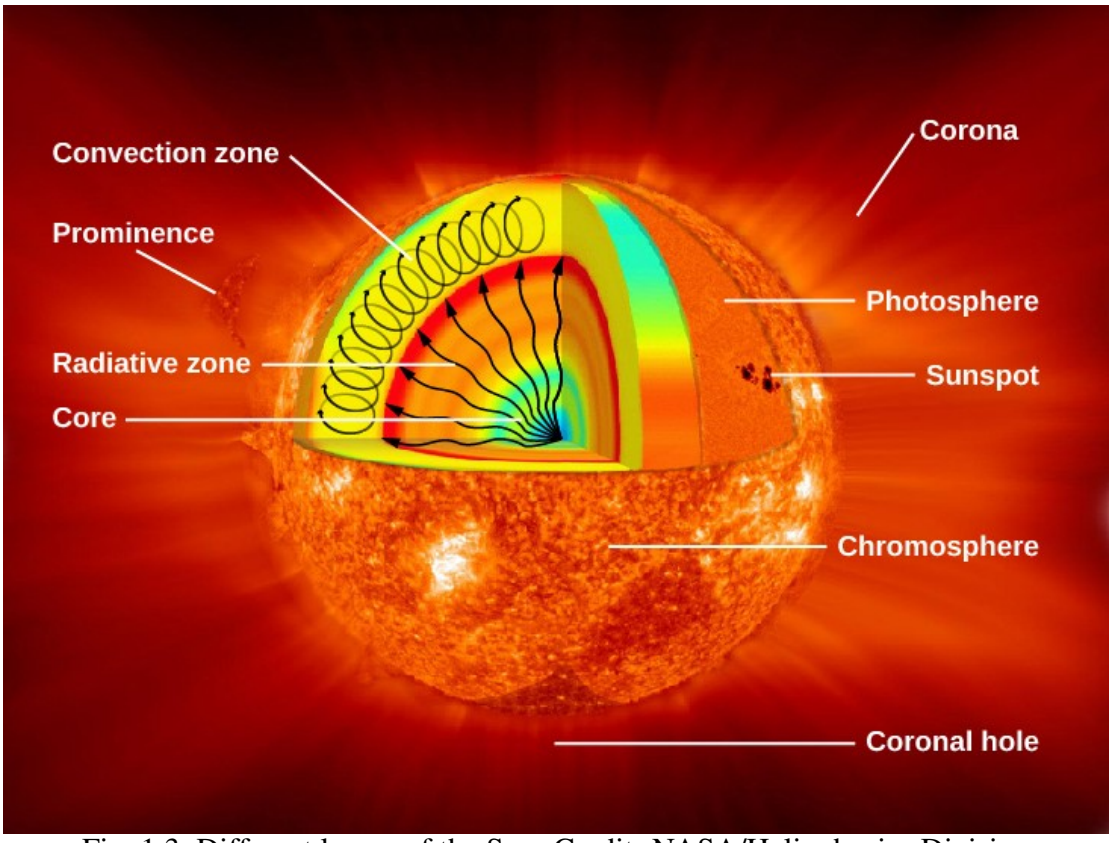

Fig. 1.3 Different layers of the Sun. Credit: NASA/Heliophysics Division

to about 0.25 solar radii. The core consists of highly dense, hot plasma, held under high pressure, which are conducive conditions for nuclear fusion. Even though the core takes up less than 1% of Sun's volume, it contains 34% of the Sun's mass. The nuclear fusion proceeds via PP1 chain reaction for 90% of the energy production via fusion:

$$^{1}\mathrm{H} + {}^{1}\mathrm{H} \longrightarrow {}^{2}\mathrm{D} + \mathrm{e}^{+} + \nu_e$$
$$^{2}\mathrm{D} + {}^{1}\mathrm{H} \longrightarrow {}^{3}\mathrm{He} + \gamma$$
$$^{3}\mathrm{He} + {}^{3}\mathrm{He} \longrightarrow {}^{4}\mathrm{He} + {}^{1}\mathrm{H} + {}^{1}\mathrm{H}$$

High energy photons produced during fusion is scattered randomly millions of times by free electrons present in the high-density core. It takes around $\sim$ 170000 years for a photon to reach the outer edges of the radiative zone. In the **radiative zone** energy produced via nuclear fusion in the core is transported in the form of electromagnetic radiation as photons. The density of this zone is so high that the gamma-ray photons undergo random walk scattering with a mean free path of $\sim$ 1 mm. The temperature in the radiative zone is 1/10 th of the core temperature(1.5 million K). The **convective zone** lies between 0.7 to 1 $R_{\odot}$, where the energy is transported by the convective motions of the plasma, wherein hot plasma rises to the top, which results in cooling causing it to sink down to be heated again by the incoming energy from the radiative zone. Since the plasma in the convective zone exhibits differential rotation, a high shear transition region is formed between the radiative zone and the convective zone, which is known as **tacholine**. The tacholine thus can be thought about as a byproduct of the rapid gradients in the rotation rates between the radiative zone which exhibits a solid body like behaviour and the convective zone which exhibits fluid-like behaviour (with rotation rates faster at the equator compared to the poles). The tacholine is thought to play an important role in the development of the solar dynamo.

Above the convective zone lies the first layer of the **solar atmosphere** called the **Photosphere**. The term originated from the Greek word 'photos' meaning light, in reference to the fact that this is the only visible part of the Sun when observing from Earth under normal circumstances using the naked eye. Using Stephan-Boltzmann law, the temperature of the photosphere is calculated to be between 4500 and 6000 K(effective temperature of 5777 K). The density of the photosphere is around $10^{-9} g/cm^3$. The photosphere is around 100 Kms thick and exhibit features called granules - which are hot cells of plasma bubbling to the surface due to convection. Each granule on average has a lifespan of around 20 minutes. Above the photosphere lies the **Chromosphere**, which is 10^{-4} times less denser and extends to $\sim$ 10000 Km. The rosy red colour that Chromosphere seems to exhibit(and hence the origin of the term - Sphere of colour) is because of the H_{α} emission lines. Using the spectrum of the Chromosphere, it was found that the temperature near the bottom is 5000 K while on the top it is close to 25000 K. The rise in temperature seems to happen at around 500 Km into

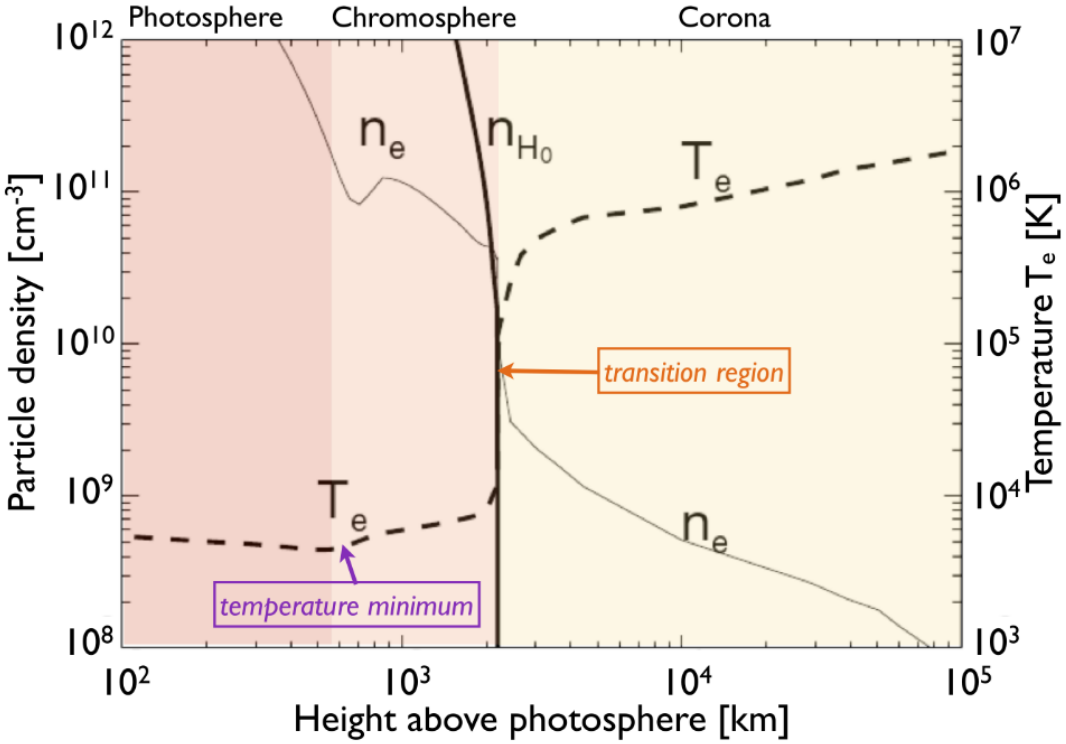

Fig. 1.4 The variation of electron number density n_e, hydrogen number density n_H and electron temperature T_e as a function of height above solar photosphere. Note the sudden discontinuity in the values along the transition region. Figure credit: Aschwanden (2004)

the Chromosphere, and this is known as the transition region. Thus, the temperature seems to increase with increasing distance from the core, which is the primary energy source. This is counter-intuitive and is known as the chromospheric heating problem. Many drivers of heating like acoustic waves, MHD-waves, reconnection etc. have been proposed to explain this paradoxical behaviour.

Above the Chromosphere lies the outermost layer of the solar atmosphere, called the **Corona**. The term Corona originates from the Latin word for 'crown' signifying its appearance(during eclipses) as an aura of hot plasma that surrounds the Sun. The Corona extends millions of Kms into outer space. However, due to its extremely dilute nature(the density of the Corona is $10^{-16} g/cm^3$ which is 10^{-12} than that of the Photosphere and hence only emits 10^{-6} times the visible light), it is obscured by the bright white light from the Photosphere. In visible wavelengths, Corona can only be seen during a total solar eclipse when the Moon blocks the Photosphere. Magnetic fields play an important role in the dynamics of the Corona.

The plasma-β parameter indicates the importance of magnetic pressure vis-a-vis gas pressure.

$$\beta = \frac{p_{th}}{p_{mag}} = \frac{nk_BT}{B^2/8\pi} \tag{1.1}$$

Here, n is the plasma number density, k_B is the Boltzmann constant, T is the temperature and B is the magnetic field strength. The β parameter helps in understanding the dynamics of the plasma and the major forces affecting it. For most of the solar Corona, plasma β<1 and hence the dynamics of the Corona is dictated by the magnetic structures that are present in the Corona. Because of this, the density of the Corona is not uniform and tends to follow the distribution of the magnetic fields. The visual appearance of the Corona is usually divided into three substructures - Active Regions, Coronal Holes and the quiet Sun. Active regions are associated with dense magnetic concentration and are hotter and denser than other parts of the Corona. Many phenomenons of interest like sunspots, flares, coronal mass ejections(CMEs) etc are associated with active regions. The coronal holes are regions with open magnetic field lines. Since heated plasma readily escapes from the coronal holes through the field lines, they appear darker than active regions. Quiet Sun regions are regions which are less 'active' compared to active regions. Nonetheless, quiet sun regions exhibit dynamic processes like nanoflares, soft X-ray jets, bright points etc.

Spectral measurements of the Corona indicates that it is heavily ionized, and the presence of certain spectral lines (Fe-XIV) indicate that the temperature of the Corona is about 1 MK. This is about 200 times hotter than the visible surface of the Sun, and this puzzling phenomenon is called the **Coronal Heating Problem**. We do not have a complete understanding regarding the dynamical processes that heat the Corona even after decades of research. Because of the low plasma β in the Corona, plasma heating can occur along the magnetic field lines. Hence the heating has to be local, with each magnetic loop exhibiting a quasi-steady heating as a result of a series of small scale impulsive energy releases (either via magnetic reconnection or wave dissipation) to account for the observed temperature profiles. A significant part of the magnetic energy released in heating event is used to accelerate particles which goes on to heat surrounding plasma. The acceleration of particle populations in these heating events and their subsequent transport towards the Earth through open magnetic field lines form the major theme of this thesis.

1.3 Role of small-scale transient events in Coronal Heating

Coronal heating via thermal conduction alone would have resulted in a temperature profile that decreased with increasing height in the Corona. The fact that we observe the opposite implies a steady supply of energy into the Corona. This energy balance can be expressed as:

$$n_e^2 \Lambda(T) - \kappa_c . \nabla T = \varepsilon_H, \tag{1.2}$$

where n_e is the electron density, T is the ambient plasma temperature and κ_c is the thermal conductivity. The term on the right-hand side signifies energy input into the Corona in units of $ergs/cm^{-3}$, while the first and second terms represent energy loss by radiation and thermal conduction respectively. $\Lambda(T)$ is the radiative loss function of the optically thin Corona. Since the coronal plasma is tenous, is optically thin and the radiation rarely interacts with the matter. In other words, the plasma is optically thin, and the Corona is transparent to the radiation. The Corona will experience net heating only if the energy supplied exceeds the radiation losses.

Since magnetic forces dominate the dynamics of the Corona (plasma-β <1), heating happens along the direction of magnetic field lines within which the matter is confined. Because of the fact that the plasma contained within a magnetic strand is a closed system with no interaction with neighbouring strands, we can parametrize the above equation using the field-aligned space coordinate z. Using RTV scaling laws (Rosner et al., 1978; Serio et al., 1981) the heating rate needed along the loop could be expressed in terms of loop density,

$$\varepsilon_H(z) \approx 2 \times 10^{-17} n_e^{7/4} L^{-1/4}. \tag{1.3}$$

Thus the heating rate is depended much more on the loop density than its length. Since the Corona is inhomogeneous in the way magnetic field lines are grouped (the densities are highest in active regions, lowest in coronal holes), the heating rate also varies across different regions of the Corona. The lowest heating requirement is in the coronal holes(3×10^5 $erg\ cm^{-2}\ s^{-1}$) and highest in the active regions($\approx 10^7$ $erg\ cm^{-2}\ s^{-1}$)(Withbroe and Noyes, 1977).

Many heating candidates were proposed over the course of years to account for this input of energy into the Corona, ε_H. Two theories have emerged as the likely candidates for coronal heating: wave heating and magnetic reconnection. Wave heating postulates that different modes of magneto-acoustic waves and/or Alfven waves transport energy from the Chromosphere to the Corona. The nanoflare hypothesis envisages small energy release episodes(due to reconnection) occurring throughout the corona (Parker, 1988).In this thesis, the focus will be on coronal heating via such magnetic reconnection episodes. For a review

of coronal heating by waves see Heyvaerts and Priest (1983); Kudoh and Shibata (1999); Matthaeus et al. (1999); Ofman (2010); Wentzel (1976). Magnetic disturbances caused by the turbulent photospheric motion of the plasma can only travel at a maximum speed given by the Alfven speed,v_A. This in turn effects a time constraint as to how the coronal loop responds to the footpoint motion. If the time-scale taken by the loop foot-points to change is longer than the Alfven wave transit time along the loop,then the loops will have enough time to adjust to the footpoint motion,and the currents will dissipate in a quasi-static way giving rise to what is termed 'DC' heating. If the opposite is true, the loop footpoints would have already changed by the time the current dissipated in the previous episode of energy dissipation would have reached the loop and thus the loop will see alternating current.This is called AC heating. Energy dissipation by magnetic reconnection falls under the category of DC models(Klimchuk, 2015).

Since the solar atmosphere is an extremely dynamic environment, there can be multiple candidates for coronal heating. The interplay of high magnetic(plasma-β values range between 10^4 in the Photosphere to $\ll 1$ in the Corona), temperature (6000 K in the Photosphere to 1-2 MK in the Corona) and density($10^{12} cm^{-3}$) gradients results in a variety of spatially and temporally localized phenomenons which are capable of releasing energy. These transient events include X-class flares, Coronal Mass Ejections, filament eruptions, jets, spicules, fast magnetoacoustic wave trains etc. The underlying driver for such events could be photospheric granular flows or magnetic reconfiguration in the Corona that dissipates the built-up energy in magnetic fields. The released energy is often transported and give rise to a host of secondary phenomenons based on the location of energy release and ambient conditions. The exact mechanism by which these transient events dissipate built-up magnetic energy and how it is utilized to accelerate particles is still an open research problem. The existence of events which can release energies over a range of energies is itself an interesting problem of research. Two plausible scenarios often postulated to explain the range of energy scales observed are: self-organized criticality (Aschwanden and Freeland, 2012; Lu and Hamilton, 1991; Lu et al., 1993) and turbulent plasma interactions (Dmitruk and Gómez, 1997; Einaudi and Velli, 1999; Rappazzo et al., 2007). Uritsky and Davila (2014) showed using data from STEREO and SOHO spacecraft that quiet-Sun events which supply most of the energy needed for coronal heating are in a driven self-organized critical state.

The idea that an ensemble of small heating events happening across the Sun can result in heating of the Corona was first put forth by Eugene Parker in a series of papers(Parker, 1983, 1985, 1987, 1988). The importance of small-scale flare like events heating the Corona can be understood by looking at the power-law index α of the observed flare occurrence rates(Fig

1.5). We can write

$$\frac{dN}{dE} = AE^{-\alpha} \tag{1.4}$$

The total energy released by these events is the integral of the first moment of the power-law distribution given in eq.

$$\begin{aligned} W(E_{min} \leq E \leq E_{max}) &= \int_{E_{min}}^{E_{max}} \frac{dN}{dE} E dE \\ &= \frac{A}{2-\alpha}\left[E_{max}^{-\alpha+2} - E_{min}^{-\alpha+2}\right] \end{aligned} \tag{1.5}$$

The total energy W,will diverge if $\alpha > 2$ as $E_{min} \to 0$. The value E_{max} is limited by the finite size of the Sun as the amount of magnetic free energy that could be accumulated is proportional to the length scale of magnetic loops. For the largest of flares observed E_{max} is estimated to be 10^{33} ergs. The bigger flares, although more energetic, are sporadic and only contribute $\sim 20\%$ of the energy required for coronal heating. Smaller flares are more frequent and contribute the remaining 80% of the energy required to heat the Corona. The change in the slope for the smaller events may be an indication of the difference in the physical processes that result in energy deposition and resultant heating.

We now explain the nanoflare model proposed by Parker in more detail. The nanoflare heating model was proposed in part due to the inability of wave heating theory(which was the then-prevailing view regarding the major drivers for coronal heating) to propose an efficient mechanism to heat up the X-ray corona. It was noted that waves, except maybe Alfven waves, dissipate their energy much before it reaches the corona. Parker (1988) suggested that coronal heating instead happens via dissipation of current sheets formed because of the continuous shuffling and braiding of magnetic fields whose footpoints are frozen into the photospheric plasma. The mechanical driver for this process is the random walk like motion that the foot-points of the fields undergo because of granular motion in the photosphere. We quantitatively explain the process now.

The solar corona is filled with loops which are frozen into the plasma as a consequence of the high conductivity of the plasma. In the simplified model, the loops each with width w starts out as a uniform field (i.e, almost parallel to each other) at time t=0. The loop footpoints are separated by a distance L and are located in the photosphere. For ease of depiction, the field lines are opened up and aligned in 2D. A cartesian coordinate system is used with the z-axis aligned along the direction of the field line. Thus z=0 and z=L denote the footpoints and the region between the two planes is the corona(0<Z<L) (Fig 1.6). At time t=0, the magnetic field is a uniform potential field and can be written as:

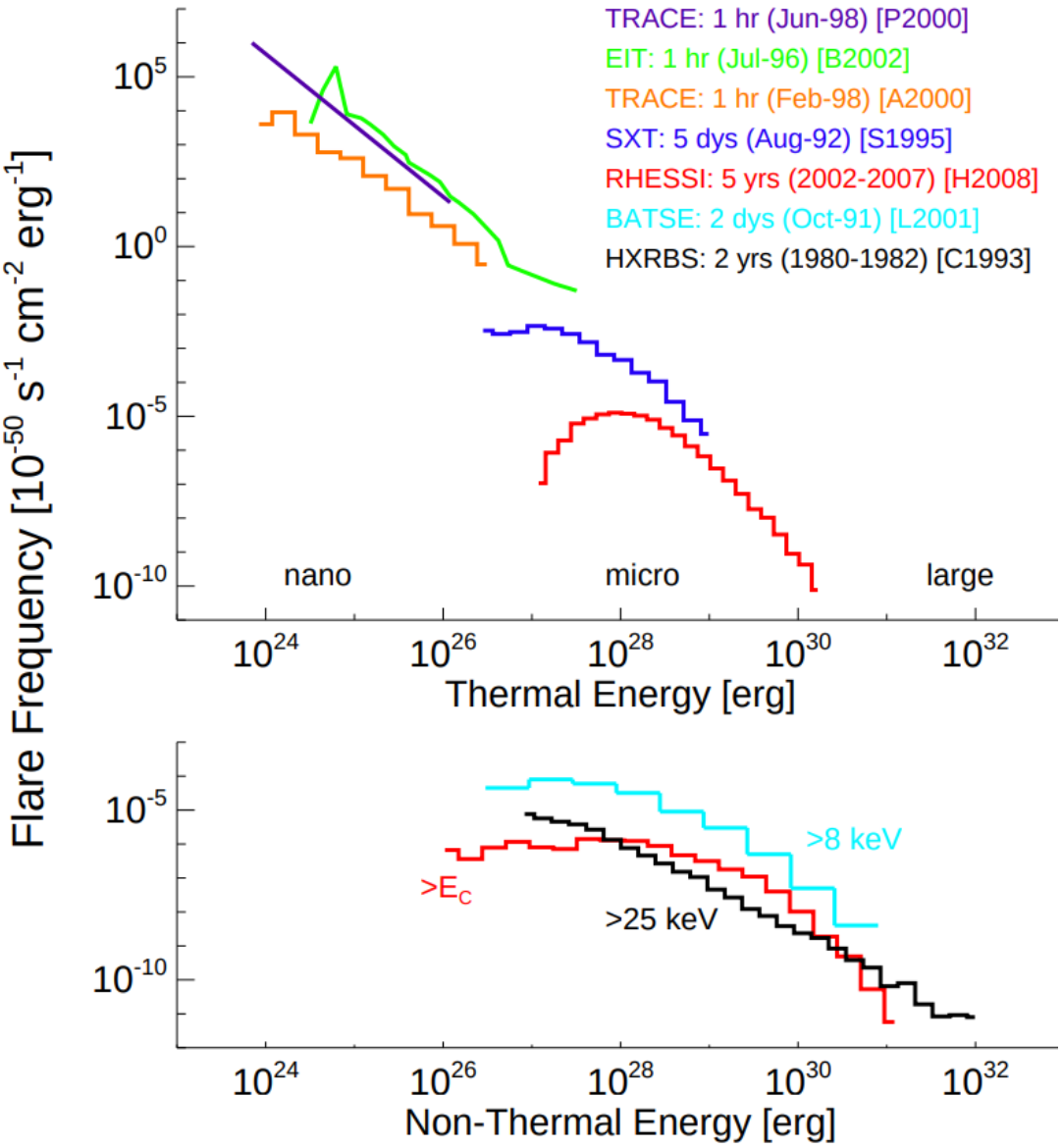

Fig. 1.5 The combined energy distributions for solar flares using data reported in Crosby et al. (1993) for SMM/HXRBS data; Lin et al. (2001) for CGRO/BATSE data; Hannah et al. (2008) for RHESSI data; Shimizu (1995) for Yohkoh/SXT data; Parnell and Jupp (2000) for SOHO/EIT. Figure Credit: Hannah et al. (2011)

$$B(r,\theta) = B\theta\hat{z} \tag{1.6}$$

Here B_0 is the field strength. Since the photosphere, in which the footpoints are anchored, exhibit turbulent motions because of granular and supergranular flows of plasma, it is reasonable to assume that magnetic field will be twisted and tangled with each other. The deviation of field line from the vertical as a function of time can be expressed as

$$tan\theta(t) \approx < v > t/L. \tag{1.7}$$

As expected at t=0 there is no deviation. If B_0 is the vertical field strength, then from above equation the horizontal field strength $B_\perp$ is $B_0 tan\theta(t) \approx B\langle v\rangle t/L$. The work done by the footpoints gets stored in the magnetic field configuration at a rate given by:

$$\begin{aligned} W &\approx < v > B_\perp B/4\pi \\ &= (B^2/4\pi) < v >^2 t/L \quad ergs\ cm^{-2}\ s^{-1}. \end{aligned} \tag{1.8}$$

The rate of power input is thus linearly dependent on time. Parker then argued that based on the necessary heat input to account for observed coronal temperatures is about $10^7 ergs\ cm^{-2}\ s^{-1}$. For a coronal loop of L=$10^{10} cm$, B=$10^2 G$ and footpoint velocity <v> = $0.5 km\ s^{-1}$, this amount of energy buildup happen after the deviation from the vertical reaches a critical value of about $\theta \approx 14^\circ$, for the energy dissipation to occur at the needed rate. For footpoint motions with velocities of 0.5 $km\ s^{-1}$ velocity, this horizontal displacement would be reached in t= $5 \times 10^4 s$. When θ reaches this critical value($\approx 14\circ$), the energy stored in the stressed magnetic fields is rapidly dissipated via magnetic reconnection. If the dissipation timescale is larger than the energy buildup timescale, the critical value θ would assume a larger value. Thus the heat input to the corona is inversely proportional to the effectiveness of the energy dissipation in the Parker reconnection model. For the time it takes to reach this critical value the flux bundle would have traversed a distance, vt = 2.5×10^4 Km which is approximately equal to the size of a typical supergranule. Thus it is reasonable to assume that the time-duration of one random step equals the lifetime of a granule, $\tau \approx 500$ s. Hence the step size of each random step is $l = v\tau$=250 Km. This corresponds to a total of $n = t/\tau = 10^2$ random steps in its traversed pathlength history. The vertical length scale to which each random step intertwines a flux bundle is given by $\Delta L = lL/vt = 10^3$ Km. The free energy associated with each such winding is of the order of the magnetic energy density multiplied by the volume of each winding,

$$\varepsilon = l^2 \Delta L B_{\perp}^2 / 8\pi \approx 10^{24} ergs. \tag{1.9}$$

This is the oft-quoted value for these small energy releases. Since this is around nine orders of magnitude smaller than the energy released in any big flares, it is called a nanoflare. It should be noted that free energy available with a single nanoflare will be in the range of energies ranging from 10^{24-27} ergs depending on the local conditions such the intensity of the magnetic field, loop lengths etc.

In the years following the postulation of the nanoflare hypothesis, observations were limited by instrumental limitations. The spatial scale resolution needed to resolve magnetic strands in which nanoflare like heating events happen is $\approx$ 200 Km. With the advent of new space-borne and balloon-borne instruments, we are now in a position to quantitatively probe this challenging problem. Observations using Extreme ultraviolet Imaging Telescope(EIT)(Delaboudinière et al., 1995) aboard Solar and Heliospheric Observatory(SOHO), the Transition Region and Coronal Explorer(TRACE)(Handy et al., 1999) and Atmospheric Imaging Assembly(AIA) (Lemen et al., 2012) onboard Solar Dynamics Observatory(SDO) have shown as that solar corona is characterized by loops of several length scales. Even though these instruments cannot image at the scale of individual reconnections in magnetic strands, the data show indirect evidences to support impulsive heating such as enhanced densities observed in loops presumably caused by non-steady heating(Warren and Warshall, 2002), presence of $T > 5$ MK plasma component(Schmelz et al., 2009), flatter temperature profile of loop which can result from low-frequency heating(Aschwanden et al., 2000) etc. Recent observations using the High Resolution Coronal Imager(Hi-C)(Kobayashi et al., 2014)-which has a higher resolution than existing instruments- revealed braided magnetic strands similar to the tangled magnetic field lines postulated by Parker(Morton and McLaughlin, 2014).

1.4 Particle acceleration in transient events

A significant part of the magnetic energy released in transient events is thought to be expended in producing energetic particles. These particles then interact with the ambient plasma, producing secondary emission over a wide range of wavelengths. In the absence of highly sensitive instruments capable of detecting small energy release events directly, these secondary electromagnetic emission characteristics enable us to study the processes involved. The processes involved in utilizing the free energy to accelerate particles are thought to be highly efficient. The impulsive phase of flares usually last $\sim$ 10 minutes and generate about 10^{32} ergs of energy and release them into the solar atmosphere and the corona. In order to gain a good understanding of the coronal heating processes, it is crucial to understand

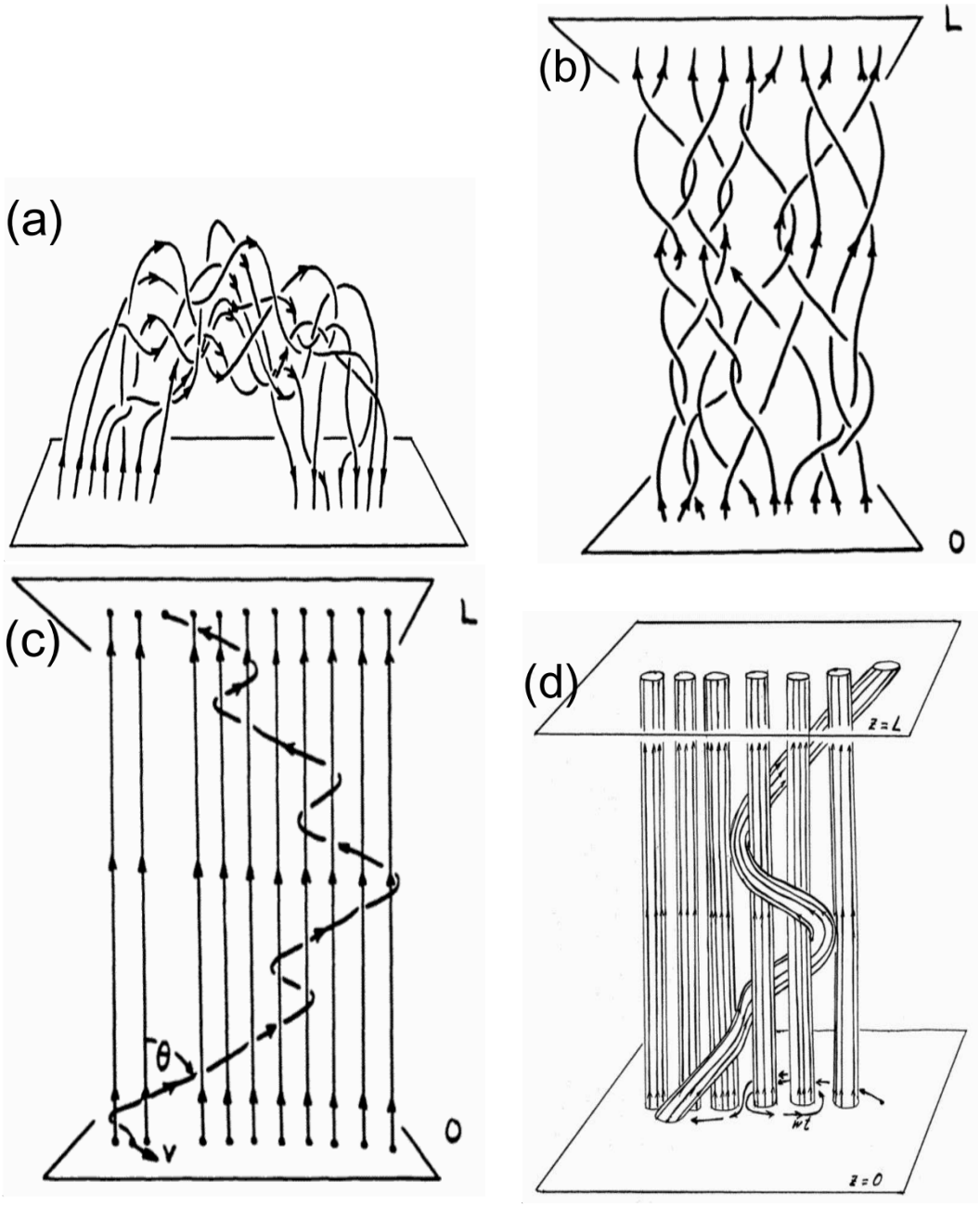

Fig. 1.6 (a) The field lines tangled together due to random twisting by the photospheric driver in a bi-polar magnetic reconnection region above the photosphere (b) The loop lines are projected to a 2D plane with z=0 and z=L representing the two footpoints. (c) wandering field lines getting twisted at random angles θ. Fig credit:Aschwanden and van Ballegooijen (2018)

these particle acceleration processes, especially in small-scale events. In this section, we will focus on characteristics X-ray and Radio emissions which form an essential role in our

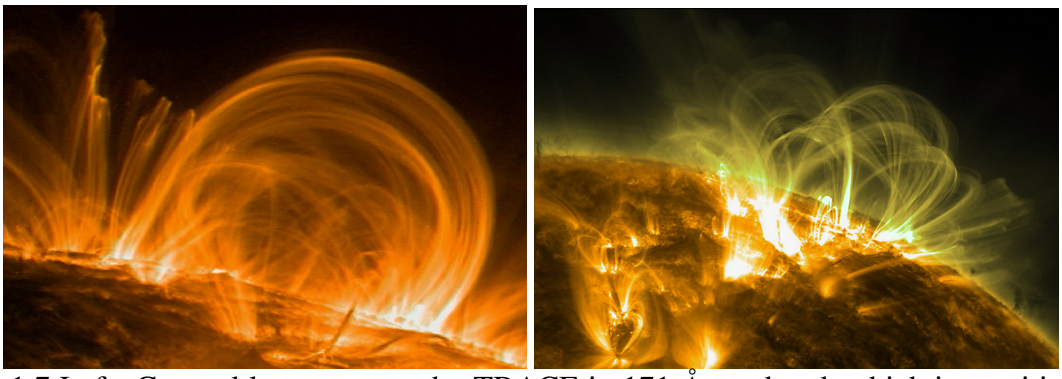

Fig. 1.7 Left: Coronal loops as seen by TRACE in 171 $\mathring{A}$ passband, which is sensitive to emission at about 1 MK. Right: A composite image created using SDO AIA 171 $\mathring{A}$ and 191 $\mathring{A}$ channels, which represents upper transition region and coronal plasma respectively. Image credit: TRACE/NASA, SDO/NASA

analysis. These emissions are almost always due to accelerated particles and can serve as an important diagnostics of the process involved. We now give a brief description of the three major types of acceleration that a particle can undergo - DC electric field, stochastic acceleration and shock acceleration. For a detailed review and explanation of these topics, the reader is referred to Arnold O. (1993); Miller (2000); Vlahos et al. (1986)

In **DC electric field acceleration**, electrons and ions are subjected to static electric field acceleration over a distance. Since the electric force on both these species acts in opposite directions, net acceleration can happen only if the electric field is large enough to overcome this frictional drag. This regime is called runaway acceleration and is thought to be a common occurrence in solar flares. The minimum electric field required to effect runaway acceleration can be derived by equating the electric force to net collisional drag time-scale (Benka and Holman, 1992, 1994; Holman, 1985, 1995; Spicer, 1982; Zarro et al., 1995).The electric field thus required is known as Dreceier electric field, given by (Dreicer, 1960, 1959),

$$E_D = e \ln\Lambda / \lambda_D^2. \tag{1.10}$$

Here ln Λ is the Coulomb logarithm, $\lambda_D = v_{th}/\omega_p$ is the Debye length, $v_{th} = (k_B T/m_e)^{1/2}$ is the thermal speed of the electron and $w_p = (4\pi n_e e^2/m_e)^{1/2}$ is the electron plasma frequency. In the presence of an electric field $E > E_D$ a thermal particle with velocity, v_T, where T is the thermal temperature, will be accelerated out of the thermal population into a non-thermal one. However, the length scales needed to accelerate particles above 100 KeV (which are regularly observed in flares) is of the order of 10 Mm. Such large current sheets develop tearing-mode instabilities, which will partition the current sheet into small magnetic islands.

Super-Drecier electric fields, however, can accelerate particles into typical flare energies over much shorter distances and hence are feasible candidates for particle acceleration. This also implies that the acceleration region is compact. Electrons can be accelerated to the observed HXR energies in the flare over much shorter distances, which also can explain the 'burstiness' of HXR emission observed in more prominent flares (Litvinenko and Somov, 1995; Litvinenko, 1999; Martens, 1988; Martens and Young, 1990).

Stochastic acceleration occurs via wave-particle interactions. Unlike DC field acceleration, the particles get energised by the AC field of waves. This interaction between waves and particles results in the energisation of particles provided the waves and particles interact constructively. Energy transfer between the waves and particles are most efficient when the wave frequency is in resonance with the gyro-frequency of the particle. The stochasticity of the process is because waves cover a whole spectrum of frequencies, and the interactions with waves and particles can result in either energy gain or loss, depending on how resonant the wave frequency is with the gyro-frequency of the particle (Melrose, 1980a,b). Thus a particle gains or loses energy in a somewhat random manner. Stochastic acceleration mechanism could be described using wave-particle interaction theory in which a coupled equation describes how the wave photon spectrum $N(k,t)$ changes via interaction of particles and in return how the particle distribution $f(v,t)$ changes because of the interaction with waves. The dispersion relations that can be derived from the simultaneous solution of these coupled equations give information regarding the suitability of different modes of waves for an efficient stochastic acceleration of different species of particles (Arnold O., 1993; Sturrock, 1994). It can be shown that ion gyrofrequency resonates with Alfven waves, magneto-acoustic waves and ion sound waves whereas electron gyro-frequency resonates with whistler waves and Langmuir waves. The presence of loop-top HXR emission in flare loop is thought to be a consequence of stochastic acceleration. The electrons are temporarily trapped and repeated accelerated due to the turbulence resulting from reconnection (Masuda et al., 1994; Petrosian and Donaghy, 1999).

Shock acceleration refers to the scenario in which particle gains net energy via a crossing of a shock front. Shocks are thought to be ubiquitous in the solar atmosphere because of the high gradients in the magnetic field and the discontinuous boundaries formed as a result. New observations suggest the presence of shocks in the outflow region of magnetic reconnection in solar flares resulting in the acceleration of electrons to relativistic velocities. The net energy that a particle gains during shock acceleration depend on the number it crosses the shock front (Anastasiadis, 2002; Anastasiadis and Vlahos, 1994). In Fermi first-order acceleration scenario, the available energy gain for a particle is limited by the ratio of upstream and downstream magnetic field strengths. Further acceleration can happen if a

magnetic mirroring scenario exists upstream of the shock. In this case, the particle can be reflected at the shock front and gain energy at the crossing. Also, only $\approx 1\%$ of the electrons will be aligned perpendicularly to the magnetic field, thus limiting the efficiency of the net energy gain (Wu, 1984). However, if a pre-energized spectrum of particles up to 100 keV is injected into the shock, particles could be accelerated up to 100 MeV via first-order Fermi acceleration. The stochastic acceleration can supplement the limited energy gain via first-order Fermi acceleration due to a cloud of magnetic mirrors.

Since the exact mechanism behind coronal heating is still an unresolved problem(mostly due to the observational capabilities of the current spacecraft), it is prudent to investigate the resultant radiation produced by the interaction of accelerated particles and the solar atmosphere. Two relevant wavelength regimes in this regard are the X-ray and radio emissions. Both these regimes act as direct indicators of accelerated particle and help decipher the conditions that existed at the acceleration site during their production.

1.4.1 X-ray emission from the Sun

Accelerated electrons will experience collisions in the partially ionized plasma of corona and Chromosphere, because of the Coulomb electrostatic force. During such a Coulomb collision, a small part of the energy is lost by the accelerated electron, which is radiated as a photon. An electron will undergo several such collisions in a field of ions, effectively experiencing a collisional drag force. As a result, the electron slows down until it is completely thermalized. Thus the radiation resulting out of this process is known as 'bremsstrahlung' which is a German word for braking radiation. Bremsstrahlung radiation is the predominant way of producing X-rays in the solar atmosphere and can result via both electron-electron and electron-ion interaction. The bulk of X-ray radiation below $\sim$ 300 KeV results from electron-ion interactions. In the most elementary model of X-ray emission,(called the Lorentz model) background electrons needed for a neutral plasma are ignored. Thus electron-ion collision assumes preference over electron-electron collision. Since the atomic number Z is large, the heavy ion target could be considered stationary with respect to fast electrons (Fig 1.8. The cross-section σ_R of this scattering is given by the Rutherford formula(Lifshitz et al., 1995),

$$\sigma_R = \frac{4\pi Z e^2}{M^2 v_e^4} \int_{b_{min}}^{b_{max}} \frac{db}{b} \tag{1.11}$$

Here e is the charge of the electron in esu, M is the reduced mass which comprises of the mass of electrons m_e in grams and the mass of proton m_p,and v_e is the electrons speed in cms^{-1}. The collision is characterized by b, the impact parameter which is a measure of the

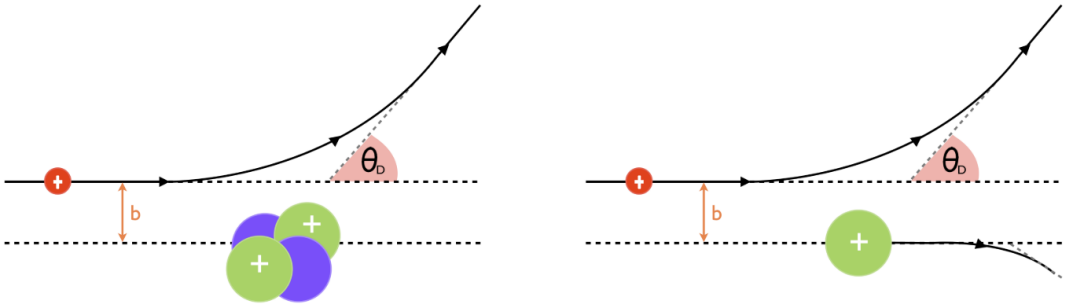

Fig. 1.8 Left: Collision as considered in the Lorentz model. The heavy-ion is unperturbed by the proton. Right: However, in actual collisions, both the particles are perturbed, and momentum is transferred. Figure credit: Natasha Jeffrey

closest approach between ion and the electron. The integral

$$ln\,\Lambda = \int_{b_{min}}^{b_{max}} \frac{db}{b} \tag{1.12}$$

is defined as Coulomb logarithm lnΛ. The Coulomb logarithm gives a quantitative measure of net deflections for a range of impact parameters from an arbitrary b_{min} to $b_{max} = \lambda_D$, where λ_D is the Debye length. For a fully ionized plasma, a value of $\ln\Lambda \sim 20$ is often used. As mentioned earlier, an electron traversing through a column of ionized plasma, will experience a net collision drag. The Lorentz collisional time, which is defined as the timescale for the particle momentum to reach zero in the direction of travel is given by,

$$\tau_0^{-1} = \nu_0 = n_i v_e \sigma = \frac{4\pi n_e Z e^4 ln\Lambda}{m_e^2 v_2^3}. \tag{1.13}$$

Unlike the special case of electron-ion collision considered, electron-electron and ion-ion collisons also occur in the solar corona. Timescales for these collisions can be written as,

$$\tau_{ee}^E : \tau_{ii}^E : \tau_{ei}^E \sim 1 : \left(\frac{m_i}{m_e}\right)^{1/2} : \left(\frac{m_i}{m_e}\right) \tag{1.14}$$

It is clear from the above equation that e-e collision exhibit the quickest equilibration time. In other words the accelerated electrons lose energy fastest via electron-electron interaction. The energy loss rate for e-e collisions then can be written as

$$\frac{dE}{dt} = -\frac{E}{\tau_{ee}} = -\frac{2E}{\tau_0} = -\frac{2E\Gamma}{v_e^3} = -\frac{Kn_e}{E} v_e \tag{1.15}$$

where K = $\Gamma m_e^2/2n_e$. The electron energy loss after traveling along a distance z in the column from an initial energy E_0 is then given by,

$$E^2 = E_0^2 - 2K\int_0^z n(z')dz' \tag{1.16}$$

The term in the integral in the above equation denotes the column density. If the density is assumed to be uniform, then $N(z) = n_0 z$. Hence,an electron with inital energy E_0 will come to a complete stop after traveling a distance z_{thick} given by,

$$z_{thick} = \frac{E_0^2}{2Kn_0}. \tag{1.17}$$

Equation 1.17 describes the collisional thick-target scenario(Brown, 1971) which is often used to account for X-ray emission during solar flares. For typical chromospheric densities of $n_0 = 10^{13} cm^{-3}$, an electron with initial energy of 30 keV will be collisionally stopped after traveling just $\sim$ 400 Km. However in the corona where densities of $n_0 = 10^9 cm^{-3}$ are typical, the same electron will be stopped only after $\sim$ 30000 Kms.

An X-ray detector in space would be able to measure the angle-averaged X-ray flux I ($photons\ cm^{-2}\ s^{-1}\ keV^{-1}$) produced by an electron distribution($electrons\ cm^{-2}\ s^{-1}\ keV^{-1}$) undergoing Coulomb collisions in the solar atmosphere as (Kontar et al., 2011)

$$I(\varepsilon) = \frac{1}{4\pi R^2}\int_\varepsilon^\infty \int_V n(r)F(E,r)\sigma(\varepsilon,E)dEd^3r \tag{1.18}$$

where R = 1AU is the Sun-Earth distance, ε is the photon energy in keV, V is the emission volume in cm^3, n is the number density in cm^{-3}, r is the position on the Sun, and σ is the bremmstrahlung cross section. The goal of detecting the X-ray flux I is to recover the electron flux distribution F. For the studies conducted in this thesis, X-ray data is taken from RHESSI spacecraft and its analysis is described in chapter 2.

1.4.2 Radio emission from the solar corona

Radio emissions, in general, are classified into coherent and incoherent emissions. **Incoherent emission**(or continuum emission) results from thermal bremsstrahlung - in which electrons and ions in the upper solar atmosphere undergo collisions interacting with heavy ions and emit thermal X-rays(free-free emission). **Coherent emission** is produced when plasma moving parallel to the magnetic field develops kinetic instabilities. Since the underlying particle population responsible for these emissions depends on the local plasma and magnetic conditions, different regions in the Sun have dominant emission modes. Studying

coherent radio emission enable us to trace even small populations of non-thermal electrons. Radio emission is also a valuable tool to detect the transport electrons across different layers of the solar atmosphere and even into interplanetary space.

The two major characteristic frequencies important for radio emission with regards to the solar atmosphere are: the electron plasma frequency given by

$$\nu_p = \frac{\omega_p}{2\pi} = \sqrt{\frac{n_e e^2}{\pi m_e}} \approx 8980\sqrt{n_e}\ Hz \tag{1.19}$$

and the electron gyro-frequency given by,

$$\nu_g = \frac{\omega_p}{2\pi} = \frac{eB}{2\pi m_e c} \approx 2.8 \times 10^6 BHz. \tag{1.20}$$

Here n_e is the local plasma frequency, e and m_e are the electron charge and mass and B is the magnetic field strength.

In this thesis, we focus on coherent radio emission from the solar corona to understand particle acceleration and transport in the solar atmosphere. Coherent emission involves the formation of beam distributions, which in turn leads to emission of Langmuir waves. These Langmuir waves couple with a pre-existing population of low-frequency waves to produce the observed radio emission. Since the radio emission is coherent, the observed brightness temperatures are high(they can be as high as 10^9 to 10^{10} K. Radio bursts produced by such mechanisms come in a variety of forms according to how they behave in the frequency space. They are classified according to their frequency drift rate as type I, II, III, IV and V (Wild et al., 1963b)(Fig 1.9). Within these broad divisions, there are variations in the behaviour, and they can be further subdivided. Here we focus only on type I and type III emission.

Type I emission is the most commonly observed and are associated with active solar regions. They are also known as solar noise storms. They consist of short narrow-band spikes often called bursts superposed on top of a slowly varying continuum. They persist for hours and even days in some cases. The bursts represent small particle-acceleration episodes and hence carry important information regarding the underlying processes involved.

Type III emissions are associated with travelling electron beams and can originate from their passage either in the corona or the interplanetary plasma. We concentrate here primarily on IP type III emission. Electrons emanating from the acceleration site in the solar corona often escape into the IP medium streaming along the Parker spiral with a velocity ≈ 0.3 c. They develop bump-in-tail instability in the velocity space, which generates Langmuir waves. These waves undergo nonlinear wave-wave coupling with pre-existing low-frequency waves to produce electromagnetic emissions at the local plasma frequency.

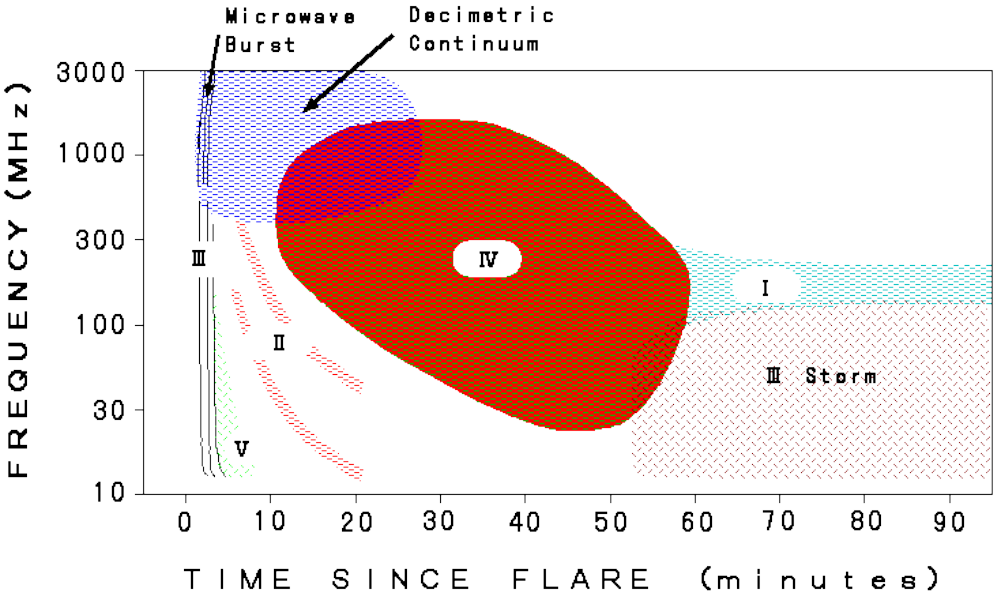

Fig. 1.9 Type of radio bursts. Figure credit: NICT Japan

1.5 Solar Energetic Particle (SEP) events

In a typical energy release event in the solar corona $\sim 10^{30-35} electrons\ s^{-1}$ are typically produced at the acceleration site (Krucker et al., 2007). These particles are often accelerated to near-relativistic velocities and are an example of the efficient particle acceleration processes prevalent in the solar corona. In big flares and CMEs, most of the accelerated particles participate in heating the ambient plasma. However, some particles can access open magnetic field lines and escape outwards into interplanetary space. If these particles are travelling towards Earth, they can be detected by detectors onboard near-earth spacecraft. Their arrival at 1AU is marked by a significant increase in the flux level of the particles compared to the background solar-wind in the time-series data measured by the detectors. They have been known since their first detection using the Interplanetary Monitoring Platform(IMP) satellites in 1966(Lin, 1970). These events are often called Solar Energetic Particles (SEP)(Fig 1.10).

SEPs are the only direct measurements of the particles accelerated at the Sun. Energy spectra of the SEP at 1AU contains information regarding their acceleration mechanism, coronal transport, injection characteristics into the heliosphere and interplanetary transport. Decoupling these effects using the measured spectra is a matter of ongoing research. Initially, the solar sources responsible for SEP generation were not obvious. However, with advances in remote sensing observations, we now know that two major sources of SEP events are flares and CMEs. SEP association with solar events is usually done by 1) checking for temporal association in electromagnetic emissions with the inferred release times of SEP and

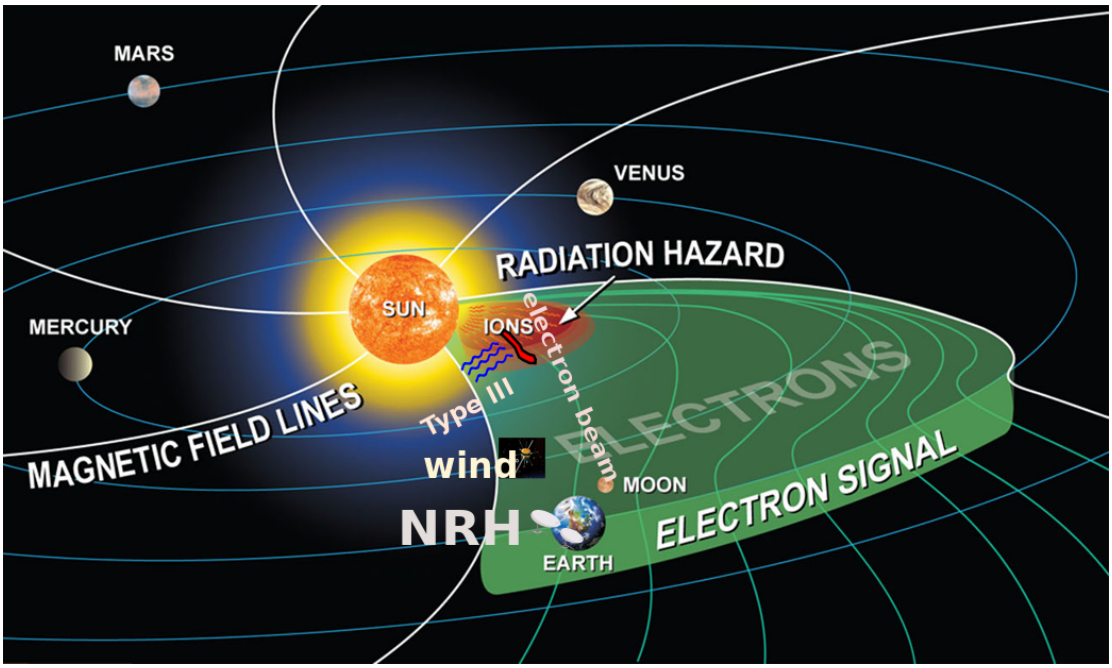

Fig. 1.10 The cartoon shows an electron beam travelling along the Parker spiral magnetic field line towards the Earth. Type III emissions are formed when the electron beam interacts with the plasma. These emissions are detected by Nancay Radio Heliograph. Thus type III emissions are a good indicator of interplanetary transport of energetic particles. These particles are later detected in-situ by particle detectors onboard spacecrafts such as WIND. Figure courtesy of NASA and modified.

2)spectral shape characteristics of the event measured at 1AU. Reames (1990) showed that SEP's usually fall into two categories, classified according to their time duration -'impulsive' and 'gradual' events. The proposed classification grouped all the flare accelerated SEPs as impulsive and CME shock accelerated SEPs as gradual. This suggested that there is two distinct acceleration mechanism at play(Fig 1.11). Recent observations suggest this classification is relevant for extreme cases and an average SEP will be created by a mix of impulsive acceleration (similar to that in flares) and gradual shock acceleration(similar to that observed in CMEs)(Kallenrode, 2003). Currently, there is a host of spacecraft capable of detecting SEP events near-Earth(ACE, WIND, STEREO). Bigger events are capable of accelerating particles to GeV energies which (if directed towards Earth) can be detected on Earth as Ground Level Enhancements(GLEs) by neutron monitors. Several studies have reported the existence of delayed events. Using data from ACE for 79 beam like events, Haggerty and Roelof (2002) found a median delay of 9.5 minutes between the inferred injection times at the Sun for the SEP electrons and start of type III emission. The cause for these apparent delays is not certain, though many mechanisms like coronal shocks, delayed reconnection and particle propagation effects etc. have been proposed(Cane, 2003). One of

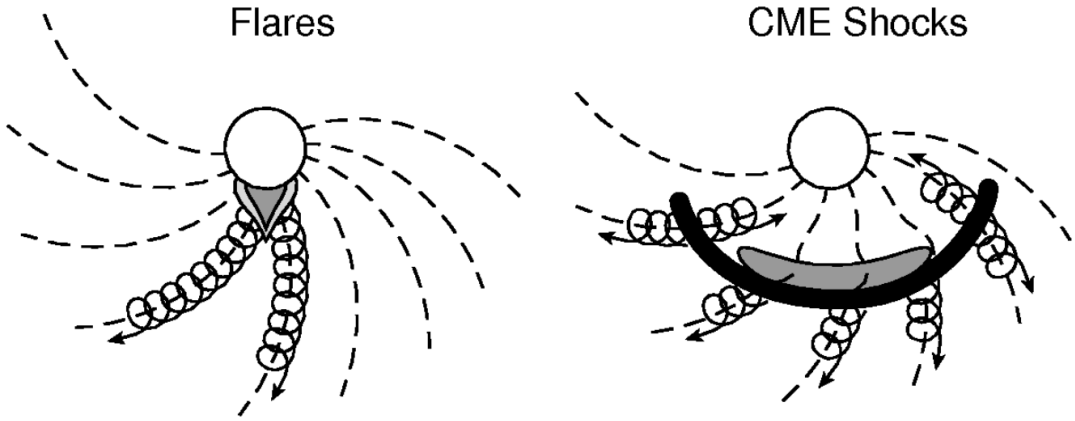

Fig. 1.11 Impulsive and Gradual SEP event acceleration scenarios. SEP's accelerated in flares are 'impulsive' in nature with small duration, small decay constant. Acceleration of impulsive events happens much lower in the corona and are rarely associated with CME's. Gradual SEPs, on the other hand, is always associated with CMEs. They are much longer in duration and have large decay constant. Figure credit: Reames (2013)

the aims of this thesis is to study the transport effects and the apparent delays it can cause on SEP particles during its propagation phase. For this, we use pitch-angle scattering based Monte-Carlo simulations.

SEPs carries particular significance in relation to space weather hazards. They can cause severe radiation damages to humans living in space, as well as result in higher radiation dosages in high-altitude flights. SEPs resulting out of big flares(like the Carrington event) would not be stopped by the Earth's magnetic field and can create havoc in power-grid transformers, microelectronic chips and thereby disrupting normal life as we know it. Many studies have focussed on forecasting SEPs with the aim of giving enough time for the operators of spacecrafts and humans in space to take corrective and evacuation measures with limited success (Kahler, 2005; Laurenza et al., 2009; Leka and Barnes, 2007; McIntosh, 1990; Swalwell et al., 2017).

1.6 Thesis Outline

As outlined in the previous sections, understanding particle acceleration and propagation in the solar atmosphere and the heliosphere is crucial to aid our understanding regarding coronal heating. We have carried out studies using observational data from multiple space and ground-based instruments and combined it with theoretical models and simulations to get a better picture regarding the processes involved.

In **Chapter 2** we survey small electron acceleration events which were detected near Earth. This is relevant, given the importance of small acceleration events in possibly heating the corona. Combining observations from multiple instruments, we estimate the electron acceleration energetics involved in such events. We also quantify similarities and differences with large SEPs.

In **Chapter 3** using the high temporal solar radio noise storm data, and high spatial resolution observations of the noise storms, we constrain the power input of such weak electron acceleration events. Noise storm bursts closely resemble nanoflares, which are postulated to be tiny reconnection events that deposit energy that heats the corona.

In **Chapter 4** our focus was on events which had simultaneous HXR and in-situ electron observations. HXR observation, in combination with type III burst occurrence, is a good proxy for electron injection into the corona and interplanetary space during an energy release process. We also investigated whether the HXR producing electrons and the 1AU electrons belonged to the same parent populations by comparing their respective spectral indices and other physical properties.

Chapter 2

Survey of small electron acceleration events

2.1 Introduction

The solar corona is a few hundred times hotter than the underlying layers of the solar atmosphere.Since it is farthest away from the Sun's core,(which is the primary energy source), this seems to defy the second law of thermodynamics. This phenomenon discovered over five decades ago is termed the coronal heating problem for which we don't have a complete understanding as yet. There are two major candidates for coronal heating - magnetic reconnection and waves. A likely scenario is one in which the solar corona is being repeatedly being heated by a combination of particle acceleration and bulk heating of plasma arising from magnetic reconnection. Such reconnection episodes often result in large eruptive phenomena such as flares and coronal mass ejections(CMEs). They have been studied extensively using a variety of ground and space based instruments and we now know that they release energies ranging from 10^{22} to 10^{33} ergs/s. The is the free magnetic energy that is pumped into the corona as a result of magnetic reconnection. Large flares usually release 10^{30} to 10^{33} ergs/s. However, in this chapter we study the particle acceleration aspects of small reconnection events which release $< 10^{26}$ ergs/s. Since the power involved in such events is almost six orders of magnitude smaller than that for large flares, they are known as microflares. The major motivation for focusing on smaller transient events is because they are more common than bigger ones - although they are harder to detect. Since large flares are quite infrequent they cannot account for steady-state coronal heating- the relatively more frequent micro and nanoflares are better candidates. Flares are one of the most efficient particle acceleration phenomenons known in the universe, and can accelerate electrons to over

1 GeV and ions to over 100 MeV. A large fraction of this released energy is manifested in the form of energetic particles resulting in non-thermal particle distributions (Aschwanden, 2012; Aschwanden et al., 2017; Holman et al., 2011; Kontar et al., 2011; Miller et al., 1997; Vilmer, 2012; Zharkova et al., 2011). Hence it is important to investigate the particle acceleration characteristics of smaller events which will enable us to better understand how energy is deposited in the corona, eventually heating it to a million K.

The underlying reservoir for such particle acceleration events is generally understood to be the excess energy stored in stressed magnetic fields, that is released via the process of magnetic reconnection. This scenario is supported by a host of theoretical and observational studies (Kontar et al., 2017). Such studies combined with simulations are slowly improving our understanding of particle acceleration processes in reconnection regions(e.g. (Arzner and Vlahos, 2004; Dahlin et al., 2015; Vlahos et al., 2016) and references therein). Parker (1988) postulates that continual shuffling of magnetic field footpoints in the photosphere would lead to frequent small-scale reconnection events that give rise to nanoflares. Nanoflares have since gained considerable momentum as potential candidates for coronal heating (e.g. Barnes et al. (2016); Klimchuk (2015) and references therein). Recent simulations have demonstrated the spontaneous development of current sheets with a high filling factor, even away from magnetic nulls (Kumar and Bhattacharyya, 2016b; Kumar et al., 2015); these current sheets can serve as potential sites for small electron acceleration events. However, since these nanoflares are very small, it is very difficult to observe them directly (e.g. (Joulin et al., 2016; Testa et al., 2013)), and one can only make indirect inferences about them. There are only a few claims in the literature regarding detection of nanoflare (or even smaller) energy releases at radio wavelengths (Mercier and Trottet, 1997; Ramesh et al., 2012). In most instances, the observation and interpretations are concerned only with the radiative signatures arising from the electrons that are accelerated by the reconnection episodes.

To illustrate this point, it is instructive to outline how a flare is thought to work. The shuffling motions of the magnetic footpoints in the photosphere leads to storage of energy in stressed coronal and chromosphere magnetic fields. The stressed fields tend to relax to a lower energy state via magnetic reconnection which dissipates the excess magnetic energy. This dissipated energy is used to accelerate electrons to energies greater than 20 KeV within a short time span. Most of these accelerated electrons will precipitate down to denser layers of the solar atmosphere along the magnetic field lines and interact with ambient electrons and protons, producing hard X ray bremsstrahlung radiation. However, a fraction of these accelerated electrons will escape into the interplanetary medium through open magnetic field lines. These escaping electrons will eventually arrive at 1AU where instruments aboard spacecraft such as ACE,STEREO etc will detect them in-situ. We are concerned with the

second stage of the reconnection-electron acceleration-observed radiation chain. In this chapter, we study the energy budgets and other characteristics of accelerated electrons.

Since our focus is on small reconnection events,we only study impulsive electron events detected at 1 AU that are unaccompanied by soft X-ray flares and CMEs, (e.g. (Simnett, 2005)), so that we can be reasonably sure that the energy releases involved are indeed small. Electron beams travelling outwards through the corona have well-established radio signatures, called type III bursts in the corona (e.g. Saint-Hilaire et al. (2012); Vilmer (2012)), and interplanetary (IP) type III bursts in the IP medium (Krupar et al., 2014, 2015). There is recent evidence for very weak type III bursts (Beltran et al., 2015; Cairns et al., 2017; Sharma et al., 2018) that could provide interesting information regarding the relatively weak events that generate the electron beams responsible for this emission. One of the most interesting questions that could be asked regarding the particle acceleration aspects of the flares relates to the number of electrons accelerated. It is also important to understand if there are any differences in how energy release and subsequent transport happens in smaller reconnection events compared to larger flares.These aspects have been studied in the past for bigger flares and a comparison with our study(which concerns only smaller flares) will help in better understanding the particle acceleration mechanisms.

2.2 Event Shortlisting

Solar transient events result in broadband radiation. Different wavelengths arise from different physical processes, and hence to get a complete picture, it is essential to use multi-wavelength studies. Further, particles that are accelerated in the transient events often escape into interplanetary space. Energetic electrons are often detected near earth by particle detectors on-board satellites. These electrons form a part of energetic particles (electrons + protons + ions) which are collectively called Solar energetic particles (SEP) event. SEPs are normally associated with transient events such as flares and CMEs. These particles are regularly accelerated to near-relativistic energies of over 100 KeV. Hence to understand the process of particle acceleration in flaring process it is important to do a simultaneous study of all the detectable signatures from the event, viz hard X-rays(HXR), soft X-rays(SXR) , coronal and interplanetary radio emission and particles detected in situ near the earth. We carried out an extensive survey using data from several instruments spanning the years 2004–2015, which covered the maxima of solar cycles 23 and 24 (and the intervening minimum) to find small transient events.We only study impulsive electron events detected at 1 AU that are unaccompanied by big flares or CMEs, so that we can be reasonably sure that the energy releases involved are small. Since our focus was on small events, our

search centered around small impulsive electron events observed in situ at 1 AU by the Electron,Proton and Alpha Monitor(EPAM) detector aboard the Advanced Composition Explorer(ACE) spacecraft. We next give brief descriptions of the instruments used to detect the energetic electrons.

2.2.1 Detecting electron events

The Advanced Composition Explorer (ACE) spacecraft was launched on August 25,1997 on-board a Delta II rocket. ACE is an Explorer mission that was managed by the Office of Space Science Mission and Payload Development Division of the National Aeronautics and Space Administration (NASA). To not contaminate the magnetic measurements to be carried out by different instruments on the spacecraft, it traveled over a million kms to reach Earth-Sun Libration point(L1) where it will be far away from Earth's magnetic field. By orbiting at L1, ACE will be in constant communication with NASA's deep space antennas as the Earth orbits around the Sun. Using its six advanced sensors and three monitoring instruments ACE measures solar wind,interplanetary magnetic field and SEPs accelerated by transient events and gives a comprehensive picture of the heliosphere and factors affecting Sun-Earth interaction. The ACE mission is currently into its 20th year is expected to and continue till $\sim$ 2022. ACE is a spin-stabilized satellite with a spin period of 12s(5 rpm).

For measuring SEPs, we use data from the Electron,Proton and Alpha Monitor(EPAM) instrument on-board ACE.EPAM was developed by John Hopkins University(JHU)/Applied Physics Laboratory(APL) from the flight spares of the HI-SCALE instrument flown aboard Ulyesses. The EPAM is composed of five telescope apertures of three different types. Two Low Energy Foil Spectrometers (LEFS) measure the flux and direction of electrons above 30 keV (geometry factor = 0.397 cm^2sr), two Low Energy Magnetic Spectrometers (LEMS) measure the flux and direction of ions greater than 50 keV (geometry factor = 0.48 cm^2sr), and the Composition Aperture (CA) measures the elemental composition of the ions (geometry factor = 0.24 cm^2sr). The telescopes use the spin of the spacecraft to sweep the full sky. Solid-state detectors are used to measure the energy and composition of the incoming particles.

Of the two electron detectors (LEFS60 and LEMS30) we only used data from the electrons detectors on LEMS30. The LEMS30 sensor is oriented 30°from the spin axis of the satellite. The LEMS30 telescope measures energetic (0.047–4.75 MeV) ions and non-relativistic (38–315 keV) electrons in twelve energy channels (four for electrons and eight for ions). A rare-earth magnet in front of the LEMS30 detector sweeps out any electrons with energy $\leq$ 500 keV. These electrons are measured in the B detector referred as DE30 (Deflected Electrons). The DE30 detector measures pure electrons with a geometric factor of 0.140

cm^2sr within a full-cone opening angle of 51°. For an SEP event to be shortlisted we required that there should be clear signatures in the first three energy channel of the LEMS30 electron detector, namely DE1,DE2 and DE3. Taken together these three channels covered a energy range of 38-173 KeV. In terms of particle velocities this is equivalent to 0.39c to 0.62c (where c is the speed of light). We furthermore require that these impulsive electron events are

- not associated with large GOES soft X-ray flares or CMEs,
- associated with IP type III bursts, and
- associated with reliable west limb signatures in RHESSI HXR data.

We also searched the Solar Geophysical Data data base (for events prior to 2009), USAF-RSTN and e-CALLISTO data for possible association with microwave bursts, which would indicate chromospheric activity. None of the events we shortlisted were associated with microwave bursts. The lack of chromospheric activity suggests a coronal origin for these events, as does the steepness of the energy spectra e.g. (Potter et al., 1980). We describe the shortlisting process in more detail below.

2.2.2 Onset at the Sun

The release time of the accelerated electrons at the Sun could be inferred from the observations at 1AU.The impulsive electron events are detected at 1 AU in four energy channels by ACE/EPAM. Each of these energy channels can be associated with with an average electron speed v(E). On plotting t_{1AU} against c/v we obtain t_{sun} as the intercept on the time axis and L/c as the slope of the plot (Krucker et al., 2007; Krucker et al., 1999; Potter et al., 1980). Here L is the path length taken by the electrons to travel from the Sun to 1 AU. In order to accurately measure the energy spectrum of the detected electrons,we have excluded events that were not clearly resolved in the first three energy channels of ACE/EPAM. The arrival time of the electrons at 1AU t_{1AU} is related to the release time at the Sun t_{sun} by:

$$t_{1au} = t_{sun} + \frac{L}{v(E)} \tag{2.1}$$

The expected arrival times for each energy channel are plotted as colour coded dashed lines in the ACE/EPAM panel of Fig 2.1. We make two important assumptions:

- Particle injection at the sun is impulsive and energy independent
- Particles initially detected by the instrument at 1 AU traveled scatter free along a path of length L.

2.2.3 Shortlist 1: Non association with CMEs and GOES flares

CMEs and flares can produce energetic particles which can escape into the interplanetary medium through open magnetic field lines and get detected near earth as Solar Energetic Particle(SEP) events. Particles from SEPs have been measured by a fleet of in-situ instruments aboard satellites like ACE,STEREO,Ulyesses, Wind. It is thought that there are generally two distinct classes of SEP particle populations - the flare accelerated particles(FAPs) and particles accelerated at CME shocks(PACs). These two distinct classes were initially identified from their light curve characteristics:flare accelerated particles are typically impulsive and CME shock accelerated particles are usually gradual. Impulsive events have sharp rise and decay times while gradual events often show a ramp like rise profile followed by a long decay of tens of minutes or even hours. We now understand that these distinct classes of SEPs are not mutually exclusive as previously thought. The magnetic energy at the acceleration site is converted into energetic particles by a combination of mechanisms that produce a mix of impulsive and gradual acceleration processes. Since the aim of our study was to understand these acceleration mechanisms in small reconnection events, we only focus on those events that have no associations with CMEs and big GOES flares. For studying such association we used data from two instruments- the Large Angle Spectrometric Coronograph(LASCO) on board the Solar and Heliospheric Observatory(SOHO) for CME data and X-ray Sensor(XRS) measurements on-board Geo-Stationary Orbiting Earth Satellite(GOES) for SXR flare data. Here we give a short summary of both the instruments.

2.2.4 The SOHO/LASCO instrument

The SOHO mission was a joint project between NASA and ESA, launched on December 2, 1995. Though designed for a nominal mission life of two years, it continues operating, making it the longest serving heliophysics space mission till date. SOHO was placed in the L1 point which is located 1.5 million kilometers from Earth. Thus SOHO shares the same spatial region as ACE spacecraft. Our instrument of interest, LASCO is a wide-field white light and spectrometric coronagraph which consists of three telescopes with a combined observing heliocentric distance range of 1.1 $R_{\odot}$ to 32 $R_{\odot}$. The three telescopes that make LASCO are C1(which spans 1.1 to 3.0 $R_{\odot}$), the C2(which covers from 2.0 to 6.0 $R_{\odot}$) and C3 (which covers the outer corona from 3.7 to 32 $R_{\odot}$). The LASCO team maintains a database of detected CMEs from the instrument called the SOHO LASCO CME CATALOG. This database contains all CMEs manually identified since 1996 using the data from C2 and C3 telescopes. Each recorded CME has a list of attributes such as the height time measurments, acceleration,mass, kinetic energy etc. The CME height-time measurements and acceleration

data could be used to interpolate the position of CME relative to injection site of particles. We used data from this catalogue for identifying potential associations of SEP events with CMEs.

2.2.5 The GOES satellites

The GOES missions are a joint effort of NASA and the National Oceanic and Atmospheric Administration(NOAA). GOES satellites operate in a geo-stationary orbit above the continental United States with the aim of continuously providing climate data for weather prediction and to extend knowledge of the atmosphere and its processes. The GOES-12 and subsequent satellites carries Soft X-ray Imager(SXI) instrument and Space Environment Monitoring(SEM) instruments. These instruments enable continuous monitoring of the Sun at Xray wavelengths and helps in predicting and monitoring solar flares. GOES X-ray flux measurements are being made since 1974 using the XRS instrument. There are two XRS instruments aboard each GOES satellite, providing solar soft X-ray fluxes for the wavelength bands of 0.5 to 4 A (short channel) and 1 to 8 A (long channel). The data from the long channel which covers the range 1-8 A($\sim$1.6-12.4 keV)of SXR flux is used to classify flares. The GOES class is a logarithmic scale with letters A,B,C,M and X representing the exponents of SXR fluxes of 10^{-8} to 10^{-4} W/m^2 with the mantissa signifying the sub-scale. For example if the SXR flux value is 1.4×10^{-7}, the corresponding flare class is B1.4. Anything above $10^{-4} W/m^2$ is considered to be X class.

To check CME associations we crosschecked with the CME catalogue to identify CMEs within $\pm$ 20 minutes of the identified onset time($t_{\odot}$). The evaluation was particularly strict for west limb eruptions. Any SEP event which had any CME(even a small one)within this 20 minute window was rejected. We also note that the CME accelerated particles are usually gradual SEPs, and hence any SEP event which didn't show sharp rise and fall characteristics were also rejected. To check flare association, we looked for any co-incidental GOES flares above C1 class. This means that the flux registered in the SXR instrument $< 10^{-6} W/m^2$ throughout the impulsive HXR phase.

This shortlisting procedure yields a data base of 18 events from 2004 to 2015,the details of which are summarized in Table 2.1.This includes seven out of the nine events reported by Simnett (2005). The column titled 'Onset at GOES' gives the time when one can discern a rise in the GOES soft X-ray flux. As the entries under the column titled 'GOES flux level' indicate, none of the GOES soft X-ray enhancements are above the C1.1 level. The column 'Onset at ACE-DE4' indicates the time of the peak value in the ACE/EPAM DE4 energy channel(mean energy 275 keV).

Table 2.1 Event Shortlist after the first two criterions. The asteriks marks the final shortlisted events.

Event Date	Onset at Sun (t_{sun}) (UT)	Onset at GOES (UT)	GOES flux level	Type III onset at WIND/WAVES (UT)	SEP onset at ACE-DE4 (UT)
Feb 28,2004*	03.24	03.24	B6.6	03.25	03.36
Mar 16,2004*	08.56	no-data	C0.1	08.57	09.12
June 26,2004	20.50	nil	B2.1	20.51	21.13
June 26,2004*	22.50	22.50	B2.2	22.51	23.02
June 27,2004*	02.03	02.02	B1.1	02.03	02.17
June 27,2004	04.59	05.01	B1.1	05.01	05.19
June 27,2004	13.02	13.01	C0.0	13.02	13.21
June 27,2004	14.59	nil	B1.1	15.01	15.26
June 27,2004	17.43	nil	B1.1	17.43	18.10
Dec 25,2004*	16.49	16.50	B0.0	16.49	17.03
Dec 25,2004*	22.29	22.29	B0.1	22.29	22.43
Mar 16,2005	23.03	23.02	B1.3	23.02	23.19
Jan 13, 2007	15.10	15.11	B2.2	15.12	15.21
Feb 18, 2010	18.58	18.56	A9.1	18.59	19.14
Mar 28, 2014	20.57	20.58	C0.0	20.58	21.18
Jan 20, 2015	09.48	09.49	B9.1	09.50	10.05
May 14,2015	05.08	05.10	C0.6	05.10	05.23
May 14,2015	07.28	07.29	C1.0	07.29	07.40

2.2.6 Shortlist 2: Association with IP type III bursts

The electron beams escaping from the sun will induce radio emissions called type III bursts which serve as an important diagnostic for understanding electron acceleration and transport. Type III bursts have fast drift rate($df/dt \sim 100MHzs^{-1}$) in comparison with other solar radio transients like Type I and Type II. The drift rate gives an indication of the speed of exciting electron beam. The presence of these radio Type III bursts signifies that the accelerated electrons are traveling through open-magnetic field lines towards the Earth. We used data from WAVES instrument aboard WIND satellite. WIND is a spin stabilized spacecraft launched on November 1,1994 and currently placed in orbit around the L1 Lagrange point, making it the second spacecraft in our study sharing the same orbital location.

2.2.7 The WIND/WAVES instrument

The main mission objective is to study Solar wind and its effect on magnetosphere of the Earth. The WAVES instrument on the WIND spacecraft provides coverage of radio and plasma wave in the frequency range of 10 kHz to about 14 MhZ for the electric field. Developed as a joint collaborative effort between Paris-Meudon Observatory, the University of Minnesota and the Goddard Space Flight Center, it consists of two stacks of primary sensors - three electric dipolar antenna systems(E_x, E_y, E_z), of which two are co-planar and three magnetic search coils (B_x, B_y, B_z) mounted orthogonally. For our analysis we use the data measured by the Radio Receiver Band 1(RAD1) and Radio Receiver Band 2(RAD2). RAD1 covers a frequency range of 20 kHz - 1040 kHz and RAD2 covers a range of 1.075 MHz - 13.825 MHz.RAD1 radio receivers use two super-heterodyne receivers operating in its frequency response range with one connected to E_z electric dipole antenna and the other to summation between E_z and any of the E_x or E_y antenna. RAD2 receiver also uses a two heterodyne system but for the summation used only E_y with E_z antenna. We checked for associated type III burst for all the events shortlisted in Table2.1. We find that all the events have a type III burst coinciding with the flare onset. This is an indication that the electrons were injected into interplanetary medium during the flaring process.

2.2.8 Shortlist 3: Association with HXR emission

Accelerated particles emit hard X-ray bremsstrahlung upon undergoing collision with denser chromospheric plasma and thus these emissions serve as an important diagnostic to study particle acceleration process in these transient events. Hard X-ray observations can enable the determination of the electron energy spectra and their location.

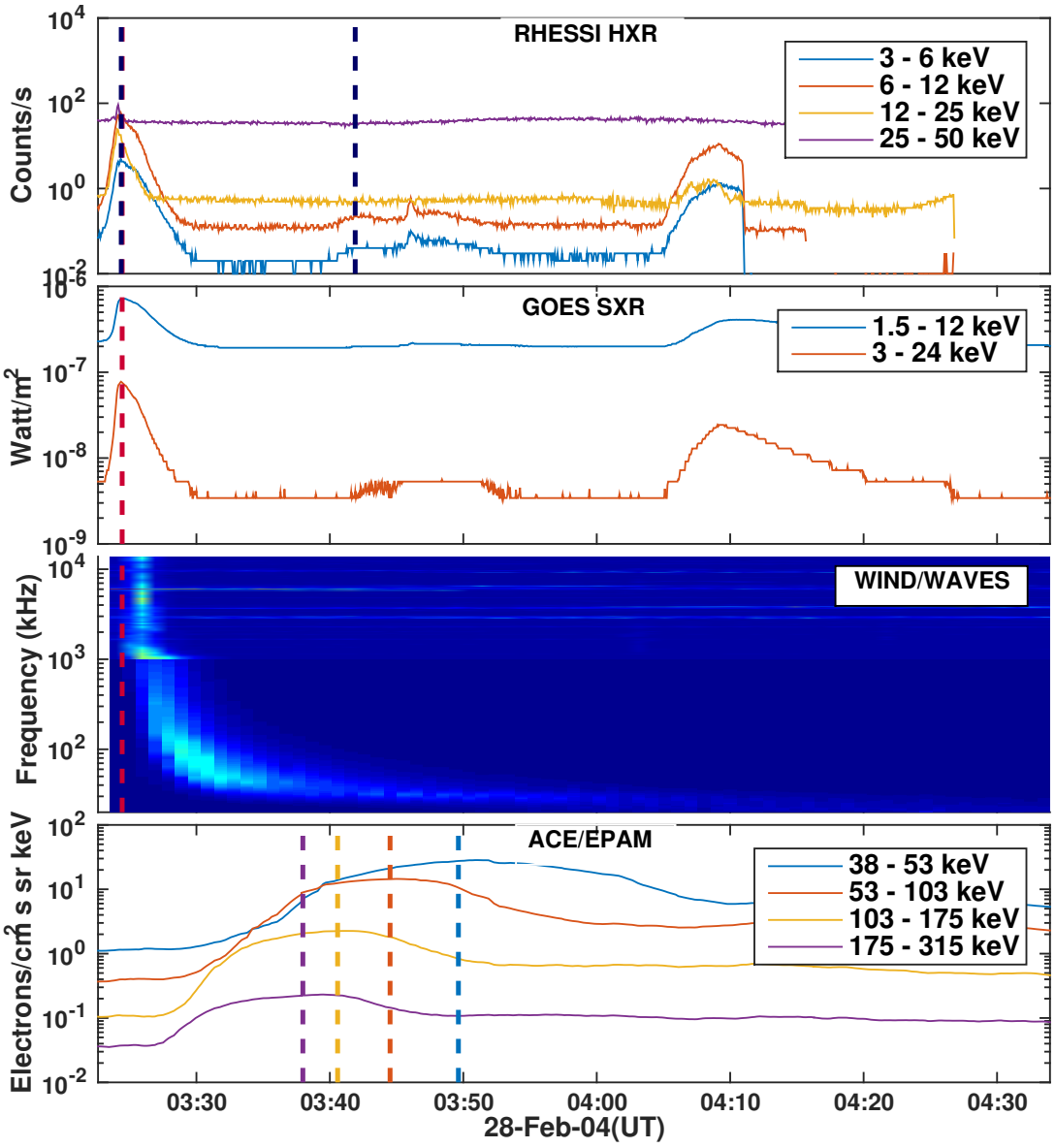
RHESSI HXR
3 - 6 keV
6 - 12 keV
12 - 25 keV
25 - 50 keV
Counts/s
GOES SXR
1.5 - 12 keV
3 - 24 keV
Watt/m2
WIND/WAVES
Frequency (kHz)
ACE/EPAM
38 - 53 keV
53 - 103 keV
103 - 175 keV
175 - 315 keV
Electrons/cm2 s sr keV
03:30
03:40
03:50
04:00
04:10
04:20
04:30
28-Feb-04(UT)

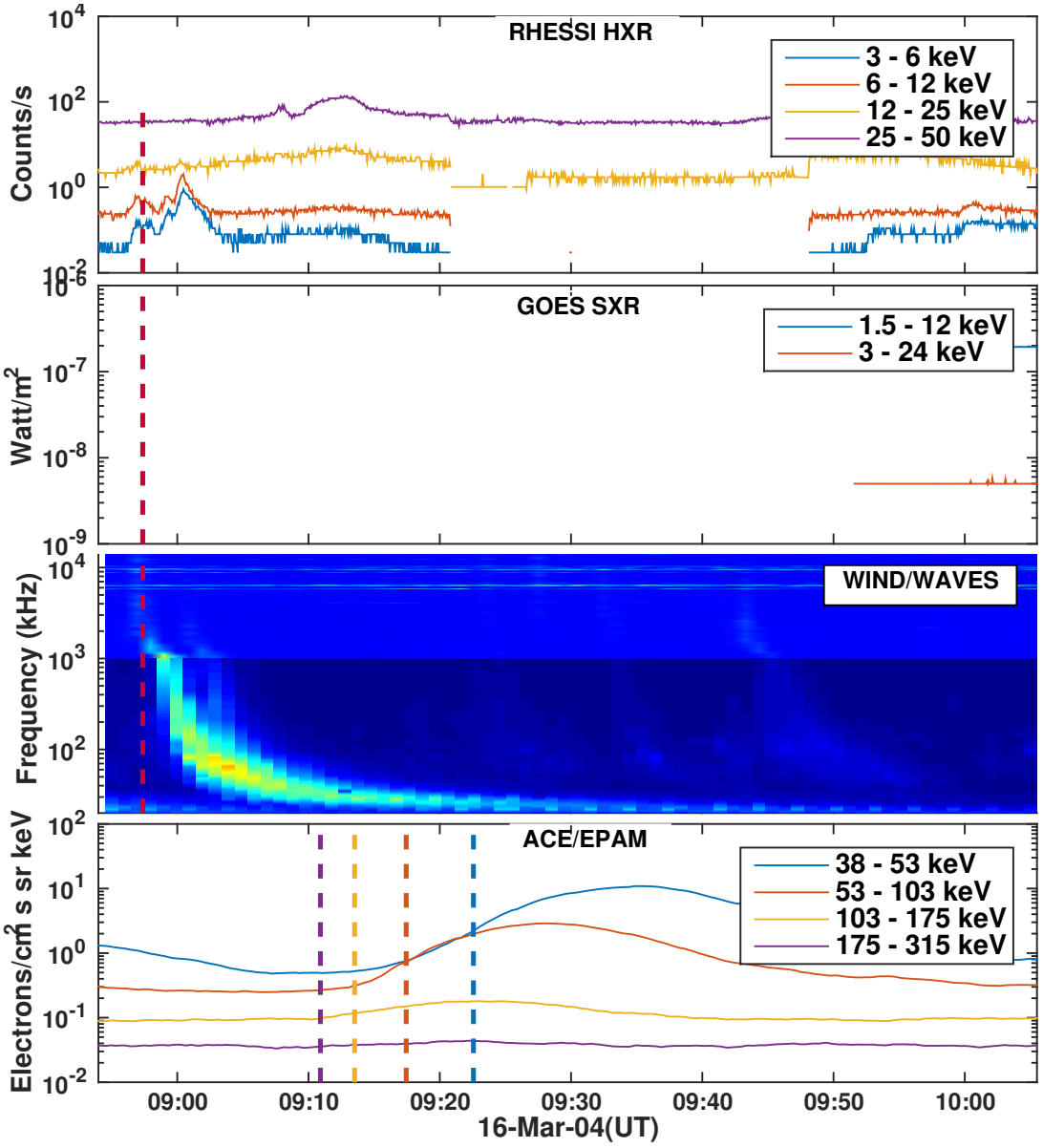
RHESSI HXR
3 - 6 keV
6 - 12 keV
12 - 25 keV
25 - 50 keV
Counts/s
GOES SXR
1.5 - 12 keV
3 - 24 keV
Watt/m2
WIND/WAVES
Frequency (kHz)
ACE/EPAM
38 - 53 keV
53 - 103 keV
103 - 175 keV
175 - 315 keV
Electrons/cm2 s sr keV
09:00
09:10
09:20
09:30
09:40
09:50
10:00
16-Mar-04(UT)

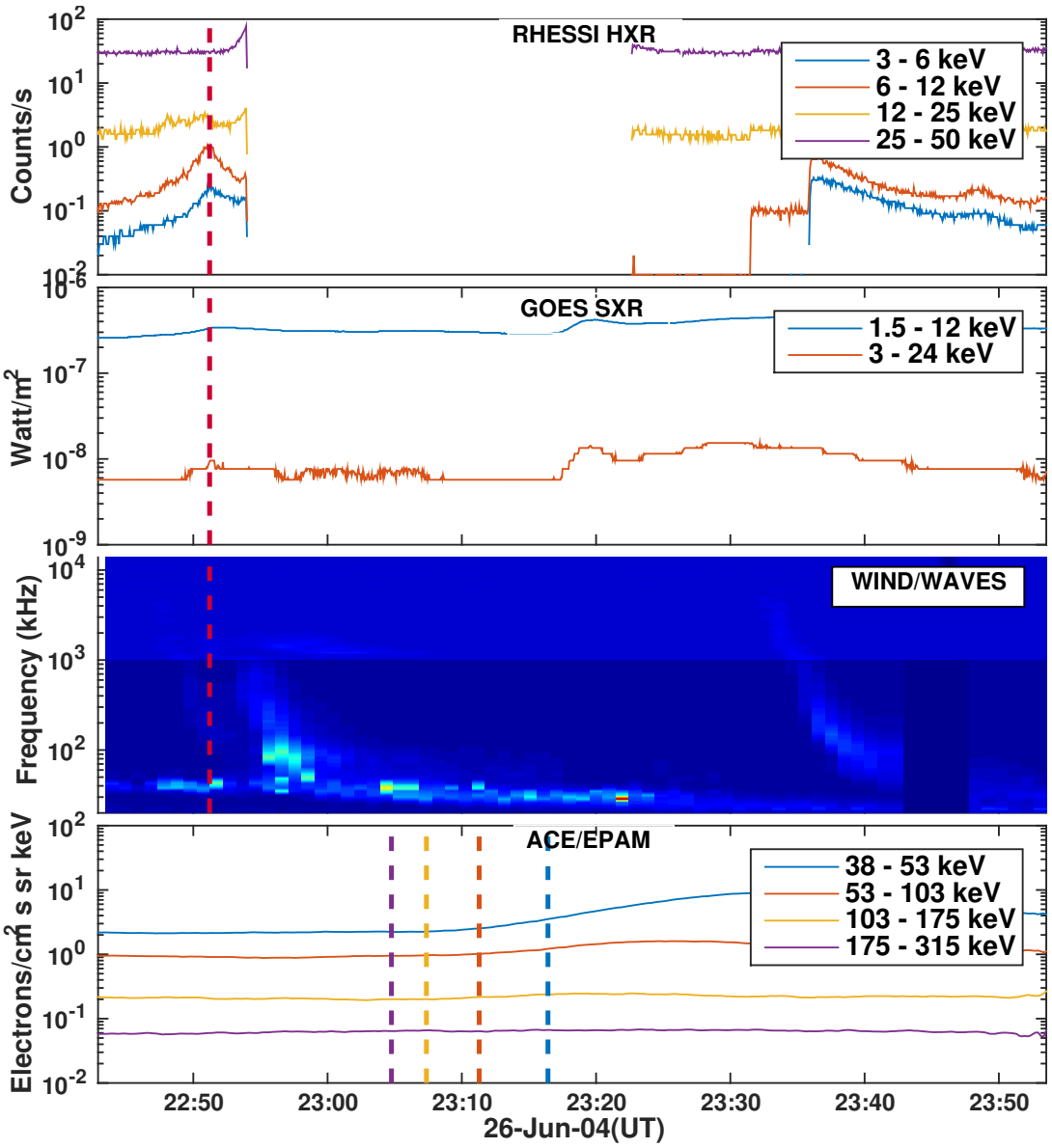
RHESSI HXR
3 - 6 keV
6 - 12 keV
12 - 25 keV
25 - 50 keV
Counts/s
GOES SXR
1.5 - 12 keV
3 - 24 keV
Watt/m2
WIND/WAVES
Frequency (kHz)
ACE/EPAM
38 - 53 keV
53 - 103 keV
103 - 175 keV
175 - 315 keV
Electrons/cm2 s sr keV
22:50
23:00
23:10
23:20
23:30
23:40
23:50
26-Jun-04(UT)

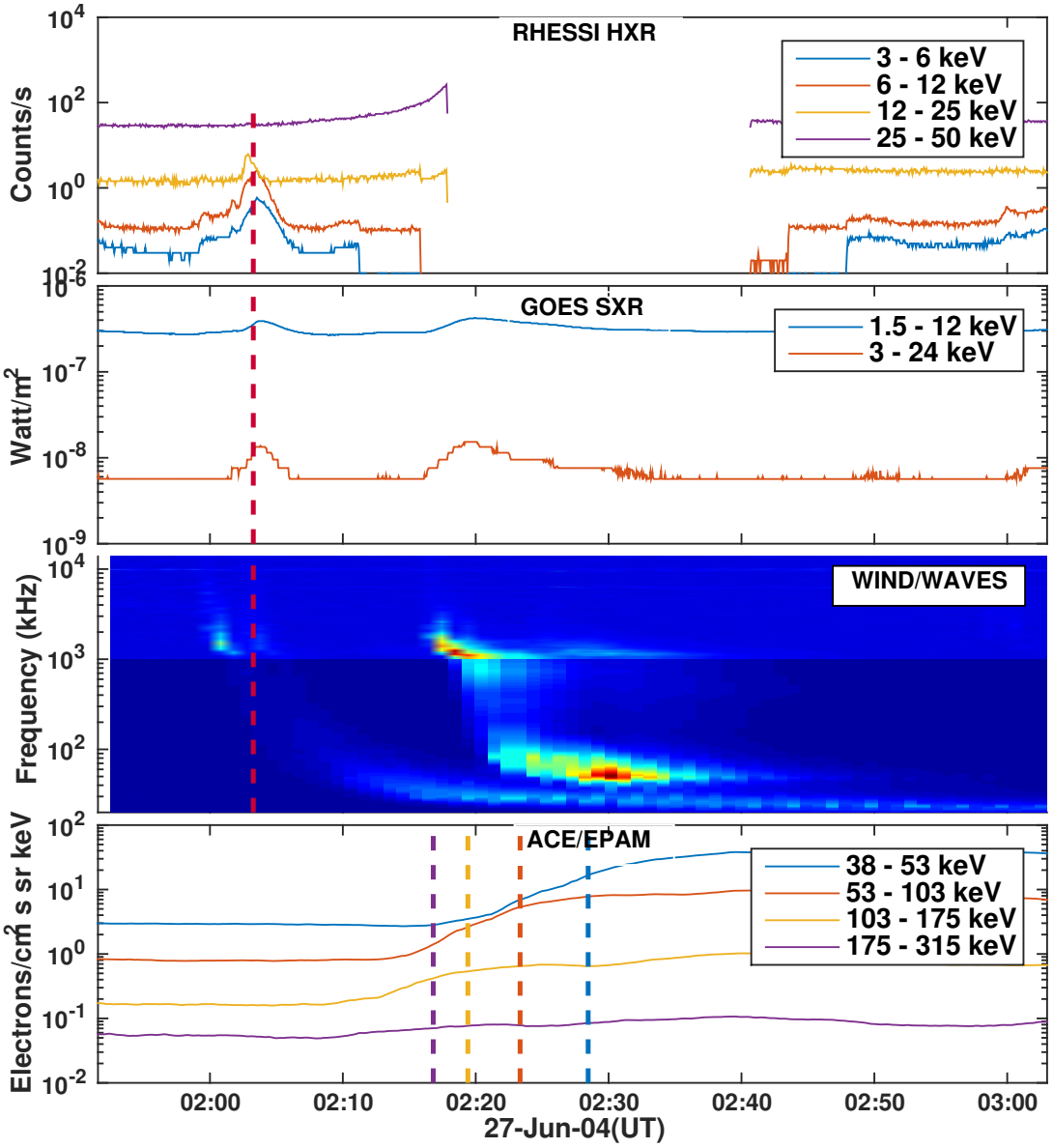
RHESSI HXR
3 - 6 keV
6 - 12 keV
12 - 25 keV
25 - 50 keV
Counts/s
GOES SXR
1.5 - 12 keV
3 - 24 keV
Watt/m2
WIND/WAVES
Frequency (kHz)
ACE/EPAM
38 - 53 keV
53 - 103 keV
103 - 175 keV
175 - 315 keV
Electrons/cm2 s sr keV
02:00
02:10
02:20
02:30
02:40
02:50
03:00
27-Jun-04(UT)

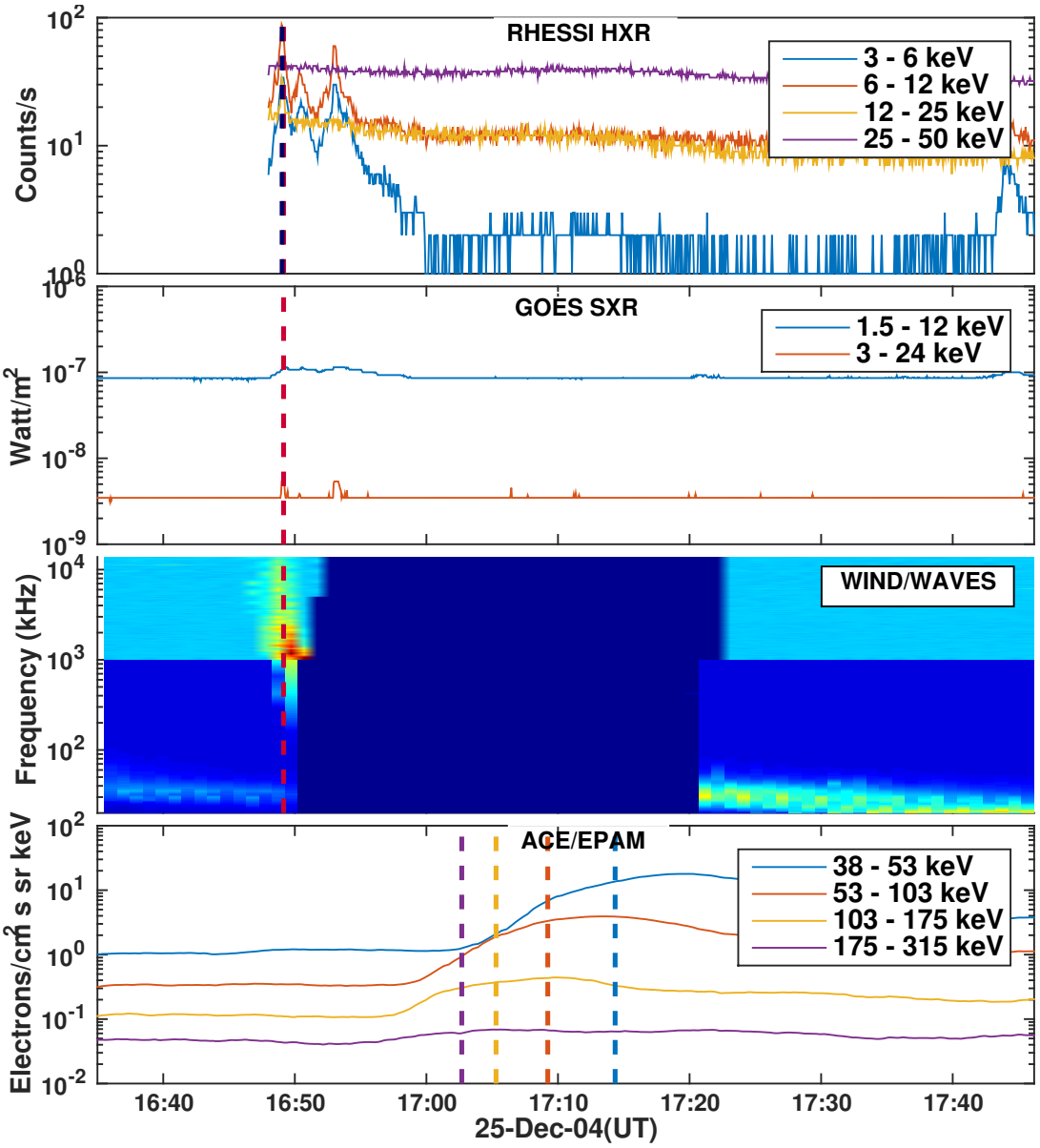
RHESSI HXR
Counts/s
3 - 6 keV
6 - 12 keV
12 - 25 keV
25 - 50 keV
GOES SXR
Watt/m2
1.5 - 12 keV
3 - 24 keV
WIND/WAVES
Frequency (kHz)
ACE/EPAM
Electrons/cm2 s sr keV
38 - 53 keV
53 - 103 keV
103 - 175 keV
175 - 315 keV
16:40
16:50
17:00
17:10
17:20
17:30
17:40
25-Dec-04(UT)

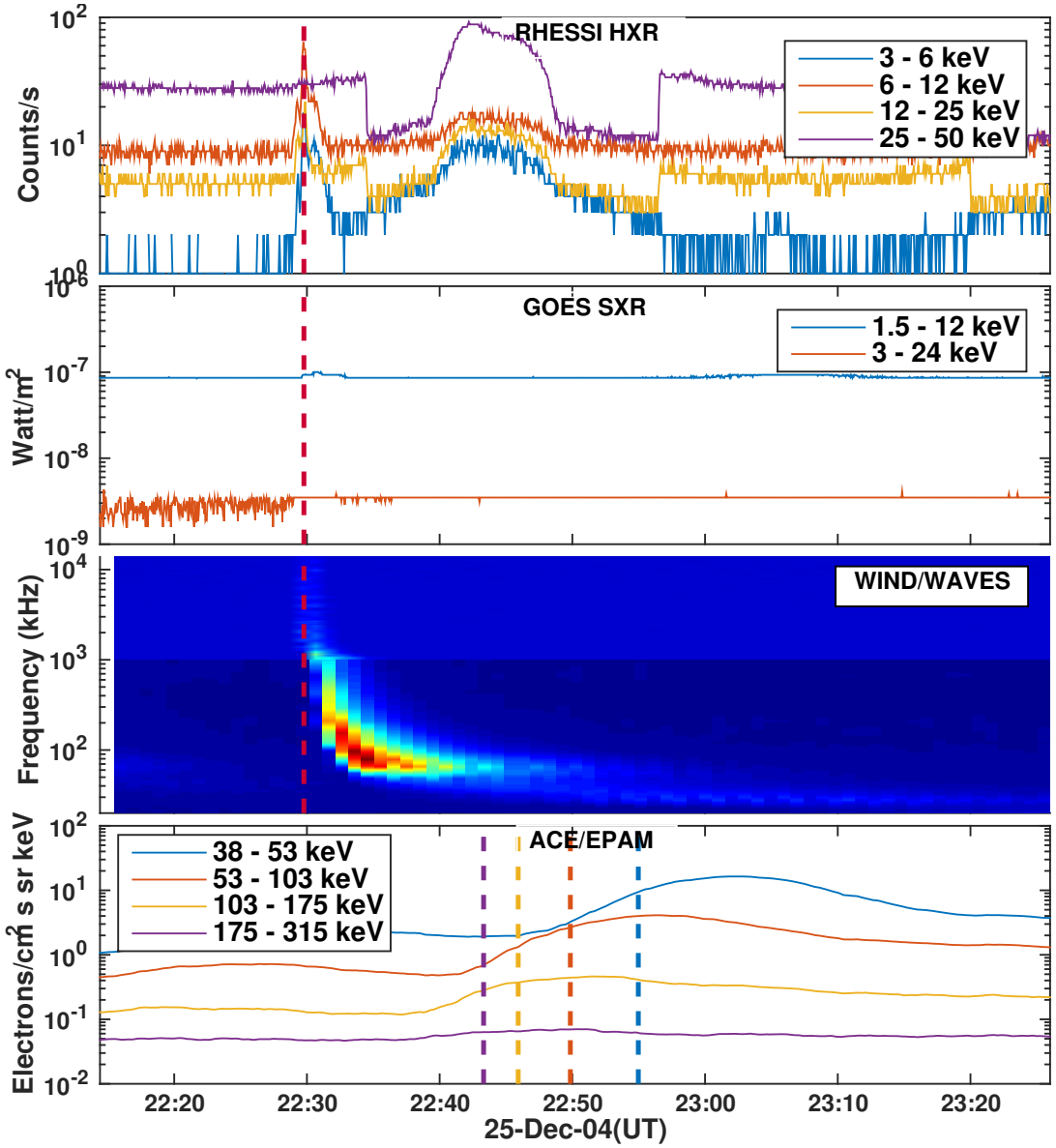

Fig. 2.1 Stacked plots for each of the six shortlisted events. The top panel shows the corrected RHESSI HXR photon counts. The dark red dashed line depicts the quantity t_{sun}, which corresponds to the peak of the HXR emission in the 12-25 keV channel. The dark blue dashed line depicts the timing of the HXR flare from the RHESSI flare list, (where available). Since our shortlisted events are very weak, only two events are found in the RHESSI flare list. The second panel shows the GOES SXR flux. The third panel is the WIND/WAVES dynamic spectrum, showing the interplanetary type III burst associated with each event. The bottom panel shows the time evolution of the electron flux in the four ACE/EPAM energy channels. The thick dashed lines correspond to the expected arrival times of the electrons in the different energy channels, assuming that they are released at t_{sun} and travel a distance of 1 AU.

RHESSI - HXR data

We use data from NASA's Reuven Ramaty High Energy Solar Spectroscopic Imager (RHESSI) for HXR observations. RHESSI was launch in February 2002 into a near-circular, 38°inclination orbit using a PEGASUS launch vehicle as part of NASA's Small Space Explorer's Mission (SPEX).RHESSI consisted of a imager which was made up of nine bi-grid rotation modulation collimators(RMCs), which was placed in front of nine cryogenically cooled germanium detectors(GeDs) with one for each of the RMC. The RHESSI is a spin-stabilized satellite with a rotation period of 4s. RHESSI was the first HXR instrument in space which offered excellent spatial($\sim$ 2 arcsec below 100 keV), spectral($\sim$ 1 keV FWHM) and temporal($\sim$ few ms) resolution. It was also able to observe over a wide range of energies compared to previous HXR missions(from $\sim$3 keV upto $\sim$17 MeV). An automated attenuator system placed on top of the detectors helped RHESSI to have high dynamic range ($\sim 10^7$) without saturation during intense flares. RHESSI was decommissioned on October 14,2008 after 16 years of service.

For our third and final shortlist we require that the shortlisted events using criterion mentioned in 1 and 2 have a discernible HXR signature located near the west limb of the Sun. This criterion criterion ensures that the events were well connected magnetically to the earth so that the escaped electrons could reach earth without much scattering. After this final criterion we have a list of six events, listed in Table2.2. The RHESSI team maintains a flare-list which automatically adds entries based on enhancements from the background levels. Only two out of the six events we shortlisted were in the flare-list. This is because the other four events were too faint to be included in the list.

2.3 Data Analysis

The stacked plots in Figure 2.1 give a consolidated view of the acceleration process by combining data from different instruments. The current model of a flare is as follows.Magnetic free energy released during magnetic reconnection accelerates particles and heats the ambient plasma. These accelerated particles travel downward and emit hard X-rays via thick-target Bremsstrahlung upon encountering the relatively dense chromosphere. Electrons which do not precipitate downwards and which have access to an open magnetic field lines instead will be injected into the interplanetary medium, exciting type III radio bursts and later detected near the Earth as SEP events.

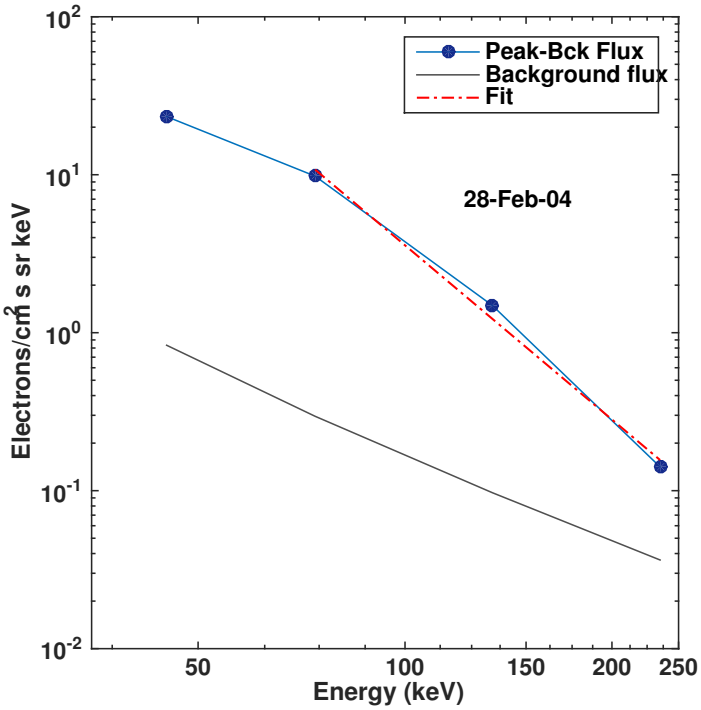
Peak-Bck Flux
Background flux
Fit
28-Feb-04
Electrons/cm2 s sr keV
Energy (keV)

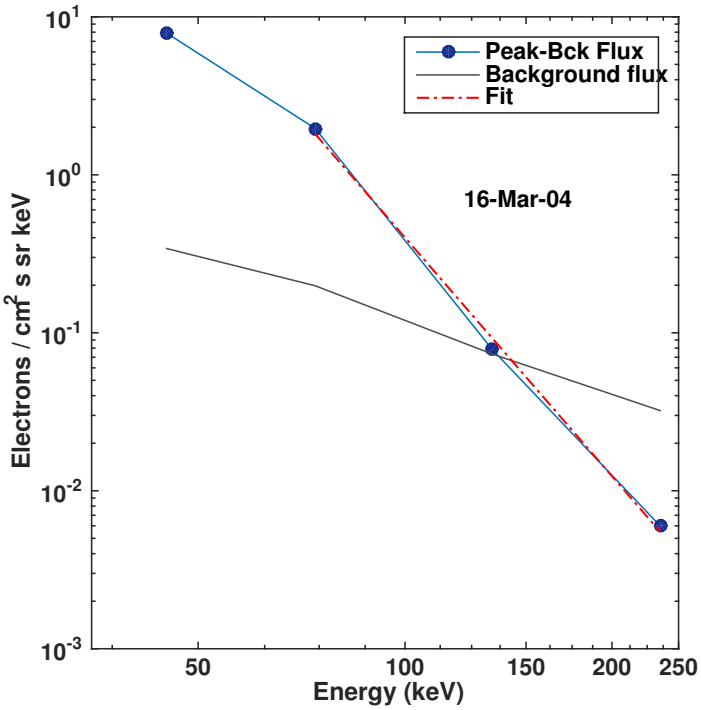
Peak-Bck Flux
Background flux
Fit
16-Mar-04
Electrons / cm2 s sr keV
Energy (keV)

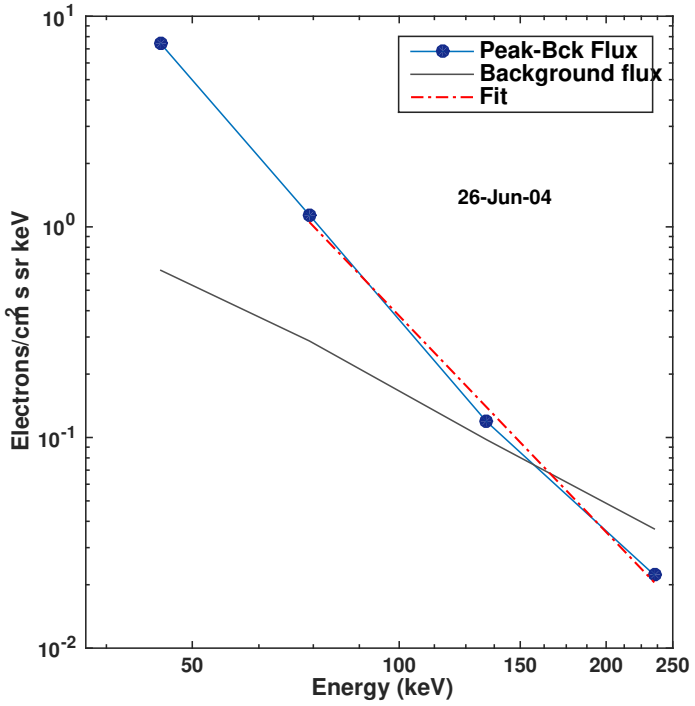
Peak-Bck Flux
Background flux
Fit
26-Jun-04
Electrons/cm2 s sr keV
Energy (keV)

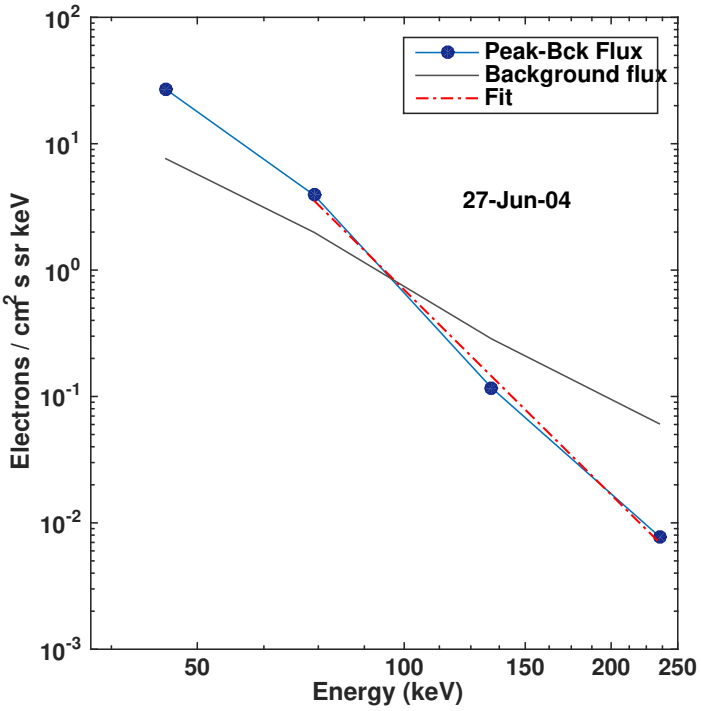
Peak-Bck Flux
Background flux
Fit
27-Jun-04
Electrons / cm2 s sr keV
Energy (keV)

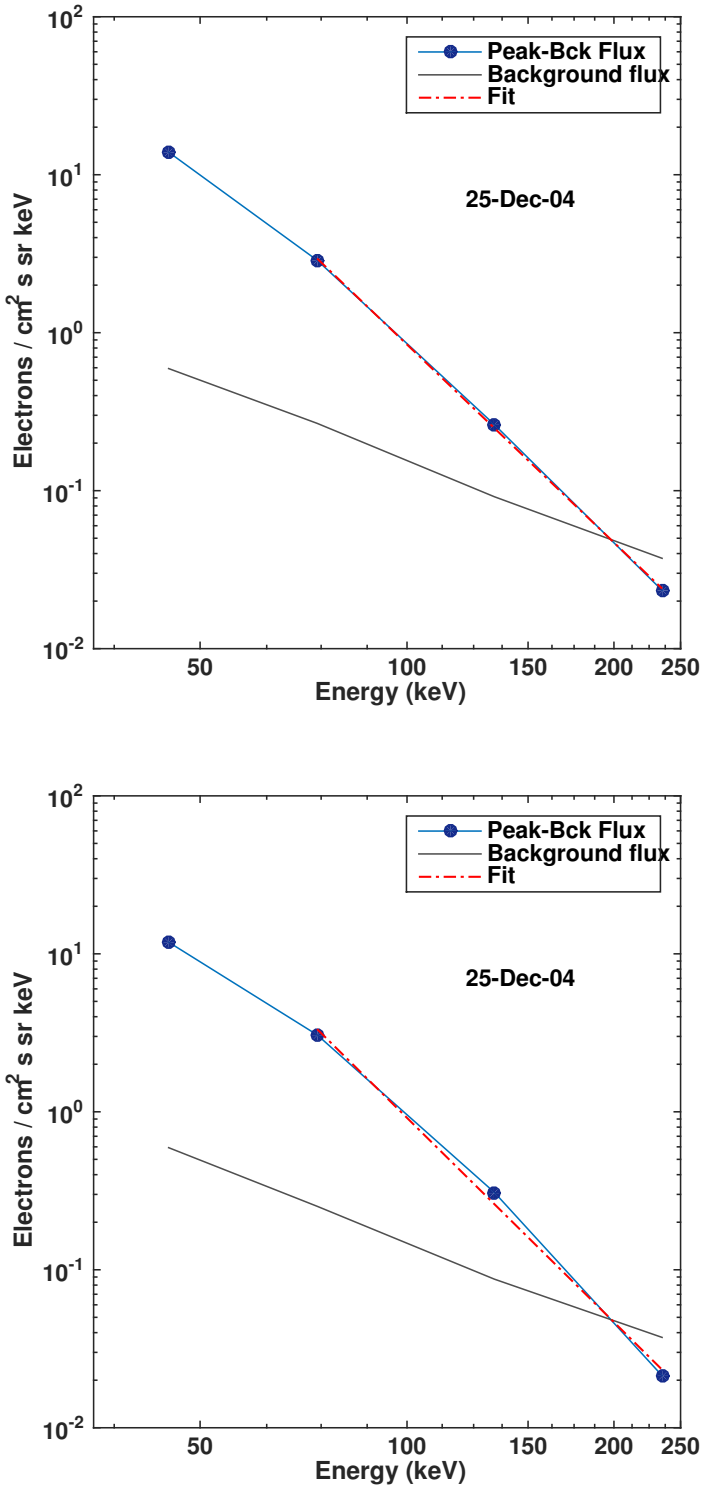

Fig. 2.2 Fits to the ACE/EPAM electron data for each of the six shortlisted events. The background spectrum was subtracted from the spectrum at the event peak.We observe a break in the spectrum for all the events at 74 keV. We fit a power law to the spectrum above the break. This is depicted by the thick blue line in the graphs. Results are tabulated in Table 2.2.

2.3.1 Escaping electrons detected at 1 AU

We use data from the four electron detectors DE1-4, which detects electrons with energies from 38 to 315 keV in the LEMS60 sensor of ACE/EPAM. The peak mean energies of the four channels are 45,74,134 and 235 keV. The differential energy spectrum of electrons can be represented as

$$dJ/dE \propto E^{\delta_{1AU}} \tag{2.2}$$

Here, J is the 12 second averaged electron flux from each of the four detectors with units $keV^{-1}cm^{-2}s^{-1}sr^{-1}$, and E is the peak energy of the channels in keV. The spectral index gives important clues regarding the physical process that accelerated the electrons. The power law fits for each event are shown in Fig 2.2. The values of δ_{1AU} are given in Table 2.2. The spectral index gives important clues regarding the physical process that accelerated them and also the origin of these particles. For example a soft spectra indicates the coronal acceleration of the particle while a harder spectra indicates that the particles are accelerated in a flare. We typically observe a break in spectra at around 74 keV. Since the energy resolution of the spectra is limited by the number of channels measuring the intensities of electrons this break has an error margin of 30 keV. By contrast, the break energy for electrons of SEPs associated with larger flares are around 40 keV(Krucker et al., 2007; Oka et al., 2013).

Number flux,power and energy in Escaping Electrons

Since a power law represents the electron distribution in the energy space adequately, we can write:

$$F(E) = F_0(E_0/E)^{\delta_{1AU}}, \tag{2.3}$$

where F(E) is the differential electron flux at 1 AU (electrons $keV^{-1}s^{-1}sr^{-1}cm^{-2}$). F_0 is the peak differential energy flux at a specific energy E_0. Thus the flux of the electrons above E_0 is simply the integral of the above equation. In other words,

$$\int_{E_0}^{\infty} F(E)dE = \frac{F_0E_0}{(\delta_{1AU}-1)} \text{ electrons}\,\text{s}^{-1}\,\text{sr}^{-1}\,\text{cm}^{-2}. \tag{2.4}$$

The electrons injected into the interplanetary medium usually spread by the time they arrive at 1 AU. We take this spread to be about a solid angle cone of of 30°(Krucker et al., 2007). Thus the total number of electrons crossing 1 AU is given by

$$\Omega(1AU)^2 \int_{E_0}^{\infty} F(E)dE = \Omega(1AU)^2 \frac{F_0E_0}{(\delta_{1AU}-1)}\ \text{s}^{-1},$$

Table 2.2 Final shortlist and spectral parameters

Date	RHESSI Peak Time(UT)	Flare Position Heliocentric x,y(arcsec)	γ	δ_{1AU}	δ_{hxr}
Feb 28,2004	03.24	697, 301	3.69	4.14	4.89
Mar 16,2004	08:56	841, -144	4.38	5.25	5.54
June 26,2004	22.50	943, -162	4.66	5.45	5.80
June 27,2004	02.03	931, -176	4.24	5.10	5.13
Dec 25,2004	16.49	552, -123	3.25	4.39	4.43
Dec 25,2004	22.29	598, -132	3.10	4.12	4.06

The power carried by these electrons is the first moment of the above distribution.

$$\Omega(1AU)^2 \int_{E_0}^{\infty} EF(E)dE = \Omega(1AU)^2 \frac{F_0 E_0^2}{(\delta_{1AU} - 2)} \ \mathrm{erg\,s^{-1}} \tag{2.5}$$

The total energy carried by escaped electrons could be estimated by multiplying the power given by the above equation with total duration of a particular event. The values for power($erg\ s^{-1}$) and energy(erg) is given in Table2.5.

2.3.2 HXR producing electrons

Xray emission from the accelerated electrons is produced when it undergoes deceleration upon encountering ions in the denser chromosphere. The electrons lose part of their kinetic energy and emit photons corresponding to the energy lost. If the electron undergoing bremsstrahlung remains free afterwards we call it a free-free emission; this is the dominant mode of hard X-ray emission. X-ray photons are produced in close-range interactions unlike radio bremsstrahlung photons which involve long-range interactions. The electron ion cross-section cannot be expressed analytically and thus an approximation is often used. The Bethe-Heitler approximation is often expressed in terms of initial electron and photon energies (cf. Brown (1971). It is given by

$$\frac{d\sigma_B}{d\varepsilon} = \frac{7.9 \times 10^{-25} Z^2}{\varepsilon E} ln \frac{1 + \sqrt{1 - \varepsilon/E}}{1 - \sqrt{1 - \varepsilon/E}} (cm^2/KeV) \tag{2.6}$$

where E is the initial electron energy and ε is photon energy. In general a correction factor known as Elwert factor is added to this cross-section to account for ionic Coulomb field interactions with the electron wave function.

Given bremsstrahlung cross-section it is possible to calculate the photon spectrum for a given electron spectrum. Alternatively, the photon spectrum can be inverted to find the electron spectrum. However, even small uncertainties in the photon spectrum can significantly change the determined electron spectrum even in moderate statistics case. Thus most HXR analyses use forward modeling, wherein a model electron spectrum is assumed and the observed photon spectrum is computed using different parameters until it fits the standard assumed spectrum. The model spectrum used in RHESSI contains two parts - Thermal and Non-Thermal.

In the thermal regime the electrons are assumed to be in thermal equilibrium,i.e a Maxwellian distribution with temperature T_e. Provided the temperature is high enough, the electrons will produce bremsstrahlung radiation upon colliding with ions which are assumed to be at rest. This is a valid assumption, because even at high temperatures the ratio of ion velocities to that of electron velocities is effectively zero owing to high electron to ion mass ratio. Integrating over all energies for an iso-thermal Maxwellian distribution yields a photon spectrum of the form:

$$I(\varepsilon) \propto Z^2 Q g(\varepsilon, T_e) \frac{exp(-\varepsilon/k_B T_e)}{\varepsilon\sqrt{T_e}} (photons/\ s/\ keV) \tag{2.7}$$

Here Q is the emission measure, which quantifies the amount of emission produced per unit volume:$Q \equiv \int_V n_e^2 dV$, where n_e is the electron density and V is the emitting volume. Here $g(\varepsilon, T_e)$ is a correction term called the guant factor to account for quantum mechanical effects which was ignored in the derivation of the above equation. Hence the parameters to fit the observed photon spectrum to the model electron spectrum in the thermal regime are source electron temperature and emission measure. If the volume(density) is assumed or estimated the density(volume) can be determined using observations.

In the non-thermal regime, a power law is often used to describe the electron population. The X-ray production happens via Coulomb collisions in this case. There are two cases of interest here: i) when electron energy loss timescale is less than the Coulomb timescale and ii)the electron energy loss timescale is greater than the Coulomb timescale. In the first case, (called thick target emission), electrons lose all their energy to collisions. This type of emission happens in high density areas such as the chromosphere. In the second case, electrons don't lose all the energy within the observed timescale or when a low density emission area such as the corona is involved.

HXR counts obtained from RHESSI for all the six events were analyzed using SSW/OSPEX software. Because all the events were weak, we used the maximum available integration time corresponding to the FWHM of the event to increase the count statistics. As mentioned above,

Table 2.3 Number of HXR producing and escaping Electrons

Date	Number of hxr producing electronsN_{hxr} (>74 keV)	Number of escaping electronsN_{esc} (>74 keV)	Escaping fraction $\eta = (N_{esc}/N_{hxr})\%$
Feb 28,2004	1.82×10^{33}	1.16×10^{32}	6.36
Mar 16,2004	3.60×10^{30}	5.35×10^{30}	148.3
June 26,2004	2.31×10^{31}	1.07×10^{30}	4.64
June 27,2004	5.21×10^{31}	6.03×10^{31}	115.7
Dec 25,2004	1.89×10^{32}	3.31×10^{31}	17.44
Dec 25,2004	8.57×10^{31}	3.65×10^{31}	42.62

the photon spectrum consists of a thermal core followed by a non-thermal tail. Only data from the front detectors of RHESSI was used as the rear detectors are tuned for photons above 200 keV. For determining the photon spectral index γ we applied a broken power-law fit to the tail and a variable thermal function to the core at low energies. The γ thus determined is listed in Table 2.2. If the population of electrons detected at 1AU is the same as that of the HXR site, Datlowe and Lin (1973) noted that a thick-target model for HXR emission should satisfy $\delta_{1AU} = \gamma + 1$, while for the thin-target model it should satisfy $\delta_{1AU} = \gamma - 1$.

From the calculated photon spectral index, γ and the the estimated spectral index of the escaping electrons δ_{1AU} we see both the quantities follow the relation $\delta_{1AU} = \gamma + 1$ with a correlation coefficient 0.86. This suggests that the HXR emission was produced via thick target mechanism. A thick target fit was then applied to the spectrum with a constant isothermal fit whose parameters were determined in the fit to estimate the γ and were held fixed for the current fitting of thick-target function. The thick target function gives the parameters - integrated electron flux at the HXR production site, injected electron spectrum which is determined by inverting the photon spectrum. The HXR electron spectrum, contains 5 parameters: the low energy cutoff, the break energy, the high energy cutoff, the power law index between the low energy cutoff and break energy and the one between break energy and high energy cutoff. The low energy cutoff is important to keep the energy finite in the powerlaw distribution. We denote the powerlaw index between the break energy and the high energy cutoff by δ_{HXR}.Fig2.6 shows a scatter plot between δ_{HXR} and δ_{1AU}. Both the quantities follow a linear relation with a correlation coefficient of 0.90. This suggests that the HXR producing population and the those detected at 1AU indeed have a common physical origin.

Number Flux, power and energy in HXR producing electrons

From the injection flux obtained from the thick target fit($\dot{N}_{>E_c}$), we could compute the number of electrons released above the break energy. To account for the fact that the we only calculate the flux of escaping electrons above 74 keV we scale the corresponding number of HXR electrons above 74 keV using:

$$\dot{N}_{>74keV} = \dot{N}_{>E_c}\left(\frac{E_c}{74}\right)^{\delta_{hxr}-1} \tag{2.8}$$

Following the same logic followed in the case in-situ SEP electrons 4.20 , the power in the HXR emitting electrons above E_c is given by

$$P_{HXR} = (74keV)\dot{N}_{>74keV}\frac{\delta_{hxr}-1}{\delta_{hxr}-2} \tag{2.9}$$

As before, in the case of escaping electrons, multiplying P_{HXR} by the total duration of the HXR emission yields the total energy in the non-thermal HXR producing electrons. These quantities are listed in Table2.5. From these quantities it is possible to estimate the ratio(η) of escaping electrons to the HXR producing electrons. We find that η for our events range from 6% to over 100%. Similar numbers reported for bigger flares are 0.01%-0.1%Krucker et al. (2007).

2.3.3 Thermal HXR emission

The thermal energy content of the HXR emission generated by the accelerated electrons, U_{th} is given by

$$U_{th} = 3k_BT\sqrt{\varepsilon_{em}V} \tag{2.10}$$

where ε_{em} is the emission measure and V is the volume of the region as discussed below. The emission measure is product of the electron density n_e,ambient plasma density n_i and the volume V. For doing this we make the assumption that, plasma filling factor ≈ 1. For finding V we fit a guassian to the 70% contour level of the HXR images. We used the PIXON algorithm for imaging. Pixon algorithm gives sharper images as compared to CLEAN algorithm. The volume was computed using the formula

$$V = A^{3/2} \tag{2.11}$$

Using this method we found the volume to be $\sim 10^{25}cm^3$ which is very low compared to volumes usually reported for radio noise storms(Subramanian and Becker, 2006) or large

Table 2.4 Fit Parameters of the Events

Date	Thermal Temperature(MK)	Emission Measure($10^{46} cm^{-3}$)	Energy Cutoff (keV)	Density of thermal plasma($10^{10} cm^{-3}$)	Volume ($10^{25} cm^3$)
Feb 28,2004	13.53	9.27	14.4	4.50	5.05
Mar 16,2004	11.08	0.95	12.34	3.33	0.86
June 26,2004	11.32	1.08	9.38	2.10	2.43
June 27,2004	11.50	1.73	10.01	2.34	3.15
Dec 25,2004	10.05	0.68	11.2	2.22	1.39
Dec 25,2004	10.23	0.13	10.89	0.84	1.78

Table 2.5 Energy characteristics of Events

Date	Energy in thermal HXR emission (ergs)	Energy contained in HXR electrons (ergs)	Energy carried away by escaping electrons (ergs)	Power in HXR electrons (ergs/s)	Power in escaping electrons (ergs/s)
Feb 28, 2004	1.06×10^{28}	5.79×10^{26}	3.38×10^{25}	1.69×10^{24}	9.07×10^{21}
March 16,2004	1.19×10^{27}	1.69×10^{24}	4.94×10^{24}	1.18×10^{23}	8.78×10^{20}
June 26,2004	2.40×10^{27}	9.94×10^{24}	1.05×10^{23}	4.17×10^{23}	4.89×10^{21}
June 27,2004	3.51×10^{27}	1.18×10^{25}	9.55×10^{24}	1.15×10^{23}	5.39×10^{21}
Dec 25,2004	1.28×10^{27}	2.16×10^{25}	7.32×10^{24}	1.08×10^{23}	3.15×10^{21}
Dec 25,2004	6.48×10^{26}	1.02×10^{25}	6.05×10^{24}	3.87×10^{23}	3.26×10^{21}

flares(Krucker et al., 2007; Lin and Hudson, 1971). We note that this value is similar to those reported of smallest of microflares (Hannah et al., 2008). Using the emission measure thus determined as parameters for the thermal fit to the HXR spectrum and the ambient plasma density n_i determined from the thick target fit, we calculate the electron density n_e. The emission measure was found to be $10^{45} cm^{-3}$ for all events. The ambient plasma density was found to be $\sim 10^{10} cm^{-3}$ for most events. Using these values, the typical background electron densities are $\sim 10^{10} cm^{-3}$. These numbers are a magnitude higher than that of 'cold flares' as reported by Fleishman et al. (2011). The total thermal HXR energy thus calculated is $\sim 10^{28}$ erg.The values for the emission measure, ambient plasma density and volume for each event are tabulated in Table 2.4.

2.3.4 Summary

In this chapter we have investigated the energy budgets involved in small electron acceleration events in the solar corona. The events show very little soft-Xray emission and hence they closely resemble the cold,tenuous flares reported by Fleishman et al. (2011, 2016). The spectral indices of the escaping electrons (detected at 1AU) and of the downward precipitating ones(inferred from the HXR emission),suggest that they arise from the same population. We also compute the number of electrons, power and total energy involved in these events both at the HXR production site as well as in the escaping population. We observe that the ratio of number of escaping electrons to that of HXR electrons range from 6% to over 100%. By comparison this ratio is only $\sim 0.2\%$ for large flares (Krucker et al., 2007). The total energy in the HXR producing electrons is $\approx 10^{24}$ – 10^{26} while the same for electron population that escaped into the interplanetary medium is $\approx 10^{23}$ to 10^{25} erg.

Since the events under our study are not associated with any flares or CMEs,small-scale magnetic reconnection in the high corona is the only possible driver behind the generation of these events. Even without the presence of big transient events we observe particles accelerated to near-relativistic energies. Further study of these events including imaging studies are necessary to properly understand how particle acceleration in these events proceed. Studying such events might help throw more light onto the energy release mechanism of even small events like the nanoflares which are thought to ultimately heat up the corona to the observed temperatures.

This study is limited by the sensitivity of the current instruments.Current instruments are not able to resolve coronal loop strands where tiny magnetic reconnections actually occur. Availibility of instruments capable of resolving the individual magnetic strands in combination with instruments that can simulatenously measure plasma structures from the

chromosphere to the corona can be more insights into how acclerated particles play a major role in these small scale energetic events.

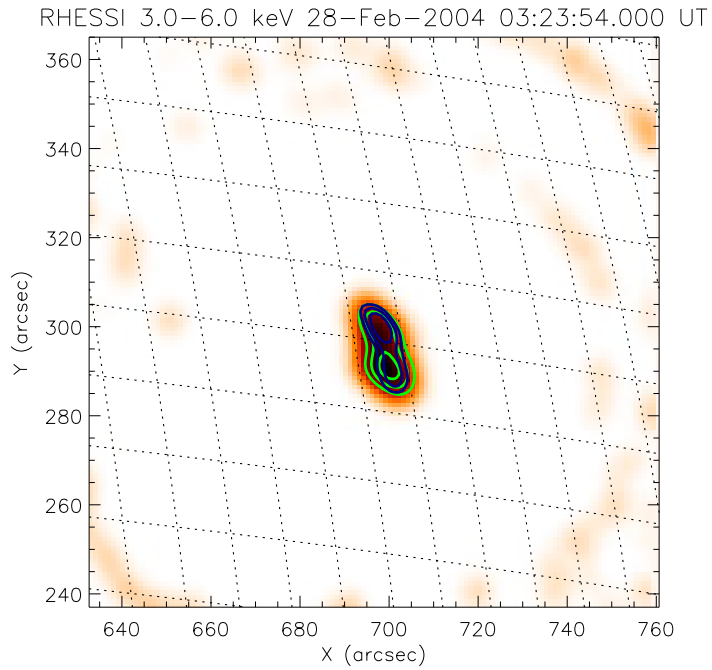

(a) 2004 Feb 28

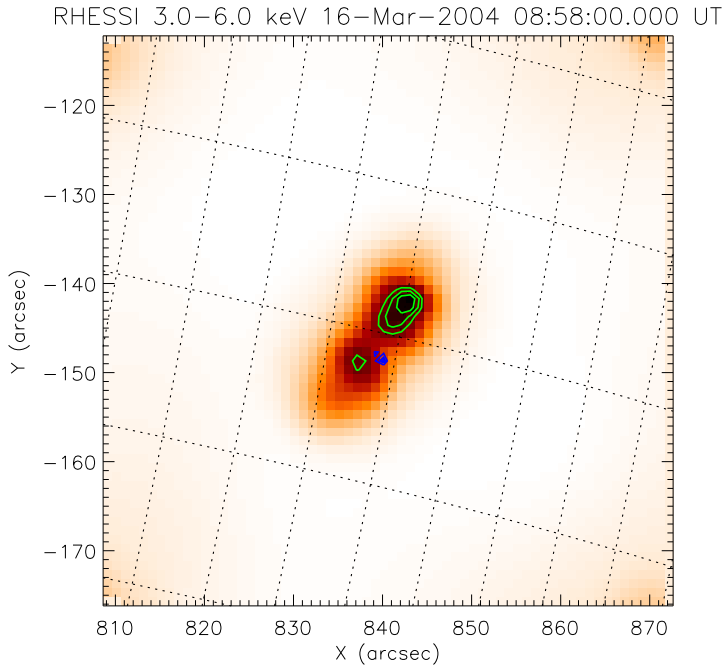

(b) 2004 Mar 16

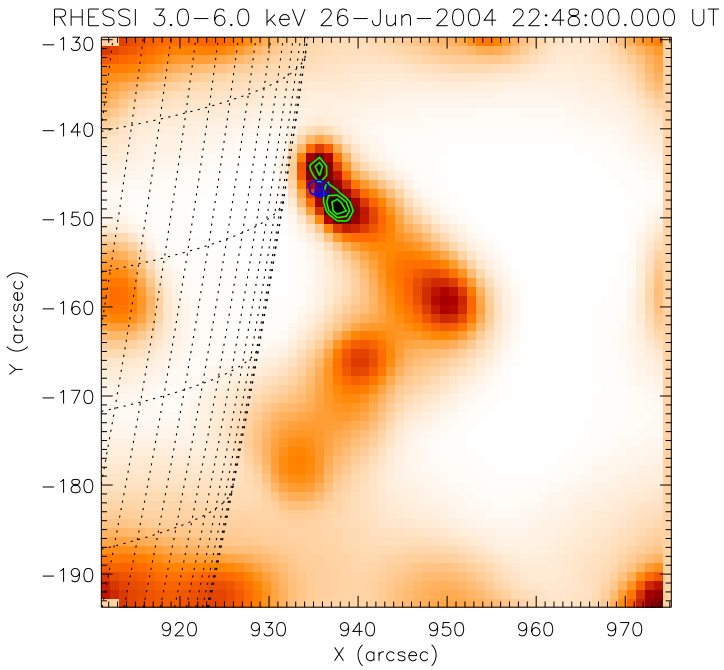

(c) 2004 Jun 26

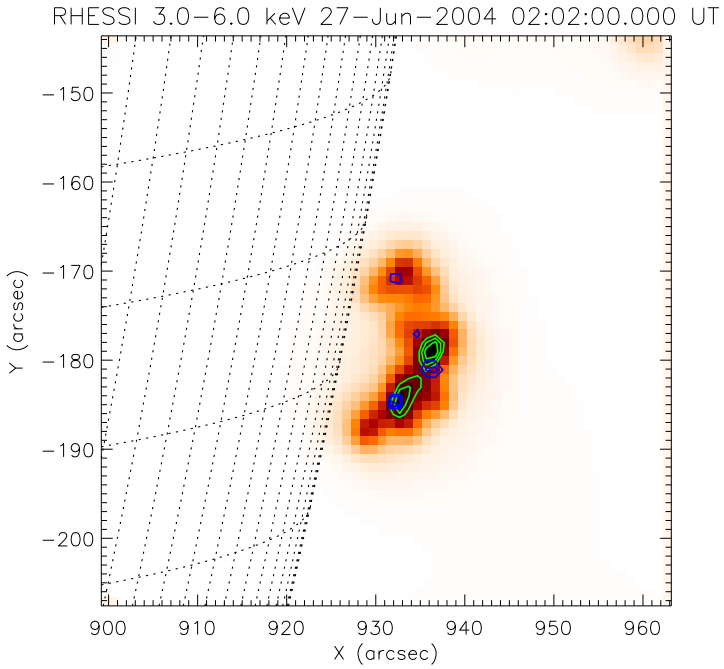

(d) 2004 Jun 27

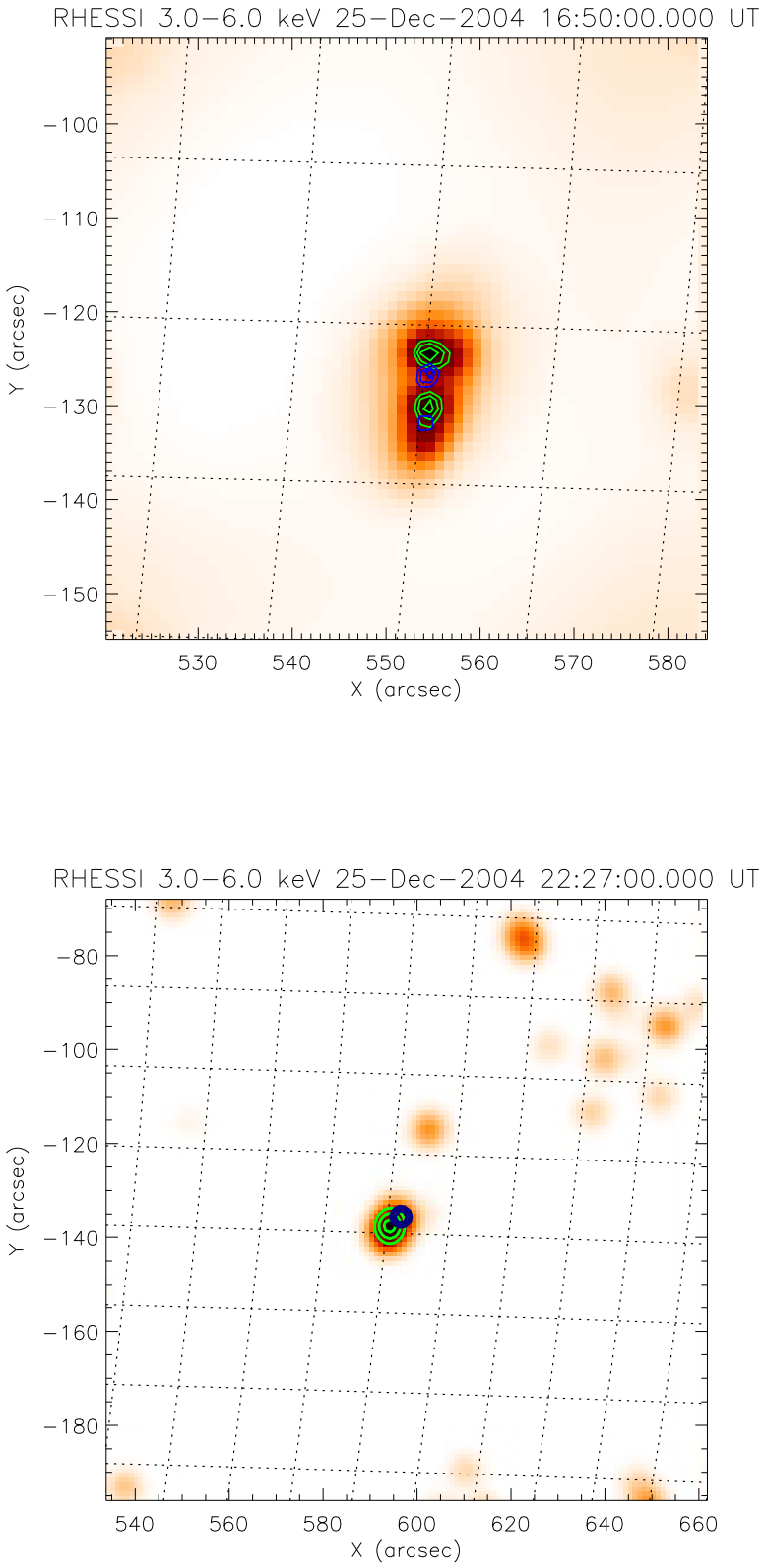

Fig. 2.3 HXR images using the Pixon algorithm in the OSPEX/RHESSI routine for the six events in our final shortlist. The green contours show 70%, 80%, and 90% emission levels in the 3-6 keV band. The blue contours show the 70%, 80% and 90% emission levels in the 6-9 keV band.

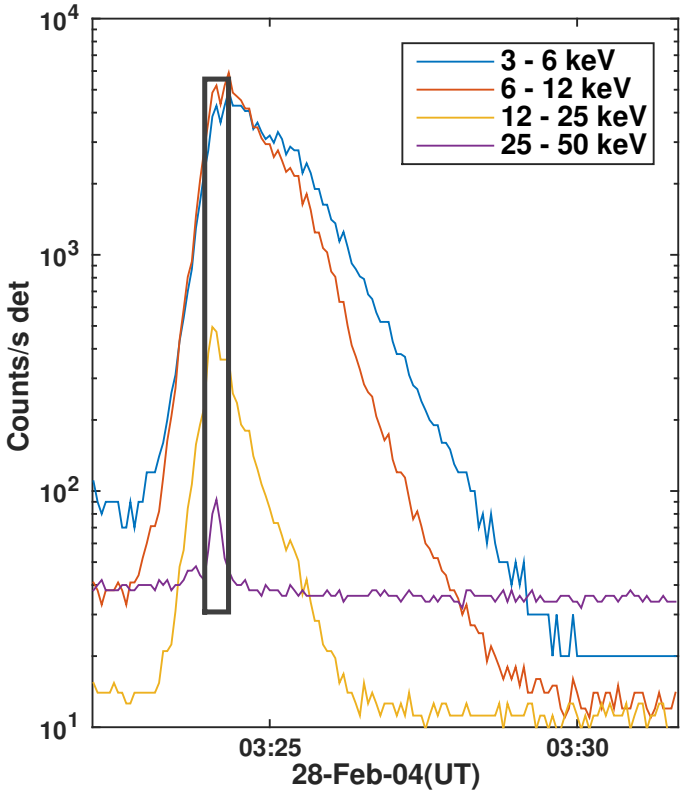
3 - 6 keV
6 - 12 keV
12 - 25 keV
25 - 50 keV
Counts/s det
10^4
10^3
10^2
10^1
03:25
03:30
28-Feb-04(UT)

!ht]

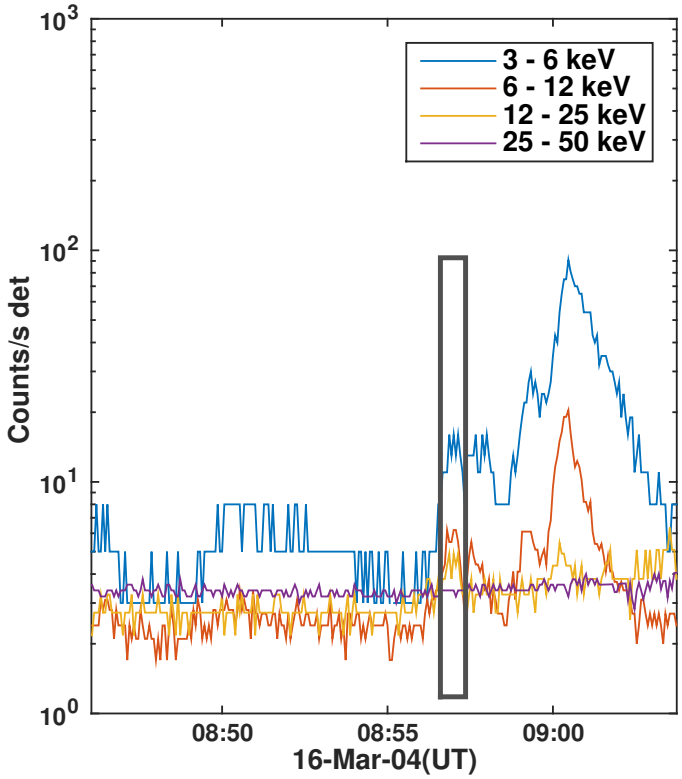
3 - 6 keV
6 - 12 keV
12 - 25 keV
25 - 50 keV
Counts/s det
10^3
10^2
10^1
10^0
08:50
08:55
09:00
16-Mar-04(UT)

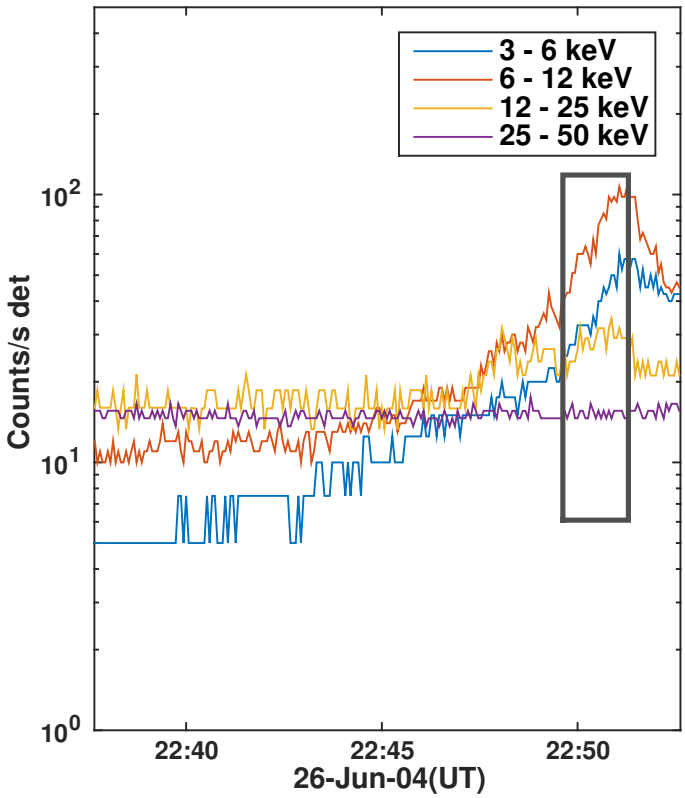
3 - 6 keV
6 - 12 keV
12 - 25 keV
25 - 50 keV
Counts/s det
10^2
10^1
10^0
22:40
22:45
22:50
26-Jun-04(UT)

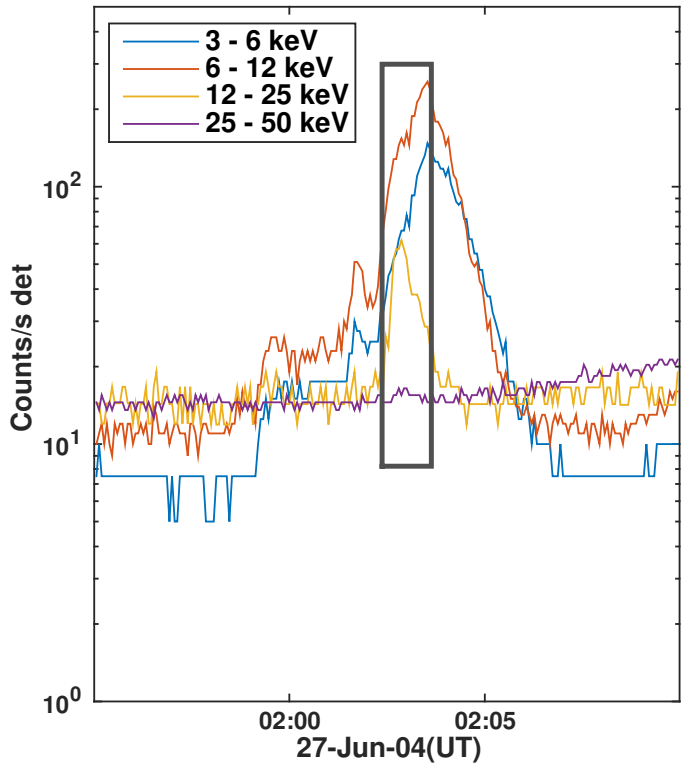
3 - 6 keV
6 - 12 keV
12 - 25 keV
25 - 50 keV
Counts/s det
10^2
10^1
10^0
02:00
02:05
27-Jun-04(UT)

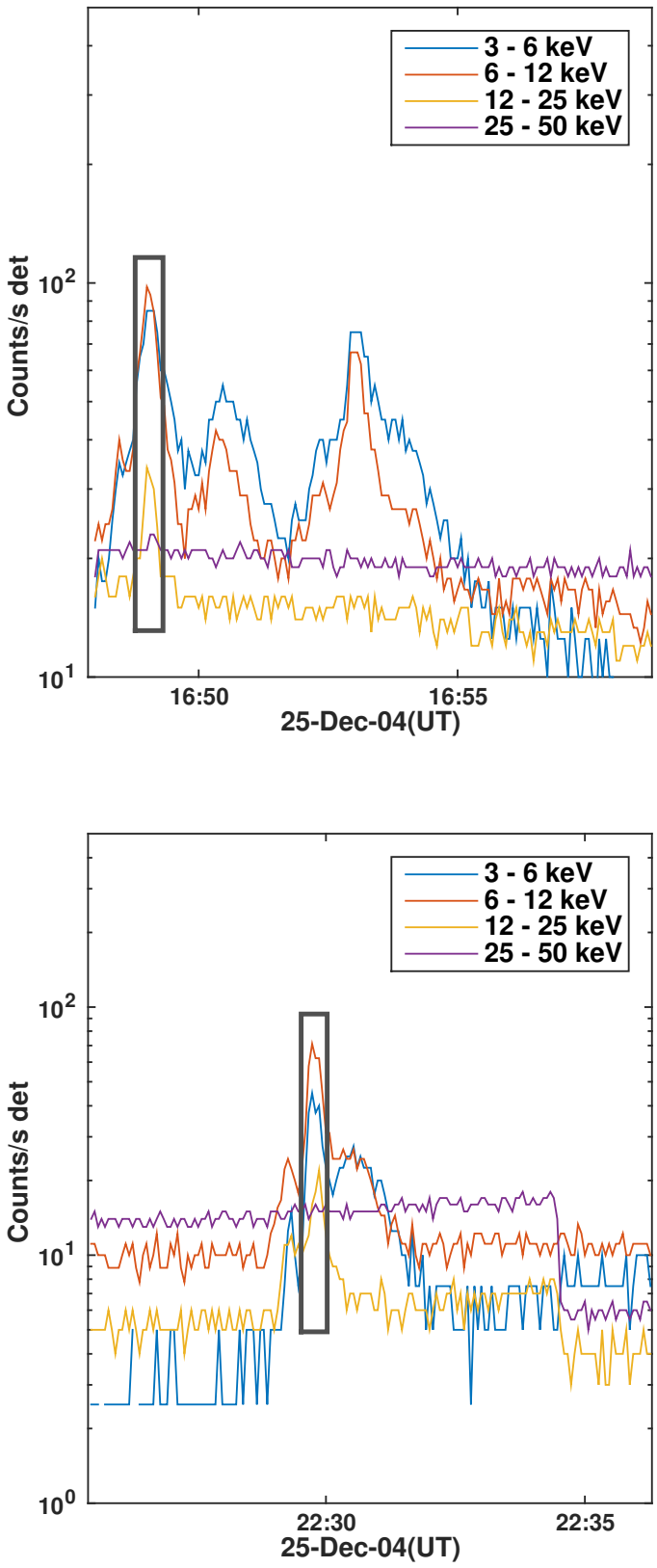

Fig. 2.4 The HXR light-curves for each of the six shortlisted events. The energy bands used for plotting the graph were 3-6 keV,6-12 keV, 12-25 keV, 25-50 keV, 50-100 keV.Due to weak nature of the events, there is little data in the highest energy band for most events. The shaded rectangle show the time strips used to generate the photon spectrum used in OSPEX.

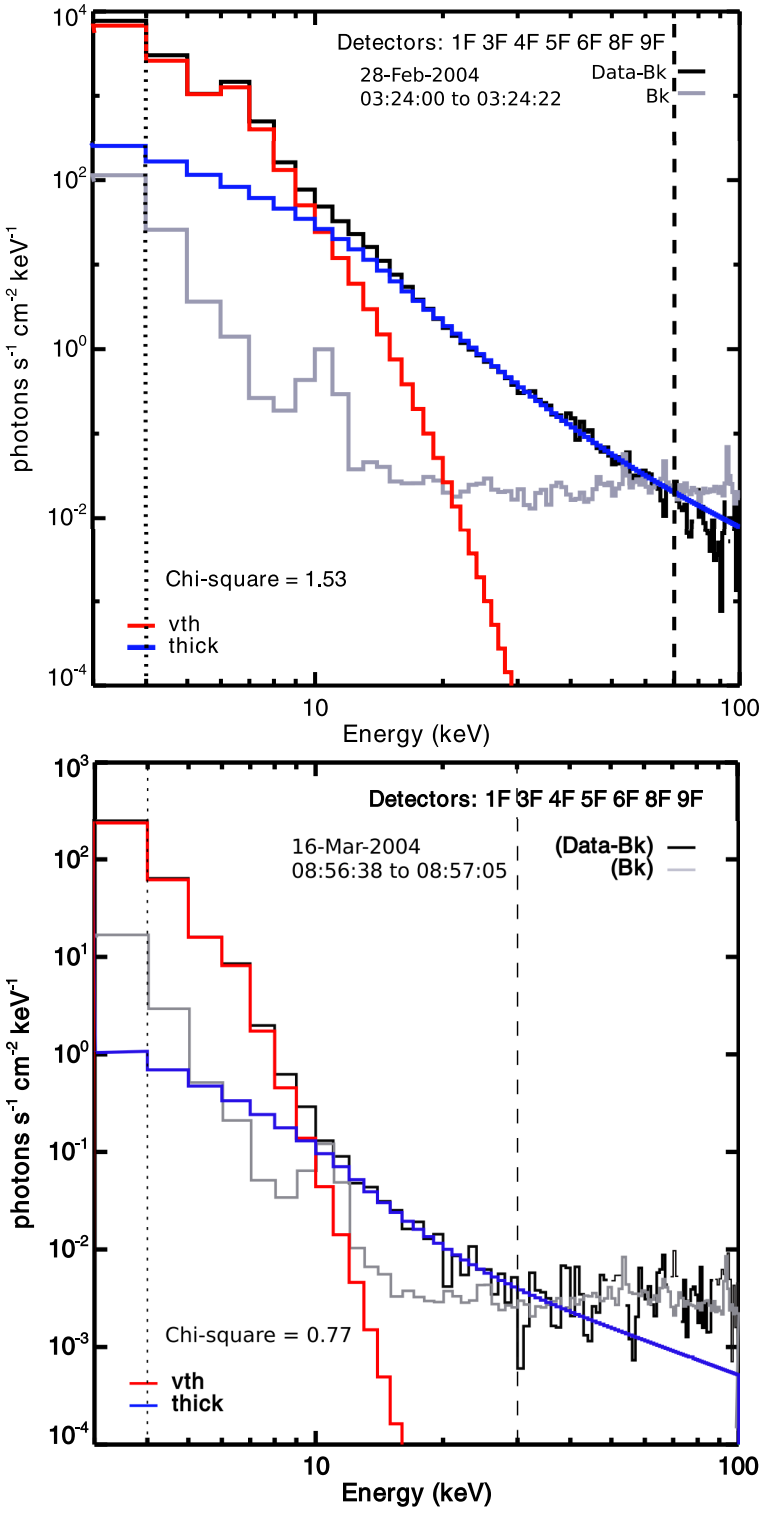
Detectors: 1F 3F 4F 5F 6F 8F 9F
28-Feb-2004
03:24:00 to 03:24:22
Data-Bk
Bk
Chi-square = 1.53
vth
thick
photons s-1 cm-2 keV-1
Energy (keV)
Detectors: 1F 3F 4F 5F 6F 8F 9F
16-Mar-2004
08:56:38 to 08:57:05
(Data-Bk)
(Bk)
Chi-square = 0.77
vth
thick
photons s-1 cm-2 keV-1
Energy (keV)

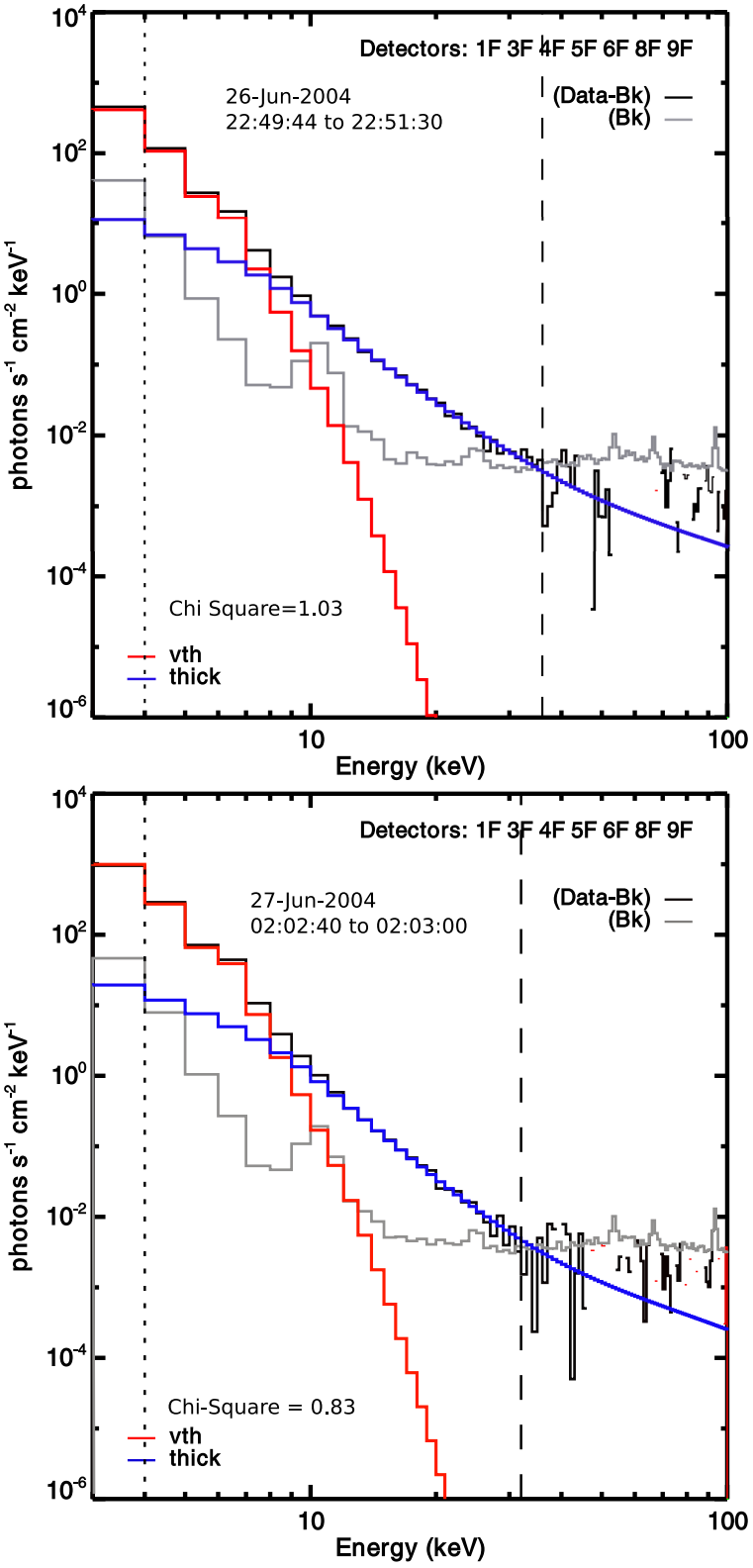
Detectors: 1F 3F 4F 5F 6F 8F 9F
26-Jun-2004
22:49:44 to 22:51:30
(Data-Bk)
(Bk)
Chi Square=1.03
vth
thick
photons s-1 cm-2 keV-1
Energy (keV)
Detectors: 1F 3F 4F 5F 6F 8F 9F
27-Jun-2004
02:02:40 to 02:03:00
(Data-Bk)
(Bk)
Chi-Square = 0.83
vth
thick
photons s-1 cm-2 keV-1
Energy (keV)

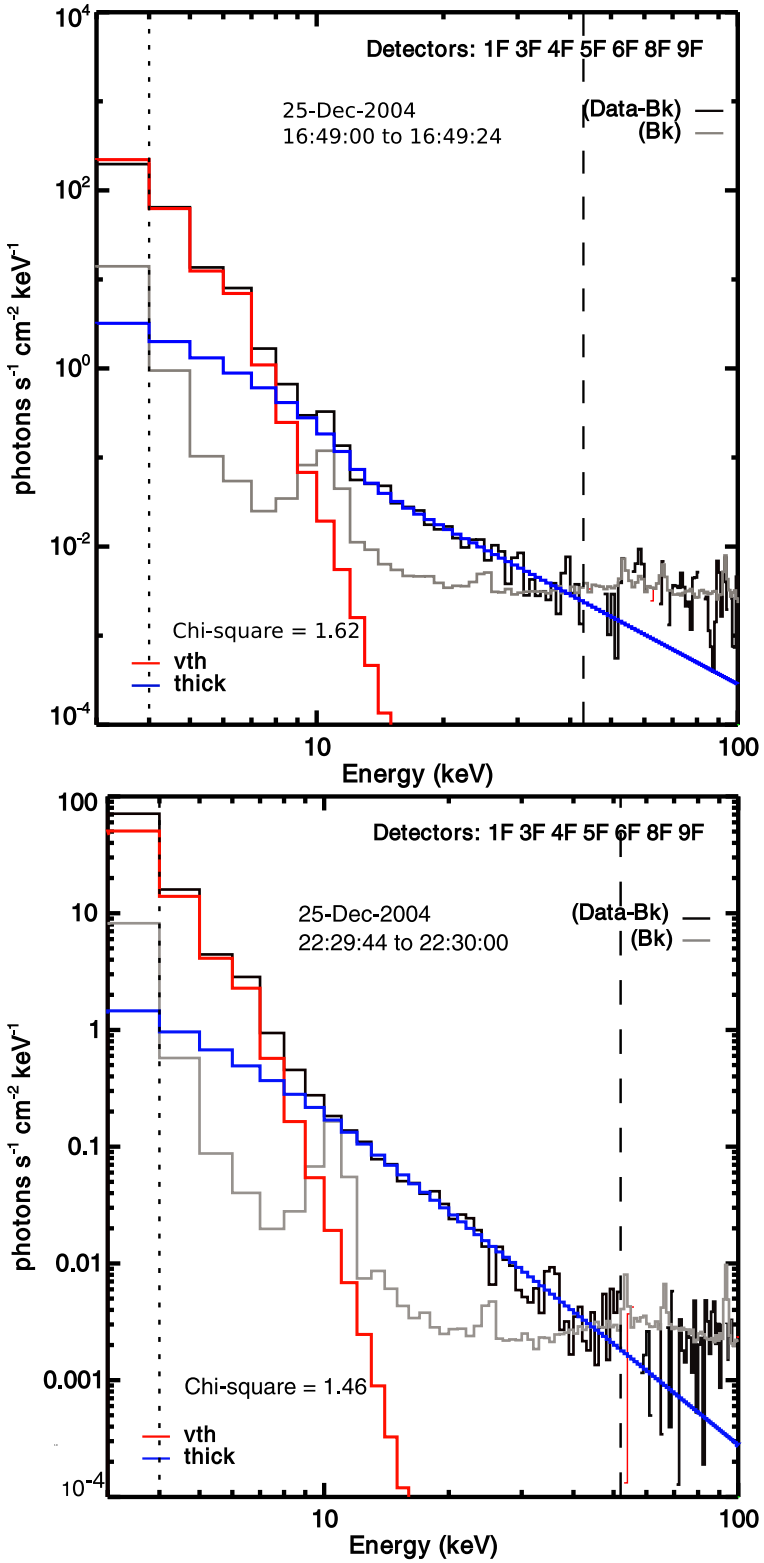

Fig. 2.5 The OSPEX spectral fits for each of the six shortlisted events. RHESSI front detectors 1,3,4,5,6,8,9 were used to accumulate the data. Since the events are weak, we restrict the fit to energy ranges which have counts above the background emission levels. The dashed vertical lines indicate the range of energies used for the fit.A photon spectral index γ is obtained through a broken power law fit (not shown). The emission measure and thermal temperature are obtained from a variable thermal function fit. The thick target fit gives the hxr producing electron spectral indice δ_{hxr}. Results are tabulated in Table 2.2.

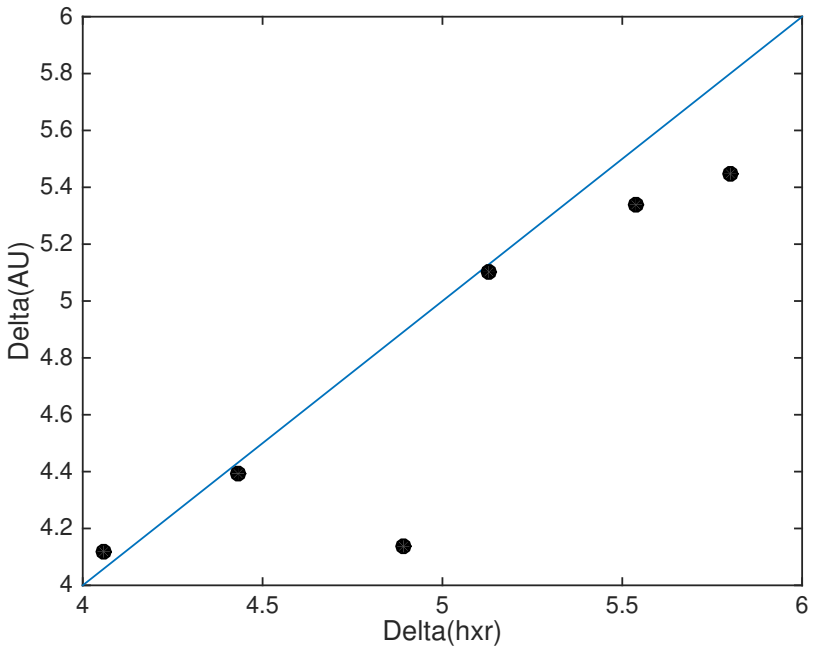

Fig. 2.6 Scatterplot between δ_{1AU} and δ_{hxr}. The two indices are linearly related with a correlation coefficient of 0.91

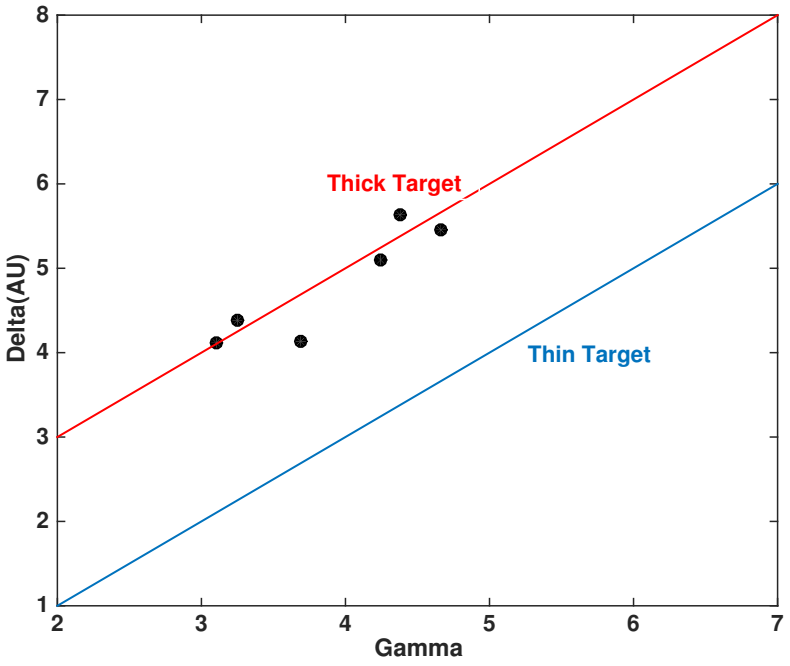

(a) Thick target relation of spectral indices

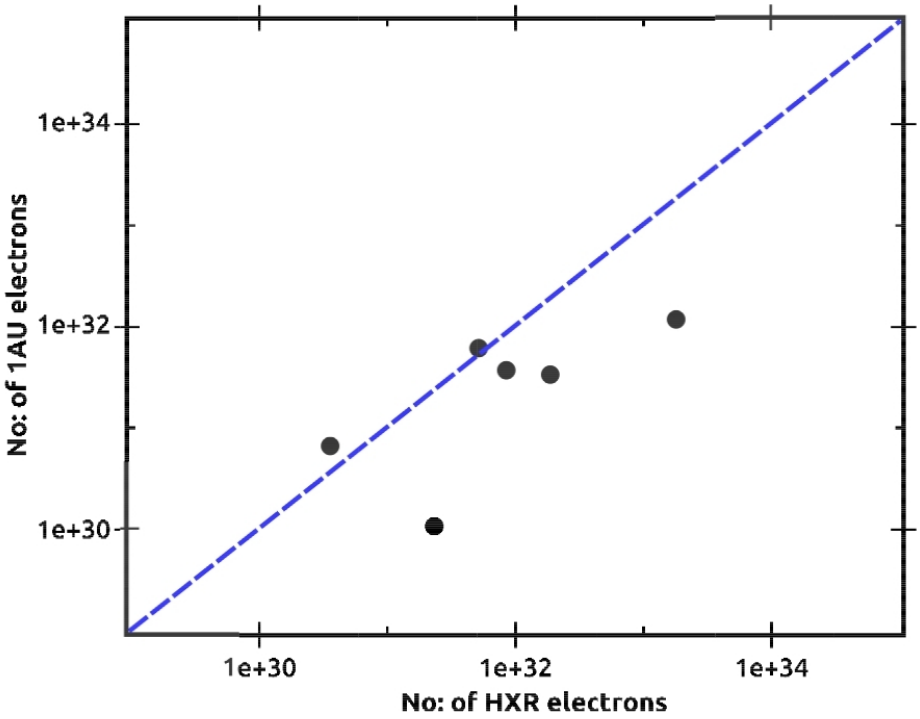

(b) Spectral dependence of γ and δ_{1AU}

Fig. 2.7 The left figure shows a scatterplot of the photon spectral index γ plotted against δ_{1AU} (Table 2.2). We note that the data points fit $\delta_1 = \gamma + 1$ with a correlation coefficient of 0.94. This indicates that the HXR radiation is most likely produced via thick target emission. The right figure shows a scatterplot of the total number of > 74 keV electrons detected at 1AU plotted against the number of > 74 keV electrons involved in HXR emission

Chapter 3

Energetics of small electron acceleration episodes in radio noise storm

3.1 Introduction

3.1.1 Solar Radio storms

The Sun is a prolific emitter at radio wavelengths. We have known about radio emission from the Sun since the early 1900s after a direct correlation was found between the transatlantic telegraph signal strength and the number of sunspots on the Sun. However the first systematic observations of radio sun was carried out by Hey in 1942(Hey et al., 1946) using a directive radar antenna at meter wavelengths. He traced back the source of radar jamming(which caused major panic in British military circles), to the Sun. As is the case with any war related research, these findings were kept classified and were published only after the war, attracting much needed attention to this new field. We now know of many different types of radio emissions(usually known as type I,II,III,IV and V) classified according to their spectral characteristics (Kundu, 1965). Radio emissions from the Sun can range from Quiet sun emission to those resulting from transient events such as flares and CMEs. Coherent solar radio emission results when the electron distribution for the radio emission form bump-in-tail instablilities along the parallel direction of the magnetic field and emit coherent plasma waves,which eventually give rise to the observed radio emission. Incoherent emissions are mainly thermal in nature and are often produced through free-free Coulomb collisions.

In this chapter we focus on Type I radio noise storms. They are the earliest known type of radio emission discovered from the Sun. They are also the most common phenomenon at meter wavelengths. They comprise short narrow-band bursts superimposed on a slowly varying continuum and can last for several hours or even days(Elgaroy, 1976). The bursts

can either occur in 'showers' wherein they show intense emission over a short period of time or in 'chains' wherein they usually drift towards lower frequencies. The bursts in the solar noise storm usually lasts between 0.1 to 3s and have brightness temperatures as high as 10^9 K(corresponding to a flux of 1-100 sfu). Both the bursts and continuum exhibit strong circular polarization. Type I solar radio bursts are often detected above the leading edges of large sunspots. Imaging observations show that the bursts and continuum are not co-located and the burst source is displaced perpendicular to the continuum source (Klein, 1995, 1998). However it is generally believed that the bursts result because of the acceleration of non-thermal electrons trapped in coronal loops. It is yet to be ascertained if a single burst arises from electrons accelerated in one reconnection episode or whether it is a collective signature of multiple reconnection episodes.

3.1.2 Coronal heating

Despite being situated far above the relatively cooler($\approx$ 6000K) photosphere, it has been known since the 1940s that the solar corona is as hot as 10^6K. Over the past five decades since the discovery of the coronal heating problem many theories have been proposed to explain it. Thermal conduction as a possible cause was soon ruled out as it would mean the temperature profile of the corona would be distance dependent according to second law of thermodynamics. Radiative losses would cool down corona in a matter of days implying there should be steady flow of energy into the corona. As outlined in the first chapter a series of small heating events should be responsible for this heating. Larger events are so few and far between that they cannot supply the energy needed to heat the corona. A model by Parker (1988) envisages constant shuffling and braiding of coronal magnetic field lines due to photospheric granular and super granular flows which exhibit random walk features. This twisting of field lines results in the build up non-potential energy until the angle between field lines crosses a critical value. Thereafter the energy is dissipated in the form of a small magnetic reconnection event with an energy output $\sim 10^{24}$ergs s^{-1}. This amount of energy is around nine orders of magnitude smaller than that involved in normal flares and hence these events are commonly called 'nanoflares'. The released energy is expended in accelerating non-thermal particles and in heating up surrounding the plasma via thermal conduction. The temperature response of most instruments on-board current satellites are not sensitive enough to measure the emitted thermal radiation, and hence these small energy releases are very difficult to observe in thermal emission. Bursts of radio emission at metric to decametric wavelengths are signatures of small populations of accelerated, non-thermal electrons in the solar corona. The number of non-thermal electrons producing the emission is very small compared to ambient thermal electrons. However, since the emission process is coherent, the

radio emission has very high brightness temperatures and is hence easily observable. Type I bursts, which are signatures of non-thermal electrons accelerated in small episodes without any accompanying flares thus provide an excellent opportunity to study the dynamics of small scale electron acceleration (Ramesh et al., 2012; Suresh et al., 2017). This is particularly important for understanding coronal heating since it has long been postulated that a series of such impulsive heating events are candidates for coronal heating (Ishikawa et al., 2017; Klimchuk, 2015; Klimchuk and Cargill, 2001; Testa et al., 2014; Tripathi et al., 2010). Type I bursts thus provide a perfect test bed to examine open questions like the mechanism of energy release, particle acceleration, rate of heating etc. In this chapter we estimate the energetics of non-thermal electrons in noise storm bursts. We use high resolution imaging data of solar noise storms reported by Mercier et al. (2006, 2015). They combined data from the Nancay Radioheliograph(NRH) with the data from the Giant Metrewave Radio Telescope(GMRT) to obtain metre wavelength images of unprecedented resolution and fidelity. We combine this with high temporal resolution data from the NRH. Using the particle acceleration framework developed by Subramanian and Becker (2004, 2006), and the estimated timescales burst we derive the ratio of the non-thermal electron number density to that of thermal electrons. Finally we estimate the power input to the accelerated electrons that produce the noise storm emission compare it with the coronal heating budget.

3.2 Data Analysis

3.2.1 Noise storm imaging

We use high spatial resolution imaging data obtained by Mercier et al. (2015) for our study. In this study, they combined short baseline data from the NRH with long baseline data from the GMRT and reported the smallest known core size(for the two common frequencies of GMRT and NRH - 327 MHz and 236 MHz). Combining the visibilities increases the effective resolution to 20 arcsec (compared to a typical resolution of 3 arcmin for NRH). By combining data from both the instruments, a higher field of view, better dynamic range and high spatial resolution could be achieved. However one downside is the reduced temporal resolution of ~ 2 sec compared to the time cadence of 0.125 s for data from the NRH alone. We therefore use the high spatial GMRT-NRH data for source sizes and the high temporal resoultion NRH-only data for estimating burst durations and inter-burst time interval.

3.2.2 Noise storm light curves

The Nancay Radioheliograph

As mentioned in the previous section we use high temporal resolution data from the NRH for our studies (Kerdraon and Delouis, 1997). The NRH, established in 1956 is one of the oldest radio astronomy facilities in the world. The NRH is located around 200 km south of Paris in Nancay. It is a T shaped array interferometer with 47 antennas distributed along two perpendicular branches known as the EW array(19 antennas) and NS array(25 antennas). The Nancay Radioheliograph (NRH) images the Sun at around 10 frequencies ranging from 150 to 450 MHz. The maximum baseline is 3200 meters. A standard observation run has a duration of 7 hours centred on the hour of passage of the sun with the meridian of Nancay. The data is correlated and integrated at 125ms for all the observation frequencies.

Noise storm events

In this chapter we study the four well-observed noise storm events reported by Mercier et al. (2006, 2015). Since the imaging studies were done only using the frequencies common to GMRT and NRH (236 MHz and 327 MHz) we limit our studies to those frequencies. The lightcurve data include 327 MHz observations from 08:44 to 09:15 UT on 2002 Aug 27; 327 MHz observations from 11:39 to 12:15 UT on 2004 Aug 14; and 236 MHz observations from 10:44 to 11:15 UT on 2003 Jul 15 and from 11:34 to 12:03 UT on 2006 Apr 06 (table 3.1).

Fig3.1 shows a typical noise storm lightcurve; the spiky bursts superposed on top of a slowly varying continuum can be clearly distinguished. Since our goal concerns the statistics of the bursts (and not the continuum), we developed an algorithm to extract the bursts efficiently from the continuum. The process is illustrated in Fig 3.1. We start with a peak finding algorithm which marks the local maxima(hills) and minima(valleys). The valley positions crudely mark the continuum envelope. To subtract out the continuum we fit a polynomial interpolation function to the positions of the valleys to obtain the background trendline. By using this approach we were able to trace both the global and local undulations of the light curve. Each point of the burst is subtracted from this trendline to obtain the background-subtracted light curve. To exclude false detections we ensured that there is only a single local maxima(hill) between adjacent valley points. Each burst was fitted with a Gaussian to obtain distributions of amplitude, burst widths and inter-burst timescale. The peak flux from the light curve and the smallest source size for each of the noise storms from Mercier et al. (2015) can be combined to obtain the brightness temperature. The brightness temperatures thus derived are listed in table3.2. The high values of brightness temperature indicates the non-thermal nature of the emission.

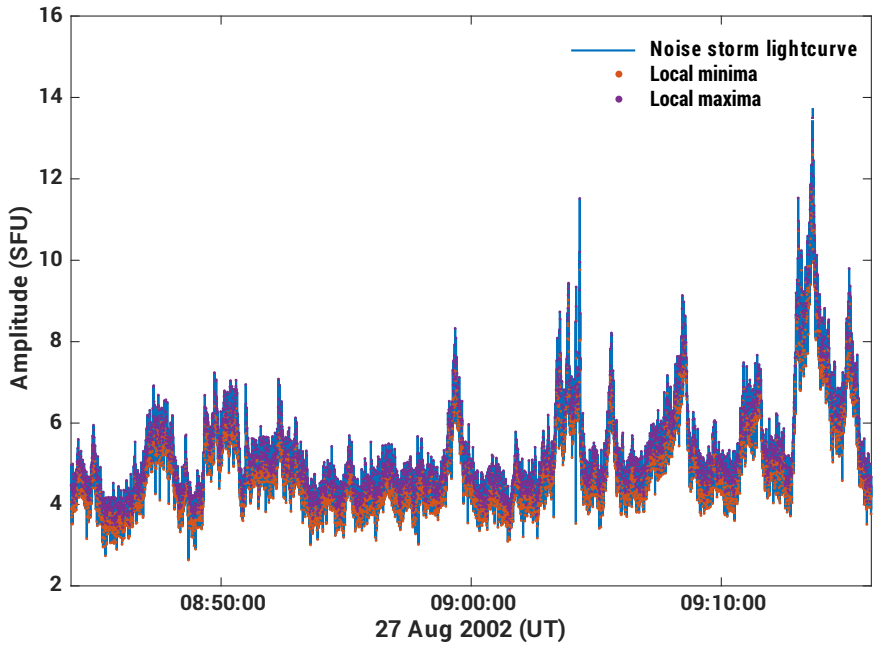

(a)The light curve for the noise storm event of Aug 27 2002 with the local maxima and minima marked. We use a differential peak finder algorithm to locate the maxima and minima.

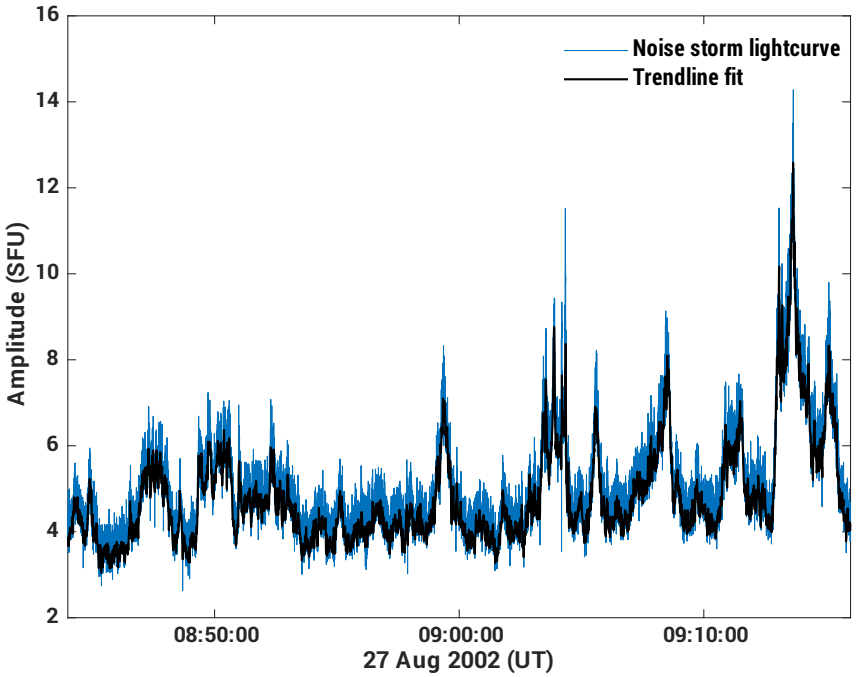

(b)The locations of local minima in Fig 1a are used to construct the background trendline, which is marked in black.

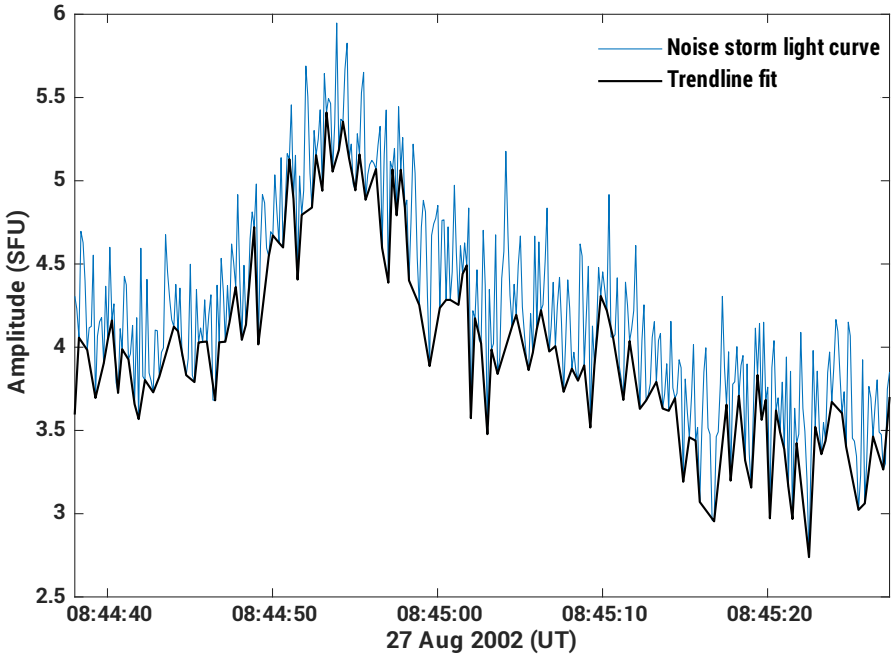

(c)A closeup of the lightcurve displayed in Fig 1b. It is evident that the trendline accurately traces both global and local features.

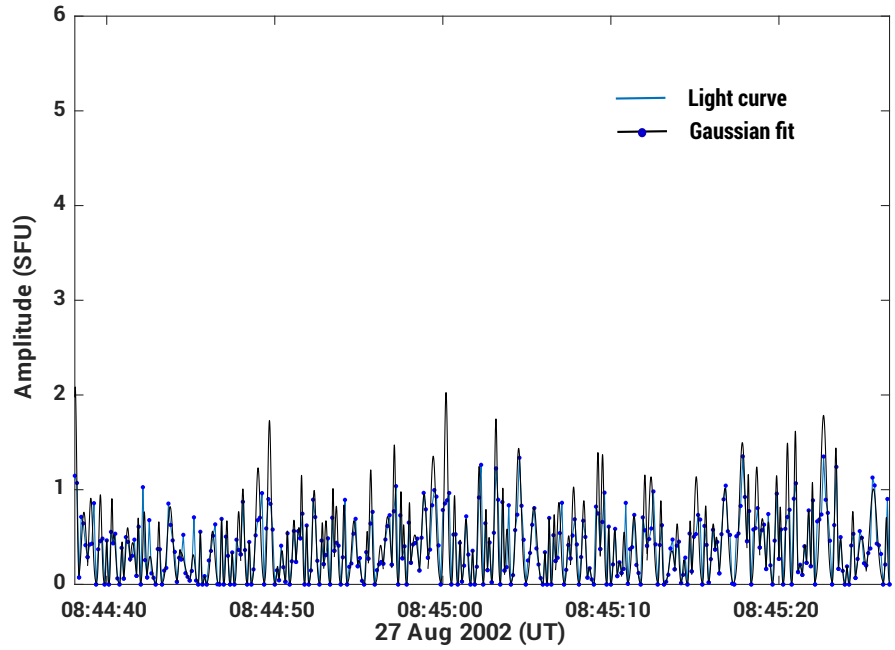

(d)The background-subtracted lightcurve with gaussian fits to each of the burst overplotted

Fig. 3.1 Background subtracted spikes for all the events are shown. Each burst is fitted with a Gaussian to extract the peak amplitude, burst width and inter-burst times.

Table 3.1 Details of the noise storm events studied.

Date	Observation timerange (UT)	Observation frequency (MHz)	Smallest source size (arcsec)	Derived Heliocentric Distances ($R_\odot$)
2002 Aug.27	08:44-09:15	327	31	1.20
2003 Jul.15	10:44-11:15	236	57	1.24
2004 Aug.14	11:39-12:15	327	45	1.21
2006 Apr.06	11:34-12:03	236	35	1.28

3.2.3 Type I bursts - Histograms

Each burst is identified using an algorithm that checks for zeros in the first derivative. We also check the second derivative to check if the extrimum is a maxima or a minima. Only those local maximums/minimums which are uniquely determined both in the normal pass and reversed pass are recorded as a valley/hill. An individual burst is defined as one with has two valleys and one unique peak. A Gaussian function is fit to each burst to determine its amplitude and width. We then create histograms of burst amplitudes, widths and inter-burst separation for each observation.

The histograms of peak-flux for each noise storm is shown in fig3.2. They are similar to the noise storm histograms shown in Mercier and Trottet (1997). For each histogram, we fit a power law of the form $dN/dA \simeq A^{\alpha}$ where A is a measure of the amplitude, dN is the number of events recorded between A and A+dA and α is the slope of the dN/dA on a log-log plot. The results are shown in Fig 3.2. If these small-scale heating events had to contribute to the coronal heating, Hudson (1991) pointed out that their powerlaw index α would have to be < -2 . For events considered in our study we got power-law indices in the range -5.2 <α < -1.6. Our values are comparable to already reported values; -3.5 <α <-2.8 (Mercier and Trottet (1997),Ramesh et al. (2012) and Iwai et al. (2013, 2014)). Suresh et al. (2017) found a value of α = -2.3 using numerous weak, short-lived narrow band emission features in the quiet sun using the Murhcison wide field array. Knizhnik et al. (2018) showed that energy released in small scale reconnection events in the corona obey power-law statistics.

Histograms for burst widths and inter-burst durations are shown in Fig3.3 and Fig3.4 . For the theoretical framework that we will use,we need the average values of the burst-widths and inter-burst duration. The histograms for the burst-width are skewed towards the left; hence we use an inverse Gaussian function,

$$f(x;\mu,\lambda) = \left[\frac{\lambda}{2\pi x^3}\right]^{1/2} \exp\left\{\frac{-\lambda(x-\mu)^2}{2\mu^2 x}\right\} \tag{3.1}$$

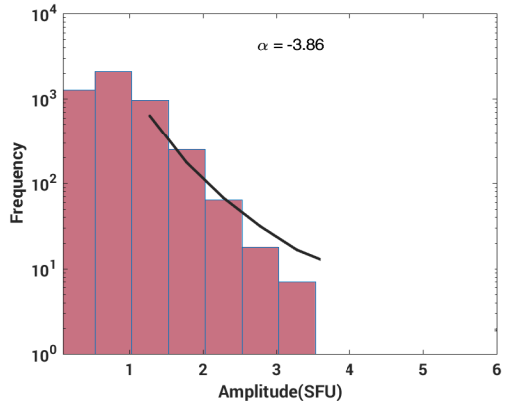

(a) 2002 Aug.27

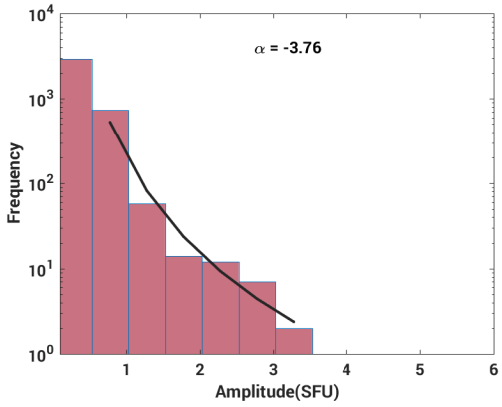

(b) 2003 Jul.15

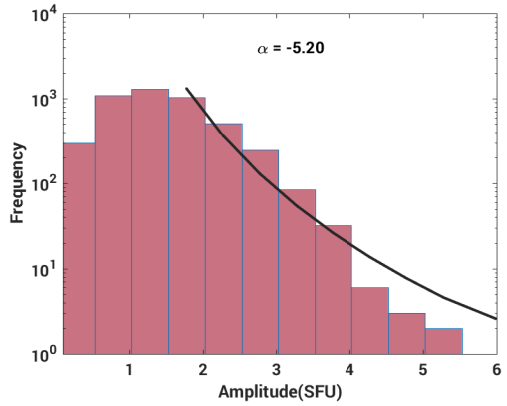

(c) 2004 Aug.14

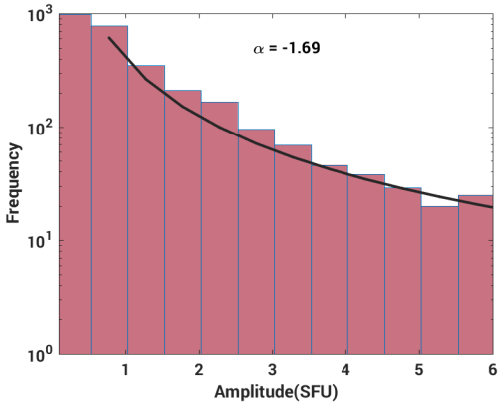

(d) 2006 Apr.06

Fig. 3.2 Histograms of occurrence frequency versus flux for each of the noise storm episodes we study. The power law fit is shown by the black curve.

to fit them. Here, μ (> 0) is the mean and λ (> 0) is the shape parameter. The fits are denoted by the black lines superposed on the histograms in Fig 3.3. Since the histograms for inter-burst timescales are not as skewed,we use the gamma distribution,

$$f(x;\alpha,\beta) = \frac{\beta^{\alpha} x^{\alpha-1} e^{-\beta x}}{\Gamma(\alpha)}, \tag{3.2}$$

to fit them. Here α (> 0) is the shape parameter, β (> 0) is the scale parameter and $\Gamma(\alpha)$ is the complete Gamma function. The mean of this distribution is α/β. The fits are shown in Fig 3.4 . The mean values of the burst-width and inter-burst duration are listed in columns 3 and 4 respectively of Table 3.2 .

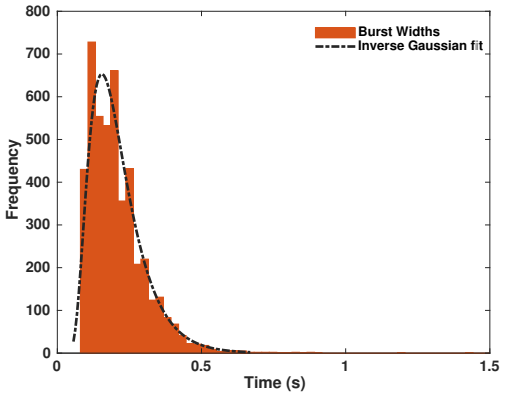

(a) 2002 Aug.27

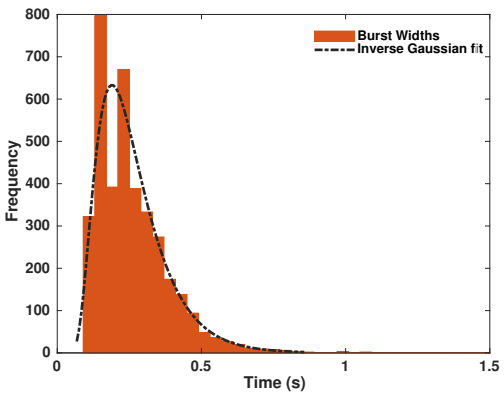

(b) 2003 Jul.15

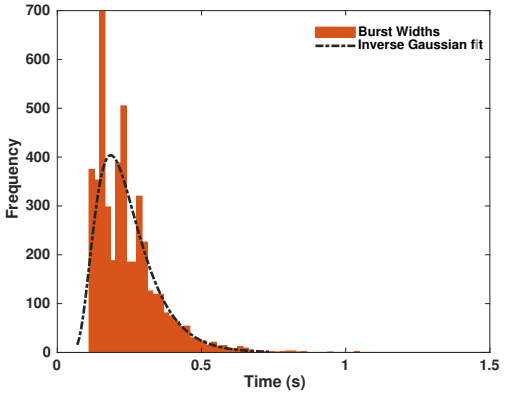

(c) 2004 Aug.14

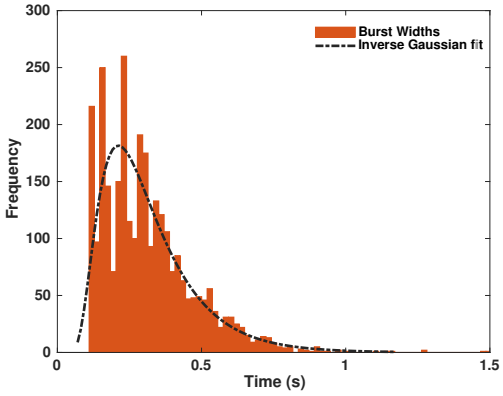

(d) 2006 Apr.06

Fig. 3.3 Histograms for burst widths. The widths are obtained by fitting a gaussian to each burst in the noise storm lightcurve.

3.3 Energetics of accelerated electrons

3.3.1 Background

Even though noisestorms are the earliest known radio emissions from the Sun, we still do not have a clear idea regarding the chain of events that eventually results in the observable radio emission. Most noise storms are observed during non-flaring or quiet times. Noise storms are thought to be associated with the restructuring of coronal magnetic fields as they are often observed above large sunspots which are known sites for emergence of new flux. Noise storms are generally polarized in the sense of the o-modes. This together with their high brightness temperatures suggest a plasma emission origin. Noise storm emisssion can occur via the following scenarios(Li et al. (2017)):

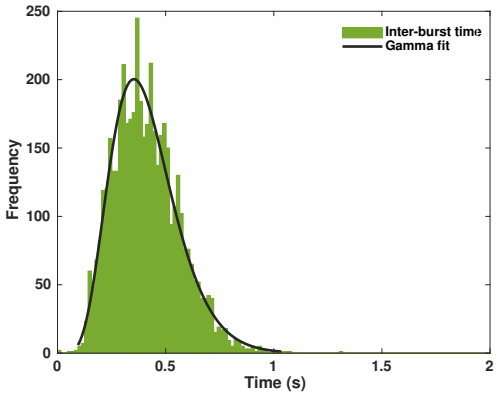

(a) 2002 Aug.27

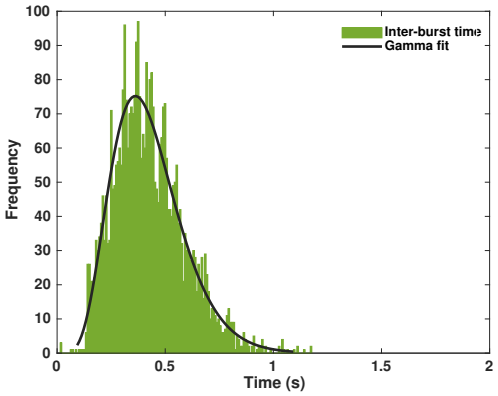

(b) 2003 Jul.15

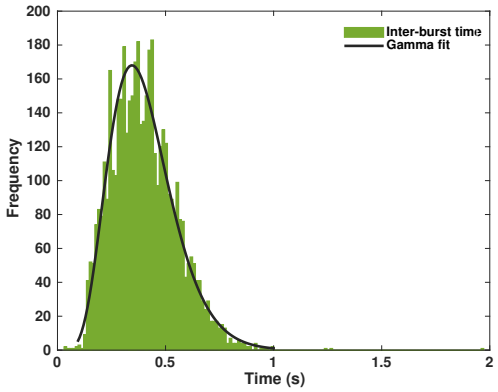

(c) 2004 Aug.14

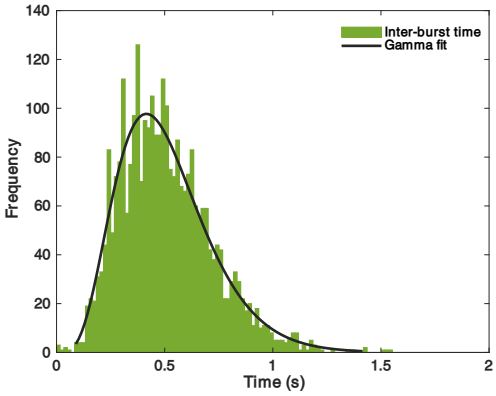

(d) 2006 Apr.06

Fig. 3.4 Histograms of the inter-burst duration. The Inter-burst duration is defined as the time duration between two adjacent peaks in the noise storm lightcurve.

- Reconnection between existing coronal magnetic field lines and the emerging flux. Some noisestorms are known to start after a new flux emergence crosses a threshold level, indicating temporal correlation between the events. However there have also been observations where noisestorm emission seems to happen without much flux emergence, suggesting this is not a prerequisite.(Spicer et al., 1982; Zwaan, 1978, 1985)

- Magnetic Moving Features(MMF) driven reconnection. Magnetic moving features are bipoles moving in a radial direction from a sunspot, with velocities $< 3\ kms^{-1}$. Observations show that MMFs can cause magnetic cancellation and merging during their motion. The complex magnetic topology that arises leads to magnetic reconnection leading to electron acceleration and noise storm emission (Bentley et al., 2000; Harvey and Harvey, 1973; Sheeley, 1969).

- Interchange reconnection between dense active region loops slowly expanding into ambient coronal field lines. Low energy electrons are accelerated at the null point which could ultimately result in noise storm emission (Chertok et al., 2001; Del Zanna et al., 2011).

To understand more about the noise storms it is important to understand how the non-thermal electrons are accelerated in the first place. Subramanian and Becker (2004) developed a generic second-order Fermi acceleration mechanism to estimate the energy in the accelerated(nonthermal) electrons. A brief description of the theory is as follows:

As the electrons undergo repeated collisions with magnetic scattering centres, it can be shown that electrons over a critical energy ε_c in the high-energy tail of the thermal electron distribution will undergo net acceleration or net gain of energy over collisional losses. The time evolution of the Green's function for the electron distribution is

$$\frac{\partial f_{\rm G}}{\partial t} = \frac{1}{p^2}\frac{\partial}{\partial p}\left(p^2\,\mathscr{D}\frac{\partial f_{\rm G}}{\partial p}\right) + \frac{\dot{N}_0\,\delta(p-p_0)}{p_0^2} - \frac{f_{\rm G}}{\tau}\,, \tag{3.3}$$

Here f_G is the Green's function for the electron distribution function. The first term on the RHS characterizes electron diffusion in momentum space due to collision with the magnetic scattering centres. The second term on the RHS denotes the injection of electrons at a momentum p_0 and third term accounts for the escaping electrons from the acceleration region. Noise storms can last for hours or even days. As mentioned earlier they have narrowband spiky bursts superposed on top of a quasi-periodic continuum. We now focus on the steady-state solution; i.e; the time-scales we now study are much longer than the the timespan of an individual burst. Motivated by existing studies(Chandran and Maron, 2004; Luo et al., 2003; Miller et al., 1996; Ptuskin, 1988) we adopt a momentum diffusion coefficient given by

$$\mathscr{D} = D_0\,p^2\,, \tag{3.4}$$

The steady state ($\partial/\partial t \to 0$) solution to Green's function then becomes

$$f_{\rm G}(p,p_0) = A_0\begin{cases}(p/p_0)^{\alpha_1}\,, & p \le p_0\,,\\[2ex] (p/p_0)^{\alpha_2}\,, & p \ge p_0\,,\end{cases} \tag{3.5}$$

The exponents α_1 and α_2 are related to D_0 and τ via

$$\alpha_1 \equiv -\frac{3}{2} + \left(\frac{9}{4} + \frac{1}{D_0\tau}\right)^{1/2}, \quad \alpha_2 \equiv -\frac{3}{2} - \left(\frac{9}{4} + \frac{1}{D_0\tau}\right)^{1/2}, \tag{3.6}$$

The stochastic acceleration timescale is related to D_0 via

$$t_{\rm accel} = \frac{1}{8D_0}. \tag{3.7}$$

We note that the solution to the Green's function for a single momentum $p = p_0$ does not include losses; it therefore only applies to a situation where the electron acceleration timescale is shorter than its loss timescale(in other words for energies $\varepsilon > \varepsilon_c$, thereby resulting in net acceleration. The loss time-scale for electrons emitting Langmuir waves is equal to the Coulomb loss timescale given by

$$t_{loss} = \frac{6.37 \times 10^{22} \varepsilon^{3/2}}{\Lambda n_e} \tag{3.8}$$

For $t_{accel} < t_{loss}$, it can be seen from Eq 3.7 and Eq3.8 that the particle should have energy ε, greater than a critical energy ε_c, given by

$$\varepsilon_c \equiv 1.57 \times 10^{-16} \left(\frac{\Lambda n_e}{D_0}\right)^{2/3} \tag{3.9}$$

Here n_e is the background (thermal) electron density. Since we assume the observed emission to be (fundamental) plasma emission, the background electron density corresponds to the plasma level from which the emission originates. In other words, $n_e = (1/81) \times 10^6 f^2\,{\rm cm}^{-3}$, where f is the observing frequency in MHz. For an observing frequency of 327 MHz, $n_e = 1.3 \times 10^9\,{\rm cm}^{-3}$, while $n_e = 6.8 \times 10^8\,{\rm cm}^{-3}$ for an observing frequency of 236 MHz. Given that noise storms typically occur over active regions, these values are typical.

It should be noted that even though some individual particles with energy $\varepsilon > \varepsilon_c$ may lose energy, on average they will experience net acceleration or gain of energy. From equation 3.9, we can write the following expression for critical momentum p_c corresponding to ε_c:

$$p_c \equiv 1.64 \times 10^{-21} \left(\frac{n_e}{D_0}\right)^{1/3} \tag{3.10}$$

Assuming that only higher energy (tail-end) of Maxwellian(thermal) distribution with $p > p_c$ is subjected to net acceleration, Subramanian and Becker (2004) obtained the following expression for the non-thermal electron distribution function(f) which is a convolution of the Green's function (f_G) with the tail of the thermal Maxwellian distribution:

$$f(p) = \frac{n_e \left\{ \xi^{\alpha_1/2}\, \Gamma\left(-\frac{\alpha_1}{2}, \xi\right) - \xi^{\alpha_2/2} \left[\Gamma\left(-\frac{\alpha_2}{2}, \xi\right) - \Gamma\left(-\frac{\alpha_2}{2}, \xi_c\right)\right] \right\}}{\sqrt{2\pi}\,(m_e kT)^{3/2}\,(\alpha_1 - \alpha_2)\, D_0\, \tau}, \tag{3.11}$$

From the moments of the distribution function(f) in Eq 3.11 for the non-thermal(accelerated) electrons, the number density,

$$n_*\,(\mathrm{cm}^{-3}) = \int_{p_c}^{\infty} p^2 f(p) dp \tag{3.12}$$

and its energy density,

$$U_*\,(\mathrm{erg\,cm}^{-3}) = \int_{p_c}^{\infty} \varepsilon\, p^2 f(p) dp = \frac{1}{2m_e} \int_{p_c}^{\infty} p^4 f dp\,, \tag{3.13}$$

can be computed. Here m_e is the electron mass, $\varepsilon \equiv p^2/2m_e$ is the electron kinetic energy. Consequently, the expression for the ratio of the nonthermal electron density (n_*) to the thermal one (n_e) is

$$\frac{n_*}{n_e} = \frac{2\,\xi_c^{(3+\alpha_1)/2}\,\Gamma\left(-\frac{\alpha_1}{2},\,\xi_c\right)}{\sqrt{\pi}\,(3+\alpha_1)(\alpha_2-\alpha_1)\,D_0\,\tau} + 2\,e^{-\xi_c}\left(\frac{\xi_c}{\pi}\right)^{1/2} + \mathrm{Erfc}\left(\xi_c^{1/2}\right)\,, \tag{3.14}$$

where $\xi \equiv \frac{p^2}{2m_e kT}$ and $\xi_c \equiv \frac{p_c^2}{2m_e kT}$. The ratio of the energy density in the nonthermal electron population (U_*) to that in the thermal population ($n_e kT$) is

$$\frac{U_*}{n_e kT} = \frac{2\,\xi_c^{(5+\alpha_1)/2}\,\Gamma\left(-\frac{\alpha_1}{2},\,\xi_c\right)}{\sqrt{\pi}\,(5+\alpha_1)(\alpha_2-\alpha_1)\,D_0\,\tau} + \frac{2\sqrt{\pi\xi_c}\,(3+2\,\xi_c)\,e^{-\xi_c} + 3\,\pi\,\mathrm{Erfc}\left(\xi_c^{1/2}\right)}{2\,\pi(1-10\,D_0\,\tau)}\,. \tag{3.15}$$

Here T is the temperature of the thermal electrons, which we assume to be 10^6 K.

The brightness temperature T_b of the noise storm, defined by,

$$T_b = 1.22\times 10^{10}\frac{S}{f^2\theta\phi}\,, \tag{3.16}$$

where S is the observed flux in sfu, f is the observing frequency in GHz, and θ and ϕ are the source dimensions in arcseconds. The brightness temperature is the equivalent blackbody temperature of the observed radiation in Rayleigh-Jeans limit. The values of the brightness temperature for each observed noise storm are listed in table3.2 . The high values of the brightness temperature in comparison with the thermal coronaal temperatures($\sim$ 1 MK), indicates that the observed radiation is non-thermal. One of the main objectives of this chapter is to use the observed data to estimate the power in the accelerated electrons responsible for radio noise storm emission. We use the high temporal resolution light curves to constrain the

Table 3.2 Observed parameters of the noise storms.

Date	Number of bursts detected	Average duration of bursts (s)	Average inter-burst interval(s)	Brightness Temperature (K)	Powerlaw index amplitude
2002 Aug.27	4681	0.20	0.41	$3.34\text{x}10^8$	-3.86
2003 Jul.15	3764	0.22	0.42	$8.84\text{x}10^8$	-3.76
2004 Aug.14	4617	0.21	0.40	$6.37\text{x}10^8$	-5.20
2006 Apr.06	2968	0.27	0.50	$1.24\text{x}10^{10}$	-1.67

following important free parameters in the model: the acceleration time-scale(t_{accel}), which is interpreted as the time between bursts and the residence time of the electron(τ) in the acceleration region, which is interpreted as the burst duration. The inter-burst time-scale is representative of the lifetime of an individual acceleration region, while the duration of a burst is indicative of the time an electron spends in the acceleration region over the numerous collisions it suffers with scattering centres inside the acceleration region. The dimensions of the noise storm emission region are determined from the high-resolution NRH-GMRT images (listed in Table 3.1)

3.3.2 Results and discussion

Noise storm continua

The mean values of the burst duration is identified with mean residence time in the acceleration region (τ) for each noise storm event. Similarly, the mean value of the inter-burst duration is identified as mean acceleration time-scale(t_{accel}). The ratio of these quantities, $\tau/t_{\rm accel} < 4/5$, for the non-thermal electron energy density U_* to remain finite (Subramanian and Becker, 2006). Knowing τ and t_{accel}(or equivalently D_o via Eq3.7) enables us to calculate α_1 and α_2(Eq3.6), which are listed in table3.3. A knowledge of α_1 and α_2 enables us to calculate the ratio of the nonthermal electron density to the thermal one (n_*/n_e), the energy density of the nonthermal electron population (U_*), the ratio of the energy density in the nonthermal electron population to the thermal one ($U_*/(n_e kT)$) and the energy per electron (U_*/n_*) for each observed instance of the noise storm continuum. These quantities are listed in table 3.2. Only electrons above the critical energy(ξ_c) can be accelerated out of the thermal pool. The quantity $(2/3)\xi_c \equiv (p_c^2/2m_e)/(3/2)kT_e$, also listed in table 3.3, is a measure of how far removed this critical energy is from the energy characterizing the bulk thermal electrons.

Table 3.3 Derived parameters for the noise storm continua.

Date	α_1	α_2	$U_*/n_e kT$	$\frac{n_*}{n_e}$	U_*/n_* (erg per electron)	$(2/3)\xi_c$
2002 Aug.27	2.76	-5.76	6.55×10^{-7}	$8.47\text{x}10^{-9}$	$1.29\text{x}10^{-8}$	13.26
2003 Jul.15	2.66	-5.66	2.76×10^{-4}	$5.32\text{x}10^{-6}$	$8.71\text{x}10^{-9}$	8.85
2004 Aug.14	2.67	-5.67	8.69×10^{-7}	$1.14\text{x}10^{-8}$	$1.27\text{x}10^{-8}$	13.05
2006 Apr.06	2.65	-5.65	6.91×10^{-5}	$1.10\text{x}10^{-6}$	$1.01\text{x}10^{-8}$	9.90

Noise storm bursts

We have discussed results pertaining to the noise storm continua so far. Since the continua could be thought of us an ensemble of several individual noise storm bursts we can extend the results calculated in the previous section to a representative burst. Using the smallest observed sources sizes reported by Mercier et al. (2015), we can calculate the volume ; $V = L^3$, where L is the spatial extent corresponding to the source size in arcsec listed in column 3 of Table 3.1 . Using the volume,V, we can find the power P, supplied to the accelerated electron population.

$$P = V\frac{dU_*}{dt} = t_{\text{accel}}^{-1} V U_* \ \ \text{erg s}^{-1} \tag{3.17}$$

The energy (E) contained in a single representative burst is equal to the power (P) divided by the number of bursts that occured during the observation time interval.

$$E = P\frac{\text{duration of event}}{\text{number of bursts}} \ \text{erg} \tag{3.18}$$

The values of P and E for each noise storm episode are listed in column 2 and 3 of table 3.4. The nonthermal energy density per burst is calculated by dividing the total energy per representative burst (E, column 3 of table 3.4) by the volume (V) of the emission region. This quantity is listed in column 4 of table 3.4. We assume that the ratio of nonthermal to thermal energy in the bursts is the same as that for the continuum (column 4 of table 3.3). For each event, we divide the number in column 4 of table 3.4 by the corresponding number in column 4 of table 3.3 to estimate the thermal energy density "per burst". Evidently, the thermal energy density exceeds the nonthermal energy density by three to seven orders of magnitude.

Table 3.4 Parameters of a representative burst

Date	Power in electrons (erg s^{-1})	Energy in accelerated electron population per burst(erg)	Nonthermal energy density per burst (erg cm^{-3})	Thermal energy density per burst (erg cm^{-3})
2002 Aug.27	$4.03x10^{21}$	$7.24x10^{20}$	$0.63x10^{-7}$	0.10
2003 Jul.15	$3.35x10^{24}$	$8.06x10^{23}$	$1.69x10^{-5}$	0.06
2004 Aug.14	$1.67x10^{22}$	$3.70x10^{21}$	$1.06x10^{-7}$	0.12
2006 Apr.06	$2.61x10^{23}$	$7.39x10^{22}$	$4.52x10^{-6}$	0.07

3.4 Conclusions

In this chapter we focus on Type I noisestorms which are examples of small particle acceleration episodes in the solar corona. They are associated with active regions and can last for hours or even days. Type I noise storms could be thought as sites where electrons interact with ensemble of small acceleration sites(in the form of current sheets/magnetic scattering centres which are thought to form throughout corona because of turbulent motion of magnetic field lines (Kumar and Bhattacharyya, 2016a; Kumar et al., 2014; Pisokas et al., 2018)). Since the model needs to explain steady heating of corona, constant acceleration and subsequent energy release is expected (Klimchuk, 2015). Type I noise storms perfectly fit this criterion.

Since radio emission associated with noise storms is coherent, we are able to study the energetics of these small events even though the number of nonthermal electrons being generated in these events are very small. We have used high-resolution imaging data for four noise storms using combined observations with the GMRT and the NRH. We use the high temporal resolution data from the NRH to constrain parameters of the model for stochastic acceleration of electrons developed by Subramanian and Becker (2004). Using an algorithm to extract individual bursts from the continuum we calculate the inter-burst interval(time difference between the peaks of two adjacent bursts) and the time-width of bursts. We interpret the inter-burst interval as the electron acceleration time and burst duration as the residence time of electrons in the acceleration region.

We find that the non-thermal electrons are a very small fraction of the thermal population in all the cases. This fraction ranges from 10^{-9} to 10^{-6} (table 3.3). Similarly, the energy density in the nonthermal electron population per burst is only $\approx 10^{-7}$–10^{-3} times that in the thermal population. This may be contrasted with the "cold" small acceleration events studied by James et al. (2017), where the lack of soft Xray emission associated with their events implies that the acceleration process produced mostly nonthermal electrons (and very few thermal ones). To produce a representative burst the power input into the accelerating

the electrons according to our model ranges from 10^{20} to 10^{23} erg/s (table 3.4). Type I bursts are thus likely contributors to active region coronal heating. However more work is needed to understand more about these weak heating events.

Chapter 4

Investigating particle acceleration and transport from the Solar corona

4.1 Introduction

Sun is a powerful particle accelerator capable of accelerating electrons and ions to relativistic energies. Solar energetic particles (SEPs) are a class of particles which are accelerated at the Sun which then streams along the interplanetary medium. Often they reach Earth through open magnetic field lines and form an important element of the space-weather that can affect life on the Earth as well as in space (Reames, 1990). They were first observed in 1942 when ionization chambers built to observe cosmic rays showed a strange increase in the intensity levels. This puzzling phenomenon was later traced back to solar flares a few months after their first detection (Lange and Forbush, 1942). Initially, it was thought that SEPs were exclusively produced in solar flares and this thinking led to the development of a paradigm where SEPs were always associated with a point source injection and transport while other characteristics such as elemental abundances, energy spectra and spread of distributions were ignored. Wild et al. (1963a) reported the first evidence of multiple particle acceleration processes at play when he showed that two distinct types of radio signatures(type III and type II) are associated with SEPs. The impulsive phase of acceleration is often associated with the presence of type III burst, which are fast frequency shifting radio signatures, produced by wave-plasma interactions by the streaming electrons. The second category of SEPs is associated with type II bursts which are produced by moving shock waves produced in the corona as a result of CME or sometimes flares.

We have now evidence that SEPs display a variety of time-intensity profile characteristics, elemental abundances and radio signatures. Cane et al. (1986) pointed to the

correlation between the X-ray time-intensity profiles : short-duration(impulsive) and long-duration(gradual), and the resultant SEP proton/electron abundance ratios. This distinction between gradual and impulsive time-intensity profile of soft X-rays later got extended to the time-intensity profiles of the SEP events itself (Gosling, 1993; Kahler, 1994, 1992; Reames, 1990, 1995, 1997). The initially developed picture was that of gradual SEP events (time-intensity profile shows a rapid rise with a prolonged decay) being accelerated in CME driven shocks and impulsive SEP events (time-intensity profile shows a sharp rise and decay with much shorter event duration) being accelerated in flares, with no mixed events. However, recent observations are challenging this paradigm, with the current view being that the gradual and impulsive SEPs are limiting cases. In the current view, a continuous mixture of both the classes can occur which implicitly suggests that impulsive and shock acceleration occurs in a varying degree at the Sun and the resultant time-intensity profile can depend on a variety of factors including and not limiting to acceleration characteristics, injection profile, interplanetary transport diffusion and magnetic scattering. The exact ways these factors affect the SEPs are still a matter of ongoing research.

Nonetheless, it is instructive to look at peculiar distinctions exhibited by gradual and impulsive classes of SEPs. As mentioned before the first classification of the two classes was based on elemental abundances. The gradual events were shown to have higher e/p and p/He ratio (Cane et al., 1986; Kallenrode et al., 1992). The gradual events also show a significant increase in the Fe/O and Ne/O ratio as well. A scatter plot of these two quantities(from Reames (1999)) shows a clear separation between the two classes of events even-though event-to-event variation do happen. The gradual events tend to show broad longitudinal distribution while impulsive events show a confined distribution with only events with the best magnetic connectivity to the Earth being observable. This suggests the inherent differences in the acceleration mechanisms that initiate these events. The broad distribution of gradual events should thus be happening not because of cross-field transport but because of the nature of shock wave that accelerated them in the first place. Lastly, we look at the radio signatures, which are temporally associated with the two classes of events. In general slightly more than 20% of all SEP events(both gradual and impulsive) show no association with any radio transients. In the case of gradual and impulsive events which has some radio emission associated, we see some clear distinctions. Impulsive SEP events will always have a type III and will have an associated type II 75% of the cases. Whereas in the case of gradual events, there is a type II association in 100% of cases and an associated type III in 50% of the cases(Kouloumvakos et al., 2015).Impulsive SEPs also has shorter HXR and SXR duration compared to gradual events. A detailed description of the differences between gradual and

impulsive events could be found in Cliver (2009); Kahler et al. (2012); Kallenrode (2003); Reames (1995, 2013).

4.2 Interplanetary transport

The transport of the injected SEP population is influenced by how the Interplanetary magnetic field(IMF) is structured and by the small, turbulent magnetic field fluctuations which are superimposed on top of this magnetic field. The postulation of solar wind and its subsequent discovery is considered to be one of the major scientific triumphs of the past century. The existence of steady stream of supersonic particle streams which we now call the solar wind was predicted by Parker (1958), motivated by the observations of Biermann(1947) on the existence of corpuscular radiation emanating from the Sun. Due to the high conductivity of the plasma combined with low plasma β conditions means the magnetic field dragged by the solar wind is frozen into the plasma and form into the shape of a spiral because of the rotating motion of the Sun. The IMF thus acts as tracers of the plasma flow out of the Sun. Solar wind streams past the Earths orbit with about 400 $km\ s^{-1}$, with a density of 5 atoms $/cm^{-3}$ and magnetic field of 5 nT.

The Archmedian spiral spanned by the IMF can be described by azimuthal and radial coordinates:

$$r - r_0 = \frac{-v}{\Omega cos\theta}(\phi - \phi_0), \tag{4.1}$$

where v is the solar wind speed, Ω is the solar rotation speed, r_0 is the radius of the Sun, r is the radial distance from the Sun, θ is the solar latitude and $\psi = \phi - \phi_0$ is the longitudinal difference between two points on a field line. Since the Sun finishes a rotation in approximately 27 days, on average, it will rotate 13.3 degree per day. Thus the IMF would be making an angle of 60 degree w.r.t to a parcel of solar wind ejected out by the time it takes the parcel with a velocity of v = 400 $km\ s^{-1}$ to reach 1 AU in about four days. Interestingly the spiral angle subtended by the IPM with radial direction depends on the velocity of the solar wind. Slower wind speeds result in tighter spirals compared to faster ones. Since the solar wind consists of slow and fast components, the differential winding rate of the IPM spiral structure will lead to the formation of an interacting region called co-rotating interacting region(CIR).

The average spiral angle at 1 AU is 45 degree for the median velocity of v = 400 $km\ s^{-1}$. However, the solar equatorial plane is tilted with respect to the Earth's equatorial plane by about 7.25 deg, with the angle θ ranging between $-7.25 \leq \theta \geq 7.25$, which changes the polarity pattern of the magnetic field. Thus the IPM would anti-sunwards 7-14 days in a solar rotation and sunwards during the rest of the rotation. Also, it has been observed that there

are sectors of magnetic field polarities depending upon the polarities at the source region in the Sun. This global interplanetary magnetic field with its positive and negative sectors resembles a ballerina's skirt.

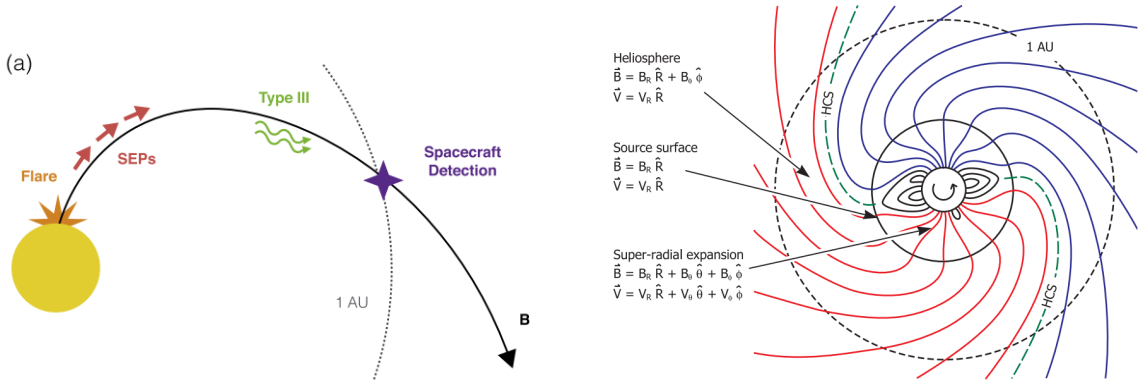

Fig. 4.1 a) A cartoon showing SEP electrons streaming through IMF line. The wave-particle instability causes the emission of type III radio bursts. Note that the type III is streaming on the same field line as of the particle. This is one of precondition for an SEP detection. (Fig credit: Graham et al. (2018). b) Schematic of the steady-state solar magnetic field in the ecliptic plane. Regions of opposite polarity (red and blue) are separated by the heliosphere current sheet. (Fig credit: Owens and Forsyth (2013)

The path length z(r) can be generally described by:

$$z(r) = \frac{a}{2}\left[\frac{r}{a}\sqrt{1+\frac{r^2}{a^2}} + \ln\left(\frac{r}{a}+\sqrt{1+\frac{r^2}{a^2}}\right)\right], \tag{4.2}$$

where $a = v/\Omega$. Thus close to the Sun, where $r/a \ll 1$ we get z $\sim$ r and near 1 AU, where $r/a \gg 1$, z $\sim r^2/2a$.

The field strength, is a function of the radial distance r, given by,

$$B(r) = B_0(r_0/r)^2\sqrt{(1+(r/a)^2)}, \tag{4.3}$$

where r_0 is the distance at which frozen in field condition becomes applicable (usually $r_0 \sim 2\ R_\odot$). A detailed derivation of these quantities could be found in Kallenrode (2013).

4.2.1 Particle Transport

It is through these IMF field lines the SEP particles injected at the Sun will propagate. The motion of these charged particles would be briefly discussed below. For a particle with charge q,mass m, moving with velocity v in the presence of electric field E and magnetic field B, its

motion is determined by the Lorentz force acting on it:

$$\frac{\mathrm{d}\mathbf{p}}{\mathrm{d}t} = q(\mathbf{E} + \mathbf{v} \times \mathbf{B}) \tag{4.4}$$

where $v = p(\gamma m)$, with γ being the Lorentz factor. Here we assume and gravitational forces are negligible and since the solar wind plasma is highly collisionless, no diffusive forces due to collisions are present as well. The particle motion can be decomposed into the gyratory motion around the field line and the translational motion along the field line. The Larmour radius which is the radius of gyration of the particle is given by:

$$r_L = \frac{v_\perp}{\omega_c} = \frac{p_\perp}{|q|B} \tag{4.5}$$

where $v_\perp$ and $p_\perp$ are the velocity and the momentum perpendicular to the magnetic field. Since the particle follows a helicoidal motion the particle velocities can be decoupled into the perpendicular ($v_\perp$) and the parallel component ($v_\parallel$). The concept of guiding magnetic field is helpful in describing the motions in the case of decoupled velocity component in the presence of the magnetic field. However, the perpendicular component of velocity can have contributions from any drift that the particle experiences in a varying electromagnetic field and the angular velocity around the IPM field line due to its gyration. Particles can experience a variety of drifts depending upon the configuration of the fields. For the case of IMF travel, two major drifts that can affect the motion of the particle are caused by inhomogeneous magnetic fields and the curvature of the field lines. Thus the velocity of the particle is a mixture of :

$$v = v_\parallel + v_\perp = v_\parallel + v_D + \omega_c = v_{gc} + \omega_c, \tag{4.6}$$

where v_D is the velocity gained in the drifts and v_{gc} is the velocity of the particle with the gyration effects decoupled. Over long times the gyration effects are averaged out, and the particle motion is purely described using the motion of the guiding centre.

One useful quantity to be defined is the ratio of parallel and perpendicular velocity components, called the pitch angle α,

$$\alpha = tan^{-1}(v_\perp / v_\parallel). \tag{4.7}$$

The cosine of the pitch angle α, $\mu = cos\alpha$ defines the direction of the velocity of the particles with respect the magnetic field line. If the particle is travelling ant-sunwards (towards the earth), then $\mu = 1$. The pitch angle scattering based focused transport technique is a major model to describe the transport of the SEP particles through the IPM.

The highly conductive plasma in the IPM implies the electric field is zero and the particle motion is entirely under magnetic field which we assume to be homogeneous for the moment. Then it can be shown that the first integral of the motion is constant,

$$\frac{1}{2}m\frac{dv^2}{dt} = \frac{dW_{kin}}{dt} = qv.(v \times B) = 0. \tag{4.8}$$

The particle kinetic energy can be decomposed into the perpendicular and parallel components. In a static magnetic field, then $v_{\|}$ is constant. This essentially means $W_{\perp}$, and hence $v_{\perp}$ is also conserved. For slowly changing magnetic fields certain quantities will be conserved called the adiabatic invariants. The first adiabatic invariant the magnetic moment m which will stay as a constant of the motion in slowly varying magnetic fields. For a particle entering into an area with diverging magnetic field its $W_{\perp}$ decreases which force $W_{\|}$ to increase to keep W constant; which increases the Larmors radius resulting in the decrease of the pitch angle. This has a resultant effect of focusing of the particle beam in SEP transport as the IPM magnetic field falls off as given in eq4.3. This focusing effect has important implications for SEP transport. The opposite can happen in the region of increasing magnetic field, with the pitch angle increasing.

4.3 SEPs accelerated in Solar flare

As mentioned before the two major sources of SEP's are solar flares and CME's. Evidence suggests two different acceleration mechanisms at play in both these cases. In this chapter, we will be exclusively focusing on SEP's that are temporally associated with solar flares. Our motivation for such a choice is explained below.

With the advancements in flare observations, we now know that solar flares can have different global properties including but not limited to the interactions that can happen between different layers of the solar atmosphere, flare geometries, energy budgets and the resultant electromagnetic signature. However the bigger picture of the flaring process starting from the pre-flare phase, the impulsive phase and after-flare cooldown is thought to follow a standard set of sequences which is usually known as the standard flare model(the model is also referred as CSHKP model named after the scientists who significantly contributed towards its development - Carmichael (1964); Hirayama (1974); Kopp and Pneuman (1976); Sturrock (1966)). In the standard flare scenario, magnetic energy stored in bipolar loops or arcade structures is released after reconnection. The accelerated electrons stream through the corona, which has collisionless plasma until they encounter denser parts of chromosphere where they undergo Coulomb collisions with ambient protons and produce hard-Xray bremsstrahlung

radiation. From the symmetry of the flare geometry, it can be seen that particles can also stream upwards through the newly reconnected coronal loops and sometimes find access to open-magnetic field lines which will give them passage through IPM field lines. So in these scenarios, the particles can be thought to be accelerated in the same site but released into closed or open magnetic field lines. The escaping electrons after streaming through the IPM field lines are eventually detected in-situ near 1AU by the particle detectors onboard satellites as SEP particles(Fig 4.2).

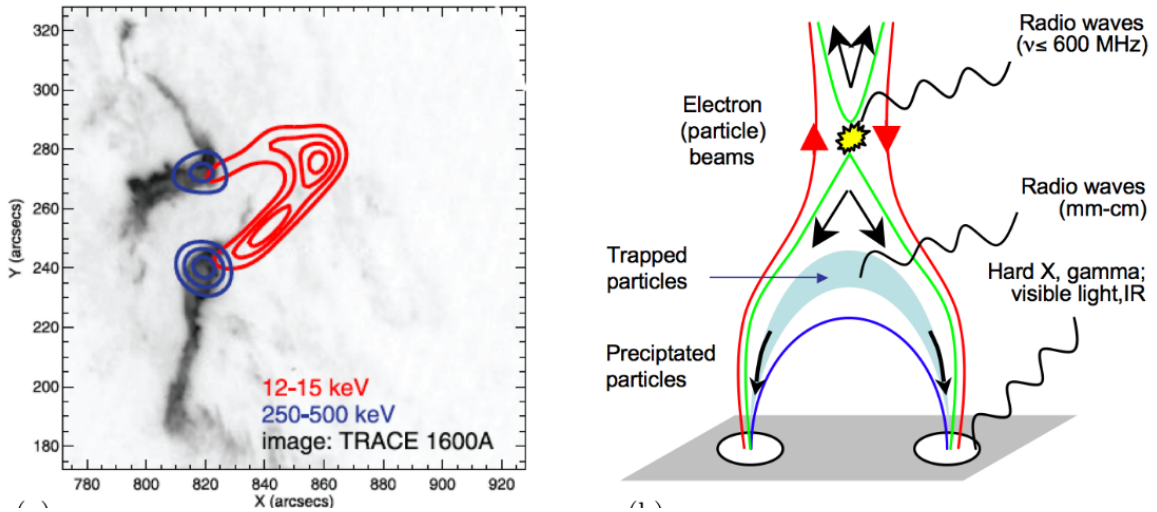

Fig. 4.2 The source morphology usually observed during the solar flare is shown in the form of a cartoon in the right panel. Energy release happens at the top of the loop, which accelerates electrons. Most often this beam of electrons is bi-directional in nature, with one part producing the HXR radiation in the chromospheric footpoints and the other, escaping into the interplanetary space as SEPs. The panel on the left show observations by RHESSI of the 2005 Jan 20 flare.(Fig credit: Klein and Dalla (2017))

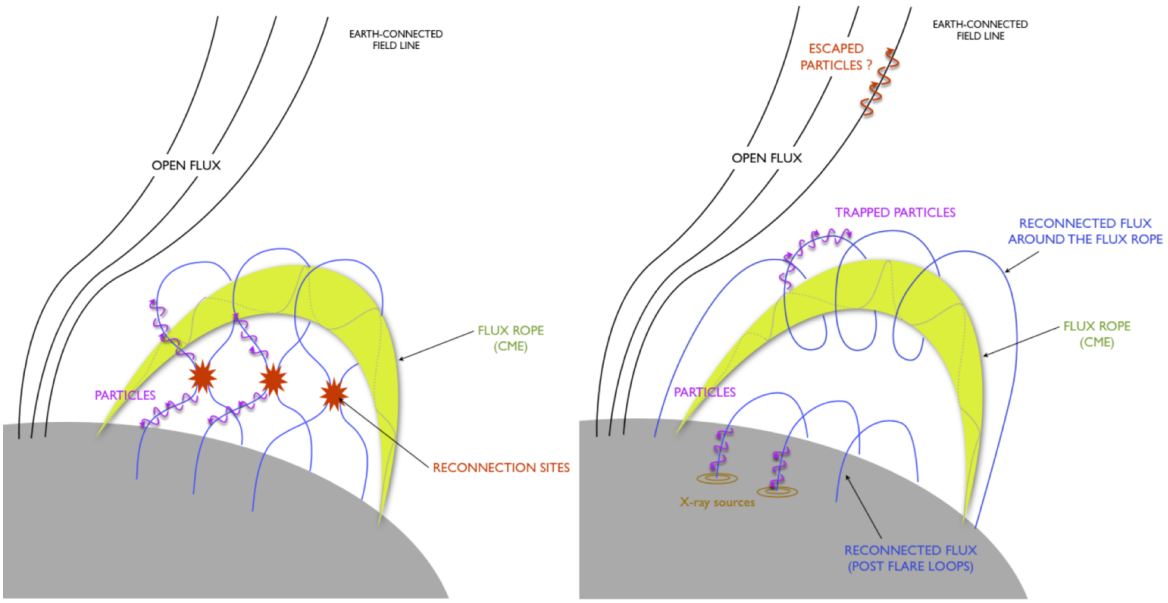

Fig. 4.3 The actual mechansim by which the accelerated particles get access to open-magnetic field line is a matter of debate. We show a likely scenario in which the particles are accelerated in a reconnection events close to a region with pre-existing open-magnetic field lines. In this scenario a reconnected magnetic field line can transfer some part of the accelerated electrons to the open magnetic-field lines while most of the accelerated electrons are trapped in the loop and goes on to heat the loop. (fig credit: Sophie Musset)

In this particular acceleration scenario, it is reasonable to assume that the electrons which stream down to the chromosphere that eventually produce HXR radiation and the escaping electrons both come from the same parent population.

If this hypothesis is true, then the spectral characteristics of the electrons found via inverting the HXR spectrum at the Sun and the energy spectra of the in-situ electrons of the SEP should match. Additionally, the onset time of the SEP electrons should match with the flare onset back at the Sun in velocity dispersion analysis. Velocity dispersion analysis involves plotting of electron onset times and their corresponding velocities of the respective energy channels to get information about onset time at the Sun, and the path-length travelled (Krucker et al., 1999). This technique is based on two key assumptions:- energy independent injection profile and scatter free propagation of the first arriving electrons. Another diagnostic that helps in determining the onset time at the Sun is the presence of type III burst. IP type III bursts are generated due to wave-particle interaction of streaming SEP electrons and local plasma Langmuir waves, and hence their onset signifies particle injection into IP medium.

Krucker et al. (1999) using Velocity Dispersion analysis(VDA) examined 12 SEP events which had good counts in <25 keV range. He reported that

1. in seven out of 12 cases, the calculated onset times match with the release times inferred from type III burst

2. in three cases the inferred release times were found to be larger than type III onset and

3. in rest two,low energy(< 25 keV) electrons coincided with type III burst onset, but high energy(>25 keV) electrons were delayed.

For cases the $t_r \sim t_{iii}$, it was found to occur in a magnetically well-connected region and in cases where a delay was noted, the Parkers field line were in far away longitudes. Analyzing just the events with high energy(>25 keV) electrons, 41 out of 58 events had an apparent delayed injection, which suggested that the low and high energy SEP electrons might be produced by different acceleration process. Other studies looking for delayed events found a median delay of 13 mins between type III burst onset and electron injection (Haggerty and Roelof, 2002). However, there are certain caveats that one needs to remember when using type III data to determine onset. Type III bursts are generated by 2-20 keV electrons, and hence there can be an inherent time-delay w.r.t high energy electrons(>100 keV) which arrive first at 1 AU (Buttighoffer, 1998; Ergun et al., 1998; Lin et al., 1981). Also, the radio emission just above the local plasma frequency can be generated when the electron beam is very close to the spacecraft. Hence if the electron beam does not extend to lower frequencies, the SEP event will be missed by the spacecraft (Cane and Erickson, 2003).

Multiple theories have been proposed to explain the delay observed with SEP electrons at 1 AU with respect to type III burst timings:

1. Ragot (2006), using simulations explored large scale wandering of particles due to magnetic field-line irregularities present on finer length-scales. He pointed out that the wide range of path lengths one obtain while using velocity dispersion analysis instead of a value centred around 1.2 AU which is the nominal Parker spiral length at 1AU invalidates this method and its underlying assumptions of scatter free travel and energy independent injection. An increase in path length by 50% was found for a turbulent field line in comparison with a smooth field line. The resulting travel delay was found to be of the order of 19-23 mins for 5 keV electrons. The delays are shorter for fast particles and longer for slower particles since the increase is proportional to the actual travel time and the particle gyro-radius.

2. Many studies have pointed out the possibility of delayed acceleration(Haggerty and Roelof, 2002; Krucker et al., 1999). Delayed acceleration can occur either due to the high energy electrons getting accelerated at a different site than where type III bursts

are produced or due to acceleration of an entirely different population of electrons by the CME shocks.

3. Cane and Erickson (2003) refuted the idea that there are different electron population that generates the type III burst (with < 25 keV producing the type III burst and > 25 keV being detected as SEP particles). Using data from WIND/TNR receiver, he concluded that there is only one electron population and it is purely because of transport effects that the electron population is delayed at 1AU. A detailed study using transport models and anisotropy information was suggested to understand this problem further.

The above-quoted results present an inconclusive and broadly confusing picture regarding solar flare acceleration of electrons, their injection and their subsequent detection. Interestingly most of the studies to date have only used radio signatures and SEP differential fluxes to develop a bigger picture. The most immediate signature after a flaring process is the HXR signature caused by the flare accelerated electrons. Studies have shown the existence of events which has temporally correlation of HXR, type III and SEP signatures. In this chapter, we propose to test the hypothesis of whether HXR producing and SEP population electrons belong to the same parent population or not. Using combined data from HXR observations, radio signatures and SEP observations, we try to quantify the temporal and spectral correlations between these two different populations.

4.4 Data Analysis

For our study, we did a survey spanning the operational lifetime of RHESSI spacecraft (2002-2018) for SEP events which had clear HXR and radio signatures. This period covered two solar maximums and one minimum. The multi-wavelength, multi-spacecraft survey for these SEP events was conducted using data from 5 different instruments aboard four different spacecraft. These were HXR counts from RHESSI/FERMI, SXR flux from GOES, radio data from WIND/WAVES and particle flux data from WIND/3DP. A short overview of RHESSI, GOES, and WIND/WAVES instruments were given in Chapter 2. Below we briefly mention the rest of the instruments that we have used.

4.4.1 Instrument overview

FERMI Gamma ray telescope

FERMI Gamma ray telescope launched on June 11,2008, is a multi-agency space mission that can study the cosmos in the energy range 10 keV -300 GeV. Due to the wide range of

energies that its detectors are capable of measuring, the FERMI mission is tasked with a host of objectives. Some of them are to understand the extreme energetic mechanisms in supermassive black-holes, pulsars and supernovae that can generate Gamma rays, searching for new laws of Physics that composes Dark Matter, acceleration mechanisms in accretion disks around black holes, investigating the mysterious gamma-ray bursts,understanding energetic processes behind solar flares and the interaction of the gamma-ray Sun and galactic cosmic rays.

FERMI consists of two major instruments - Gamma-ray Burst Monitor(GBM) and Large Area Telescope(LAT). The LAT is the most sensitive gamma-ray telescope ever developed. LAT is an imaging high energy gamma-ray telescope covering the energy range 20 MeV to more than 300 GeV. Since gamma-rays could not be focused, LAT uses plastic anti-coincidence detectors which converts the incoming gamma rays to electron-positron pair. The progress of this pair of particles is tracked using silicon strip detectors and later energy is measured when they are stopped in a caesium iodide calorimeter. FERMI spacecraft completes one orbit around the earth in 96 minutes. Since the LAT is positioned in an upward direction in reference to the earth, it is not occulted. The large field of view($\sim$ 20 deg of the sky) enables efficient surveying for gamma-ray events. LAT can be trigger activated to point to a region of interest of sky to collect data when an intense gamma-ray burst happens (Meegan, 2008; von Kienlin et al., 2004).

The GBM detector is made up of 12 Sodium Iodide(NaI) and 2 Bismuth Germanate(BGO) scintillation detectors. The NaI detectors cover the lower part of the energy range, 8keV to 1 MeV, while the BGO detectors cover the overlapping region between the NaI detectors and the LAT instrument. The NaI detectors are suitable for analyzing small solar flare, and due to the inter-calibration done with RHESSI, it complements its observations. GBM has a temporal resolution comparable to RHESSI but has a significantly lower spectral resolution. However, for the purposes of our analysis, good counts above the background are sufficient to get a good spectral fit. We have thus used FERMI GBM data wherever RHESSI data was not available.

WIND/3DP

The WIND spacecraft carries multiple particle detection experiments capable of detecting several species of particles in wide-ranging energies. The 3-D Plasma and Energetic Particle(3DP) gives full three-dimensional measurements of supra-thermal electron and ion distributions from the solar wind thermal plasma. The 3DP instrument is a suite of three detector systems: the silicon semiconductor telescopes(SST), the electron electrostatic analyzers (EESA) and the ion electrostatic analyzers (PESA). SST can measure electrons $\sim$ 25

keV to 1 MeV and ions from $\sim$ 20 keV to 11 MeV. The EESA sensors can measure electrons from $\sim$ 3 eV to 30 keV. For the purpose of our analysis, like investigating the time-intensity profile of SEP and spectrum measurement, we use data from SST. The SST is made up of three arrays of two double-ended telescopes. Four of them has a silicon semiconductor detector while the other two consists of a triplet of closely-sandwiched detectors. To achieve high sensitivity and to reduce the thermal noise the SST is thermally isolated and maintains a temperature of $\sim$ 0 deg C. All telescopes has 36 deg x 20 deg FWHM FOVs, and hence, five telescopes (#1,3-6) cover a 180 deg x 20 deg FOV. Telescope #2 has the same view angle as telescope #6 but is reserved for high-intensity fluxes. Together with the spin of the spacecraft,SST can have an angular coverage of 4π every 3 secs (Lin, 1998).

SST sampling rate is 16 Hz per spin. The data collected by the detectors are sorted into 40 angular bins each with an average solid angle of $\sim$ 18 deg. Each bin can be assigned as a pitch angle(PA) based on the IMF field direction, which can be measured using WIND MFI instrument. Thus the pitch angle distributions (PADs) of the SEPs can be calculated with high temporal resolution. The sunwards and anti-sunwards bins have a high degree of background contamination due to incident solar x-rays and are omitted from the flux and PAD calculation. In normal modes, the data is telemetered after averaging four spins ($\sim$ 12-sec resolution).

WIND/SWE

The solar wind experiment(SWE) instrument onboard WIND is a suite of three instruments: the Vector Electron Ion Spectrometer(VEIS), Faraday Cup and the Strahl detector. With these instruments, SWE is capable of making comprehensive measurements of the solar wind. Of particular interest to us is the Faraday cup, which can measure the velocity, density and temperature of the solar wind ions, in three independent directions. Faraday cup consists of a series of wire-mesh, planar grids made up of tungsten wire embedded in a collector plate. By applying a sequence of voltages to the grid, one can control E/Q ratio of particles that can pass through. Usually, this voltage is varied between two fixed levels, V_1 and V_2 at a frequency of a few hundred Hz. A phase-sensitive detector then measures the current on the collector plate and combining the existing voltage levels at the detection point the particle spectrum could be explored. From these measurements, solar wind velocity could be ascertained, which is our primary interest Ogilvie et al. (1995).

WIND/MFI

The magnetic field investigation(MFI) instrument on WIND is a deployable boom mount, triaxial instrument with a wide dynamic range of 0.1 nT to 66000 nT. A very low sensor noise level of 0.0006 nT enables accurate measurements. MFI's main mission goal is to understand the interaction of the IMF line and the solar wind. MFI can measure wide range of physical and temporal scale of magnetic features, like solar wind magnetic field sectors which can extend up to $\sim$0.5 AU and $\sim$ 100 Hr, interplanetary ejecta and bulk magnetic clouds with length scale of $\sim$0.3 AU and $\sim$30 hrs and micro-scale features like MHD wave discontinuities $\sim 10^3$ and temporal scales of $\sim$5 Hrs. It can also detect shock wave ramps in the kinetic scale with time-scale $\sim$ 500 secs (Lepping et al., 1995).

Data Pipeline

The survey conducted for shortlisting events following the criterions described below, necessitated searching multiple databases for accessing data corresponding to different instruments. For our study, we used data from 9 instruments aboard five satellites. Our data pipeline is written in MATLAB and can interface with Python and IDL as well, using a bridge. The pipeline can handle FTP,FTPS,SFTP and HTTPS protocols for file handling. It can handle data stored in FITS,CDF and ASCII file formats. There are three modes of operation - Survey, Plotting and Instrument specific. In survey mode, the user can search for events which have an accompanying flare or CME. The flare data is taken from RHESSI/FERMI GBM flare list and CME information from SOHO LASCO catalogue. The user can also manually look through data from multiple instruments of choice, in a combined manner for a certain time period. In plotting mode, the user can input any particular event, and the pipeline generates plots using data from instruments chosen. As an example, see figures 4.5 and 4.8. Instrument specific modes allow plotting of data corresponding to a particular instrument. Instrument specific modes are useful for calculating derived quantities like spectra.

4.5 Data Selection

As a first step, using the data pipeline(described above), we look for SEP events. A SEP event is defined as a pronounced 3$\times$ enhancement over the background in the lower energy channel and at least 2$\times$ increase in higher energy channel. SST has seven logarithmically separated energy channel. Thus a SEP trigger in the pipeline is initiated if temporally correlated increase(3x) is observed in the 27,40 and 66 keV energy channels of WIND/3DP SST detector(hereon referred just as WIND/3DP) and 2x increase is observed in the 108

and 181 keV energy channel. Once the SEP is confirmed, a multi-wavelength time snapshot of the event is created, with the HXR and radio data aligned on top of the SEP event. This allows one to see useful temporal association in other wavelength bands. For an event to be included in our final shortlist, we demanded the following physical conditions:

1. A clear enhancement should be visible in the HXR lightcurve for energies in the range 12-25 keV. Since the physical picture that we are interested in is the one in which solar flares impulsively accelerating electrons, part of which escapes towards the earth, having a clear HXR signature is important. Flares in HXR lightcurve usually manifest as an impulsive enhancement over the background. Flares having predominantly thermal signatures will have a very little signature in >25 keV regime, and this prevents accurate fitting of the photon spectra. Hence we have only included events which had clear HXR enhancement atleast up to 25 keV. The peak in the 12-25 keV channel is marked as the time point at which particles are injected($t_{injection}$).

2. In conjunction with HXR signature, we require that the WIND/WAVES frequency spectrum show the presence of a type III burst. We have avoided situations where there is a significant delay in the type III start w.r.t to the peak of HXR signature. The maximum allowed delay was taken to be 5 mins ,ie, $t_{III} \leq t_{injection} + 5$.

3. We also looked at GOES SXR data for all the events we considered. SXR emission is an important diagnostic for thermal emission that succeeds the HXR emission and helps in better understanding the particle acceleration processes caused by the flare. However, this was not a pre-requisite for the inclusion of an event. Eventhough this is not a shortlisting criterion, it is an important parameter to look as historically, SEP classifications into gradual and impulsive originated from the intensity of SXR flares associated with them.

4. We characterize the SEP event by looking at its rise and decay profiles (see Section below). Since SEP events can continue for hours, it becomes very difficult to judge the decay timescales. Often the tail of the SEP event gets contaminated by another SEP. Hence we impose the condition that the SEP event should be well contained in an 8000 secs time window from the HXR onset time.

After this exhaustive search, we have discovered 28 events which satisfied our criterion spanning 2002 to 2017. These events are listed in Table 4.1.

We mention here briefly two other studies which have done a statistical study of SEPs with similar selection criterion. Krucker et al. (2007) studied 16 SEP events with simultaneous

RHESSI X-ray observations which were well connected magnetically and showed clear scatter-free velocity dispersion. The time period for their study was 2002-2005, whereas ours cover up to 2018. These 16 events had an inferred solar release time from VDA analysis close to the solar-type III burst and were called prompt events. They also analyzed 15 delayed events which showed a delay(> 8 minutes) in comparison to the inferred release time and occurrence time of type III burst. They found that the prompt events are always associated with short impulsive flares, whereas delayed events had longer duration flares. James et al. (2017) shortlisted six events with clear HXR correspondence and which are not associated with big flares(GOES class less than C1.1) or CMEs. Flares that belong in GOES class C1 and below are often microflares. RHESSI detectors are not sensitive enough to detect nanoflares. In our final shortlist, there are six events(prompt) from Krucker et al. (2007) and two events from James et al. (2017).

Particles are assumed to be injected right at HXR flaring instant. This assumption is corroborated by the simultaneous occurrence of the HXR onset and the type III burst onset. Second column of table 4.1 lists, the injection time which is taken as the peak of the 12-25 keV RHESSI HXR lightcurve which we call the flare onset time. The flare onset time marks the point we assume the particles are injected into the interplanetary medium. This time is denoted as $t_{injection}$. In the third column, we list the peak time in SXR data, determined from 1-8 A lightcurve of GOES satellites. GOES satellites are replaced over the years, and hence for our survey, we used data from GOES 10(events occurring between 2002-2004) , GOES 12(events between 2004-2010) and GOES 15(events between 2011-2018). Due to the Neupert effect (Neupert, 1968), it is expected to peak later than the HXR peak times. The third column lists the GOES flare class, determined from the SXR flux level. The fourth column lists type III onset times (t_{III}), which is determined visually from the spectrogram data of WIND/WAVES. Depending on the availability of magnetic free lines, there is a possibility that electrons can slightly wander before entering the interplanetary space. We allow a tolerance of 5 minutes for the appearance of type III burst for the events ($t_{III} \leq t_{injection} + 5$). The final column lists the arrival time of SEP electrons near 1AU (t_{onset}). The onset time of SEP is determined using a time-series technique called changepoint detection, which is explained in more detail below.

Fig 4.5 depicts a time snapshot plot for the event on 2002-04-25. The different panels from top to bottom depict the event from the Sun to the near-earth detection of the SEP. The first panel shows the HXR light curves for different energy channels. Depending on data availability, this the detector used was either RHESSI or FERMI. For RHESSI data, we used corrected count rates, which takes care of pulse pileup corrections and attenuator states. RHESSI employs attenuators to prevent saturation of detectors in high-intensity

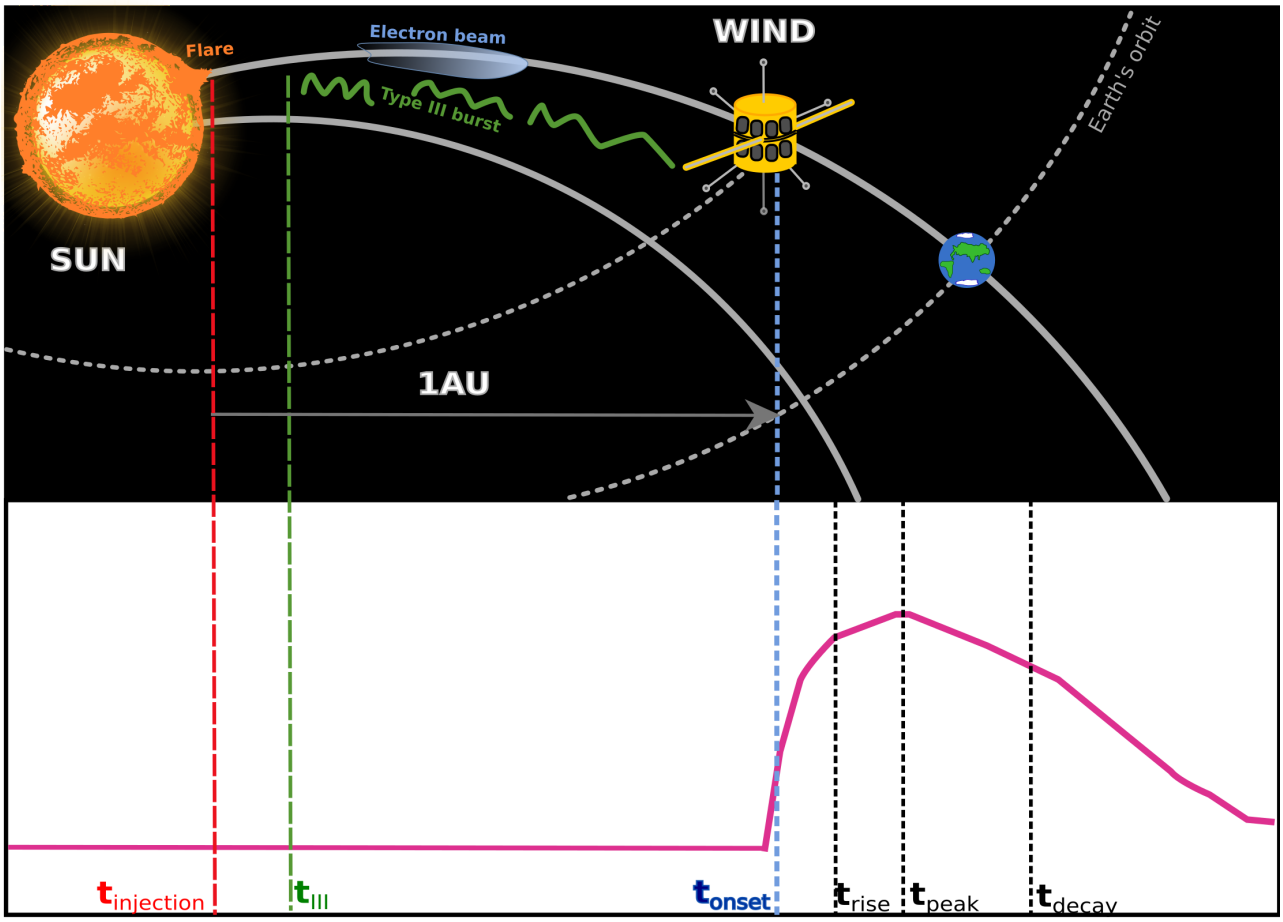

Fig. 4.4 A schematic to elucidate the different temporal quantities that we defined to quantify a SEP. The first panel shows the Sun and the Earth with the WIND spacecraft placed at L1 point with x-axis denoting the physical distance(not to scale). The flare site at the Sun is assumed to have a ready magnetic connectivity to the Parker spiral which extends to 1AU. The WIND spacecraft at L1 point 1.5 million miles ahead of the Earth, and can detect particles,waves and magnetic field. The electron beam is shown to stream along the Parker spiral which causes local plasma oscillations resulting in the emission of type III burst. The frequency of type III burst drifts as the electron beam moves from denser plasma near the corona to very diffuse plasma near 1AU. The second panel is the temporal analogue of the events depicted in the first panel with x-axis representing time. The flare onset time is the peak of HXR emission at the Sun and the particles are assumed to be injected into the interplanetary space. The is denoted by the red dashed line($t_{injection}$). The start time of type III waves is denoted by t_{III}. For all our events (Table 4.1) $t_{III} \sim t_{injection}$. After streaming through the Parker spiral of $\sim$ 1 AU it reaches the WIND spacecraft where the particles are detected by the 3DP instrument. The arrival of these SEP electrons can only be sensed when their flux is higher than the background level.This point where the flux level shows significant change over the background level is detected using changepoint detection algorithm is denoted by t_{onset}. Thus $t_{injection}$ and t_{onset} together uniquely define the arrival time of SEPs. We also define three additional quantities to uniquely define the time-intensity profile of the SEPs - $t_{rise}, t_{peak}, t_{decay}$.

flares. The HXR signature appears as a sharp rise above the background flux level. Since RHESSI is an unshielded telescope, the background flux levels tend to obscure many small flares. In this example there,6-12 and 12-25 keV peaks are well defined. We require that the flare signature should be present in 12-25 keV channel for non-thermal electrons which increases the goodness of fit when finding the spectrum. The peak of the 12-25 keV channel is determined to be at 05:55UT. This is marked by the red dashed line is presumed to be instant when the electrons are injected into the open magnetic field lines,$t_{injection}$. In the second panel, we show the GOES SXR signature from GOES 10 satellite. SXR radiation happens as a secondary step since the initially accelerated electrons undergo bremsstrahlung in the chromosphere, heats up the plasma forcing it to rise through the now empty field loops. This evaporated plasma undergo thermal bremsstrahlung producing SXR. Thus SXR radiation is a good proxy for the thermal electrons. The peak of the SXR flux happens around 2 mins later than the HXR flux. Neupert (1968) showed that the SXR thermal emission follows the time-integral of the HXR emission, which is evident in this case. The red dashed line on this panel is the extension of the injection time as determined from the HXR data. The third panel is the spectrogram data from WIND/WAVES, showing the start of type III burst. The fast frequency drifting type III burst signifies the electron beam streaming across the IPM field. The red dashed line is same as before. The fourth and fifth panels contain WIND/3DP data of the detected SEP. In the fourth panel, we show the time-intensity profile of four energy channels of 3DP. A time-shift corresponding to different arrival times of the electrons in different energy channels is clearly seen. The dashed lines with the same colour as of each channel is the expected arrival time provided the transport were scatter free, and the nominal parker spiral length was 1.2AU. However, as many studies have shown, scatter free transport is rather an exception and not the norm. The fifth panel is an expanded view showing just the 66 keV channel, which is the lightcurve that we use to quantify various parameters of the SEP. The various timings denoted in the fifth panel is explained in more detail in section 4.5.1 and also in Fig4.4.

Similar time-snapshot graphs for all the other shortlisted events are included in the appendix.

4.5.1 Quantifying SEP lightcurve

The SEPs show lots of variations in their temporal and spectral characteristics. By temporal characteristics, we mean the form of time-intensity profile and arrival times. The processes involving the generation of SEPs are complex and are poorly understood. There is much ambiguity regarding the acceleration process at the Sun that injected the SEP particle. One of the primary reason we chose to only event with prompt flare injection and not which

Event Date	Injection at Sun RHESSI HXR (UT) $t_{injection}$	Onset at GoES (UT)	GOES flux level (Watt/m^2)	Type III onset WIND/WAVES (UT) t_{III}	SEP onset WIND/3DP (UT) t_{onset}
Apr 25,2002	05.55	05.57	C1.9	05.58	06.17
Aug 19,2002	21.01	21.02	M3.5	21.02	21.26
Oct 19,2002	21.14	21.15	C5.2	21.15	21.32
Sep 30,2003	00.29	00.32	C1.1	00.32	00.48
Sep 30,2003	08.48	-	-	08.50	09.08
Dec 31,2003	18.23	18.23	M1.0	18.21	18.41
Feb 28,2004	03.24	03.24	B7.6	03.25	03.41
Dec 25,2004	22.29	22.29	B1.2	22.29	22.49
May 16,2005	02.40	02.41	M1.3	02.41	02.53
Nov 24,2005	16.09	16.10	B1.1	16.10	16.30
Nov 19,2006	22.59	23.00	A7.1	23.01	23.13
Nov 20,2006	03.35	03.35	B1.0	03.36	03.49
Jul 07,2011	14.29	14.31	C1.1	14.28	15.04
Aug 08,2011	15.35	15.35	C0.4	15.35	16.19
Aug 08,2011	18.03	18.06	M5.0	18.03	18.22
Nov 12,2013	08.11	08.12	C2.0	08.12	08.34
Nov 12,2013	21.39	21.40	C4.5	21.40	22.01
Feb 20,2014	07.51	07.51	M4.1	07.52	08.08
Mar 28,2014	20.57	20.58	C1.5	20.58	21.27
Jan 20,2015	09.48	09.49	C1.3	09.49	10.09
May 13,2015	08.01	08.01	C1.4	08.03	08.20
Dec 04,2015	14.32	14.32	B7.2	14.33	14.53
Jan 28,2016	11.58	12.00	C1.3	11.59	12.27
Jan 28,2016	21.53	21.56	C7.3	21.54	22.22
Jan 29,2016	08.14	08.15	C5.1	08.14	08.44
Jan 29,2016	16.37	16.39	C1.8	16.38	17.12
Jul 20,2016	22.05	22.08	C4.8	22.07	22.21
Apr 04,2017	09.48	09.48	C3.2	09.52	10.18

Table 4.1 The events shortlisted for further analysis. The onset times at RHESSI, GOES, WIND/RAD for type III and SEP onset times at WIND/3DP are listed. For few events there are no perceptible photon increase in RHESSI detectors. In this case GOES flare peak was taken as the onset time at the SUN. The GOES flux level is written in the format of the GOES flare class. The flare onset time(second column) is supposed to be the instant at which the particles are injected, $t_{injection}$.The onset of type III burst is denoted by t_{III} (fifth column). For all our events it follows $t_{III} < t_{injection} + 5min$. The arrival time of SEPs at WIND spacecraft is denoted by t_{onset}(sixth column).

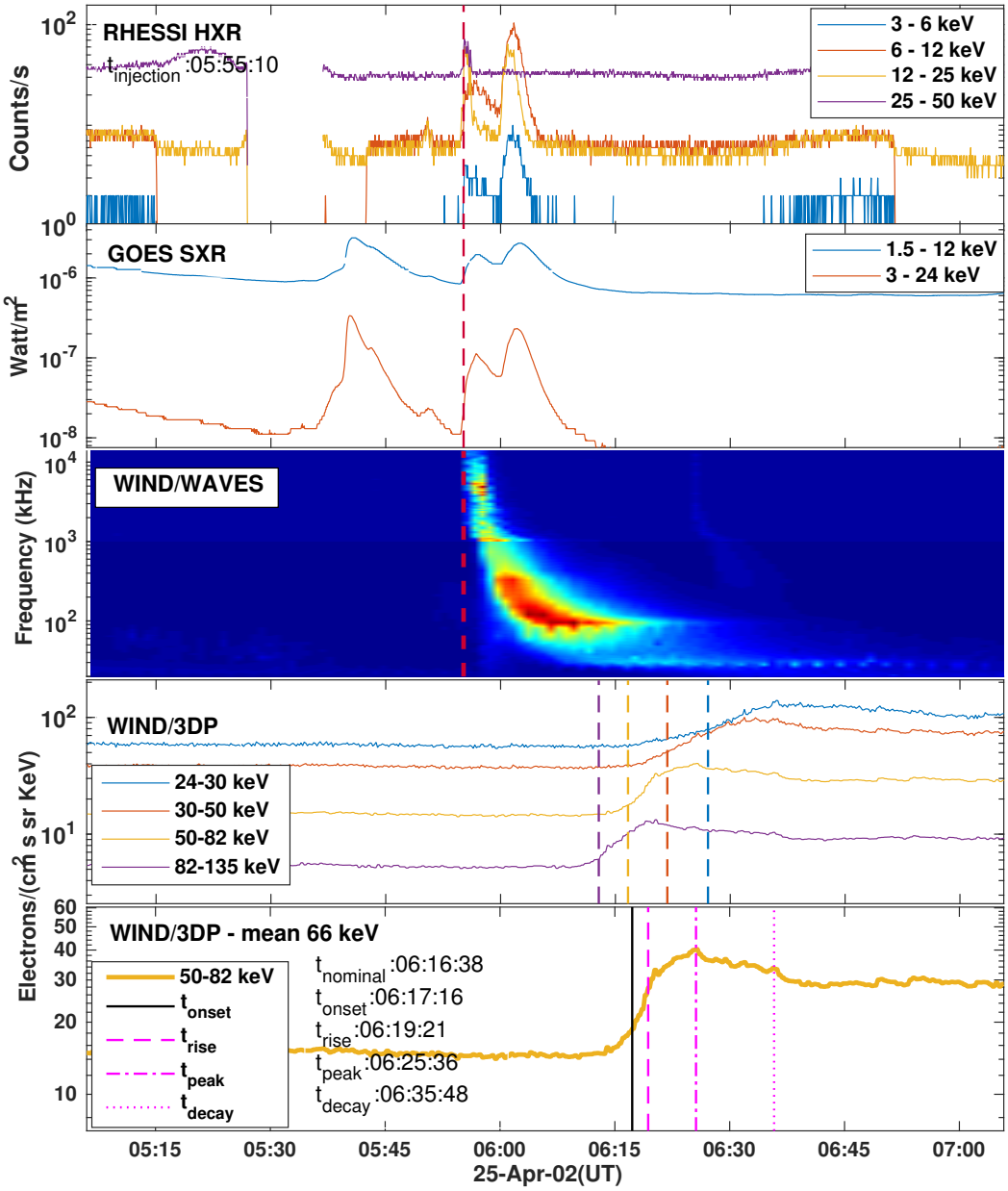

Fig. 4.5 The time profile of the event observed on 2002-04-25.The RHESSI data is shown in the top panel, with the dark blue dashed lines showing the flare time recorded in RHESSI flare list. The second panel shows GOES/SXR lightcurve. The event has C2.5 GOES flare associated with it. The third panel shows the a type III burst from WIND/WAVES indicating the release of electrons into interplanetary medium happened simultaneously with the flare. The last panel shows the detected SEP event from the in-situ data of WIND/3DP.The dashed lines shows the expected arrival times corresponding to each channel.

shows delayed injection is to avoid latent factors which could be affecting the temporal and spectral properties. The second major factor that can affect the SEP characteristics is the transport phase, where multiple processes can affect and modify the SEP population, such

that it can possibly smear out the memory of the parent population. The quantities chosen to represent the SEP in conjunction with other parameters should be able to decouple the effects of acceleration and transport.

The temporal information contained in the time-intensity measurement (also known as flux and usually measured in the units of $cm^{-2}\ sr^{-1}\ s^{-1}\ keV^{-1}$) can be used to determine a SEP uniquely. The primary quantity of interest is the delay in arrival at 1 AU. Since we are only considering events with no significant delay at the acceleration site, any delay later observed should be purely because of transport effects. For the WIND/3DP energy channel with mean energy 66 keV, the first arrival of particles should happen after 1292 seconds of the injection time at the Sun. This is valid however only if the particle propagation happened along a 1.2 AU long parker spiral in scatter-free conditions. Such conditions, however, happen very rarely. There are no standard conventions regarding the arrival of SEP population. Since there is always the influx of solar wind particles, SEP's would be detectable only when they rise above this background flux. Thus the problem can be essentially reduced to that of estimating critical points where some statistical quantity of a time-series drastically changes. This has been extensively studied by the time-series analysis community and is known as changepoint detection algorithms.

Changepoint Detection Algorithm

For our study, we use a binary segmentation method for changepoint detection. A random point is chosen, which divides the data into two segments. We use mean as the statistical quantity to measure abrupt changes. For each section, the deviation from the mean of the section, for each point is calculated. Adding this sum of deviation from both the sections yields the total residual error. This binary sectioning is iteratively continued until the total residual error attains a minimum. Thus if $y_1, y_2, y_3, ..., y_n$ is a time-series with n points, and k is the changepoint, then the total residual error with mean as the statistical quantity is given by,

$$J = \sum_{i=1}^{k-1} (y_i - \langle y \rangle_1^{k-1})^2 + \sum_{i=k}^{N} (y_i - \langle y \rangle_k^N)^2$$
$$= \sum_{i=1}^{k-1} \left(y_i - \frac{1}{k-1} \sum_{r=1}^{k-1} x_r \right)^2 + \sum_{i=k}^{N} \left(y_i - \frac{1}{N-k+1} \sum_{r=k}^{N} x_r \right)^2 . \quad (4.9)$$

The algorithm iteratively partitions the time series using different choices of the k, until J is minimized. The selection of the partition point thus determines the complexity of the algorithm. However, priors could be used to cut short this random selection significantly. In

our case, we only search in the immediate neighbourhood of the peak of the SEP lightcurve. The changepoint thus detected is taken as the t_{onset} parameter for the SEPs in our study. t_{onset} parameter is labeled using a thick black line the last panel of Fig4.5.

SEP time-intensity characterization

Another equally important quantity is a way to measure the shape characteristics of the SEP. The resultant shape of a SEP is thought to be affected mostly by the acceleration processes that generated them based on the assumption that transport effects do not convolute the memory of the injection profile. For example, SEP's generated by impulsive acceleration process(like in flares), show a sharp rise followed by a gradual decay, whereas events generated by gradual acceleration process(shocks in CMEs) show a much slower rise and decay. Since the SEP's are spread out in time, a single quantity will not be able to describe its shape properly. Hence to define the shape, we use three quantities t_{peak},t_{rise} and t_{decay} which are related to the flux gradients to characterize the observed SEP. The first quantity t_{peak} is defined as the time-point corresponding to the maximum flux value of the observed SEP light curve. t_{rise} is the time point during the rising phase where the flux values equal half the maximum value of the peak while t_{decay} is the same quantity in the decay phase (Fig 4.5). The timescales are expressed in units of time after injection. Thus timepoint corresponding to $t_{injection}$ is scaled to t=0, and only those SEPs which are fully contained within t = 0 to 8000 are considered ($t_{decay} <$ 8000) . The individual quantities can show variation from event to event, and thus for better clarity, we construct three derived quantity from these four base quantities which we define as follows,

$$\Delta t_{rise} = t_{peak} - t_{rise}, \tag{4.10}$$

$$\Delta t_{decay} = t_{decay} - t_{peak}, \tag{4.11}$$

and,

$$\Delta t_{arrival} = t_{onset} - t_{injection}. \tag{4.12}$$

The arrival timings listed in Table 4.2(column 2) for our study is different from most of the other studies since we can pinpoint the release timings($t_{injection}$) on the Sun. Other studies mostly infer the release timings from type III bursts alone, often resulting in inconclusive results, due to the difficulty in decoupling the effects of acceleration and interplanetary transport. Two established methods to determine the solar onset time is the velocity dispersion

analysis Krucker et al. (1999) and time-shifting analysis(TSA) by Haggerty and Roelof (2002). VDA can give non-physical answers if the event followed a complex injection profile and/or the first arriving particles experience some sort of scattering along its journey. However, in our case, since all the events are thought to inject particles at the flaring time itself, we have information as to when the injection actually happened. The results of VDA applied to our events are tabulated in Table 4.3. The average wind speed (col 2) preceding the event is found out using the data from The Solar Wind Experiment(SWE) instrument onboard WIND. Since Parkers magnetic field line length theoretically depends only on the solar wind speed (eq 4.2), the average wind speed could be utilized to get an estimate of the distance the particles would have to travel. Thus calculated theoretical values of the Parkers field line is given in col 3. In VDA method, a plot of the onset timings of SEP in different energy channels,t_0 against c/v, yields a line with slope D/c and intercept on time-axis at t_r, the solar injection time. These two values are tabulated in col 4 and 5 respectively of table 4.3.

4.5.2 Symmetric and Asymmetric SEPs

Another interesting aspect of our work is the characterization of the shape of the time-intensity profile of the SEPs. To our knowledge, there has not been any other statistical study of this property before. For characterizing this property we make use of the three quantities,t_{peak},t_{rise} and t_{decay}, which have defined above. More specifically, we look at the time difference between the occurrence of these quantities with reference to each other. Hence $\Delta\, t_{rise}$ and $\Delta\, t_{decay}$ would be used(Eqs 4.10 - 4.12). A histogram plot of the two quantities is shown in figure 4.6, with bin-widths of 200 secs. Evidently the $\Delta\, t_{rise}$ distribution is skewed and does not extend beyond 500 secs, while $\Delta\, t_{decay}$ is spread out. $\Delta\, t_{decay}$ distribution, shows two peaks, the first one around 250 secs and the second one around 650 secs. The first peak correspond to cases where the condition, $\Delta\, t_{decay} \approx \Delta\, t_{rise}$ holds. We call SEPs with this property, 'symmetric' as they will have an equal rise and decay part. The second peak has no corresponding $\Delta\, t_{rise}$ counterparts. Hence these are cases where there is an extended tail in the SEP time-intensity graph. We call these cases as 'non-symmetric'. The first peak of $\Delta\, t_{decay}$ and the border of $\Delta\, t_{rise}$ has a ratio ~ 0.6. Hence to quantify the shape characteristics we define a new quantity, termed as the 'symmetricty ratio', given by:

$$\textbf{Symmetricity Ratio} = \frac{\Delta t_{rise}}{\Delta t_{decay}}. \tag{4.13}$$

Event Date	$\Delta\, t_{arrival}$ (secs)	$\Delta\, t_{rise}$ (secs)	$\Delta\, t_{decay}$ (secs)	Ratio = $\frac{\Delta t_{rise}}{\Delta t_{decay}}$
Apr 25,2002 05:56UT	1326	357	337	1.059
Aug 19,2002 21:00UT	1491	215	864	0.248*
Oct 19,2002 21:14UT	1036	228	234	0.97
Sep 30,2003 00:29UT	1161	655	1810	0.361*
Sep 30,2003 08:48UT	1156	245	615	0.398*
Dec 31,2003 18:21UT	1096	429	755	0.568*
Feb 28,2004 03:24UT	1017	270	525	0.514*
Dec 25,2004 22:29UT	1190	229	484	0.473*
May 16,2005 02:40UT	781	295	350	0.843
Nov 24,2005 16:09UT	1309	48	1185	0.040*
Nov 19,2006 22:59UT	860	178	228	0.780
Nov 20,2006 03:35UT	891	231	241	0.959
Jul 07,2011 14:29UT	2217	757	832	0.909
Aug 08,2011 15:35UT	2659	215	590	0.364*
Aug 08,2011 18.03UT	1116	520	912	0.570*
Nov 12,2013 08:11UT	1355	295	572	0.515*
Nov 12,2013 21:39UT	1304	491	401	1.22
Feb 20,2014 07:51UT	1219	381	608	0.627
Mar 28,2014 20:57UT	1708	373	987	0.378*
Jan 20,2015 09:48UT	1260	235	312	0.743
May 13,2015 08.01UT	1166	200	410	0.481*
Dec 04,2015 14:32UT	1160	275	376	0.731
Jan 28,2016 11:58UT	1866	862	1296	0.665
Jan 28,2016 21:53UT	1749	458	828	0.553*
Jan 29,2016 08:15UT	2033	515	2012	0.255*
Jan 29,2016 16:37UT	2432	465	867	0.536*
Jul 20,2016 22:05UT	918	259	261	0.992
Apr 04,2017 09:48UT	1934	492	1163	0.423*

Table 4.2 The events shortlisted in table4.1 is characterized according to their temporal and shape characteristics. Electrons travel across the parker solar spiral after the injection at the Sun to reach the Earth. For the determination of these statistics we use the 50-82 KeV (mean 66 keV) channel of the WIND/3DP data. Without scatter the arrival time should be 1292 seconds after injection. However most events exhibit some form of delay. Curiously some events seems to arrive($\Delta\, t_{arrival}$) before 1292 secs indicating the travel time has been shorter which would mean they didn't strictly follow along the 1.2 AU parker spiral. $\Delta\, t_{rise}$ and $\Delta\, t_{decay}$ describe the shape characteristics of the the SEP. The ratio of these two quantities indicate whether the SEP are symmetrical in their profile or not.

We impose the criterion that for symmetric profiles,

$$\frac{\Delta t_{rise}}{\Delta t_{decay}} < 0.6 \tag{4.14}$$

and for non-symmetric profiles it should hold,

$$\frac{\Delta t_{rise}}{\Delta t_{decay}} \geq 0.6. \tag{4.15}$$

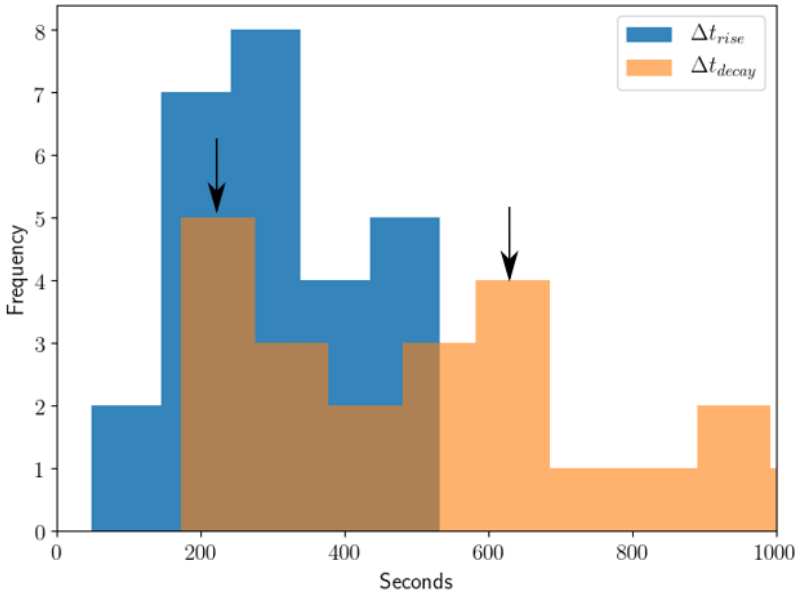

Fig. 4.6 Histograms of $\Delta\ t_{rise}$ and $\Delta\ t_{decay}$ for the shortlisted events. The shape of the histogram for both the quantities are very different. We find a well contained distribution for $\Delta\ t_{rise}$ whereas for $\Delta\ t_{decay}$ there are two peaks (marked by the arrows). The first peak is within the space of $\Delta\ t_{rise}$, representing the events with identical rise and decay phases. We call these events are symmetric. For the second peak there is no corresponding counterpart in the $\Delta\ t_{rise}$ distribution. These events correspond to the long tail events or which show high non-symmetricity.

Out of the 28 shortlisted events, 16 are non-symmetric (marked with a * in table 4.2 and table 4.3) and the rest 12 are symmetric. In Fig4.7 we have plotted the averaged light curve of both the classes of SEPs. For clarity, we plot the normalized lightcurves of events using the peak value, and they are time-shifted so that all their peaks are aligned. Thus this figure does not contain any delay information. The averaged lightcurve(thick black line) is computed by summing over the normalized flux values. The top panel contains the averaged light curve for non-symmetric events. The thick black line is the average of all the asymmetric light

curves. The long tail of the light curve which distinguishes between these two classes of SEPs is evident. The bottom panel is a similar plot for symmetric events.

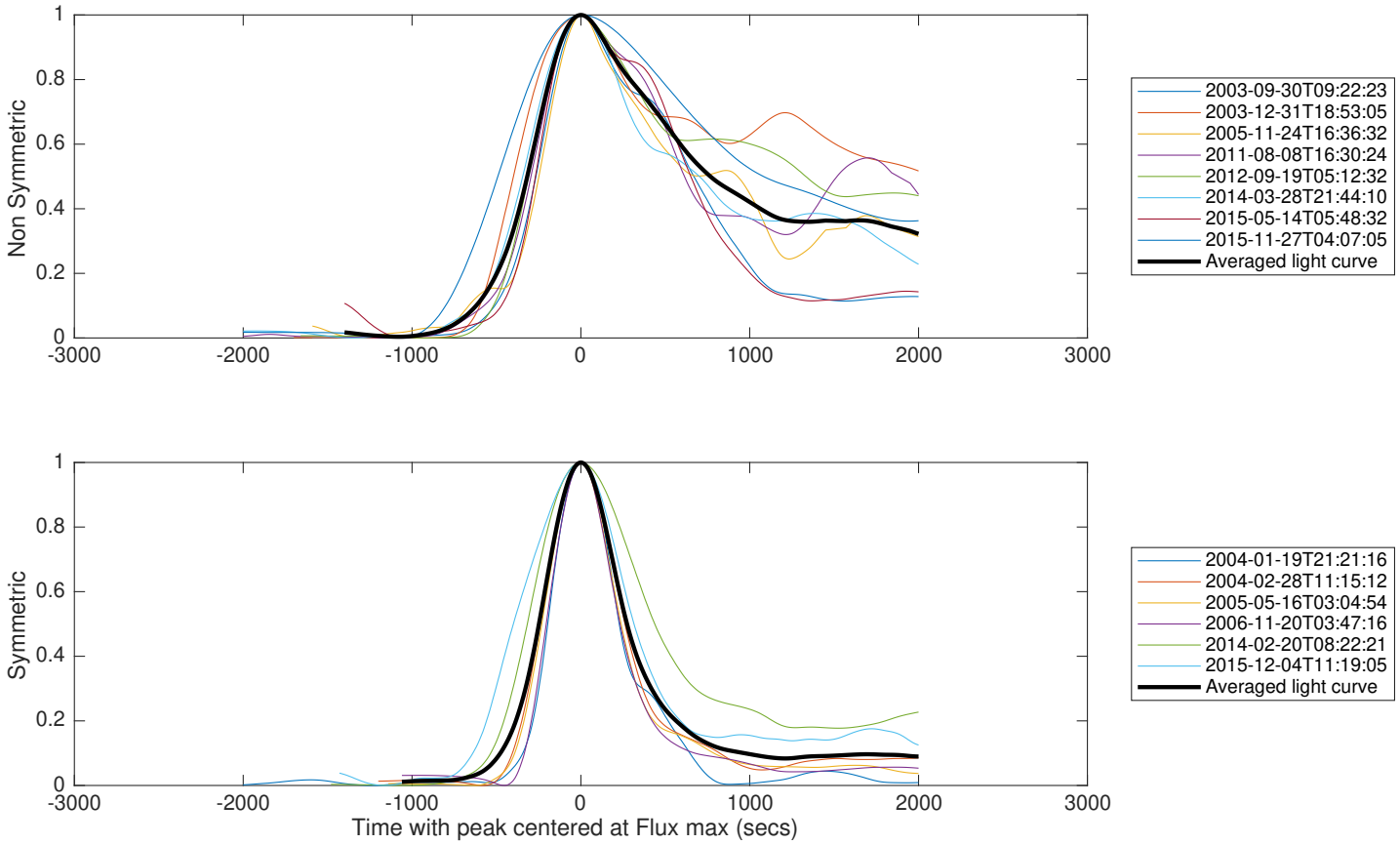

Fig. 4.7 From table 4.2 the events were classified into two classes - symmetrical and non-symmetrical. The SEP lightcurves were then aligned relative to their peak time, smoothed and plotted together. The thick black line in each of the panel show the averaged shape characteristics of the event. From this averaged lc the representative t_{rise} and t_{decay} for both the classes of SEPs could be find out.

4.5.3 Interplanetary condtions during transport

The interplanetary magnetic configuration plays an important role in the transport of SEP particles. Interplanetary CMEs (ICME) can distort the nominal IMF lines and carry relativistic particles with them. ICMEs contains dense magnetic fields which modify the directivity

Event Date	Avg. wind speed (Km/s)	Parker len (AU)	Inferred IMF len(AU)	Actual travel (AU)	VDA injection time (UT)
Apr 25,2002 05:56UT	449.37	1.14	1.21	1.23	05:56
Aug 19,2002 21:00UT	498.72	1.11	0.49	1.38	21:19*
Oct 19,2002 21:14UT	668.21	1.06	1.32	0.96	21:10
Sep 30,2003 00:29UT	297.22	1.27	1.10	1.08	00:29*
Sep 30,2003 08:48UT	315.04	1.25	1.01	1.07	08:49*
Dec 31,2003 18:21UT	300.09	1.27	0.92	1.01	18:25*
Feb 28,2004 03:24UT	450.36	1.13	0.88	0.94	03:24*
Dec 25,2004 22:29UT	496.28	1.11	0.94	1.10	22:32*
May 16,2005 02:40UT	702.91	1.05	0.82	0.72	02:38
Nov 24,2005 16:09UT	463.24	1.12	0.97	1.21	16:10*
Nov 19,2006 22:59UT	363.03	1.19	1.00	0.80	22:57
Nov 20,2006 03:35UT	419.27	1.15	1.04	0.82	03:31
Jul 07,2011 14:29UT	348.06	1.21	1.94	2.06	14:38
Aug 08,2011 15:35UT	597.49	1.07	0.92	2.47	16:06*
Aug 08,2011 18.03UT	590.24	1.08	1.05	1.03	18:06*
Nov 12,2013 08:11UT	422.12	1.15	1.02	1.26	08:17*
Nov 12,2013 21:39UT	404.70	1.16	1.08	1.21	21:43
Feb 20,2014 07:51UT	589.38	1.08	1.02	1.13	07:51
Mar 28,2014 20:57UT	429.04	1.14	1.36	1.58	21:01*
Jan 20,2015 09:48UT	298.14	1.27	1.38	1.17	09:43
May 13,2015 08.01UT	568.54	1.08	0.92	1.08	08:06*
Dec 04,2015 14:32UT	375.24	1.18	0.96	1.07	14:36
Jan 28,2016 11:58UT	341.11	1.21	1.16	1.73	12:07
Jan 28,2016 21:53UT	328.50	1.23	1.13	1.62	22:02*
Jan 29,2016 08:15UT	320.66	1.24	1.57	1.89	08:18*
Jan 29,2016 16:37UT	302.43	1.26	2.09	2.26	16:36*
Jul 20,2016 22:05UT	480.51	1.11	0.86	0.85	22:07
Apr 04,2017 09:48UT	407.95	1.16	1.42	1.79	09:55*

Table 4.3 We carried out velocity dispersion analysis on all the events to understand their deviation from the ideal case scenario of 1.2 AU path length and scatter free propagation. In the second column we have listed the avg. wind speed observed by SWE instrument of WIND over the timeperiod of the SEP. Since the length of the Parker spiral only depend on the solar wind speed, we are in a position to calculate the theoretical values of the field line. The inferred IMF field line length and the injection time, is from VDA analysis. We see some events which match their actual injection time. However there is a discrepancy for most events which would be an indication that the conditions assumed by VDA method may not be common in the interplanetary space. The fifth column shows the actual travel length which is determined from the actual time the SEPs took to travel starting from the flare peak time(assumed to be injection time of SEP) to the detection at WIND spacecraft(t_{onset}). The last column is the inferred injection time from the VDA fit for each event.

of particles, and since they are spread longitudinally, particle timing comparisons can give erroneous results. Presence of an ICME would add extra distortion of the injected electrons, and since we aim to decouple transport and acceleration effects, it is important to understand the overall magnetic conditions existing at the passage of the event. The IMF line of magnitude B makes an angle θ_B (latitude) with respect to the spacecraft and the ecliptic plane and ϕ_B(longitude) with respect to the straight line connecting spacecraft and the Sun. The fluctuations in the IMF are non-coherent with mean of $\theta_B \simeq 0$ deg and $\phi_B \simeq$ -45 deg (135 deg if the magnetic field is facing sunward in the spacecraft reference frame). Passage of ICME near the spacecraft increases the magnetic field B and makes the fluctuations more coherent (Masson et al., 2012). Helios 1 data showed the existence of linear relation between proton temperature and the proton velocity of the solar wind, which could be modelled as :

$$T_{exp}[K] = 640 \times V_{sw}[kms^{-1}] - 1.56 \times 10^5. \tag{4.16}$$

The enhanced magnetic pressure $B^2/8\pi$ inside the magnetic cloud of the ICME in comparison to the ambient pressure would force it to expand along the gradient of the magnetic pressure. Because of this reason, the proton thermal pressure would low compared to magnetic pressure. Thus inside and ICME the temperatures are lower than the ambient solar wind temperatures, and this serves as an important diagnostic of a passing ICME. It has been shown that the ICME temperature is about half of the expected proton temperature,T_{exp} (Burlaga et al., 1981; Klein and Burlaga, 1982; Richardson and Cane, 2010). Using data from MAG instrument onboard WIND we checked for variations from nominal conditions for IMF line, during the transport phase of the SEP particles (Fig 4.8). The magnetic field magnitude shown in the first panel is measured in nT. Usual values are around 5nT. Latitude and longitude coordinates specify the relative orientation of the magnetic field at the spacecraft location. The expected temperature was estimated using Eq4.16. This is shown using a dark brown dashed line in panel 3. We checked the interplanetary conditions to check the presence of shocks or ICMEs for all the shortlisted events.

Since we have information on the solar source coordinates of the origin of the SEP particles, we check for the availability of magnetic footpoints of Parker spiral. The longitude of the Parker spiral can be defined as:

$$\Phi_s = \Phi(1AU) + \frac{\Omega}{V_{sw}}(1AU - R_s), \tag{4.17}$$

where $\Omega = 2.6 \times 10^{-6} rads^{-1}$ is the angular velocity of the Sun, V_{sw} is the solar wind speed which is taken as the average of the pre-event time period starting from the solar onset. $R_s = 2.5R_\odot$ is the radius of the spherical source surface and $\Phi(1AU)$ is the longitude of

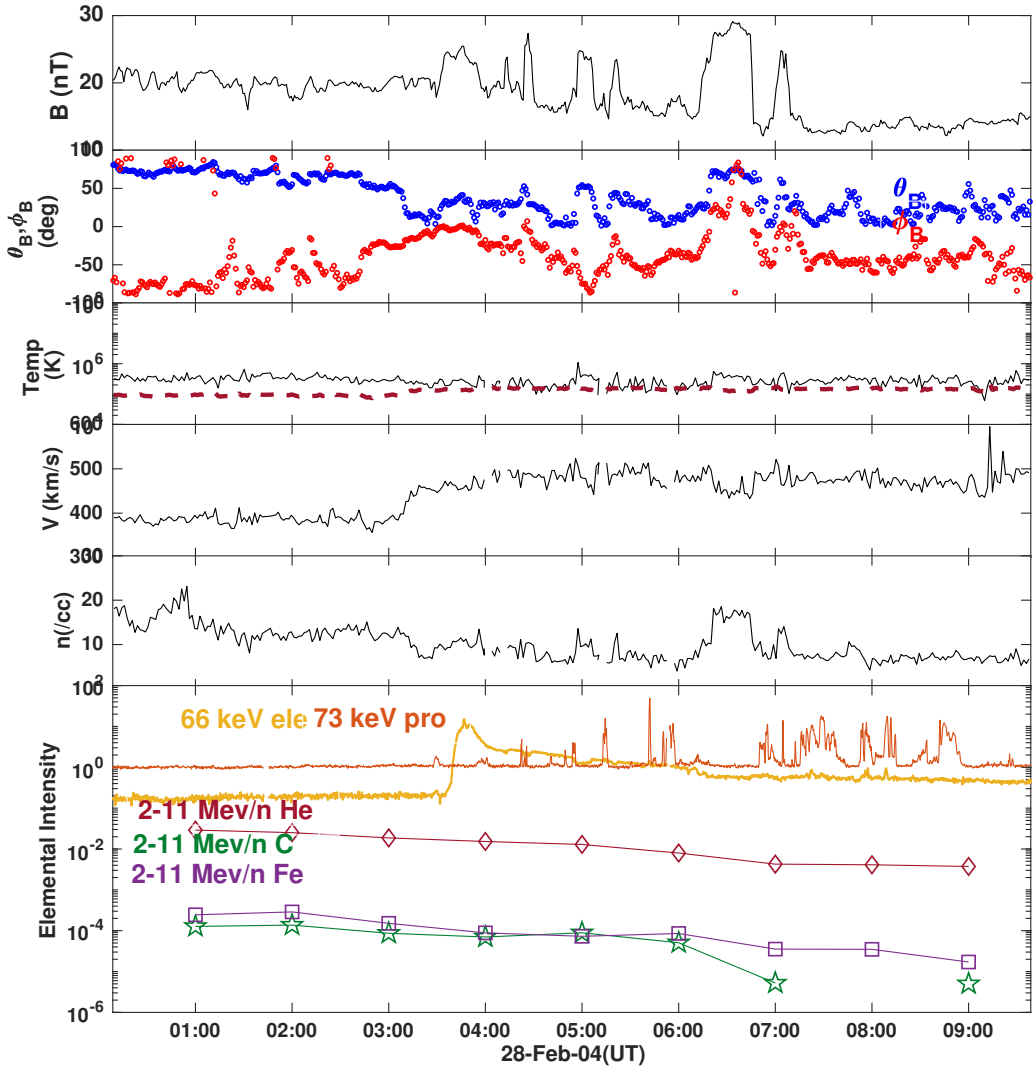

Fig. 4.8 The interplanetary magnetic field conditions for the event on 24 Feb 2004. The first panel shows the magnitude of the magnetic field (nT), the second panel shows magnetic field vectors in terms of latitude(θ_B) and longitude(ϕ_B)(using GSM coordinates). The third panel gives the temperature of the proton(black line) and expected temperature from solar wind speed(dark brown dashed line). The solar wind speed in km/s is shown in the fourth panel. The proton density(N/cm^3) is shown in the fifth panel. The bottom panel shows the enhancements of different species of particles - electrons(yellow), protons(orange),He,C and Fe

the spiral at 1AU. An event with good magnetic connectivity should ideally have access to Parker spiral footpoint readily. Usually, this is defined as any longitudes within the $\pm$ 30 deg of the source longitude and the Parker spiral footpoint (Masson et al., 2012; Wiedenbeck et al., 2013). Table 4.7 shows the connectivity for all events except for the one May 13, 2015,

whose source coordinates could not be accurately determined. The HXR burst duration is expressed in units of Stonyhurst heliographic coordinates(HGS). HGS coordinate system is centred at the Sun,with the Z axis(+90 latitude) aligned along the Sun's north pole. Positive altitude thus signifies northern hemisphere and negative values signify southern hemisphere. Similarily the longitude increases positively along the west limb. For the events shortlisted in our study, all the events which happened closer to the western limb showed a good connection to the Parker spiral footpoint with the exception of the event that happened in Sep 30,2003. Unsurprisingly all the events which occurred towards the eastern limb of the Sun showed poor connectivity. However, the fact they were still able to reach 1AU without significant delay suggests that the magnetic field structure near the Sun can be very complicated (Cliver et al., 1982; Kahler et al., 1984). Hence ready access to magnetic field lines does not seem to influence the resulting symmetricity of the events.

4.5.4 Spectral characteristics of SEP

Since all of our SEP events contain HXR observations, we can gain information about the parent location of the SEP at the Sun, energy spectra and composition of these flare accelerated particles. The question whether the acceleration process behind solar flares and that accelerate particles into near-relativistic velocities in SEPs is the same, is still an unresolved question. Many studies have concluded that these acceleration processes powering these transient events are capable of releasing $>\sim 10^{30}$ ergs of energy during the duration of the flare.

For spectral index measurement of the SEP and HXR electrons and to estimate their number, we follow the same procedure followed in Chapter 2. However, for the sake of completeness, we list the steps briefly. The WIND/3DP data covers the energy range 25-580 keV logarithmically spaced into seven energy channels. Due to low counts in the higher energy channels (>230 keV), only five were chosen, with mean energies, 27,40,66,108 and 182 keV. The peak flux spectrum is obtained by taking the maximum flux from each of the energy channel. The differential energy spectrum of electrons can be represented as

$$dJ/dE \propto E^{\delta_{1AU}} \tag{4.18}$$

For the energy channel with 66 keV mean, the peak flux is from the timepoint, equal to t_{peak}. The energy spectra were fitted by a powerlaw, to obtain δ_{1au}. A break in the powerlaw was observed for most events at 40 keV, and thus the fit was done only for energies > 40 keV. The values of δ_{1au} tabulated in col 4 of table 4.4(fifth column). Using this powerlaw index,

the number of electrons above 50 keV injected into SEP population could be estimated, by integrating over the energies. More specifically,

$$F(E) = F_0(E_0/E)^{\delta_{1AU}}, \tag{4.19}$$

where F(E) is the differential electron flux at 1 AU (electrons $keV^{-1}s^{-1}sr^{-1}cm^{-2}$). F_0 is the peak differential energy flux at a specific energy E_0. Thus the flux of the electrons above E_0 is simply the integral of the above equation.

$$\int_{E_0}^{\infty} F(E)dE = \frac{F_0E_0}{(\delta_{1AU}-1)} \text{ electrons s}^{-1}\text{ sr}^{-1}\text{ cm}^{-2}. \tag{4.20}$$

The electrons injected into the interplanetary medium usually spread by the time they arrive at 1 AU. We take this spread to be about a solid angle cone of of 30°(Krucker et al., 2007). Thus the total number of electrons crossing 1 AU is given by

$$\Omega(1AU)^2 \int_{E_0}^{\infty} F(E)dE = \Omega(1AU)^2 \frac{F_0E_0}{(\delta_{1AU}-1)} \text{ s}^{-1},$$

This number(denoted as N_{esc}) is tabulated in table 4.5

For HXR spectrum measurement, we sorted data into bins of width 0.33 and 1 keV for boundaries 3-15 and 15-100 keV, respectively, whenever RHESSI data was used. For FERMI data, the native bin divisions were used, without any modification. The spectrum was fit only between 0-100 keV for consistency (because of small count rates in >50 keV for some events) and to prevent high count rates saturating the low energy bins. For the photon spectrum, we fit a power-law function to estimate γ (col 3 of table 4.4).

For estimating the HXR inferred electron spectrum, we fit the photon spectrum with a thermal component (vth in OSPEX) and a thick-target distribution in forward-fitting basis. The spectral index above the break is denoted as δ_{hxr} (col 4 of table4.4). For estimating the number of electrons > 50 keV, the flux corresponding to the break energy was re-scaled to 50 keV and integrated using δ_{hxr} as the exponent, as shown in the following equation:

$$\dot{N}_{>50keV} = \dot{N}_{>E_c}\left(\frac{E_c}{50}\right)^{\delta_{hxr}-1} \tag{4.21}$$

Here, E_c is the break energy. Number of HXR producing electrons(denoted as N_{hxr}) are tabulated in col 4 of table4.5.

For large solar flares the number of particles escaping into interplanetary space is only a very small fraction of the number of electrons producing HXR radiation, ie ($N_{esc}/N_{hxr} \sim 0.01$ %) (Krucker et al., 2007; Lin, 1974). For smaller flares it was shown by James et al. (2017)

that the acceleration process is capable producing near equal numbers of electrons at the HXR site(N_{hxr}) and electrons escaping from the site as SEP electrons (N_{esc}),i.e $N_{esc}/N_{hxr} \sim 100\%$. Just as the particle acceleration process that generates them is not yet understood, the relationships between the detected population of in-situ electrons at 1AU and the HXR electrons at the flare acceleration site is also not clear. It is generally hypothesized that if the HXR burst and type III burst have a near-simultaneous temporal origin, then the acceleration process that generates the two types of the population should be the same.

4.5.5 Compositional characteristic of the SEP

Elemental abundances in flares can be considered as a unique signature left behind by the processes that generate them. They also reveal the source properties of the plasma that they were part of. SEPs are thus one of the rare ways in which we can directly sample the material on the Sun. For SEP's there's a well established tradition of distinguishing them on the basis of particle abundances. Small impulsive classes of SEP's are known for their $^3H_e/^4H_e$ enhancements, compared to gradual events. It has been shown than heavy ion ratios (like Fe/O)are often a good discriminator between gradual and impulsive SEP events. Reames (1998) measured Fe/O ratio for large SEP events in the range 5-12 MeV/nuc and found it to be 0.134 which is close to coronal values. In large impulsive flares this ratio is about 10 times that of the coronal values. Cane et al. (2006) introduced the definition of flare accelerated particles to be those whose normalized Fe/O ratio is larger than 2.

Since we would like to decouple acceleration effects from transport effects, we propose to study elemental abundances to see any possible correlation with the SEP characteristics. Even though transport effects can affect the abundances, heavy ions such as Fe, takes time to be scattered away. Thus measuring them in the immediate vicinity of SEP is considered to be safe from transport effects. We use data from The Energetic Particles: Acceleration, Composition and Transport (EPACT) investigation onboard WIND for our study. EPACT can measure wide ranges of charge,mass and intensity for different species of particles using 8 different particle telescopes.Using EPACT data we have measured background subtracted intensity averages for species of He, C, O, Ne and Fe. These values are tabulated in Table 4.6. SEPs could also be accelerated in shocks. We also checked the ambient solar wind conditions for checking the presence of shock passages. Shocks usually manifest as a noticeable break and increase in values of solar wind temperature, speed and density. Since they are often accompanied by ICME's a break in the IP magnetic field structure is also observed.

Event Date	HXR burst location (arcsec,arcsec)	γ	δ_{hxr}	δ_{1AU}	Peak electron rate for SEP (66 kev)
Apr 25,2002 05:56UT	-115,237	2.86	3.41	3.11	25.5
Aug 19,2002 21.00UT	488,-272	3.01	3.66	2.78	77.49*
Oct 19,2002 21:14UT	712,-283	3.92	3.79	3.85	1.59
Sep 30,2003 00:29UT	616,41	3.83	3.43	3.68	7.88*
Sep 30,2003 08:48UT	665,51	2.74	2.99	3.93	3.65*
Dec 31,2003 18:21UT	962,179	3.19	4.07	3.71	48.91*
Feb 28,2004 03:24UT	697,301	3.38	4.89	4.33	14.08*
Dec 25,2004 22:29UT	597,-132	3.13	4.00	4.04	1.55*
May 16,2005 02:40UT	-282,-232	4.01	4.10	4.22	70.12
Nov 24,2005 16:15UT	961,-143	3.16	2.40	2.68	0.186*
Nov 19,2006 22:59UT	962,-106	2.55	3.34	4.42	1.91
Nov 20,2006 03:35UT	957,-108	3.09	3.65	4.76	2.12
Jul 07,2011 14:29UT	915,260	2.95	3.79	4.45	0.523
Aug 08,2011 15:35UT	803,224	3.36	4.40	4.17	10.38*
Aug 08,2011 18.03UT	821,214	3.70	5.62	2.91	44.06*
Nov 12,2013 08:11UT	-795,-315	2.17	1.93	3.33	8.68*
Nov 12,2013 21:39UT	-719,-406	3.57	4.73	5.00	15.76
Feb 20,2014 07:51UT	441,-97	2.89	3.66	2.52	41.4
Mar 28,2014 20:57UT	853,-199	3.25	2.14	4.62	1.00*
Jan 20,2015 09:48UT	934,-238	2.56	2.76	3.62	1.73
May 13,2015 08:01UT	-	3.64	2.73	3.04	1.76*
Dec 04,2015 14:32UT	-917,-185	2.75	2.12	4.24	0.46
Jan 28,2016 11:58UT	724,136	4.60	5.73	4.85	2.22
Jan 28,2016 21:53UT	747,205	3.39	3.26	4.34	7.85*
Jan 29,2016 08:15UT	807,188	5.25	3.16	5.33	3.04*
Jan 29,2016 16:37UT	856,120	2.99	2.67	4.56	0.475*
Jul 20,2016 22:05UT	576,38	4.09	4.08	4.31	60.6
Apr 04,2017 09:48UT	908,272	2.51	3.07	4.08	2.58*

Table 4.4 The spectral indices obtained from the HXR spectral fits using OSPEX and the SEP energy spectra using WIND/3DP data. The photon spectral index γ is obtained by fitting a power-law to the photon energy spectrum of observed HXR event. The δ_{hxr} is the inverted electron injection spectral index above the break energy from the thick target fit. δ_{au} is the spectral index of the energy spectra of the SEP observed near the Earth. For calculating the SEP energy spectra the mean energy of the channel and the peak flux corresponding to that channel is used. The events marked with a dash indicates the HXR data was not sufficient to get a good fit.

Event Date	HXR burst duration(secs)	SEP duration (secs)	No of electrons(HXR) (above 50 keV) N_{hxr}	No of electrons(SEP) (above 50 keV) N_{esc}
Apr 25,2002 05:56UT	150	694	1.25e35	2.21e31
Aug 19,2002 21:00UT	65	1079	2.27e35	1.13e32
Oct 19,2002 21:14UT	185	462	4.54e34	1.25e30
Sep 30,2003 00:29UT	51	2556	2.50e33	3.38e30
Sep 30,2003 08:48UT	165	860	1.40e35	7.9e30
Dec 31,2003 18:21UT	90	1184	3.06e35	8.2e31
Feb 28,2004 03:24UT	74	895	8.46e33	1.12e31
Dec 25,2004 22:29UT	108	713	2.21e31	1.2e31
May 16,2005 02:40UT	122	645	1.45e35	5.2e31
Nov 24,2005 16:15UT	182	1228	1.69e33	1.48e31
Nov 19,2006 22:59UT	50	495	2.1e31	1.4e30
Nov 20,2006 03:35UT	132	467	1.09e33	5.5e30
Jul 07,2011 14:29UT	85	1597	2.99e35	9.28e29
Aug 08,2011 15:35UT	43	805	2.45e35	1.9e30
Aug 08,2011 18:03UT	54	1432	3.78e35	8.16e31
Nov 12,2013 08:11UT	50	867	2.49e32	9.01e30
Nov 12,2013 21:39UT	81	892	1.6e34	1.58e31
Feb 20,2014 07:51UT	88	934	1.72e35	5.68e31
Mar 28,2014 20:57UT	50	1434	5.71e32	1.5e30
Jan 20,2015 09:48UT	73	547	1.57e33	1.05e30
May 13,2015 08:01UT	79	610	1.52e34	1.35e30
Dec 04,2015 14:32UT	84	630	6.03e33	3.23e29
Jan 28,2016 11:58UT	60	2158	1.87e35	1.39e30
Jan 28,2016 21:53UT	102	1292	2.00e34	3.42e30
Jan 29,2016 08:15UT	160	2524	1.65e34	8.2e30
Jan 29,2016 16:37UT	192	1333	5.80e34	7.03e29
Jul 20,2016 22:05UT	94	520	2.75e31	3.51e31
Apr 04,2017 09:48UT	105	1703	5.47e33	4.92e30

Table 4.5 The energy spectra obtained for both the HXR and SEP electrons are integrated to estimate the number of electrons contained above 50 keV. For HXR photon spectrum a break typically happens well below 50 keV. Because of this we scale the resulting flux measurement at the break energy to 50 keV and then carry out the integration. The number is multiplied by the total duration of the flare in the 12-25 keV channel to estimate the total number of electrons above 50 keV. Similar numbers for SEP electrons were calculated by assuming the SEP electron beam will have a spread of 20 deg.

4.6 Results and Discussions

After a survey spanning 2002-2018, 28 events were shortlisted which had near-simultaneous HXR, type III signature and an associated SEP later at 1 AU. The shortlisted events were

Event Date	He	C	O	Ne	Fe
Apr 25,2002 05:56UT	7.54e-04	4.57e-06	1.07e-05	9.78e-07	1.30e-06
Aug 19,2002 21.00UT	4.66e-04	2.61e-06	6.87e-06	4.31e-07	5.88e-07
Oct 19,2002 21:14UT	2.49e-04	1.47e-06	4.00e-06	2.71e-07	3.71e-07
Sep 30,2003 00:29UT	2.12e-09	9.16e-10	1.52e-09	1.78e-10	9.30e-10
Sep 30,2003 08:48UT	2.21e-10	8.61e-10	8.61e-10	2.33e-11	2.11e-11
Dec 31,2003 18:21UT	8.99e-09	5.02e-10	5.74e-10	1.22e-11	1.05e-11
Feb 28,2004 03:24UT	1.11e-05	5.42e-08	1.45e-07	3.36e-08	1.25e-07
Dec 25,2004 22:29UT	6.31e-08	2.75e-09	2.23e-09	1.63e-11	1.01e-09
May 16,2005 02:40UT	4.95e-08	2.36e-09	9.44e-11	1.53e-13	1.51e-13
Nov 24,2005 16:15UT	3.12e-07	8.07e-10	1.26e-10	4.39e-10	7.03e-13
Nov 19,2006 22:59UT	1.09e-07	9.23e-10	5.72e-10	2.33e-13	9.45e-13
Nov 20,2006 03:35UT	2.17e-07	3.66e-09	1.32e-09	3.93e-11	1.22e-09
Jul 07,2011 14:29UT	1.16e-09	1.04e-09	1.45e-09	8.19e-13	9.33e-11
Aug 08,2011 15:35UT	9.26e-09	8.26e-10	1.42e-09	5.21e-12	7.62e-12
Aug 08,2011 18.03UT	4.99e-09	9.11e-10	5.80e-11	2.16e-13	3.18e-13
Nov 12,2013 08:11UT	1.30e-09	4.29e-10	1.26e-09	3.45e-10	1.24e-12
Nov 12,2013 21:39UT	3.24e-09	1.92e-09	5.00e-10	2.59e-10	1.42e-13
Feb 20,2014 07:51UT	3.49e-07	1.14e-09	3.17e-09	2.87e-09	7.77e-09
Mar 28,2014 20:57UT	1.90e-07	1.20e-08	1.99e-09	4.48e-09	9.26e-09
Jan 20,2015 09:48UT	5.07e-06	1.06e-08	2.93e-08	5.33e-09	1.43e-09
May 13,2015 08:01UT	4.90e-06	7.82e-09	4.07e-08	6.64e-09	2.18e-09
Dec 04,2015 14:32UT	1.32e-05	2.68e-08	8.04e-08	1.31e-08	3.03e-09
Jan 28,2016 11:58UT	5.77e-07	3.00e-09	4.03e-09	1.97e-12	6.74e-10
Jan 28,2016 21:53UT	6.86e-07	8.79e-09	6.38e-10	2.21e-13	2.15e-09
Jan 29,2016 08:15UT	5.49e-07	2.24e-09	5.46e-10	5.44e-10	5.37e-10
Jan 29,2016 16:37UT	8.56e-07	2.38e-09	1.56e-09	9.16e-10	7.17e-10
Jul 20,2016 22:05UT	3.47e-07	5.40e-09	2.30e-09	7.33e-10	1.61e-09
Apr 04,2017 09:48UT	1.13e-07	1.78e-09	2.43e-09	2.54e-10	2.65e-13

Table 4.6 The elemental abundances in a SEP carries important clues regarding its origin. Here we calculate the abundance of the various heavy-ions using the EPACT data. The averaged data over the duration of the SEP event was taken. Since we are interested in the change in abundance corresponding to the onset of the SEP, the pre-background values are subtracted and absolute values are taken.

divided into two groups according to their characteristics in their rise and decay phase. For defining the symmetricity, we define the quantity 'symmetricity ratio', which is the ratio of quantities $\Delta\, t_{rise}$ and $\Delta\, t_{decay}$. There are 12 symmetric events and 16 non-symmetric events in the shortlist. It is pertinent to ask then whether the lightcurve characteristics shown by these events is a product of the acceleration and injection profile leading to their creation

or is it due to transport effects. Finding correlations of the symmetricity ratio with other physical quantities would help us to understand how strong the effects of acceleration is on the particles.

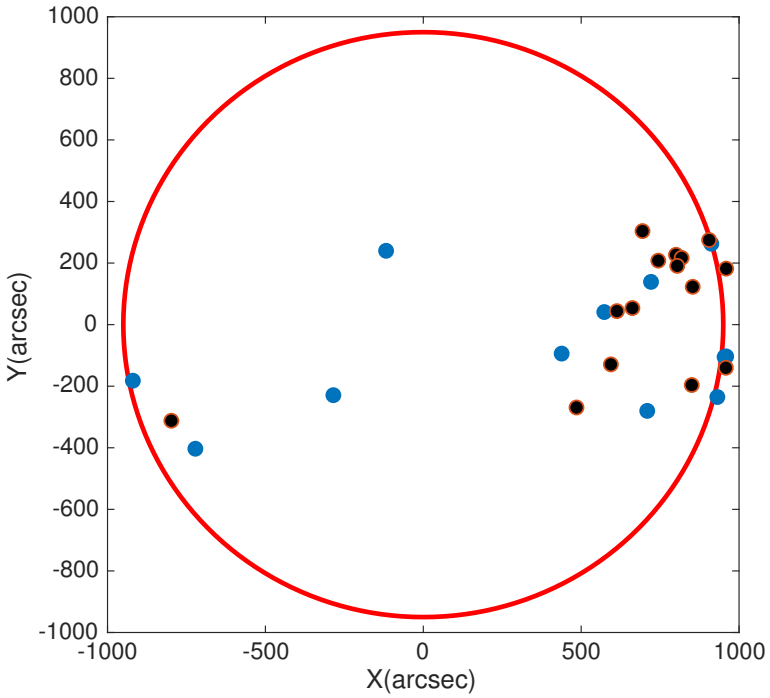

Fig. 4.9 The locations of the flare events that generated the SEPs. The blue markers denote symmetric events and black markers denote non-symmetric events. Most events are well connected to open magnetic fields.

For understanding any possible correlations that might exist between different variables(we describe them below) we use polynomial regression. Polynomial regression maps the relationship between independent variable x and dependent variables {y}, as an nth degree polynomial dependence. We use a weighted least squares algorithm to fit our regression function. For assessing the goodness of fit, we use R^2 statistics. R^2 measures the degree of effectiveness by which the model has captured the variation in the data. Theoretically, the R^2 is defined as the square of the correlation between the dependent variable and the predicted values.R^2 can take values between 0 and 1, with value 1 indicating the model was 100% successful in capturing the proportion of variance. In addition to R^2 we also employed statistical test using the p-value to measure the significance of the coefficients. Statistically, the p-value measures the chance that the hypothesis a particular coefficient is equal to non-zero. A non-zero coefficient implies the relationship implied between the independent variable and dependent variable is not an artefact of the fit. Any p-value less

than 0.05 is interpreted as that coefficient being non-zero is not by chance within the 95% confidence interval.

Dependence on location

Since RHESSI captures the Fourier components of the X-ray source due to its unique grid modulated design, we are in a position to locate the source of SEPs at the Sun. For imaging, we used the PIXON algorithm using 6-12 keV energy range RHESSI photon count rates. The peak point corresponding to >90% flux level contours was chosen as the location of the flare. These values are tabulated in table 4.4. For the event on May 13,2015 there was only FERMI GBM data. Since FERMI does not have an imaging capacity, we were unable to determine its location. Source coordinates are in the heliocentric Cartesian system with x,y and z being perpendicular to each other. The z-axis is aligned along the sun-earth observer line, pointing towards the observer. The y-axis is aligned along the solar north-pole axis with increasing values towards the north pole. The x-axis is perpendicular to both x and y with increasing values along the solar west limb (Fig 4.9). The region within W30 to W60 longitudes of the Sun is magnetically well connected to the Earth, because of the shape of the archimedean spiral. In general, events that occur on the western limb of the Sun will often find an open magnetic field line and thus can be detected near Earth. Out of 28 shortlisted events, 23 of them occur on the western limb of the Sun. Two of the events occur near the central latitudes, and the rest three occurs in the eastern limb of the Sun. Out of these five events, four of them are symmetric - including the event (Dec 04,2015) that occurred on the eastern limb. Even though this event occurred on the eastern limb, the particles arrived before the nominal parker spiral length travel time of 1292 seconds, indicating that magnetic connectivity can be very complex and more detailed studies are needed. From our location studies, we could not find any conclusive evidence regarding the occurrence location of any events and the resulting symmetricity.

Using the solar injection times $t_{injection}$ determined from the peak HXR time, we can get a measure of the effects of transport on the arrival timings of the SEP. If there were no scattering then the particles in the 66 keV mean channel should reach the detector near 1AU in 1292 seconds after traversing through a path-length of 1.2 AU. We find most events don't follow the 1.2 AU spiral length to reach 1AU,from their timing analysis. Initially it was believed that these short path-lengths were an apparent effect caused by the way particles deposit their energy in the SST foil detector. However, studies suggest there may be systemic transport effects that can take the particles through shorter paths (Tan et al 2013). Because of the simultaneous onset of type III burst we assume, particle energization and injection into IP open magnetic field line happened at the same time. Using VDA we find the inferred solar

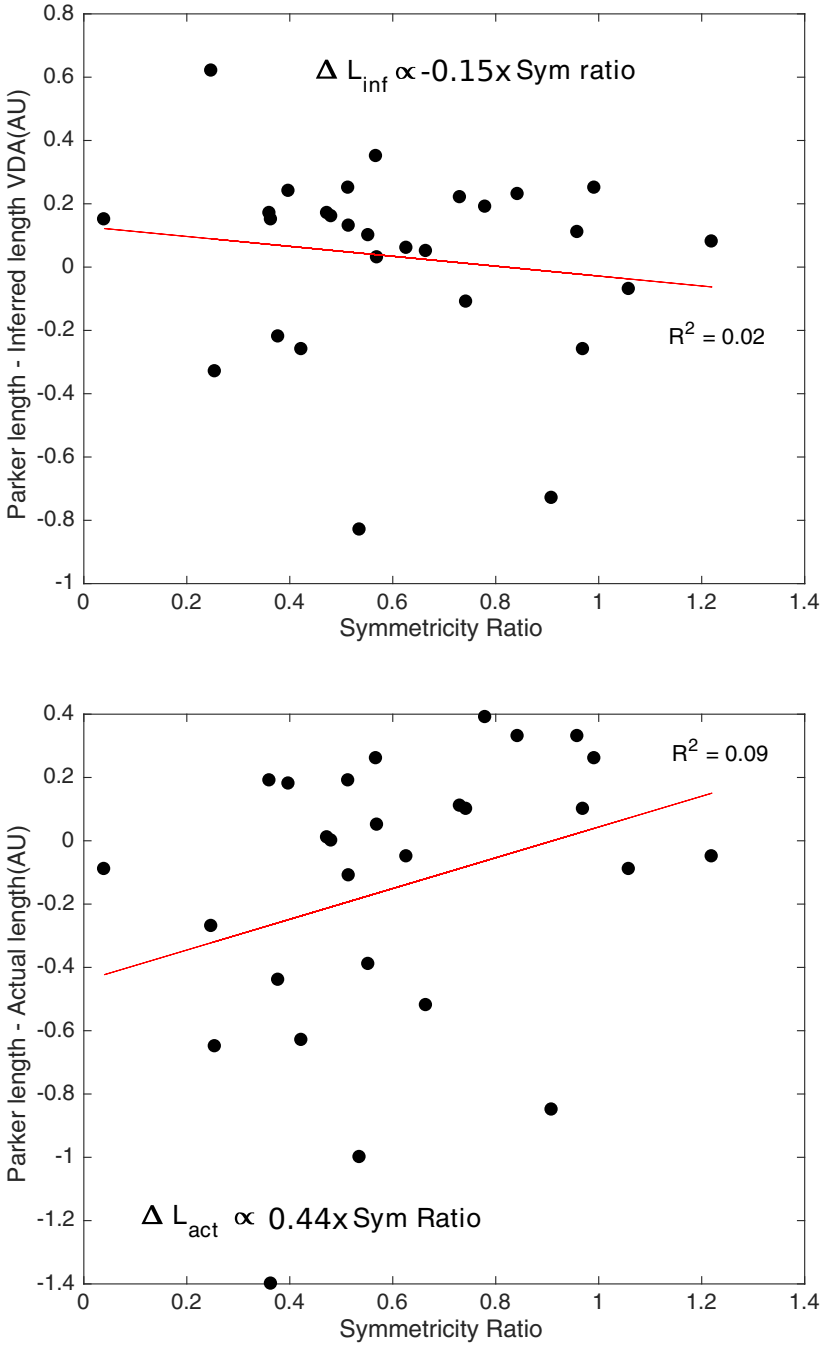

Fig. 4.10 The dependence of the path length and symmetricity ratio. In the first panel, the difference between the theoretical estimate of parker length determined from the solar wind speed and the inferred value using VDA is shown. There is a slight downward trend with a slope of -0.15. Thus the inferred path length suggests that the more symmetric particles tend to spend less time in the IP field. The second panel shows the same relation but for the actual field, length estimated using the travel time determined and the velocity of 66 keV electrons. Here we see a positive trend, with more symmetric events tending to spend more time in the field line. This shows that the scatter free assumption of VDA can give erroneous results.

injection time and the path length. VDA assumes simultaneous injection at all energies and scatter free travel. We compare the inferred path length with the theoretical estimate of the parkers spiral length, which was determined from the observed values of solar wind speed for that duration. For most events, the inferred path length is shorter than the theoretical estimate of Parker field line length determined from solar wind observations. We have also calculated the actual travel length from $\Delta t_{arrival}$ and the velocity of 66 keV electrons. The actual travel length is the product of $\Delta t_{arrival}$ and the velocity of the electrons. The actual travel length, however, was found to be higher than the theoretical parker length for most cases. This suggests that transport effects might be in play which increases the apparent travel distance. We see a decreasing trend regarding the deviation from the parker length with reference to the inferred parker length and symmetricity ratio. More symmetric events tend to spend lesser time in the interplanetary transport phase than non-symmetric events. However, when using the actual field length instead of the inferred length, we see a positive dependence on the symmetricity and the path length. This discrepancy arises because VDA ignores the extra time spent on travelling through the field line as a delayed injection. Thus the assumption of the scatter free travel used by VDA can give a different picture altogether. We employed a linear regression fit, with symmetricity ratio being the independent variable and path length the dependent variable. For the plot between symmetricity ratio and the inferred parker length, we saw a slightly decreasing trend with symmetricity, with a slope of -0.15. The R^2 for the fit was 0.02 with a p-value of 0.10. For the plot between the actual path length and symmetricity ratio, we see an increasing trend with slope 0.44, with R^2 of 0.09 and p-value of 0.19. This indicates that we cannot reject the null hypothesis(that the correlation is not resulting due to the peculiarities of the data). Hence it is not possible to say that there is a significant correlation between the path length travelled and the resulting symmetricity of the SEP event.

Dependence on low energy electrons

There are evidences that suggest electrons of energy as low as 0.1 keV being accelerated in SEP events. Wang et.al(2016) showed for electron/^3H_e rich SEP events, low energy electrons(0.4 to 9 keV) were injected around 10-20 minutes before the start of the type III burst. In this case, all the events had associated west-limb CME's with no GOES SXR bursts. The electron path lengths were found to be consistent with the nominal lengths of 1.2 AU, indicating scatter free travel. They concluded that low-energy electrons are responsible for the generation of the type III burst. Since all of their events had an associated CME, they postulated that the low energy electrons could act as a seed population, which is then accelerated by the CME shocks to higher energies. This suggests that low energy electrons

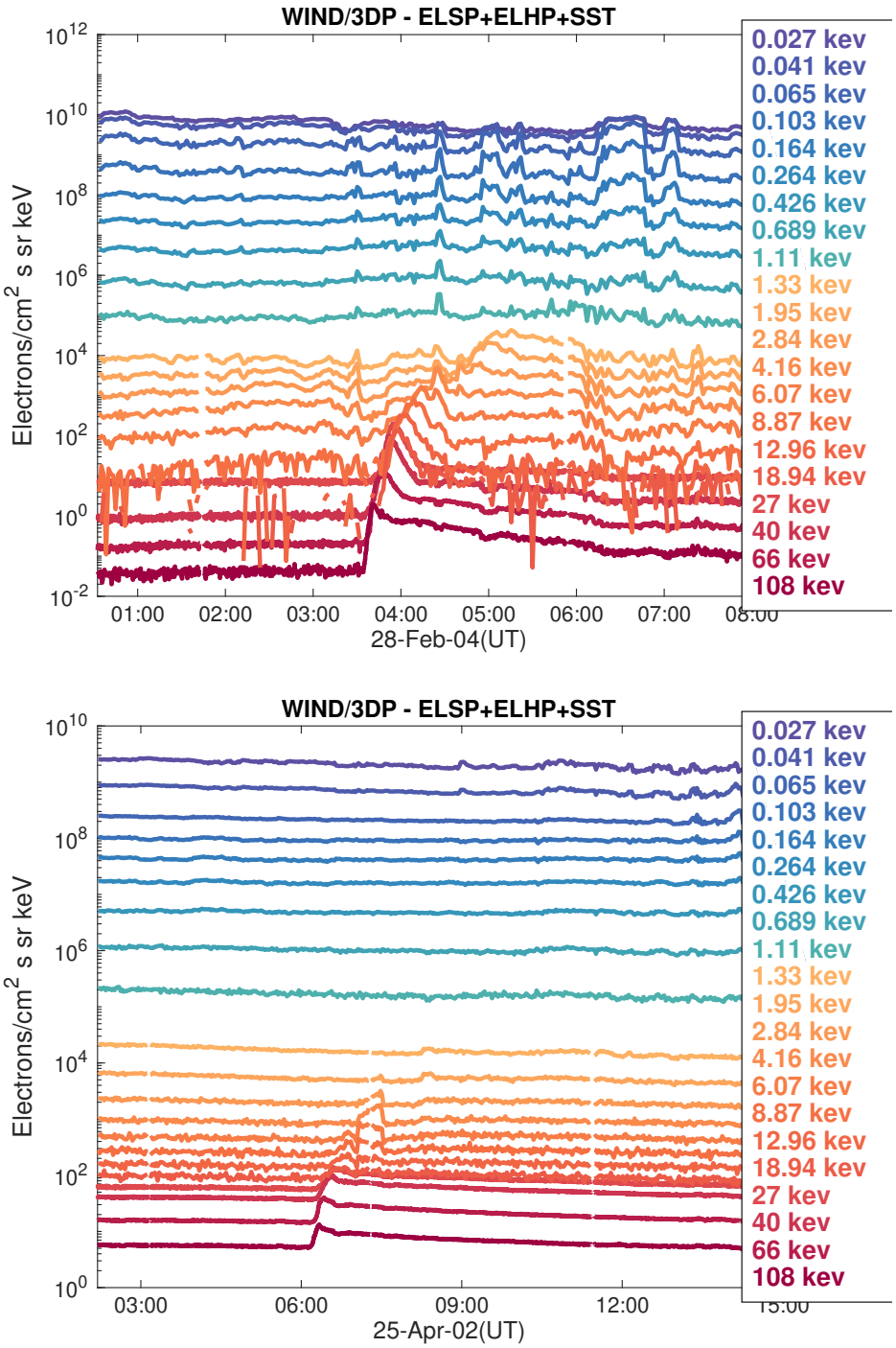

Fig. 4.11 The full coverage of 3DP detector which is suit of ELSP, EHSP and SST particle detectors. The blue lines are data from ELSP instruments and shown here is the coverage between 0.027 to 1.11 keV. The orange colored lines are data from EHSP instrument covering data from 1.33-18 keV. The red lines are data from SST instrument, and shown here is energy ranges of 27-108 keV.The first panel is the data for the event that occurred on 24 Feb 2004. An enhancement upto 1.33 keV is seen. The second figure is for event that occurred on 25 Apr 2002. Here the enhancements are only upto 8,87 keV.

and an associated CME are a pre-requisite for the acceleration of high energy electrons and both these processes happen in a different physical location.

We tried to quantify the presence of low energy electrons and the resulting characteristics high energy electrons using data from WIND/3DP, which contains data from three telescopes - ELSP,EHSP and SST. ELSP measures omini-directional fluxes in the range 5-1100 eV, EHSP measures fluxes in the range 100 eV - 30 keV and SST measures in the range 27-530 keV. Plots with fluxes covering range 0.027 keV - 108 keV is shown in Fig4.11, corresponding to events that occurred on 24 Feb 2004 and 25 Apr 2002. The first energy channel in which the electron flux corresponding to the SEP first express is variable quantity. As an example, for the event on 24 Feb 2004(first-panel Fig4.11) we see flux level enhancements in 1.33 keV whereas for the event on 25 Apr 2002, the enhancements are only seen up to 8.87 keV. Since the low energy electrons are inherently a by-product of the acceleration process, we investigated the arrival of least energetic electrons for all the events. Fig4.12 shows the scatter plot between this quantity and the SEP symmetricity ratio. A sharp downward decreasing trend is seen, implying symmetric events tend to have more low energetic electrons than non-symmetric events. The slope from the linear regression fit was found to be -13.2 with R^2 of 0.14 and p-value of 0.04. The low value of R^2 implies that the linear model does not properly capture the variations. However, the p-value less than 0.05 implies the apparent correlation is not due to any specific choices of data and cannot happen by chance in the 95% confidence interval. We found a quadratic fit better explains the data, with R^2=0.33 and p-value of 0.007.

Spectral indices and symmetricity

The spectral indices carry important information regarding the processes that generate them. For all the events, we calculated the HXR photon spectra and the inverted HXR electron spectra using RHESSI or FERMI data and 1AU electron spectrum using WIND/3DP data. The RHESSI spectra for each event was obtained by integrating the spectra around the duration of the event in the range 3-100 keV. For the photon spectra, we use a power-law fit above the break energies, which we denote as γ (Table 4.4, col 3). Assuming all the electrons would lose their energy upon streaming down from the coronal acceleration site to the denser chromosphere through bremsstrahlung collisions, we employed a thick target fit to this photon spectra to obtain the injection spectra of HXR producing electrons, which we denote as δ_{hxr} (Table 4.4, col 4). Finally, the peak electron flux from energy channels of WIND/3DP in the range 27 - 512 keV were fit with a power-law above the break to obtain the SEP spectra, denoted as δ_{AU} (Table 4.4, col 5). If the HXR producing electrons and electrons detected near 1AU had the same source population, we would expect $\delta_{AU} \sim \delta_{hxr}$,

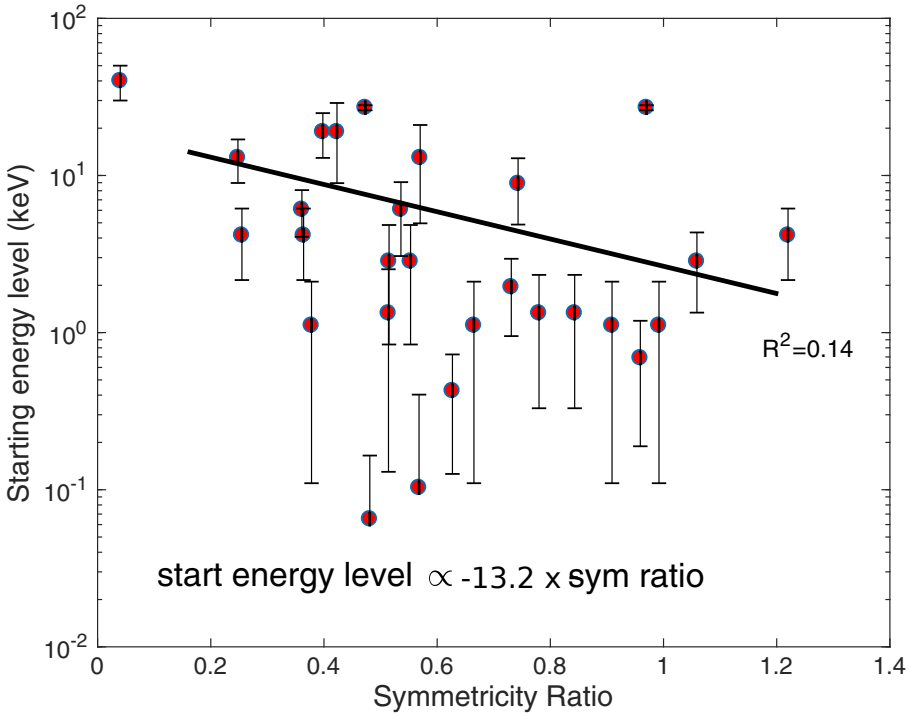

Fig. 4.12 Scatter plot showing the least energetic electrons present as a function of sym ratio.

provided the transport phase did not alter the spectral index. Since all of our events had a near-simultaneous injection of HXR electrons and SEP electrons, this assumption is reasonable. We used a linear regression fit to the ratio of δ_{AU}/δ_{hxr} and symmetricity ratio and found a linear fit with a small negative slope -0.22. The R^2 value was 0.02, with a p-value of 0.43. Out of the 28 events, only seven was out of the range $0.8 \leq \delta_{AU}/\delta_{hxr} \leq 1.2$, indicating that the spectral indices at the HXR site and at 1AU are correlated for most events (Fig4.14).

If thick target hypothesis held, then we would expect the relation $\delta_{au} = \gamma + 1$ to be valid. A linear regression fit to γ and δ_{hxr} yields a slope of 0.39 for non-symmetric events and 1.05 for symmetric events. The R^2 values for the fits are 0.070 and 0.64, respectively. A similar exercise for γ and δ_{au} yields a slope of 0.41 and 0.21 for non-symmetric and symmetric events, respectively. This significant change in slope the delta indices for symmetric events is interesting. It is not clear whether this change is a result of transport effects, acceleration characteristics or simply due to poor number statistics. Fitting a model of the form $\delta_{au} = \gamma + a$ for the symmetric and non-symmetric yields a = 0.56(95% confidence interval [0.12,0.87] and a = 0.78(95% confidence interval [0.16,1.32]) respectively. The R^2 values for both the fits were 0.44 and 0.94, respectively. Thus either of the class did not exactly follow the thick target model. For prompt events,(events with no apparent scatter)Krucker et al. (2007) reported a = 0.1. We also compared the variation of the spectral indices as a function of symmetricity

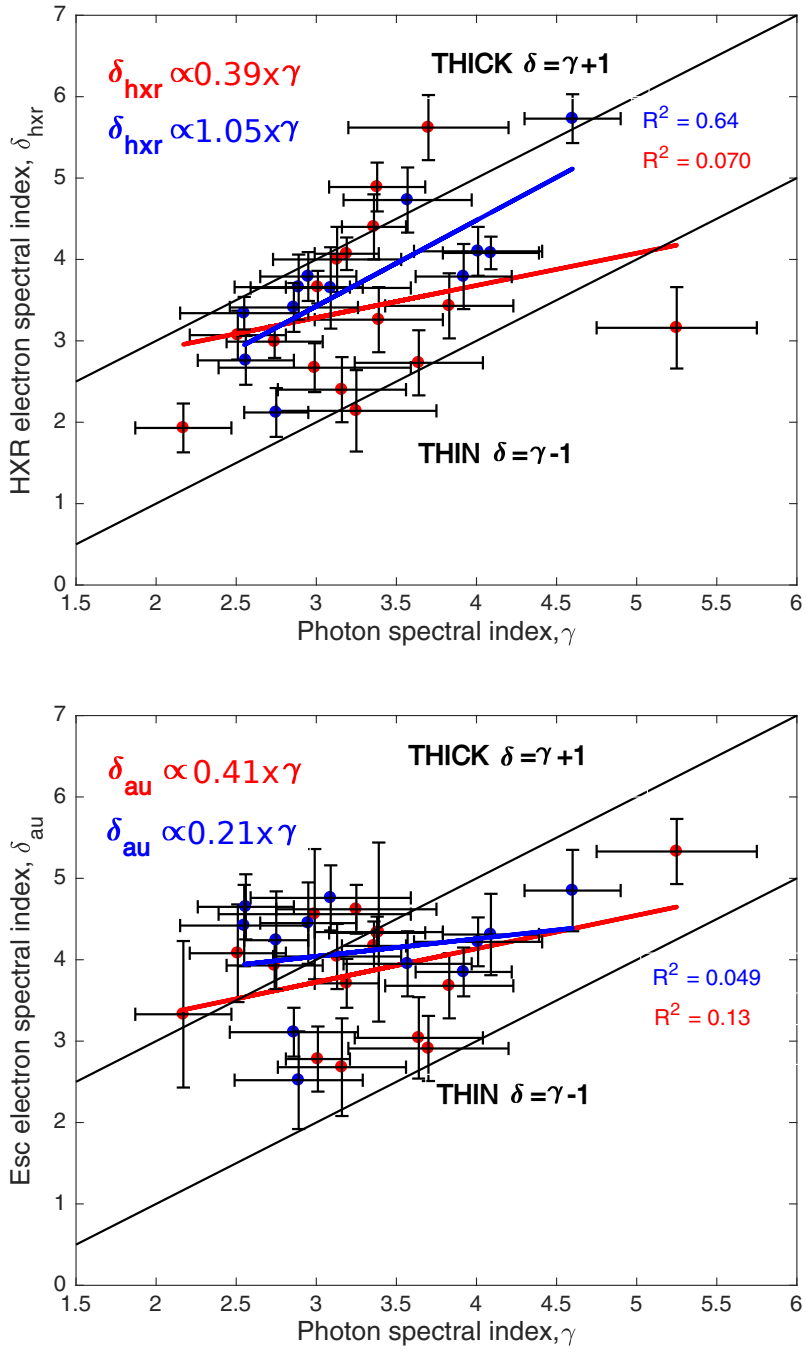

Fig. 4.13 The plots showing comparison of power-law exponent of HXR photon spectrum and the power-law exponent of the the electrons which produced the HXR emission and that of SEP electrons detected in-situ near 1 AU. The red points belong to events that produced non-symmetric SEP events and blue points to those that produced symmetric SEP events. The first panel shows the plot between γ and δ_{hxr}. Most events lie between the thick and thin target cases. The second panel show similar plot but with δ_{au}. There is a shift in the overall spectral indices, if we assume both of them started from the same population.

ratio (Fig 4.16). We see almost no relation between the value of γ and symmetricity ratio. A near-zero slope of -0.02 with R^2=1e-05 was obtained for this fit. Whereas for delta indices, we see a positive relationship with the symmetricity ratio. More symmetric events have steeper values of both δ_{hxr} and δ_{au}. The linear fit of δ_{hxr} and symmetricity ratio had a slope of 1.02 with R^2 = 0.08, while for a linear fit of δ_{au} and symmetricity ratio a slope of 0.50 with $R^2 = 0.03$ was found. The change in the slope of δ_{hxr} and δ_{au} is similar to the change of slope found in relation with γ.

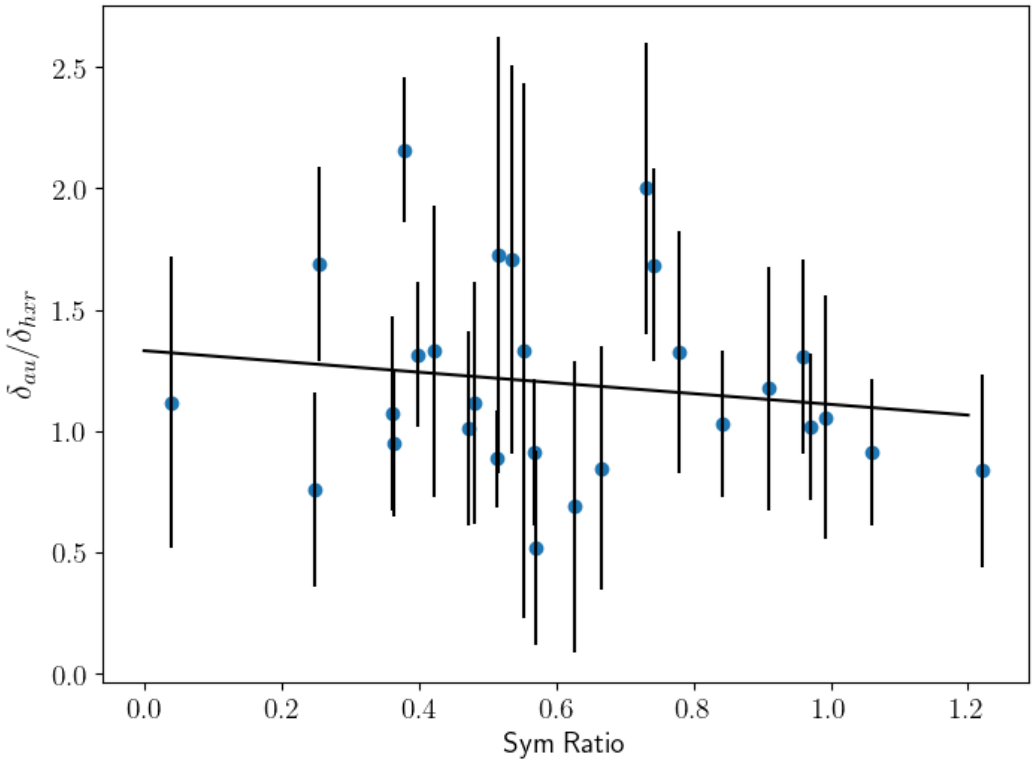

Fig. 4.14 This figure plots the ratio of the delta indices(δ_{au}/δ_{hxr}) against the symmetricity ratio. If the population of electrons causing the HXR emission and the electrons detected at 1 AU in SEP are from the same parent population, we expect $\delta_{AU} \sim \delta_{hxr}$. We find a uniform dependence on the ratio with respect to the symmetricity ratio, indicating the acceleration processes deciding the injection, may not be playing a major role in the symmetricity of the resulting SEPs. Linear regression fit showed a slope of -0.22. This fit is shown as the thick black line.

From the spectral indices, we estimated the number of electrons above 50 keV both at the HXR acceleration site as well as that of 1AU electrons. The number population of HXR electrons were estimated using the thick target fit and then integrating the spectra above 50 keV. Most of the events had a break energy below 50 keV, and in those cases, we scaled up the measured flux before adding up the numbers. For 1AU electrons an angular extent of 30 deg

was assumed(Krucker et al., 2007). It was reported in Krucker et al. (2007) that the number of escaping electrons(N_{esc}) on average is only $\sim$0.2% of HXR producing electrons(N_{hxr}) above 50 keV. For our shortlisted events, the average was found to be around $\sim$7%. However, this enhancement is due to a few outliers with a ratio of the order of $\sim$10%. These kinds of small flare events were reported in James et al. (2017) to have ratios as high as 100%. Once the outliers were removed, the ratio was about $\sim$0.4%, similar to those reported in Krucker et al. (2007). A linear regression fit to the quantities symmetricity ratio and ratio(N_{esc}/N_{hxr}) with a slope of 0.11 and R^2=0.04. This indicates that the number of electrons produced is not an indicator of resulting symmetricity of the event. This result is further illustrated in fig4.15, in which we plot the number of HXR electrons and the escaping electrons for both symmetric and non-symmetric events. The red points in the figure denote non-symmetric events while blue ones denote symmetric events. The linear regression fits to both classes yielded a slope of 2e-4 and 4e-5 respectively for non-symmetric and symmetric classes. The R^2 for both the fits were 0.57 and 0.04 respectively. We see no evident relationship between the symmetricity ratio and the number of electrons generated.

Elemental abundances and symmetricity

Multiple observational studies have shown that ion abundance in SEP's tends to vary with the acceleration process that generated them. Gradual SEP events, which are thought to be accelerated by CME shock waves, contains very fewer enchantments in $^3H_e/^4H_e$, Fe/O,Ne/O and C/O ratios when compared to impulsive SEP events which are accelerated in flares. We checked for any possible for correlation for these abundance enhancements as a function of symmetricity ratio (Fig 4.17). The Fe/O and Ne/O ratios for most events stay very close to their coronal values of 0.134 and 0.152 respectively, indicating no acceleration of such ions happened in those events. This non-dependence of the enhancements were seen across the symmetricity scale. However, six events have shown significant enhancements(values twice of coronal values) for Fe/O ratio and seven events show enhancements for Ne/O ratio. For C/O ratio, around twelve events show enhancements over coronal level. A linear regression fit to the three quantities with symmetricity ratio as the independent quantity is shown in Fig 4.17. Fe/O and Ne/O ratios show a decreasing trend with increasing symmetricity ratio while C/O shows an increasing trend with symmetricity ratio. However, this trend does not indicate the overall picture as most events show no significant enhancements for the three ratios.

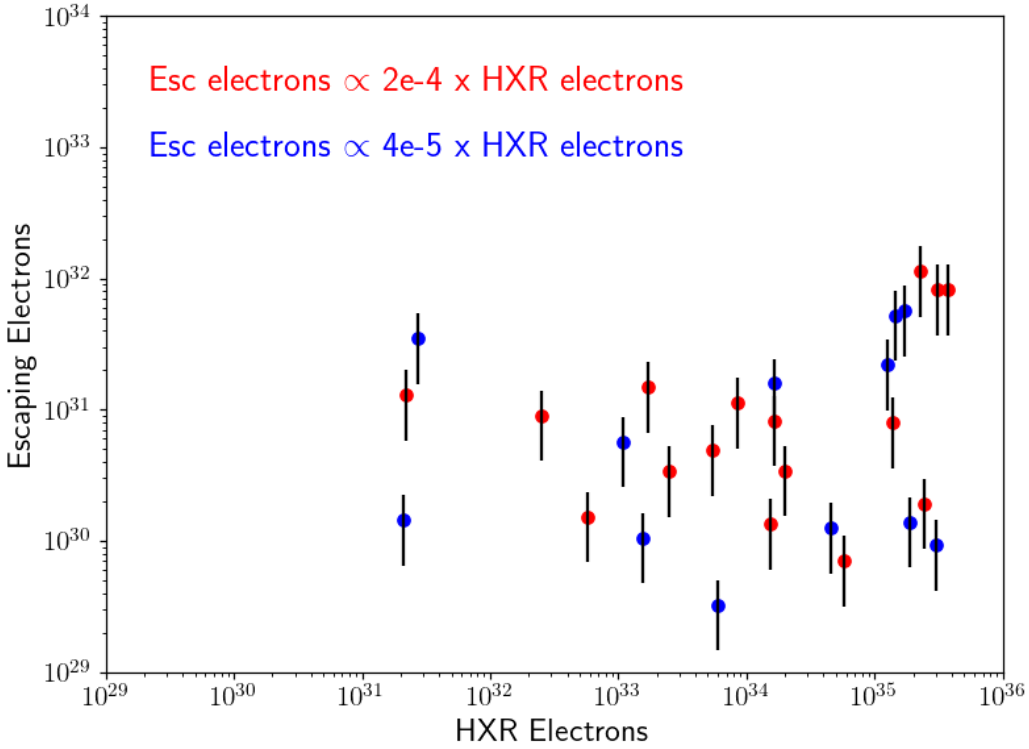

Fig. 4.15 Scatter plot between HXR electron and escaping electron populations. The red markers are for non-symmetric events, and blue markers represent symmetric events. The error bar denotes variation in the spread of electron distribution, from 10 deg to 30 deg. Both the classes of SEPs seems to produce a range of number of electrons, indicating the acceleration processes generating them may not be responsible for the symmetricity of the SEPs.

Flare intensity and symmetricity

Except the second event on Sept 30,2003, all the events had GOES SXR data. GOES flux level is used to classify the flares into different classes indicating their intensity; A(weakest), B, C, M and X(strongest). Out of 28 events, 21 of them belonged to C class or above, suggesting most of them were not weak flares. Of the remaining six, five were B class with only one belonging to A class. A linear regression to both the quantities yielded a relation of, GOES flare class $\propto$ sym $[-1\mathrm{e}-05] \times$ ratio with a R^2 of 0.02 and p-value > 0.5 for all the coefficients. Regression involving higher order terms yielded even lesser significant values. Here the independent variable was taken as the 'sym ratio' and the dependent variable as the flux level of the GOES flares. This implies that the intensity of a flare does not influence the symmetricity of the SEP.

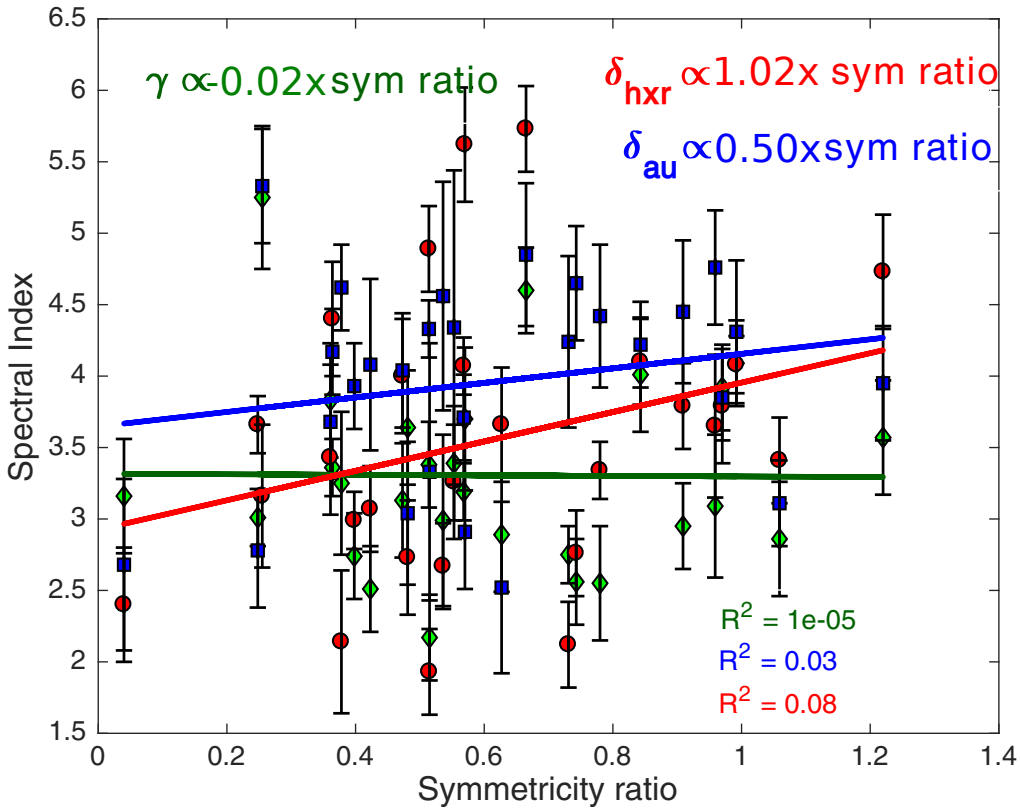

Fig. 4.16 Dependence of spectral indices and the symmetricity of the events. The green markers show photon spectral index, γ. Red markers show HXR electron spectral index δ_{hxr} and the blue markers show SEP spectral index δ_{au}. All events with symmetricity ratio above 0.6 on the horizontal axis are classified as symmetric events. The distribution of γ spectral index suggests that it has no dependence on the effect on the resulting symmetricity of the event. The electron indices both show a correlation with how symmetric the SEP would be. There is a very strong correlation for δ_{hxr} and the symmetricity ratio. Thus, more symmetric the event, the steeper the injection spectra of the electrons(based on the assumption that the source electrons for SEP and the HXR producing electrons came from the same population). However, δ_{au} show less correlation with the symmetricity ratio, suggesting that transport affects the spectral index of the SEP. The linear best fits for the three spectral indices are shown in the upper part of the plot.

4.7 Conclusion

Using data from multiple observatories, we have carefully analyzed and shortlisted 28 events that have clear HXR, radio and SEP correspondence. The inclusion of the HXR data was important to understand whether HXR producing electrons and the electrons detected near Earth as SEP particles came from the same population. HXR signature helps to accurately

Event Date	HXR burst location (lat,lon)	IMF footpoint	Connection status
Apr 25,2002 05:56UT	E07N10	W48	Poor
Aug 19,2002 21.00UT	W32S11	W43	Good*
Oct 19,2002 21:14UT	W49S13	W30	Good
Sep 30,2003 00:29UT	W40N08	W74	Poor*
Sep 30,2003 08:48UT	W44N08	W70	Good*
Dec 31,2003 18:21UT	W75N10	W54	Good*
Feb 28,2004 03:24UT	W48N13	W56	Good*
Dec 25,2004 22:29UT	W38S10	W45	Good*
May 16,2005 02:40UT	E17S17	W30	Poor
Nov 24,2005 16:15UT	W75S08	W49	Good*
Nov 19,2006 22:59UT	W85S06	W58	Good
Nov 20,2006 03:35UT	W82S06	W53	Good
Jul 07,2011 14:29UT	W85N13	W64	Good
Aug 08,2011 15:35UT	W62N17	W38	Good*
Aug 08,2011 18.03UT	W64N16	W38	Good*
Nov 12,2013 08:11UT	E59S17	W53	Poor*
Nov 12,2013 21:39UT	E53S22	W54	Poor
Feb 20,2014 07:51UT	W28S12	W35	Good
Mar 28,2014 20:57UT	W66S15	W50	Good*
Jan 20,2015 09:48UT	W82S15	W71	Good
May 13,2015 08:01UT	-	W39	-*
Dec 04,2015 14:32UT	E72S10	W58	Poor
Jan 28,2016 11:58UT	W48N04	W60	Good
Jan 28,2016 21:53UT	W51N09	W60	Good*
Jan 29,2016 08:15UT	W57N08	W67	Good*
Jan 29,2016 16:37UT	W62N04	W73	Good*
Jul 20,2016 22:05UT	W38N06	W44	Good
Apr 04,2017 09:48UT	W79N15	W53	Good*

Table 4.7 The table lists the source location in Stonyhurst heliocentric coordinates. The western limb of the Sun corresponds to W+90. Most of the events are towards the western limb. The IMF footpoint was derived from the solar wind speed with the location of the satellite taken as the reference point of 0 deg longitude. The connection status is labeled good if the source location and Parker footpoint is not separated by more than $\pm$ 30 deg.

measure the onset time of these particles from the Sun. Previously this was accomplished using the onset times of type III bursts or by backtracking the onset time at the Sun using the arrival times and velocity of detected SEP particles. Studies have shown that often, this can lead to unphysical estimations due to the assumptions involved. In our study, we only use events with near-simultaneous HXR and type III radio emission and hence the peak time of

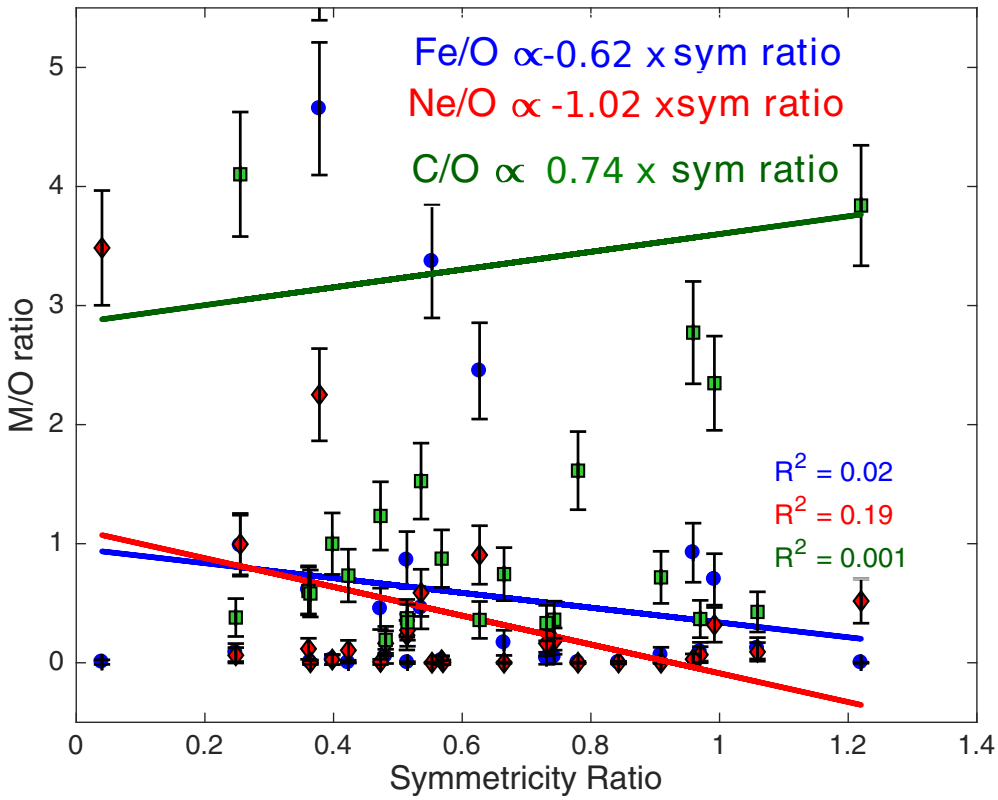

Fig. 4.17 This figure shows the scatter plot of three different elements, Fe,Ne and C with O. These ratios are chosen because studies have shown their ratios are known to change for impulsive and gradual SEPs. Thus compositional analysis give clues regarding the acceleration mechanism. The blue circles show the Fe/O ratio(background subtracted) for the duration of the SEP event. The error bars are uncertainties in the counting statistics. Likewise, the red circle are the points of Ne/O ratio and the green ones denote C/O ratio. We see a rather flat distribution for all the three ratios. All the events falling on sym ratio >0.6 belongs to the symmetric class. No evident differences regarding the composition can be seen from the plot suggesting that acceleration mechanism may not be playing a major role in the creation of symmetric and non-symmetric events. The linear fits to the data is shown in the upper part of the plot. We have avoided the outliers for each category(one each as can be seen from the upper part of the figure) for the fit.

the HXR emission could be assumed as the injection time of the electrons. This frees us from using ambiguous methods to estimate the solar onset timings. The HXR data also allows us to see the source region of the SEPs.

Due to constant outflux of particulate matter, any particle detector in space would have a high background flux level. For a SEP to be detectable, it should rise well above this background flux. To accurately estimate the onset timings of the SEPs we employ the use

of a changepoint detection algorithm. The changepoint detection algorithm looks for a critical point which denotes a rapid change in some statistical quantity - in our case, this statistical quantity is the mean. We call this quantity as t_{onset}. We also define three additional quantities to uniquely describe the shape of the time-intensity profile of the SEP. We also define three additional quantities, namely, $\Delta\, t_{arrival}$,$\Delta\, t_{rise}$ and $\Delta\, t_{decay}$ to quantify the SEP. The first quantity gives a measure of arrival time for the SEP particles with reference to the injection time determined from the HXR signature. Our study shows the presence of events which show significant delay even though a type III burst was co-incident with their HXR signature. This is a strong indication that transport effects might come into play during their transport. We observe that our events show two distinct time-intensity profile - ones that have comparable rise and decay characteristics, and ones with the unequal rise and decay profile. We quantify this using the ratio of $\Delta\, t_{rise}/\, \Delta\, t_{decay}$, which we call the symmetricity ratio. Events with the symmetricity ratio less than 0.6 were called non-symmetric and those with the ratio more than 0.6 is called symmetric.

Since Interplanetary CME's(ICMEs) can accelerate and modify the spectrum of SEP electrons, we also checked for interplanetary conditions during the transit time of the SEPs under study. We find that none of the events is associated with any ICMEs or sudden density enhancements, suggesting no external factors were influencing the transport phase of ICMEs.

Since this ratio is a proxy for the characteristics of the SEP, we checked for correlation with other physical quantities that might affect their formation, like source location, access to magnetic fields, interplanetary magnetic conditions, acceleration of low energy electrons, injection spectrum, in-situ electron spectrum and elemental abundances. We fit regression fits to these quantities with the symmetricity ratio as the independent quantity. We used p-value hypothesis testing to estimate the significance of the fit with the dependent quantity. R^2 values were used to judge the goodness of fit. Most events were found to have occurred in the western limb of the Sun. The symmetric events were found to spend more time in the IMF line. None of the above quantities gave a significant fit other than the start level of low energy electrons being accelerated. More symmetric events tend to accelerate more low energy electrons up to 0.1 keV. Even though we could not get a statistically significant fit, we see a positive trend in the spectral indices of the HXR and 1AU electrons, indicating injection profile of electron at the source site might play a role in determining the symmetricity.

To summarize, we find that:

1. The symmetricity ratio does not depend on the location of the solar source that generated the SEP.

2. We find a strong correlation between the presence of low energy electrons and the symmetricity. Symmetric events tend to contain lower-energy electrons.

3. We could not find any significant dependence between the spectral indices and symmetricity.

4. The flare intensity does not influence the symmetricity of the SEPs

More detailed simulations and observations are needed to properly understand whether the acceleration characteristics play any role in the overall time-intensity profile characteristics of SEPs.

4.8 Appendix

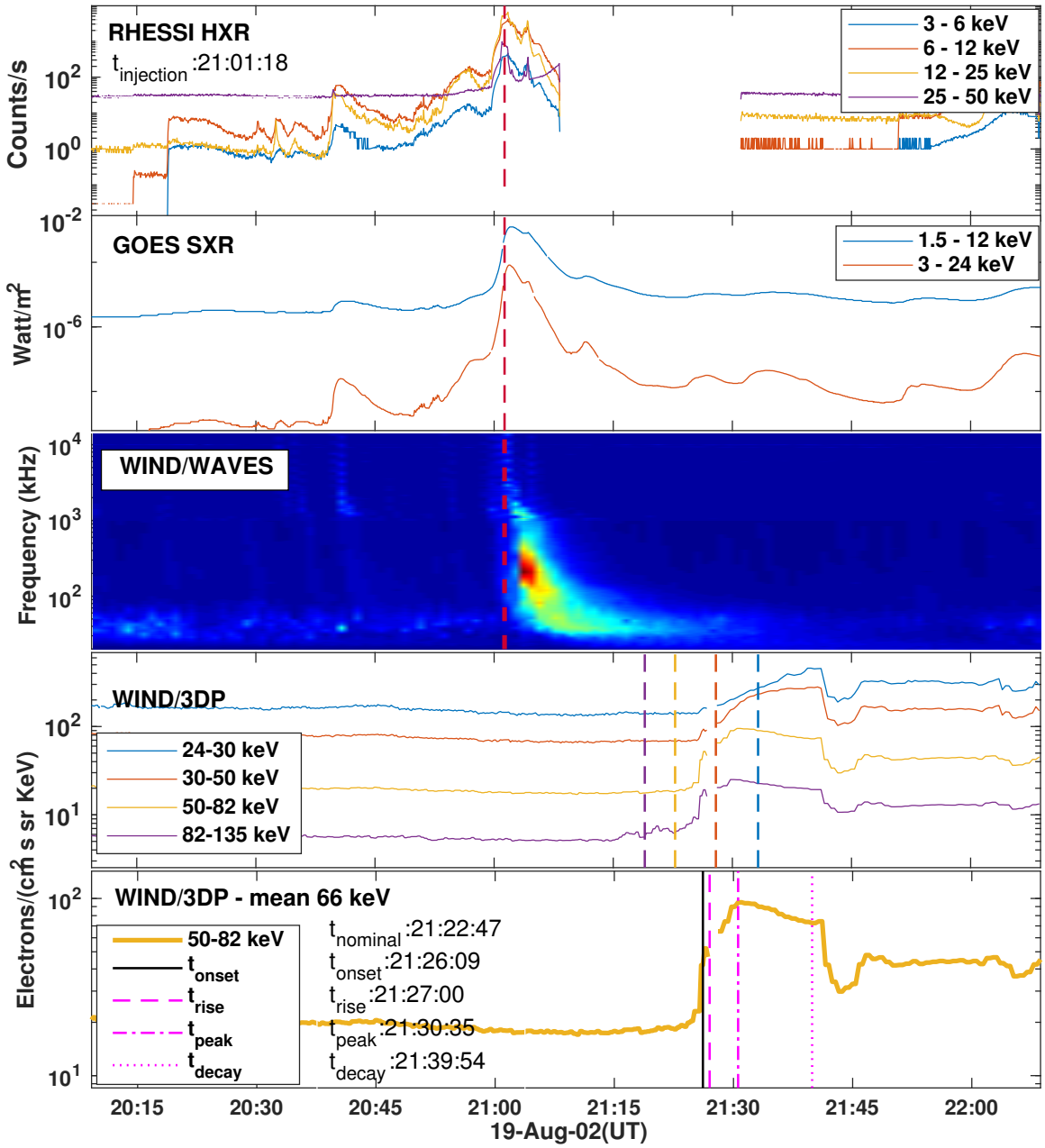
RHESSI HXR
t injection :21:01:18
3 - 6 keV
6 - 12 keV
12 - 25 keV
25 - 50 keV
Counts/s
GOES SXR
1.5 - 12 keV
3 - 24 keV
Watt/m2
WIND/WAVES
Frequency (kHz)
WIND/3DP
24-30 keV
30-50 keV
50-82 keV
82-135 keV
Electrons/(cm2 s sr KeV)
WIND/3DP - mean 66 keV
50-82 keV
t onset
t rise
t peak
t decay
t nominal :21:22:47
t onset :21:26:09
t rise :21:27:00
t peak :21:30:35
t decay :21:39:54
20:15
20:30
20:45
21:00
21:15
21:30
21:45
22:00
19-Aug-02(UT)

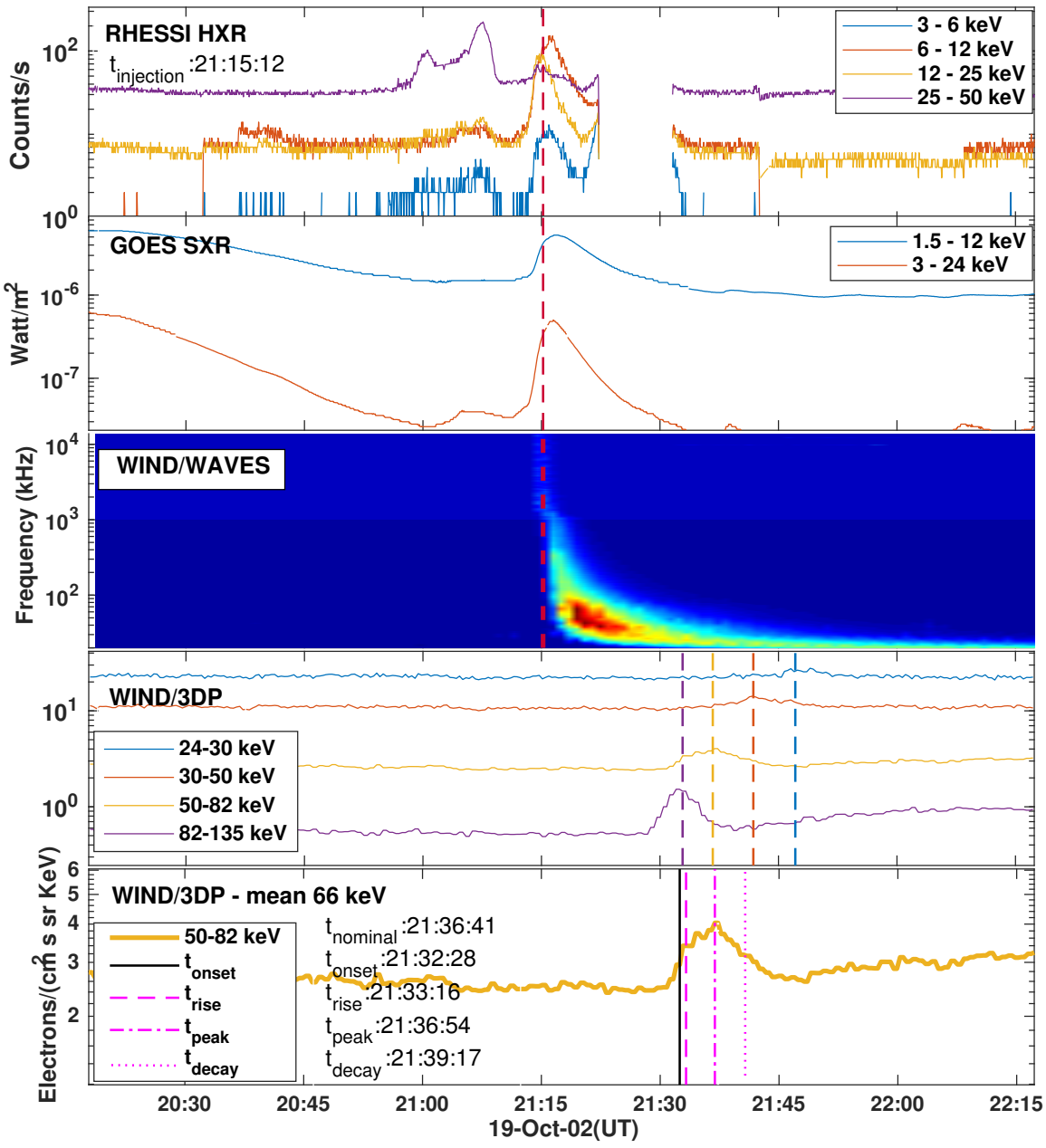
RHESSI HXR
t injection :21:15:12
Counts/s
3 - 6 keV
6 - 12 keV
12 - 25 keV
25 - 50 keV
GOES SXR
Watt/m2
1.5 - 12 keV
3 - 24 keV
WIND/WAVES
Frequency (kHz)
WIND/3DP
24-30 keV
30-50 keV
50-82 keV
82-135 keV
WIND/3DP - mean 66 keV
Electrons/(cm2 s sr KeV)
50-82 keV
t onset
t rise
t peak
t decay
t nominal :21:36:41
t onset :21:32:28
t rise :21:33:16
t peak :21:36:54
t decay :21:39:17
20:30
20:45
21:00
21:15
21:30
21:45
22:00
22:15
19-Oct-02(UT)

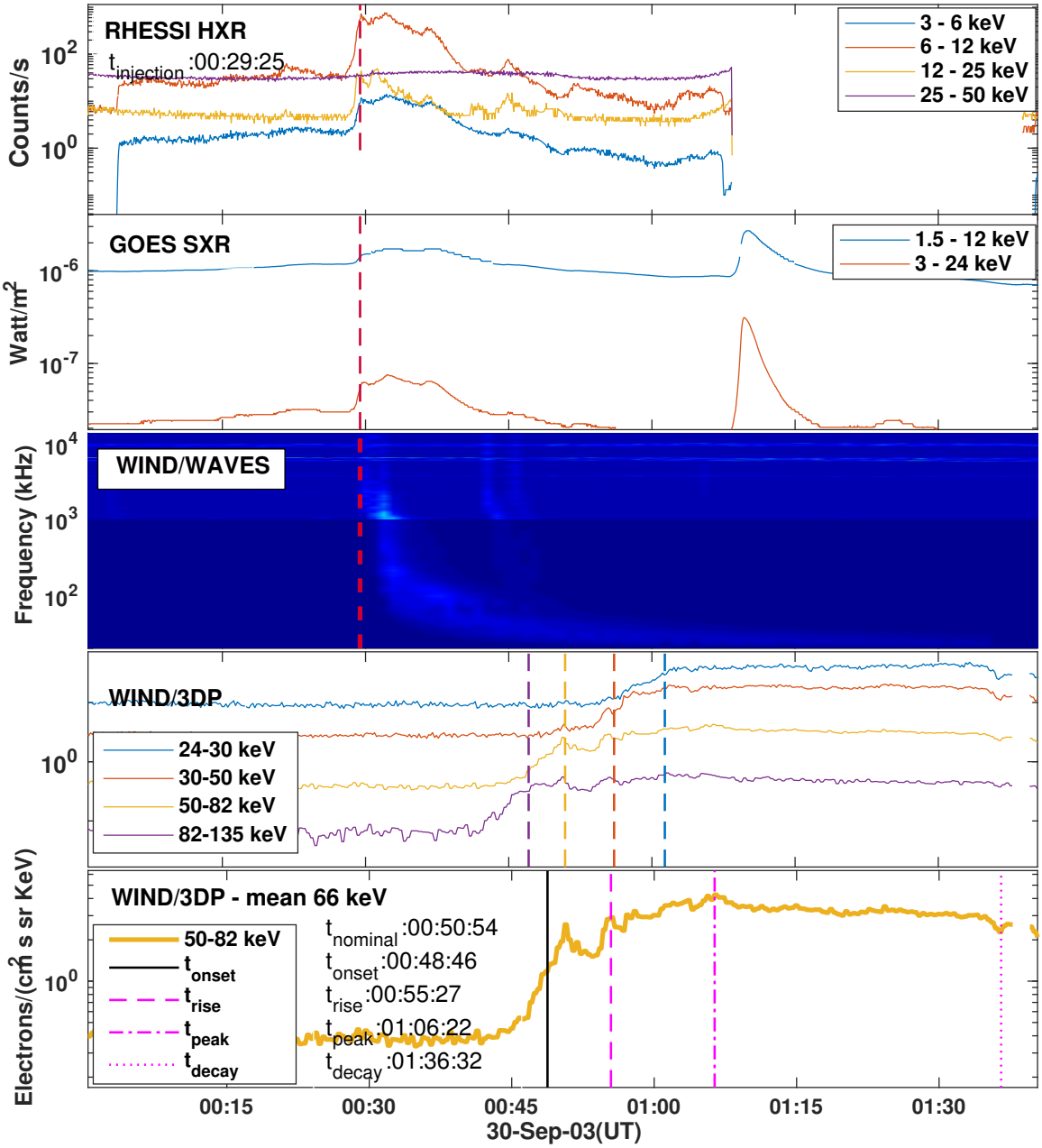
RHESSI HXR
t injection :00:29:25
3 - 6 keV
6 - 12 keV
12 - 25 keV
25 - 50 keV
Counts/s
GOES SXR
1.5 - 12 keV
3 - 24 keV
Watt/m2
WIND/WAVES
Frequency (kHz)
WIND/3DP
24-30 keV
30-50 keV
50-82 keV
82-135 keV
WIND/3DP - mean 66 keV
50-82 keV
t onset
t rise
t peak
t decay
t nominal :00:50:54
t onset :00:48:46
t rise :00:55:27
t peak :01:06:22
t decay :01:36:32
Electrons/(cm2 s sr KeV)
00:15
00:30
00:45
01:00
01:15
01:30
30-Sep-03(UT)

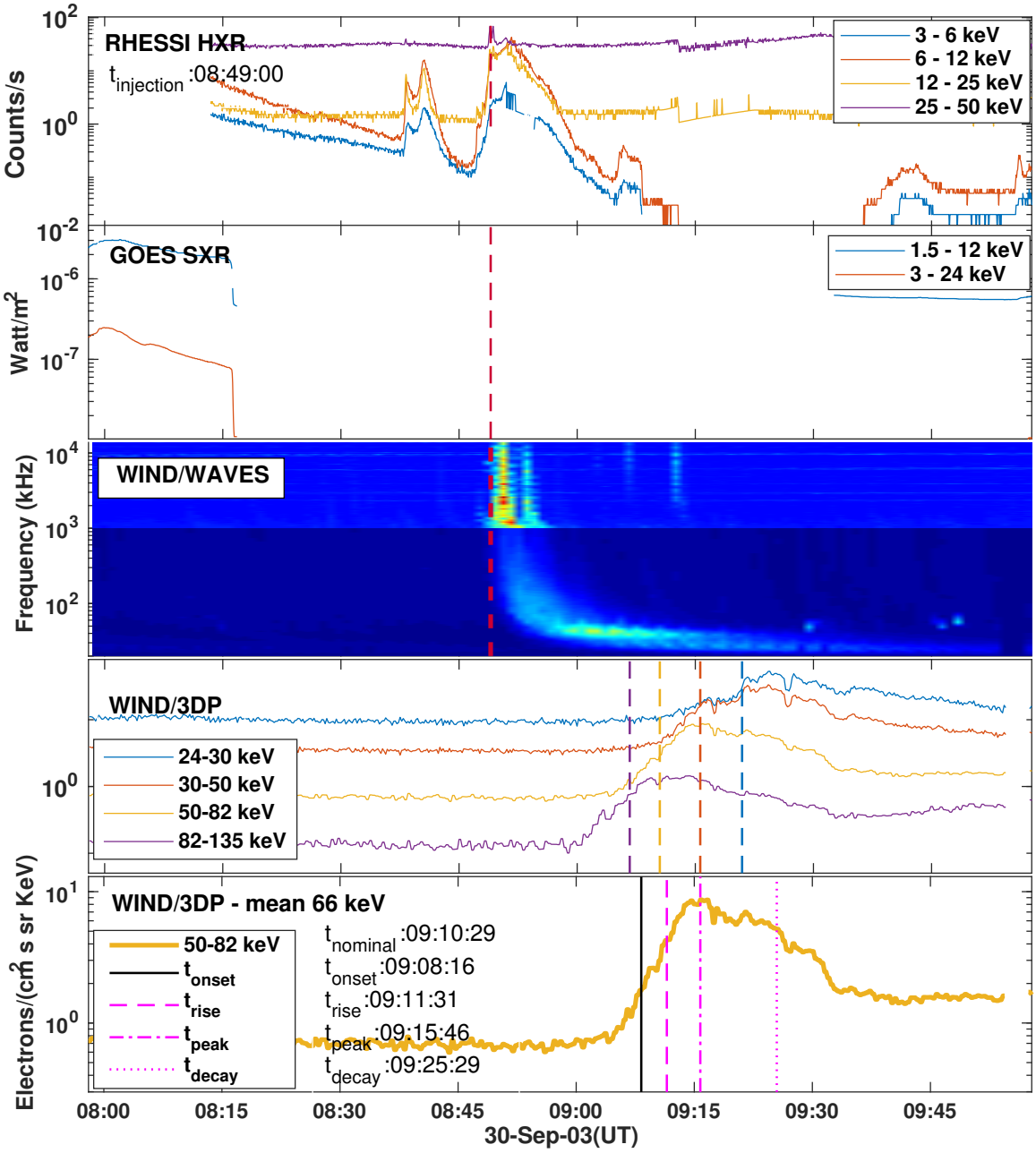
RHESSI HXR
t injection :08:49:00
3 - 6 keV
6 - 12 keV
12 - 25 keV
25 - 50 keV
Counts/s
GOES SXR
1.5 - 12 keV
3 - 24 keV
Watt/m2
WIND/WAVES
Frequency (kHz)
WIND/3DP
24-30 keV
30-50 keV
50-82 keV
82-135 keV
WIND/3DP - mean 66 keV
50-82 keV
t onset
t rise
t peak
t decay
t nominal :09:10:29
t onset :09:08:16
t rise :09:11:31
t peak :09:15:46
t decay :09:25:29
Electrons/(cm2 s sr KeV)
08:00
08:15
08:30
08:45
09:00
09:15
09:30
09:45
30-Sep-03(UT)

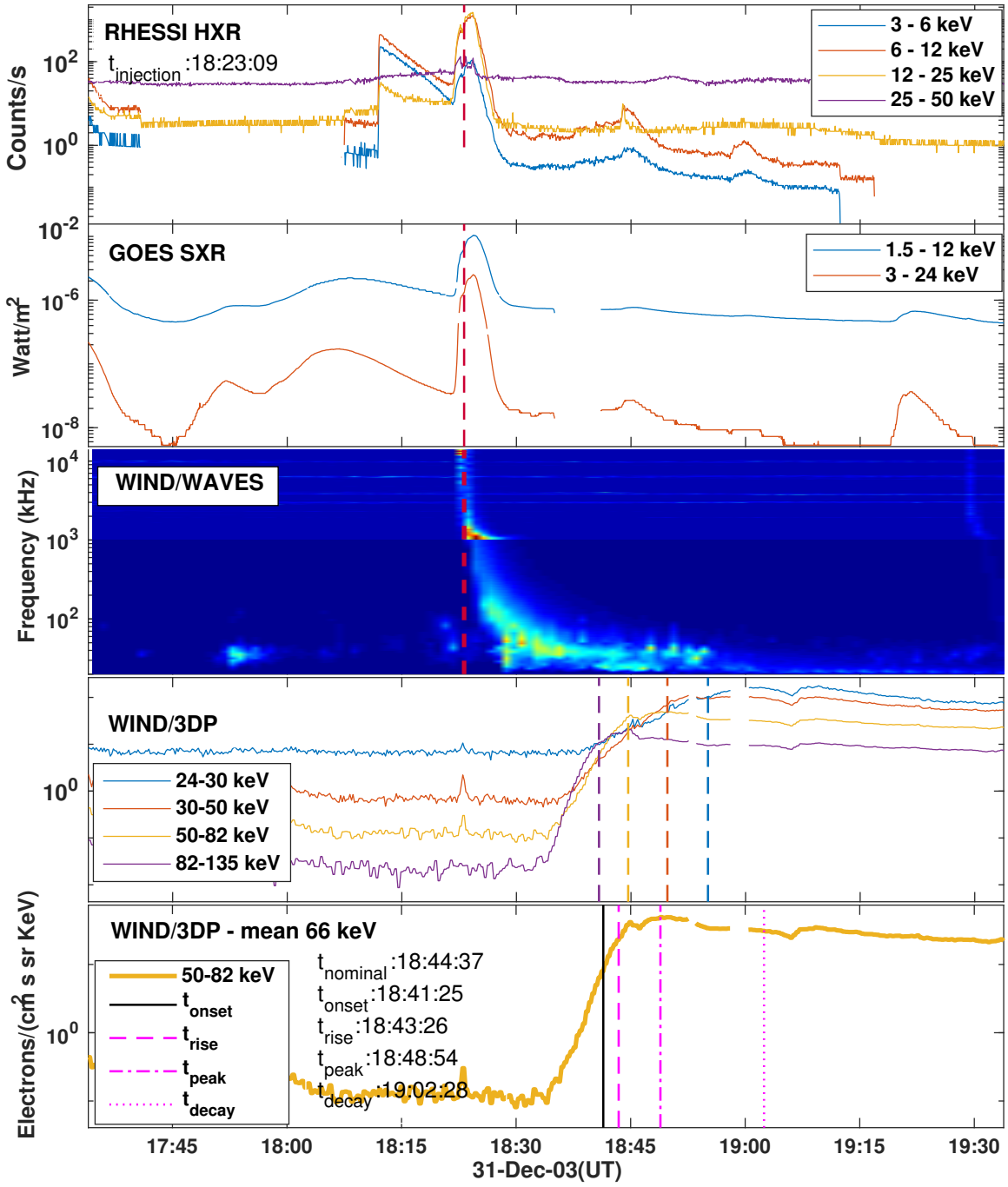
RHESSI HXR
t injection :18:23:09
3 - 6 keV
6 - 12 keV
12 - 25 keV
25 - 50 keV
Counts/s
GOES SXR
1.5 - 12 keV
3 - 24 keV
Watt/m2
WIND/WAVES
Frequency (kHz)
WIND/3DP
24-30 keV
30-50 keV
50-82 keV
82-135 keV
WIND/3DP - mean 66 keV
50-82 keV
t onset
t rise
t peak
t decay
t nominal :18:44:37
t onset :18:41:25
t rise :18:43:26
t peak :18:48:54
t decay :19:02:28
Electrons/(cm2 s sr KeV)
17:45
18:00
18:15
18:30
18:45
19:00
19:15
19:30
31-Dec-03(UT)

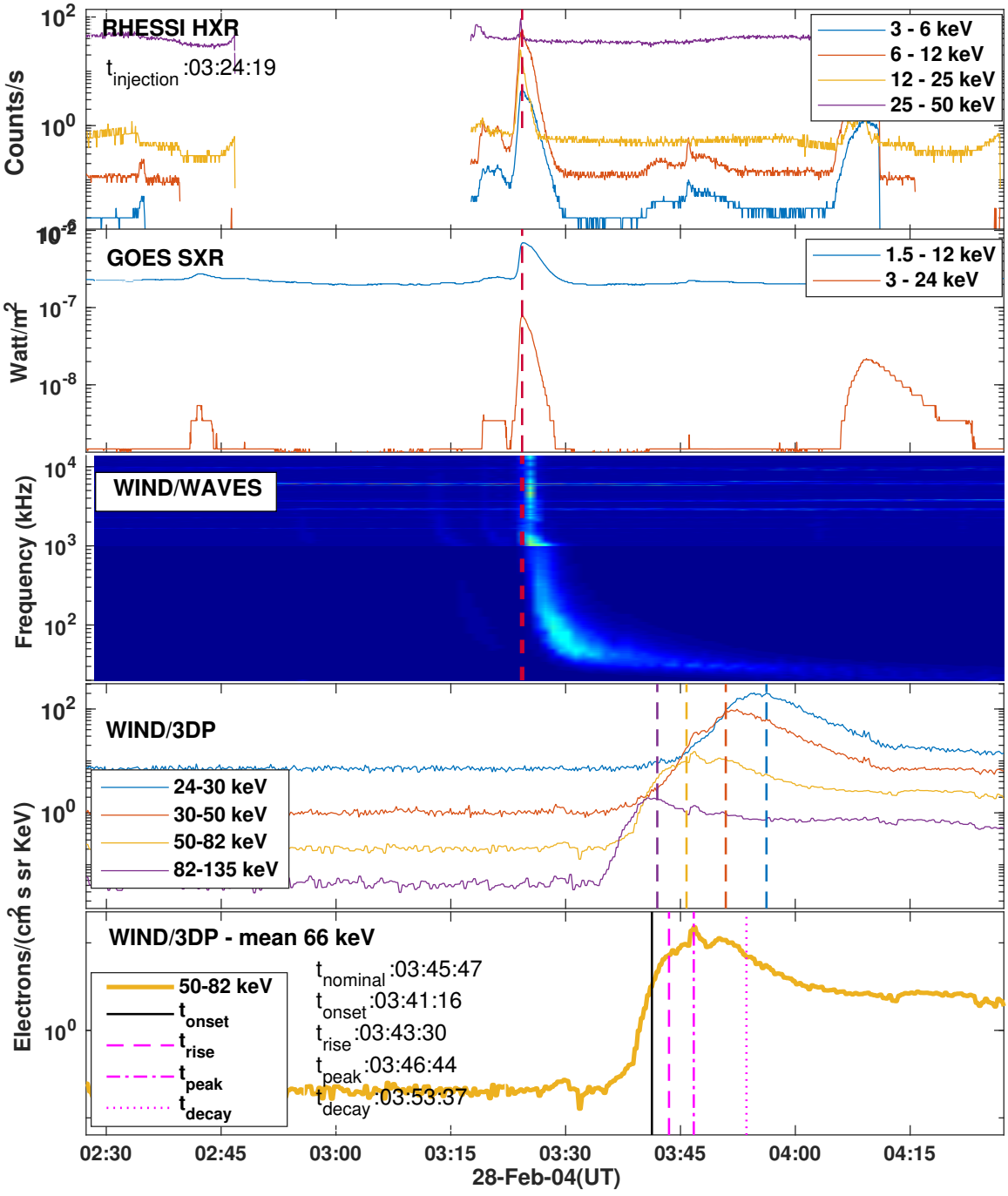
RHESSI HXR
t injection :03:24:19
3 - 6 keV
6 - 12 keV
12 - 25 keV
25 - 50 keV
Counts/s
GOES SXR
1.5 - 12 keV
3 - 24 keV
Watt/m2
WIND/WAVES
Frequency (kHz)
WIND/3DP
24-30 keV
30-50 keV
50-82 keV
82-135 keV
Electrons/(cm2 s sr KeV)
WIND/3DP - mean 66 keV
50-82 keV
t onset
t rise
t peak
t decay
t nominal :03:45:47
t onset :03:41:16
t rise :03:43:30
t peak :03:46:44
t decay :03:53:37
02:30
02:45
03:00
03:15
03:30
03:45
04:00
04:15
28-Feb-04(UT)

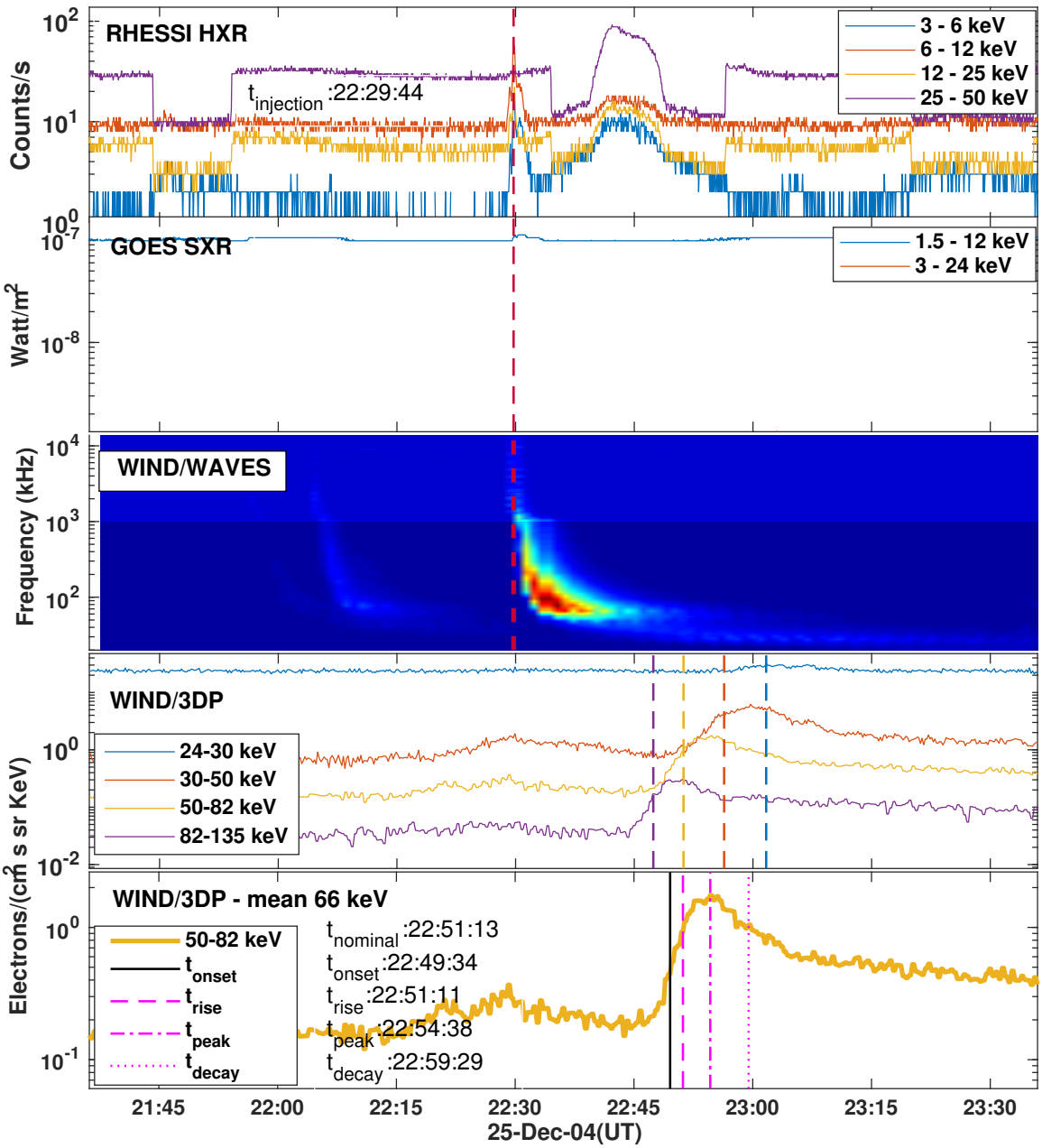
RHESSI HXR
Counts/s
10^2
10^1
10^0
$t_{injection}$:22:29:44
3 - 6 keV
6 - 12 keV
12 - 25 keV
25 - 50 keV
GOES SXR
Watt/m^2
10^{-7}
10^{-8}
1.5 - 12 keV
3 - 24 keV
WIND/WAVES
Frequency (kHz)
10^4
10^3
10^2
WIND/3DP
Electrons/(cm^2 s sr KeV)
10^0
10^{-2}
24-30 keV
30-50 keV
50-82 keV
82-135 keV
WIND/3DP - mean 66 keV
10^0
10^{-1}
50-82 keV
t_{onset}
t_{rise}
t_{peak}
t_{decay}
$t_{nominal}$:22:51:13
t_{onset}:22:49:34
t_{rise}:22:51:11
t_{peak}:22:54:38
t_{decay}:22:59:29
21:45
22:00
22:15
22:30
22:45
23:00
23:15
23:30
25-Dec-04(UT)

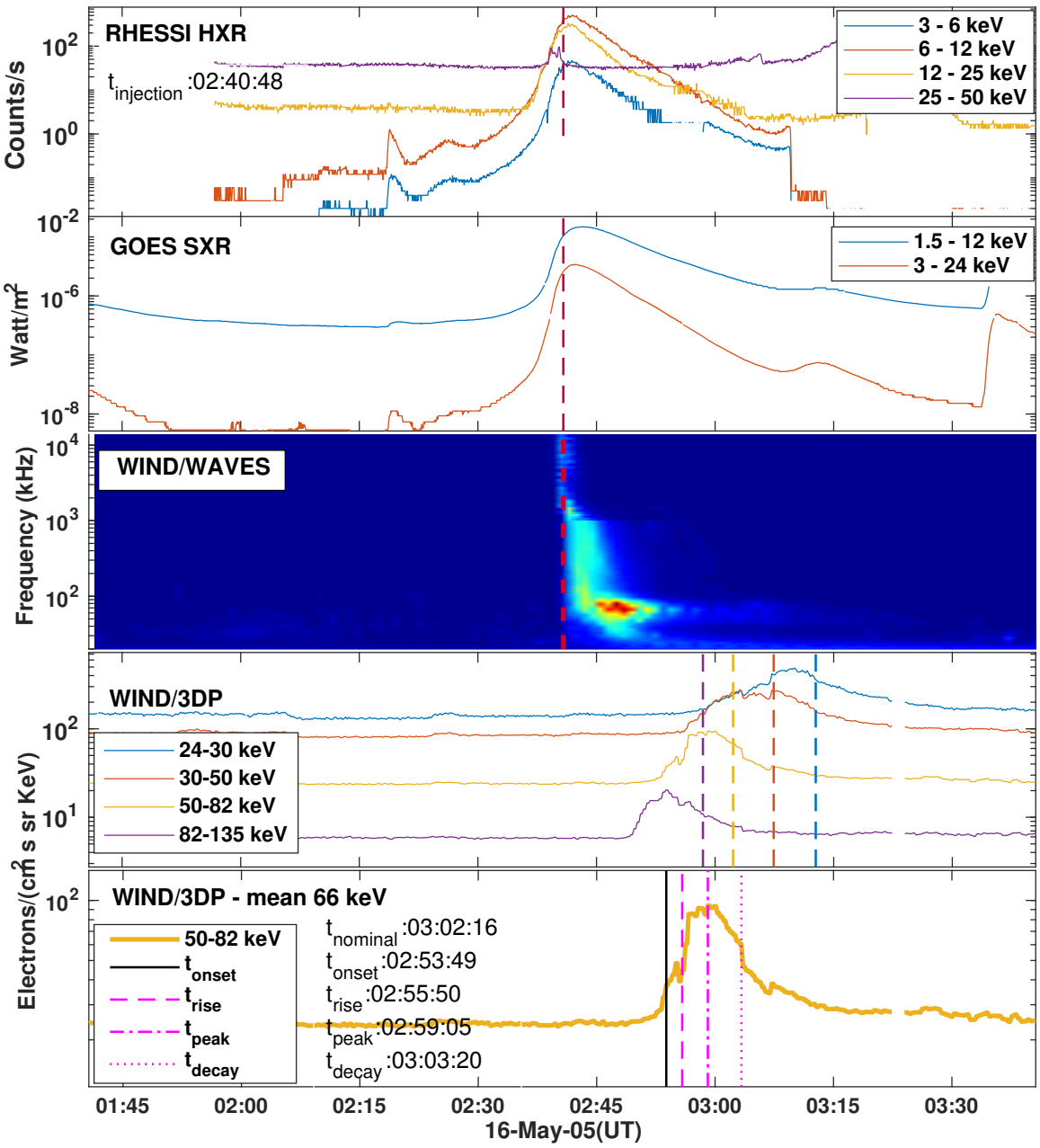
RHESSI HXR
t injection :02:40:48
3 - 6 keV
6 - 12 keV
12 - 25 keV
25 - 50 keV
Counts/s
GOES SXR
1.5 - 12 keV
3 - 24 keV
Watt/m2
WIND/WAVES
Frequency (kHz)
WIND/3DP
24-30 keV
30-50 keV
50-82 keV
82-135 keV
WIND/3DP - mean 66 keV
50-82 keV
t onset
t rise
t peak
t decay
t nominal :03:02:16
t onset :02:53:49
t rise :02:55:50
t peak :02:59:05
t decay :03:03:20
Electrons/(cm2 s sr KeV)
01:45
02:00
02:15
02:30
02:45
03:00
03:15
03:30
16-May-05(UT)

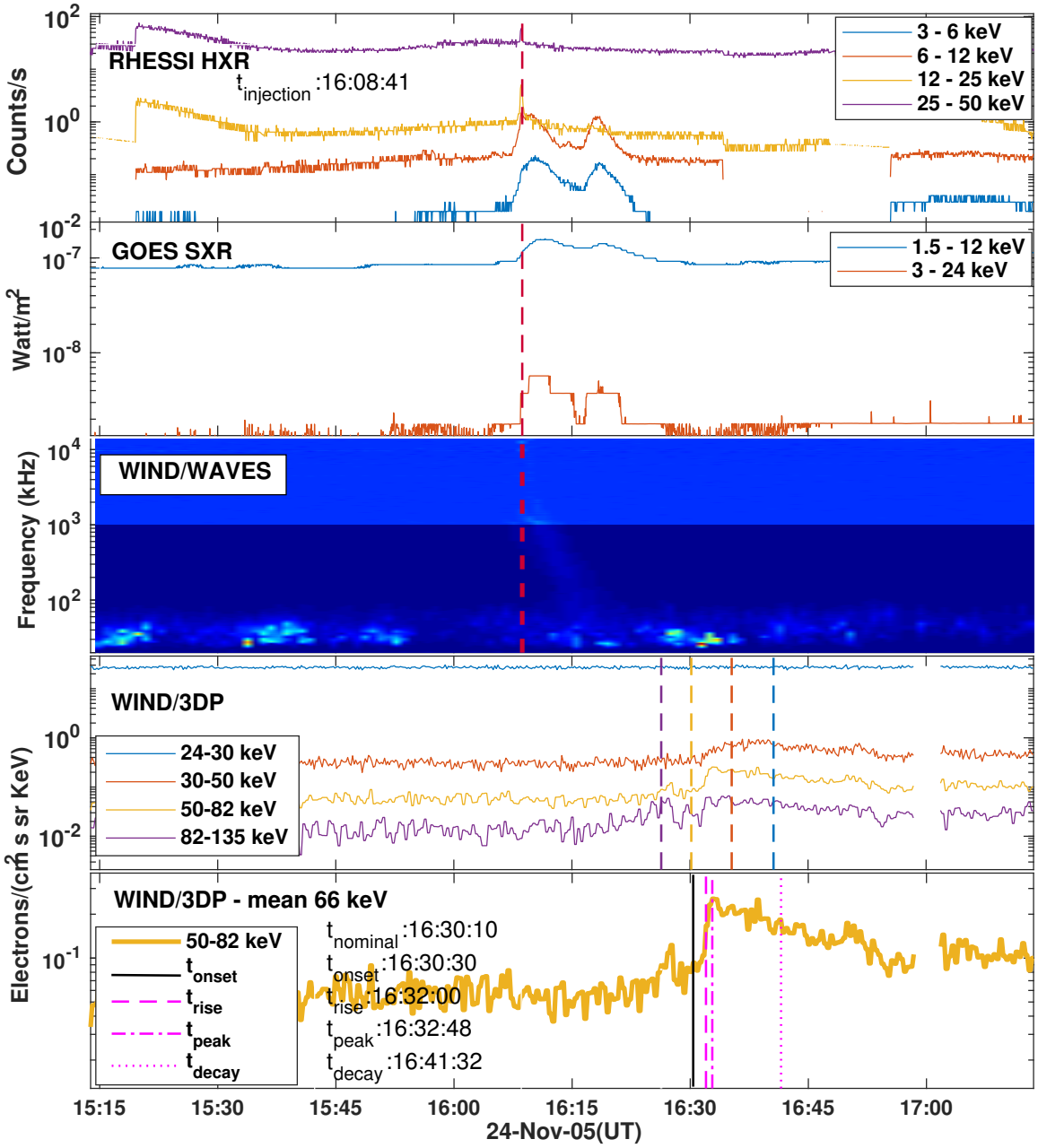
RHESSI HXR
t injection :16:08:41
3 - 6 keV
6 - 12 keV
12 - 25 keV
25 - 50 keV
Counts/s
GOES SXR
1.5 - 12 keV
3 - 24 keV
Watt/m2
WIND/WAVES
Frequency (kHz)
WIND/3DP
24-30 keV
30-50 keV
50-82 keV
82-135 keV
WIND/3DP - mean 66 keV
50-82 keV
t onset
t rise
t peak
t decay
t nominal :16:30:10
t onset :16:30:30
t rise :16:32:00
t peak :16:32:48
t decay :16:41:32
Electrons/(cm2 s sr KeV)
15:15
15:30
15:45
16:00
16:15
16:30
16:45
17:00
24-Nov-05(UT)

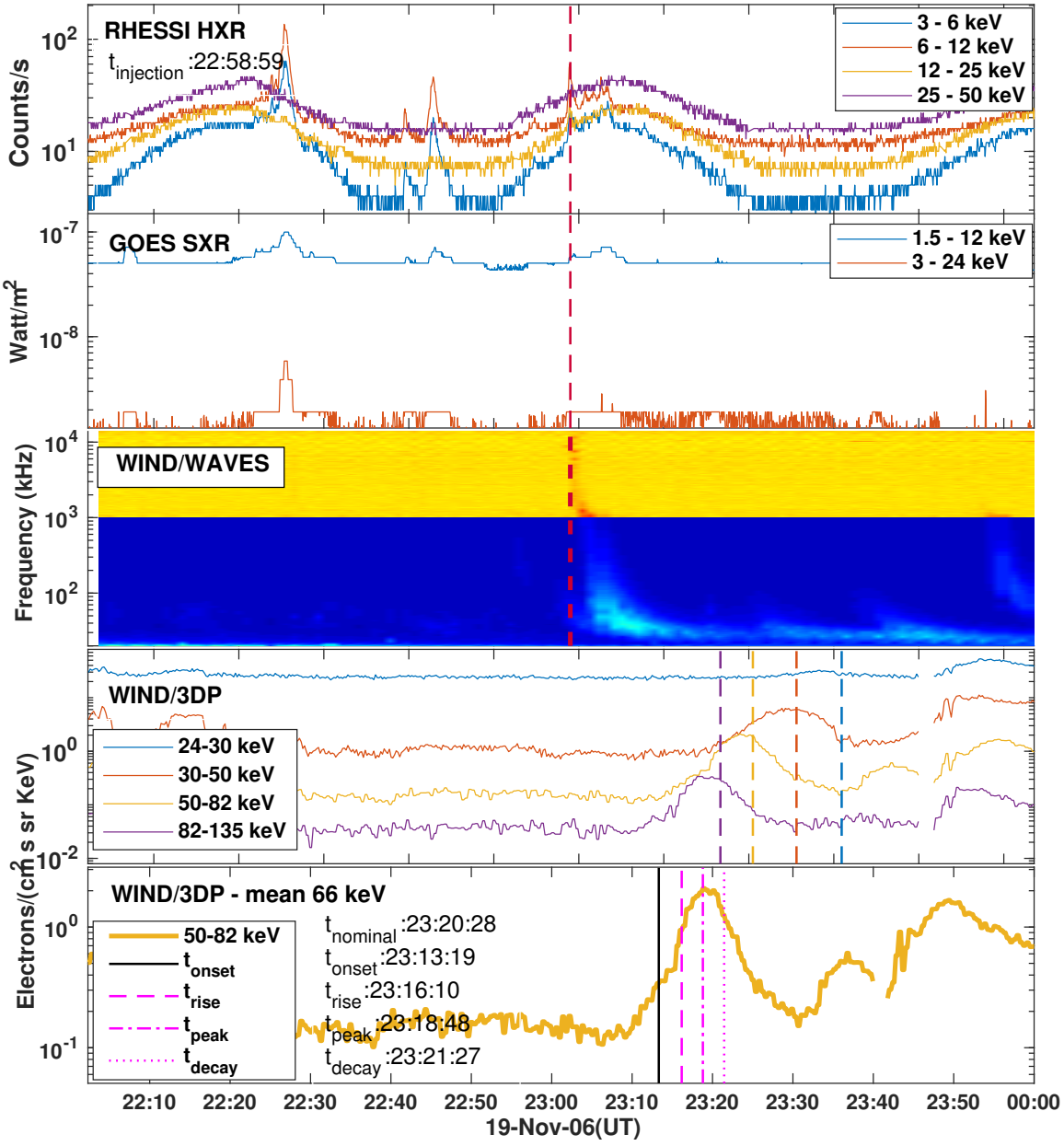
RHESSI HXR
t injection :22:58:59
3 - 6 keV
6 - 12 keV
12 - 25 keV
25 - 50 keV
Counts/s
GOES SXR
1.5 - 12 keV
3 - 24 keV
Watt/m2
WIND/WAVES
Frequency (kHz)
WIND/3DP
24-30 keV
30-50 keV
50-82 keV
82-135 keV
Electrons/(cm2 s sr KeV)
WIND/3DP - mean 66 keV
50-82 keV
t onset
t rise
t peak
t decay
t nominal :23:20:28
t onset :23:13:19
t rise :23:16:10
t peak :23:18:48
t decay :23:21:27
22:10
22:20
22:30
22:40
22:50
23:00
23:10
23:20
23:30
23:40
23:50
00:00
19-Nov-06(UT)

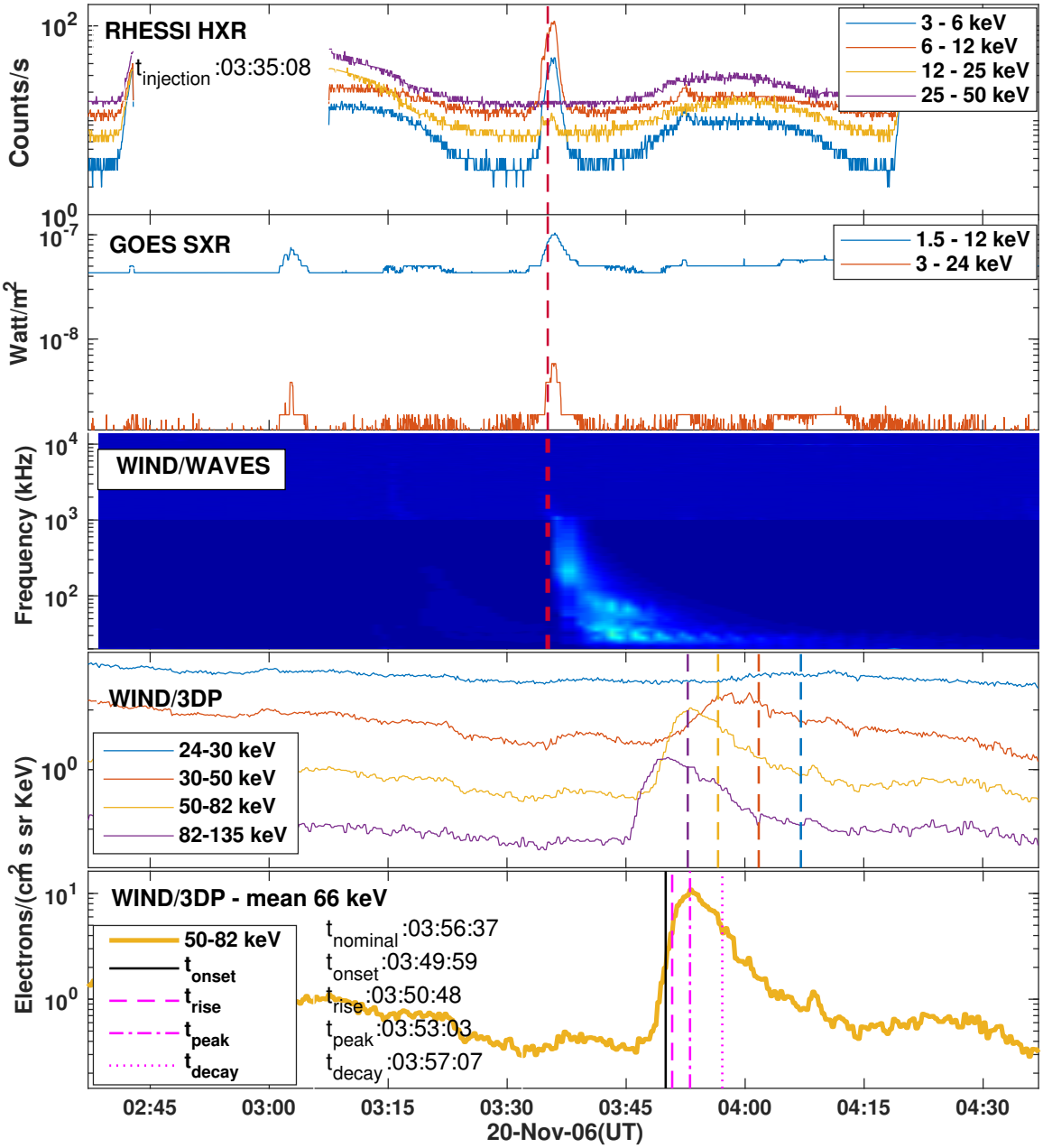
RHESSI HXR
$t_{injection}$:03:35:08
3 - 6 keV
6 - 12 keV
12 - 25 keV
25 - 50 keV
Counts/s
GOES SXR
1.5 - 12 keV
3 - 24 keV
Watt/m^2
WIND/WAVES
Frequency (kHz)
WIND/3DP
24-30 keV
30-50 keV
50-82 keV
82-135 keV
Electrons/(cm^2 s sr KeV)
WIND/3DP - mean 66 keV
50-82 keV
t_{onset}
t_{rise}
t_{peak}
t_{decay}
$t_{nominal}$:03:56:37
t_{onset}:03:49:59
t_{rise}:03:50:48
t_{peak}:03:53:03
t_{decay}:03:57:07
02:45
03:00
03:15
03:30
03:45
04:00
04:15
04:30
20-Nov-06(UT)

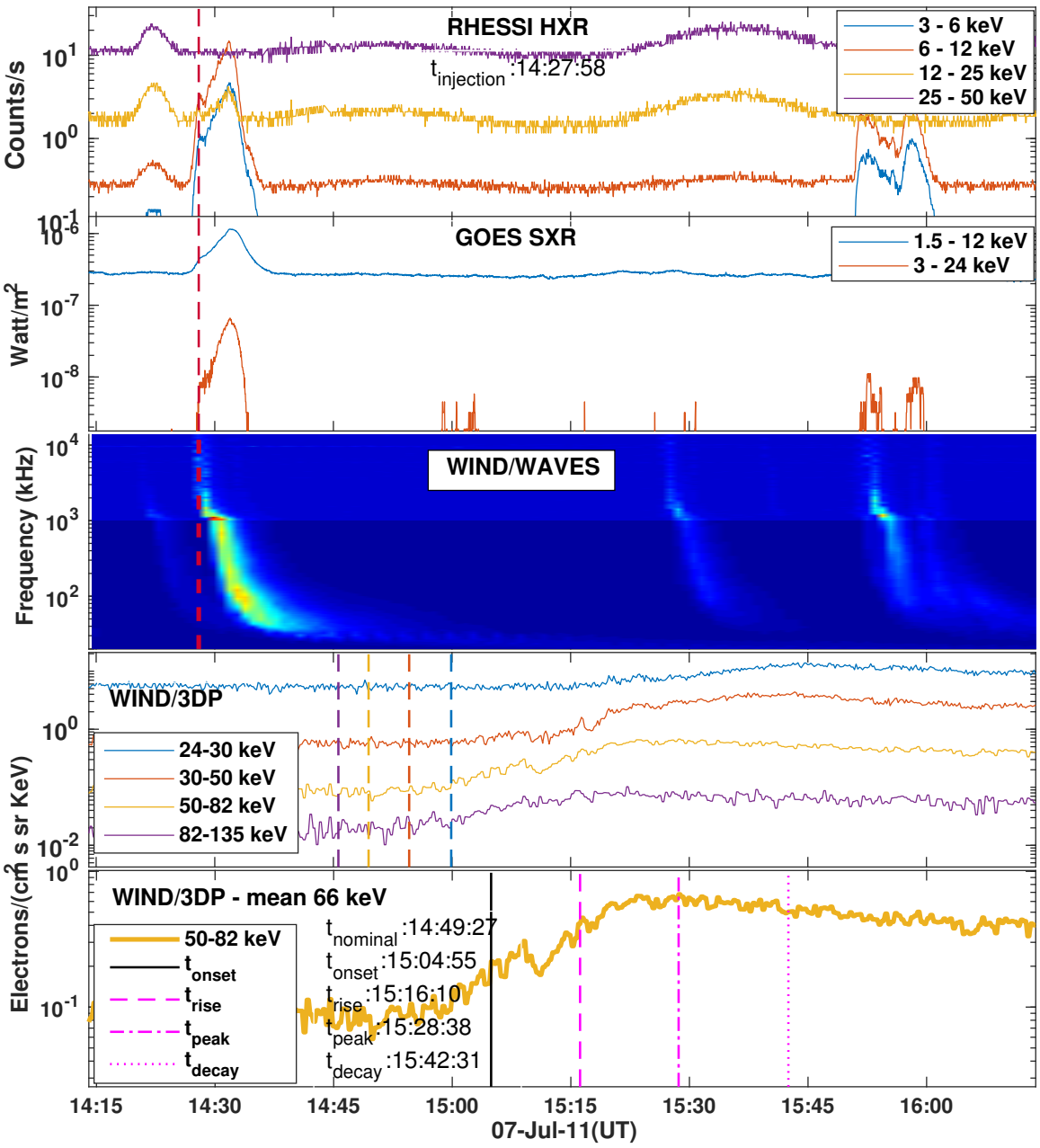
RHESSI HXR
t injection :14:27:58
3 - 6 keV
6 - 12 keV
12 - 25 keV
25 - 50 keV
Counts/s
GOES SXR
1.5 - 12 keV
3 - 24 keV
Watt/m2
WIND/WAVES
Frequency (kHz)
WIND/3DP
24-30 keV
30-50 keV
50-82 keV
82-135 keV
Electrons/(cm2 s sr KeV)
WIND/3DP - mean 66 keV
50-82 keV
t onset
t rise
t peak
t decay
t nominal :14:49:27
t onset :15:04:55
t rise :15:16:10
t peak :15:28:38
t decay :15:42:31
14:15
14:30
14:45
15:00
15:15
15:30
15:45
16:00
07-Jul-11(UT)

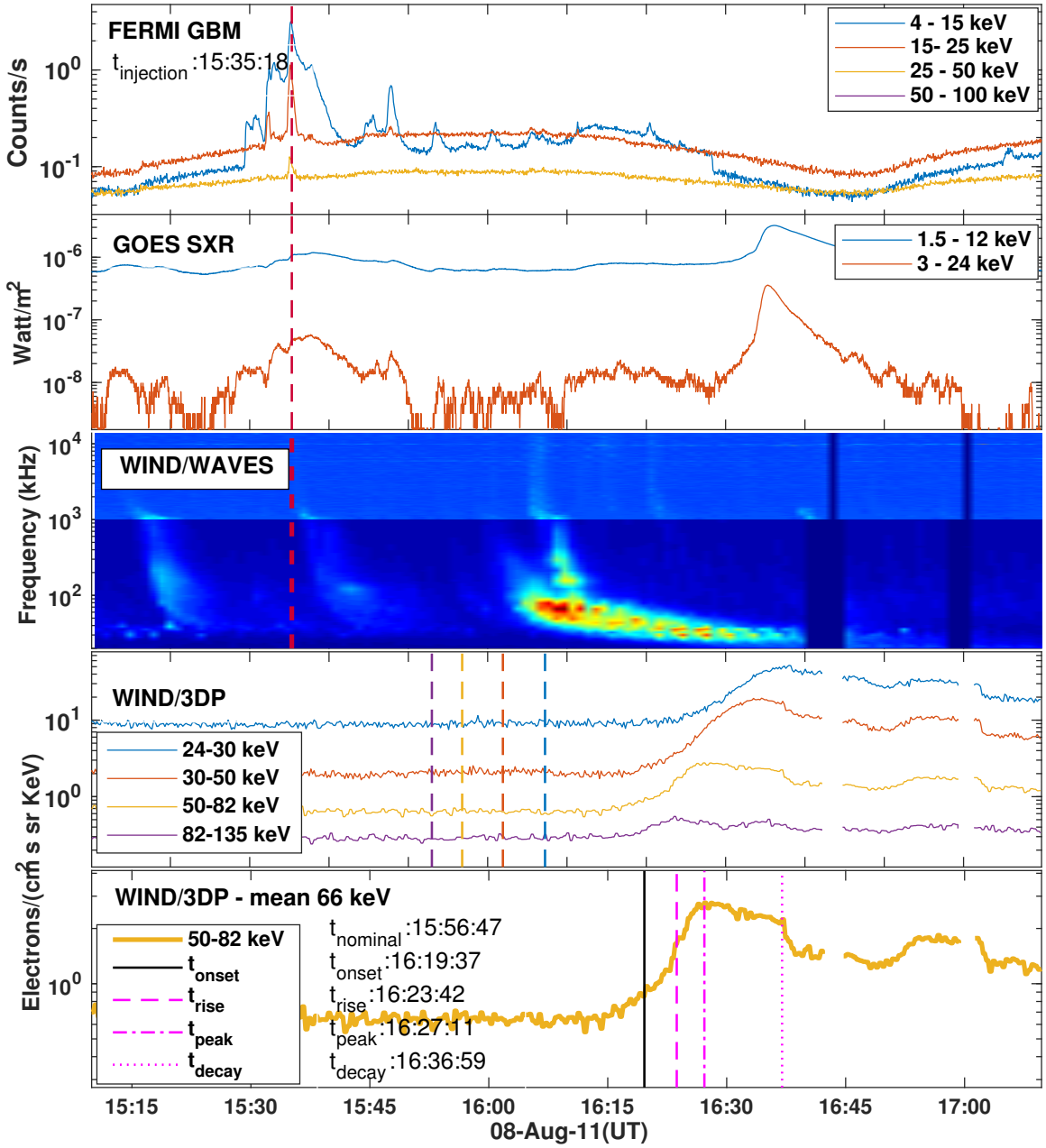
FERMI GBM
t_injection :15:35:18
4 - 15 keV
15- 25 keV
25 - 50 keV
50 - 100 keV
Counts/s
GOES SXR
1.5 - 12 keV
3 - 24 keV
Watt/m2
WIND/WAVES
Frequency (kHz)
WIND/3DP
24-30 keV
30-50 keV
50-82 keV
82-135 keV
WIND/3DP - mean 66 keV
50-82 keV
t_onset
t_rise
t_peak
t_decay
t_nominal :15:56:47
t_onset :16:19:37
t_rise :16:23:42
t_peak :16:27:11
t_decay :16:36:59
Electrons/(cm2 s sr KeV)
15:15
15:30
15:45
16:00
16:15
16:30
16:45
17:00
08-Aug-11(UT)

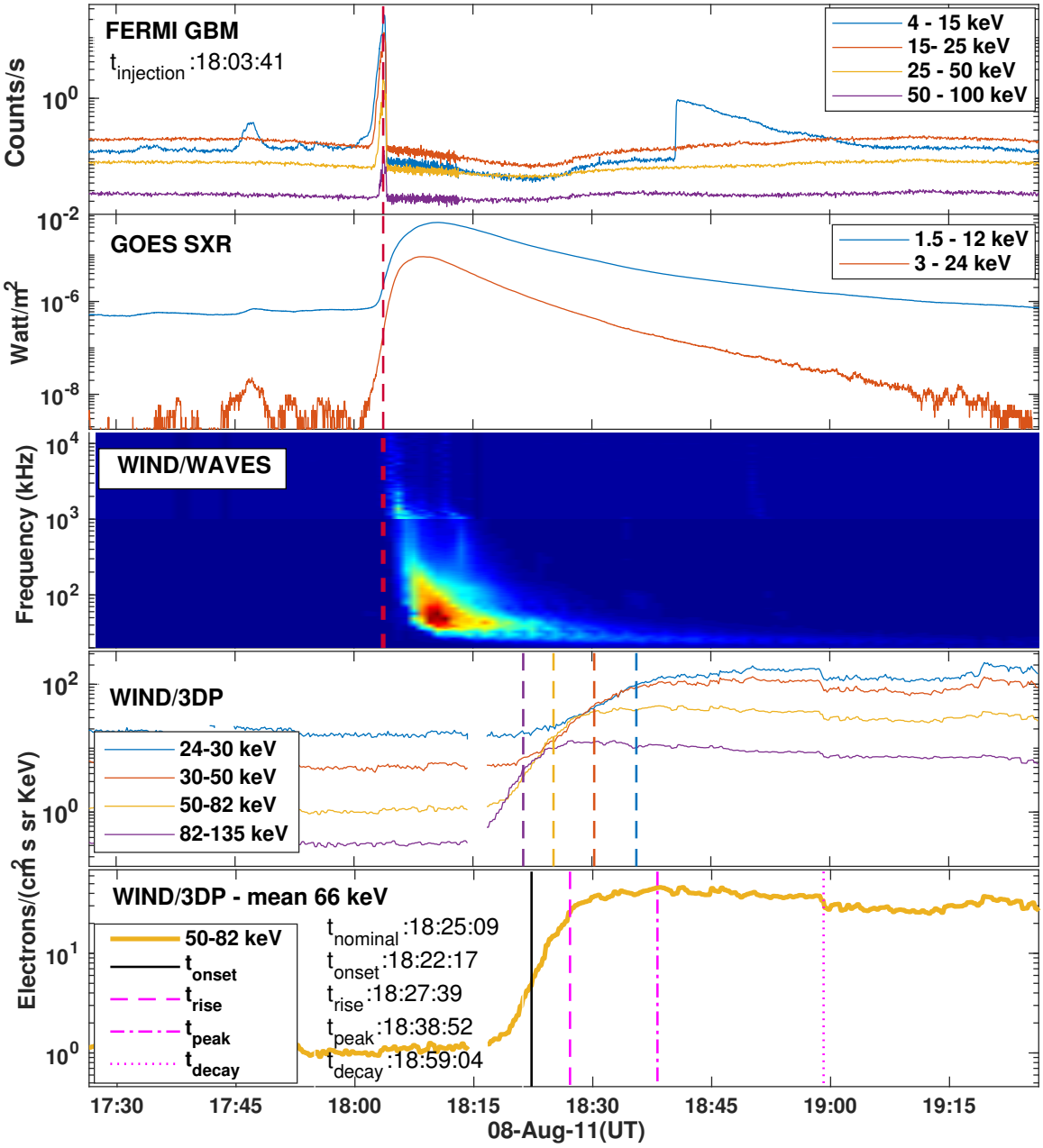
FERMI GBM
t_injection :18:03:41
4 - 15 keV
15- 25 keV
25 - 50 keV
50 - 100 keV
Counts/s
GOES SXR
1.5 - 12 keV
3 - 24 keV
Watt/m2
WIND/WAVES
Frequency (kHz)
WIND/3DP
24-30 keV
30-50 keV
50-82 keV
82-135 keV
Electrons/(cm2 s sr KeV)
WIND/3DP - mean 66 keV
50-82 keV
t_onset
t_rise
t_peak
t_decay
t_nominal :18:25:09
t_onset :18:22:17
t_rise :18:27:39
t_peak :18:38:52
t_decay :18:59:04
17:30
17:45
18:00
18:15
18:30
18:45
19:00
19:15
08-Aug-11(UT)

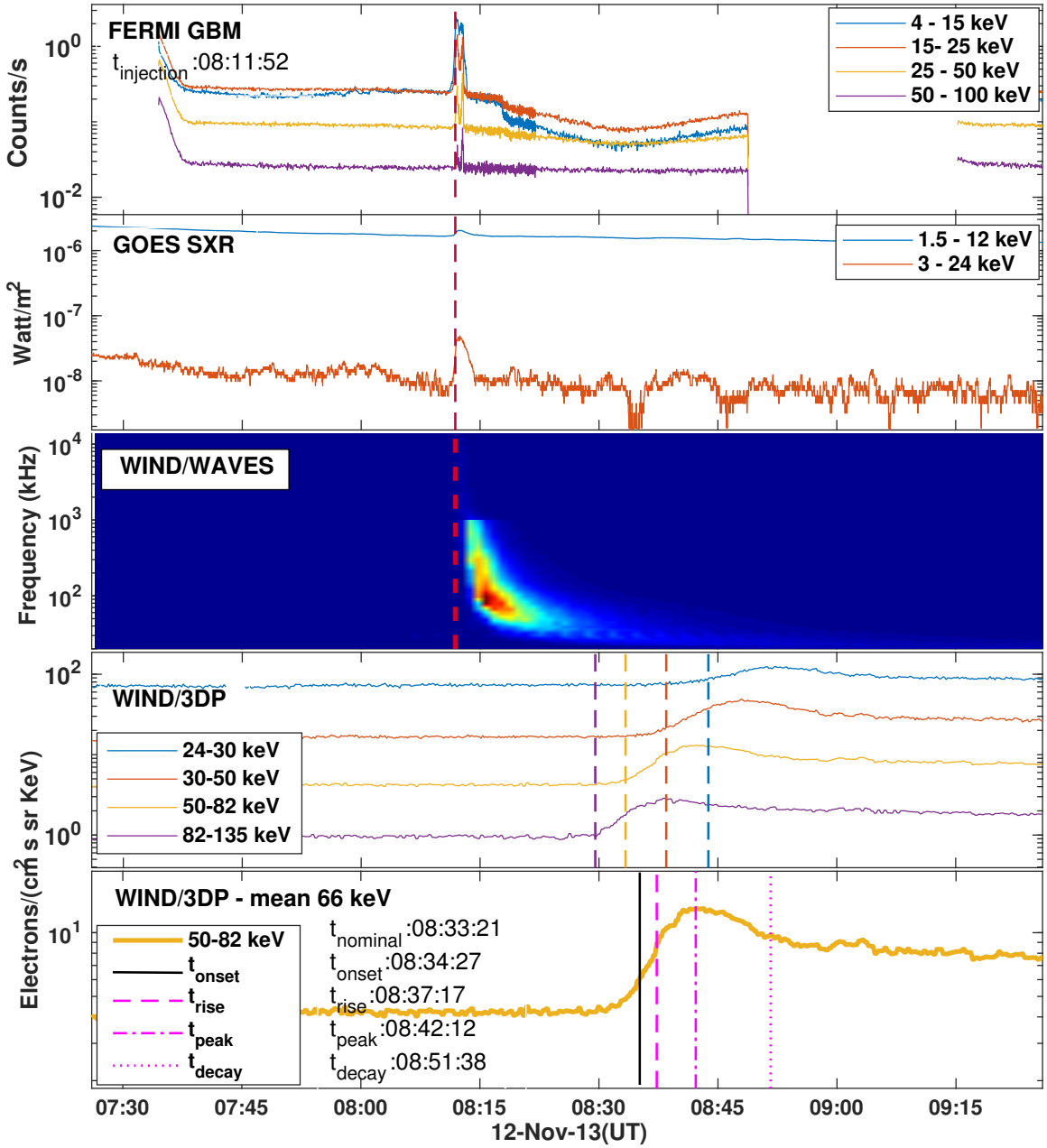
FERMI GBM
t injection :08:11:52
4 - 15 keV
15- 25 keV
25 - 50 keV
50 - 100 keV
Counts/s
GOES SXR
1.5 - 12 keV
3 - 24 keV
Watt/m2
WIND/WAVES
Frequency (kHz)
WIND/3DP
24-30 keV
30-50 keV
50-82 keV
82-135 keV
WIND/3DP - mean 66 keV
50-82 keV
t onset
t rise
t peak
t decay
t nominal :08:33:21
t onset :08:34:27
t rise :08:37:17
t peak :08:42:12
t decay :08:51:38
Electrons/(cm2 s sr KeV)
07:30
07:45
08:00
08:15
08:30
08:45
09:00
09:15
12-Nov-13(UT)

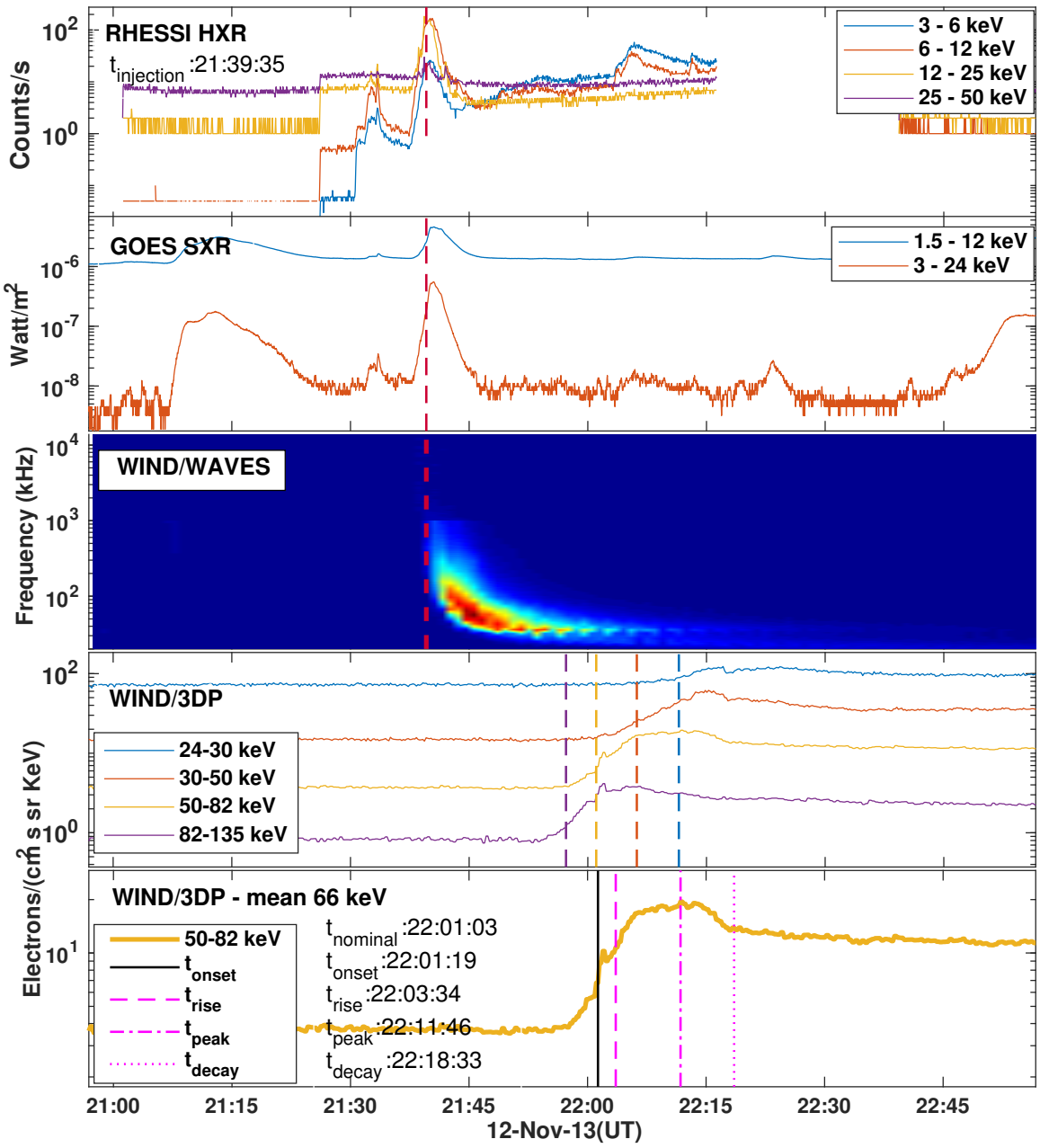
RHESSI HXR
t injection :21:39:35
3 - 6 keV
6 - 12 keV
12 - 25 keV
25 - 50 keV
Counts/s
GOES SXR
1.5 - 12 keV
3 - 24 keV
Watt/m2
WIND/WAVES
Frequency (kHz)
WIND/3DP
24-30 keV
30-50 keV
50-82 keV
82-135 keV
Electrons/(cm2 s sr KeV)
WIND/3DP - mean 66 keV
50-82 keV
t onset
t rise
t peak
t decay
t nominal :22:01:03
t onset :22:01:19
t rise :22:03:34
t peak :22:11:46
t decay :22:18:33
21:00
21:15
21:30
21:45
22:00
22:15
22:30
22:45
12-Nov-13(UT)

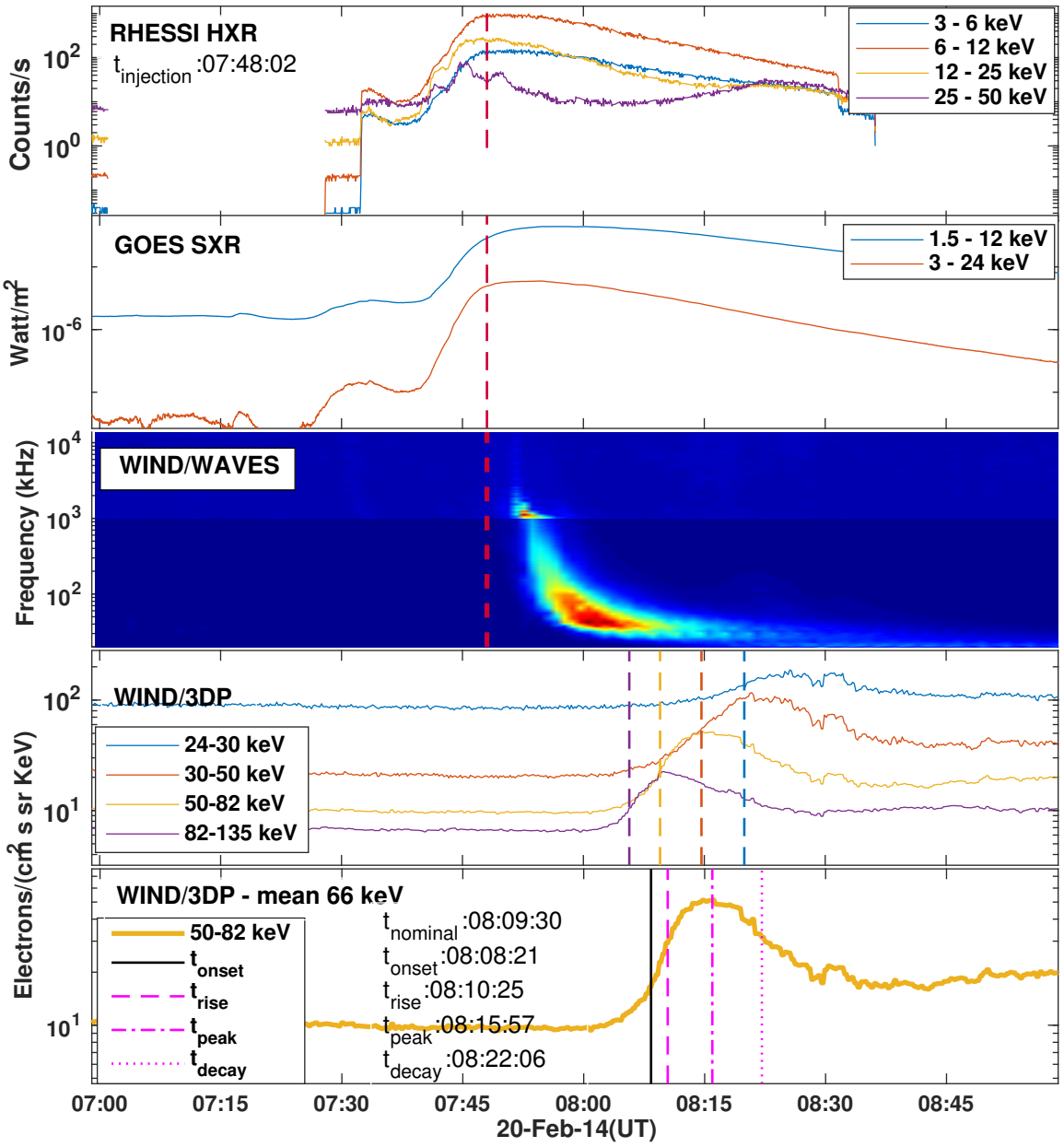
RHESSI HXR
t injection :07:48:02
3 - 6 keV
6 - 12 keV
12 - 25 keV
25 - 50 keV
Counts/s
GOES SXR
1.5 - 12 keV
3 - 24 keV
Watt/m2
WIND/WAVES
Frequency (kHz)
WIND/3DP
24-30 keV
30-50 keV
50-82 keV
82-135 keV
Electrons/(cm2 s sr KeV)
WIND/3DP - mean 66 keV
50-82 keV
t onset
t rise
t peak
t decay
t nominal :08:09:30
t onset :08:08:21
t rise :08:10:25
t peak :08:15:57
t decay :08:22:06
07:00
07:15
07:30
07:45
08:00
08:15
08:30
08:45
20-Feb-14(UT)

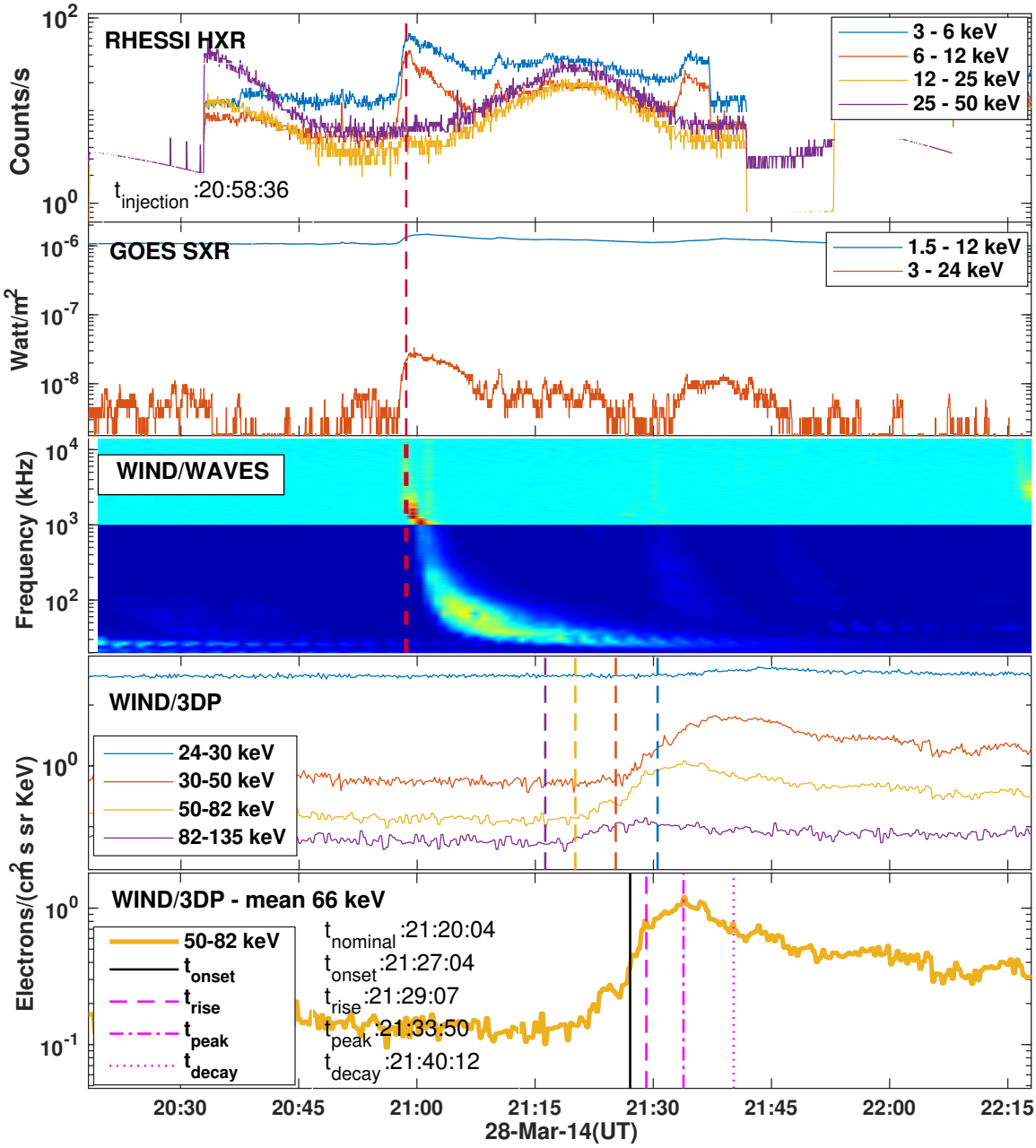
RHESSI HXR
Counts/s
3 - 6 keV
6 - 12 keV
12 - 25 keV
25 - 50 keV
t injection :20:58:36
GOES SXR
Watt/m2
1.5 - 12 keV
3 - 24 keV
WIND/WAVES
Frequency (kHz)
WIND/3DP
24-30 keV
30-50 keV
50-82 keV
82-135 keV
Electrons/(cm2 s sr KeV)
WIND/3DP - mean 66 keV
50-82 keV
t onset
t rise
t peak
t decay
t nominal :21:20:04
t onset :21:27:04
t rise :21:29:07
t peak :21:33:50
t decay :21:40:12
20:30
20:45
21:00
21:15
21:30
21:45
22:00
22:15
28-Mar-14(UT)

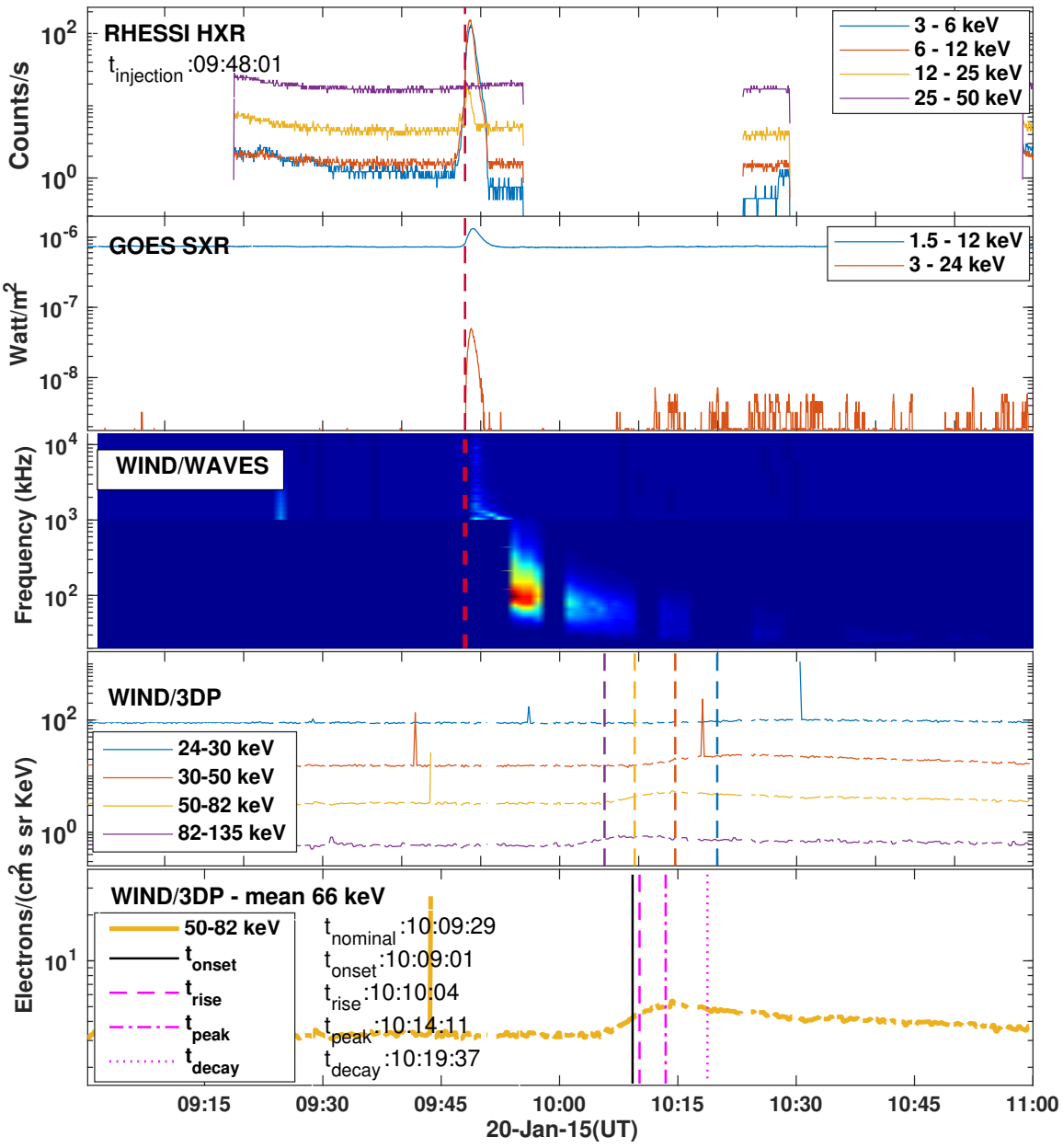
RHESSI HXR
t injection :09:48:01
3 - 6 keV
6 - 12 keV
12 - 25 keV
25 - 50 keV
Counts/s
GOES SXR
1.5 - 12 keV
3 - 24 keV
Watt/m2
WIND/WAVES
Frequency (kHz)
WIND/3DP
24-30 keV
30-50 keV
50-82 keV
82-135 keV
Electrons/(cm2 s sr KeV)
WIND/3DP - mean 66 keV
50-82 keV
t onset
t rise
t peak
t decay
t nominal :10:09:29
t onset :10:09:01
t rise :10:10:04
t peak :10:14:11
t decay :10:19:37
09:15
09:30
09:45
10:00
10:15
10:30
10:45
11:00
20-Jan-15(UT)

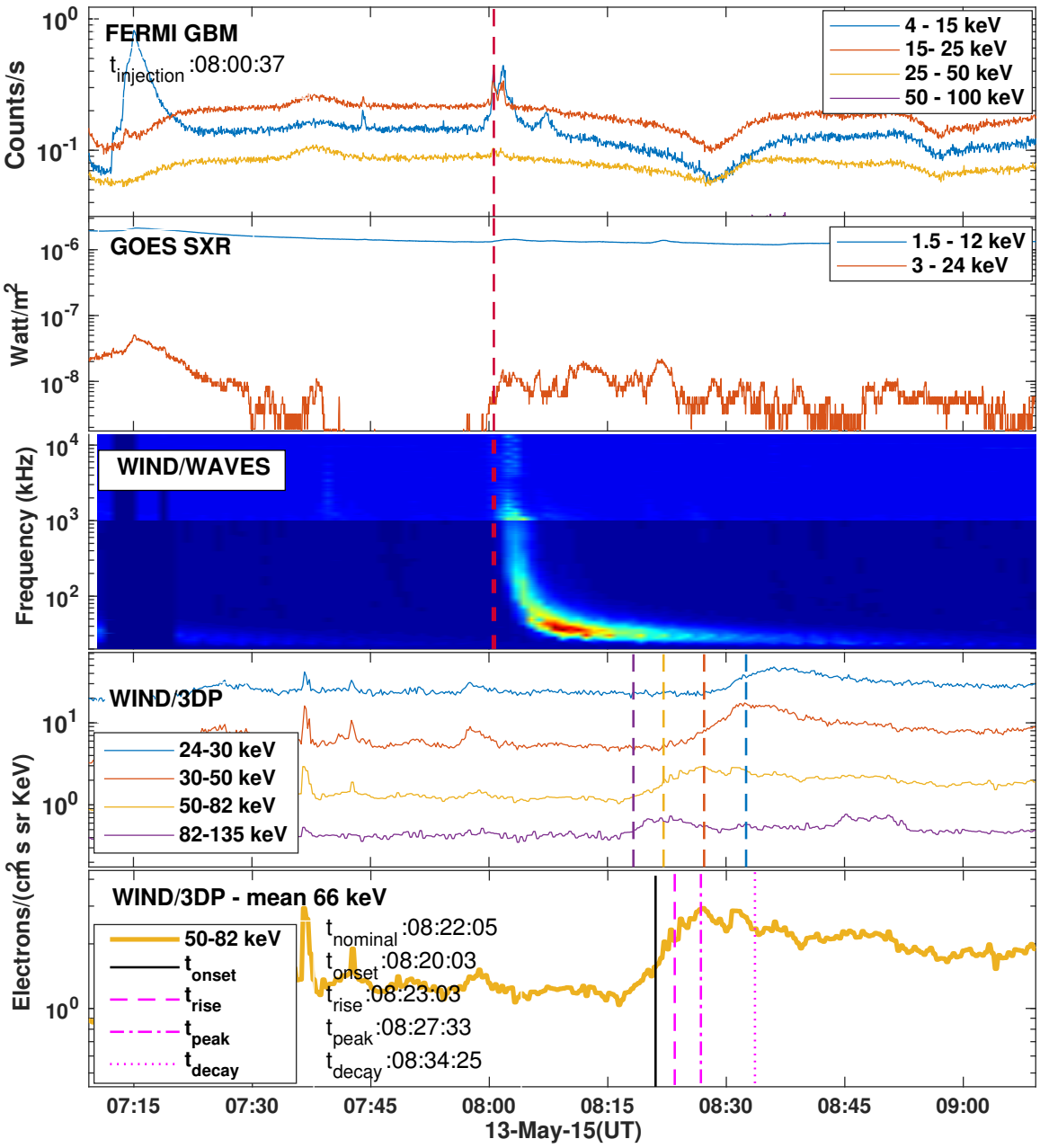
FERMI GBM
t injection :08:00:37
4 - 15 keV
15- 25 keV
25 - 50 keV
50 - 100 keV
Counts/s
GOES SXR
1.5 - 12 keV
3 - 24 keV
Watt/m2
WIND/WAVES
Frequency (kHz)
WIND/3DP
24-30 keV
30-50 keV
50-82 keV
82-135 keV
WIND/3DP - mean 66 keV
50-82 keV
t onset
t rise
t peak
t decay
t nominal :08:22:05
t onset :08:20:03
t rise :08:23:03
t peak :08:27:33
t decay :08:34:25
Electrons/(cm2 s sr KeV)
07:15
07:30
07:45
08:00
08:15
08:30
08:45
09:00
13-May-15(UT)

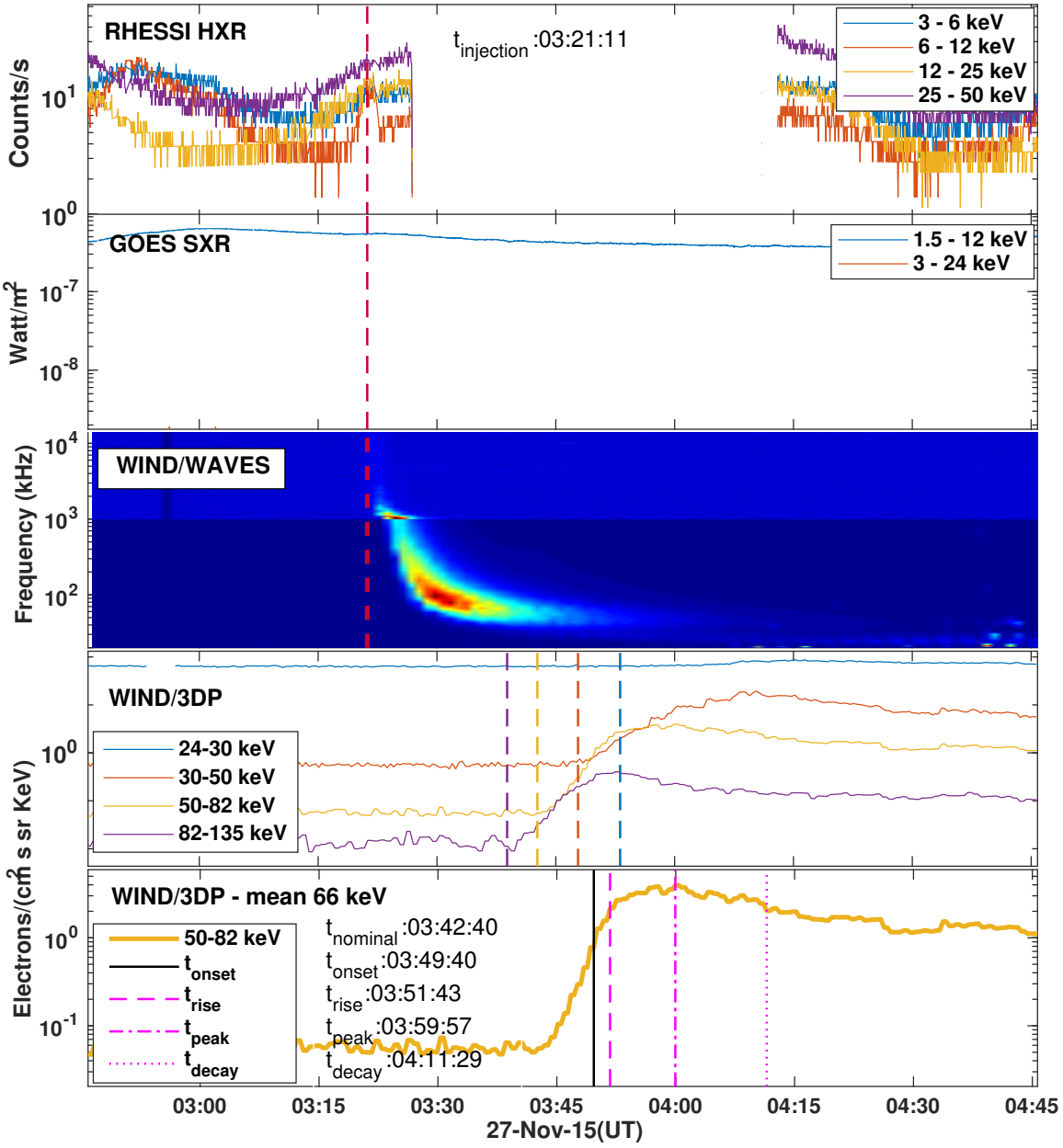
RHESSI HXR
t_injection :03:21:11
3 - 6 keV
6 - 12 keV
12 - 25 keV
25 - 50 keV
Counts/s
GOES SXR
1.5 - 12 keV
3 - 24 keV
Watt/m²
WIND/WAVES
Frequency (kHz)
WIND/3DP
24-30 keV
30-50 keV
50-82 keV
82-135 keV
WIND/3DP - mean 66 keV
50-82 keV
t_onset
t_rise
t_peak
t_decay
t_nominal :03:42:40
t_onset :03:49:40
t_rise :03:51:43
t_peak :03:59:57
t_decay :04:11:29
Electrons/(cm² s sr KeV)
03:00
03:15
03:30
03:45
04:00
04:15
04:30
04:45
27-Nov-15(UT)

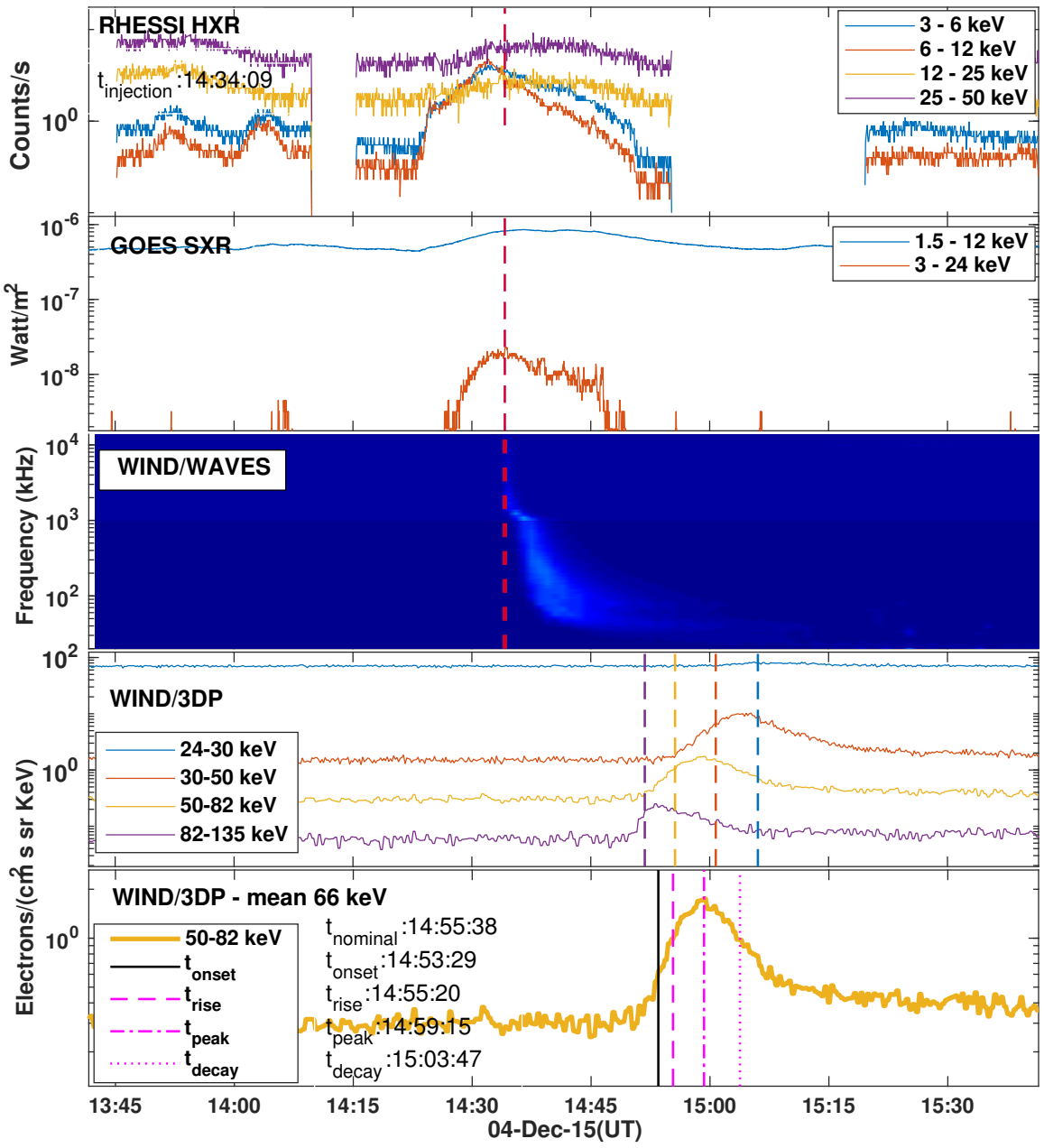
RHESSI HXR
t injection :14:34:09
3 - 6 keV
6 - 12 keV
12 - 25 keV
25 - 50 keV
Counts/s
GOES SXR
1.5 - 12 keV
3 - 24 keV
Watt/m2
WIND/WAVES
Frequency (kHz)
WIND/3DP
24-30 keV
30-50 keV
50-82 keV
82-135 keV
Electrons/(cm2 s sr KeV)
WIND/3DP - mean 66 keV
50-82 keV
t onset
t rise
t peak
t decay
t nominal :14:55:38
t onset :14:53:29
t rise :14:55:20
t peak :14:59:15
t decay :15:03:47
13:45
14:00
14:15
14:30
14:45
15:00
15:15
15:30
04-Dec-15(UT)

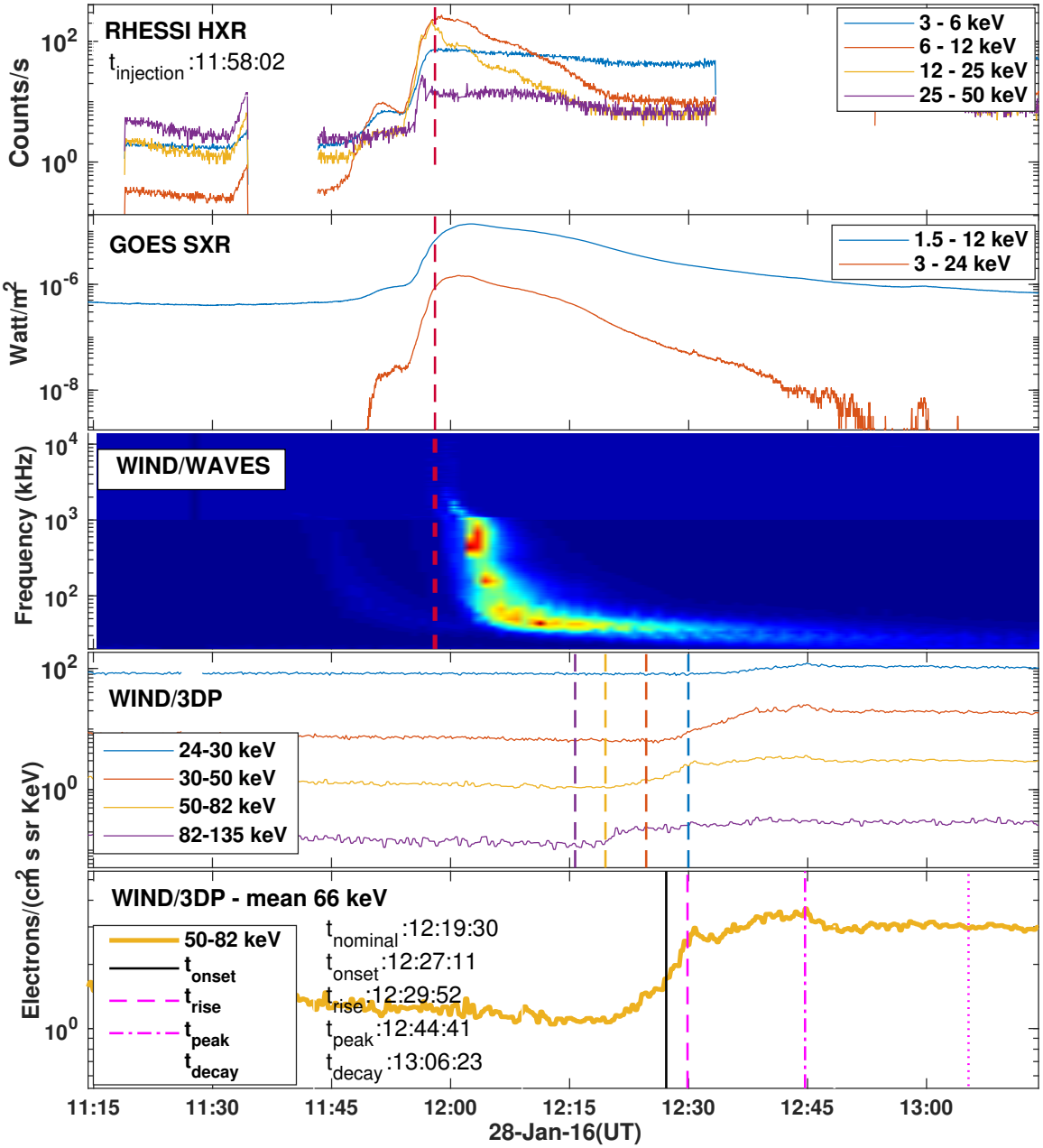
RHESSI HXR
t_injection :11:58:02
Counts/s
3 - 6 keV
6 - 12 keV
12 - 25 keV
25 - 50 keV
GOES SXR
Watt/m2
1.5 - 12 keV
3 - 24 keV
WIND/WAVES
Frequency (kHz)
WIND/3DP
24-30 keV
30-50 keV
50-82 keV
82-135 keV
WIND/3DP - mean 66 keV
Electrons/(cm2 s sr KeV)
50-82 keV
t_onset
t_rise
t_peak
t_decay
t_nominal :12:19:30
t_onset :12:27:11
t_rise :12:29:52
t_peak :12:44:41
t_decay :13:06:23
11:15
11:30
11:45
12:00
12:15
12:30
12:45
13:00
28-Jan-16(UT)

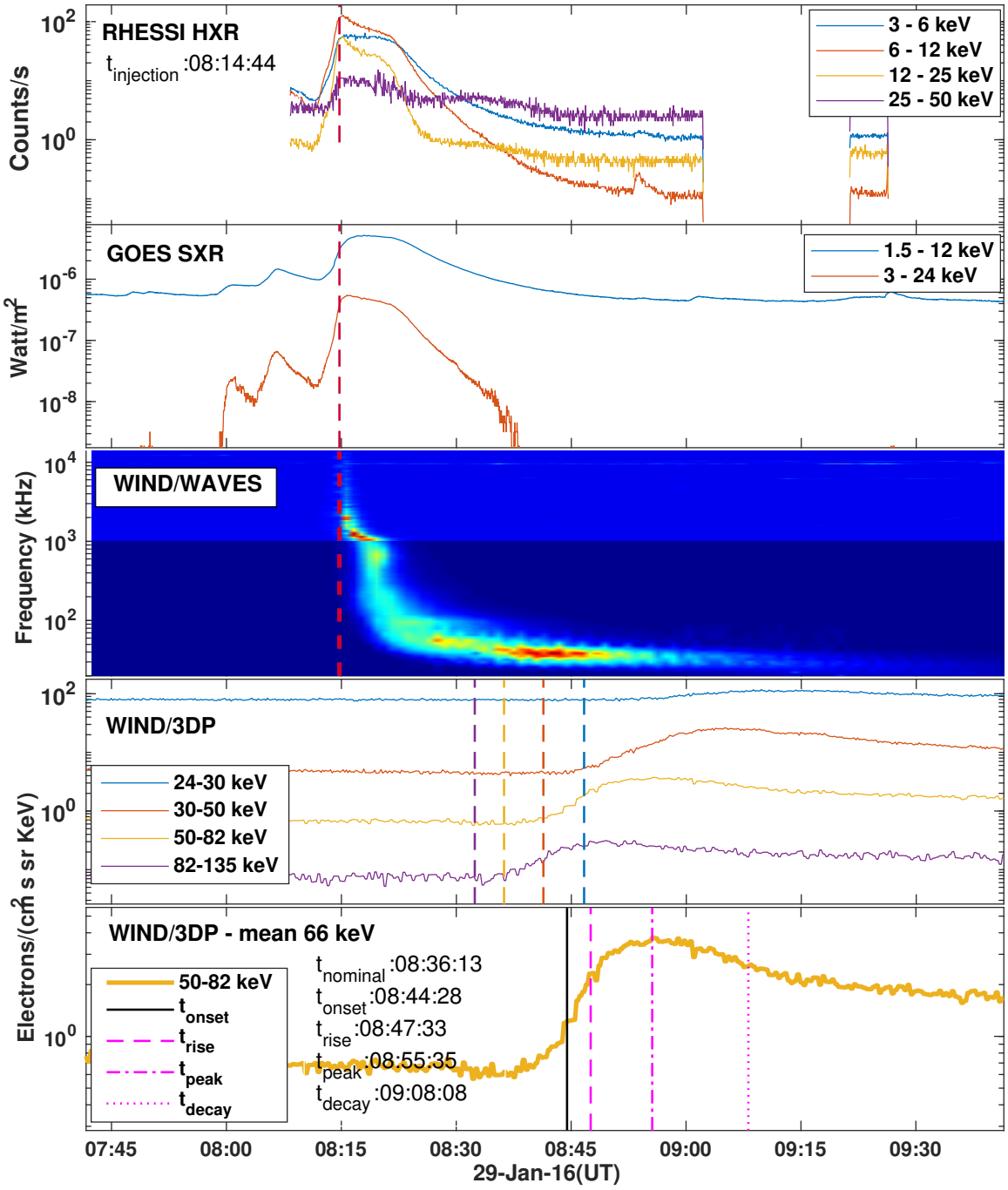
RHESSI HXR
t injection :08:14:44
3 - 6 keV
6 - 12 keV
12 - 25 keV
25 - 50 keV
Counts/s
GOES SXR
1.5 - 12 keV
3 - 24 keV
Watt/m2
WIND/WAVES
Frequency (kHz)
WIND/3DP
24-30 keV
30-50 keV
50-82 keV
82-135 keV
Electrons/(cm2 s sr KeV)
WIND/3DP - mean 66 keV
50-82 keV
t onset
t rise
t peak
t decay
t nominal :08:36:13
t onset :08:44:28
t rise :08:47:33
t peak :08:55:35
t decay :09:08:08
07:45
08:00
08:15
08:30
08:45
09:00
09:15
09:30
29-Jan-16(UT)

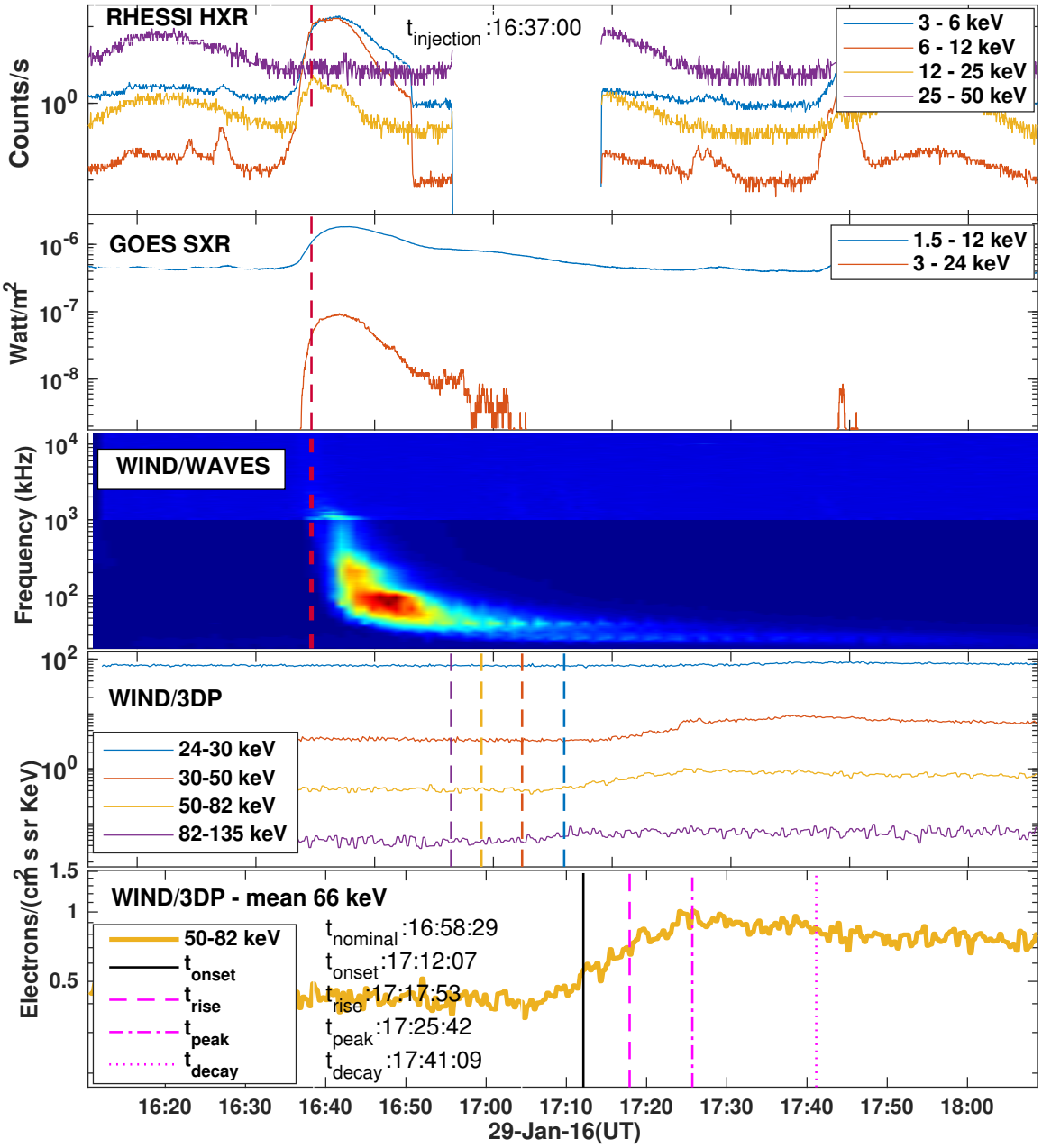
RHESSI HXR
t_injection :16:37:00
3 - 6 keV
6 - 12 keV
12 - 25 keV
25 - 50 keV
Counts/s
GOES SXR
1.5 - 12 keV
3 - 24 keV
Watt/m2
WIND/WAVES
Frequency (kHz)
WIND/3DP
24-30 keV
30-50 keV
50-82 keV
82-135 keV
Electrons/(cm2 s sr KeV)
WIND/3DP - mean 66 keV
50-82 keV
t_onset
t_rise
t_peak
t_decay
t_nominal :16:58:29
t_onset :17:12:07
t_rise :17:17:53
t_peak :17:25:42
t_decay :17:41:09
16:20
16:30
16:40
16:50
17:00
17:10
17:20
17:30
17:40
17:50
18:00
29-Jan-16(UT)

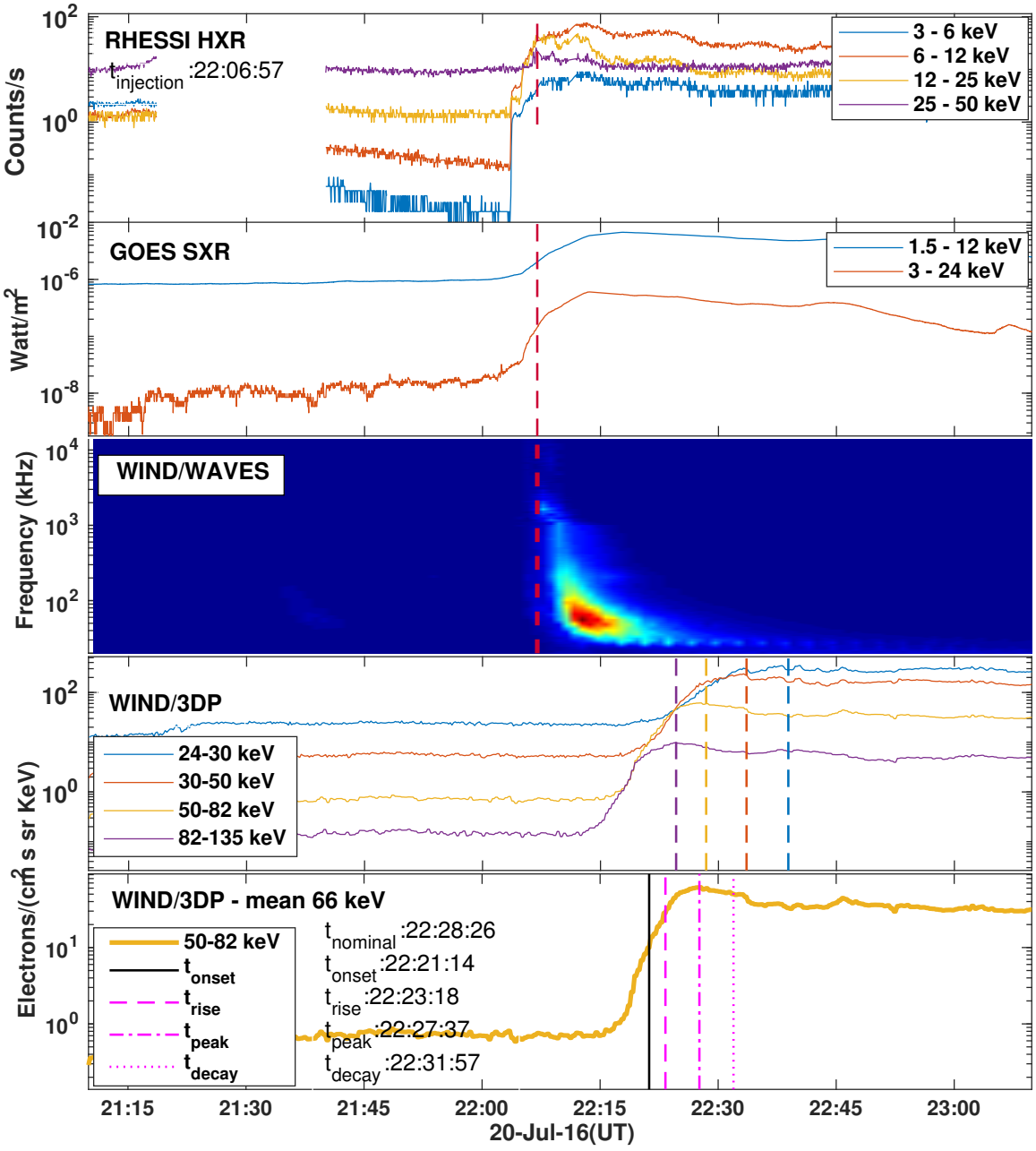
RHESSI HXR
t injection :22:06:57
3 - 6 keV
6 - 12 keV
12 - 25 keV
25 - 50 keV
Counts/s
GOES SXR
1.5 - 12 keV
3 - 24 keV
Watt/m2
WIND/WAVES
Frequency (kHz)
WIND/3DP
24-30 keV
30-50 keV
50-82 keV
82-135 keV
WIND/3DP - mean 66 keV
50-82 keV
t onset
t rise
t peak
t decay
t nominal :22:28:26
t onset :22:21:14
t rise :22:23:18
t peak :22:27:37
t decay :22:31:57
Electrons/(cm2 s sr KeV)
21:15
21:30
21:45
22:00
22:15
22:30
22:45
23:00
20-Jul-16(UT)

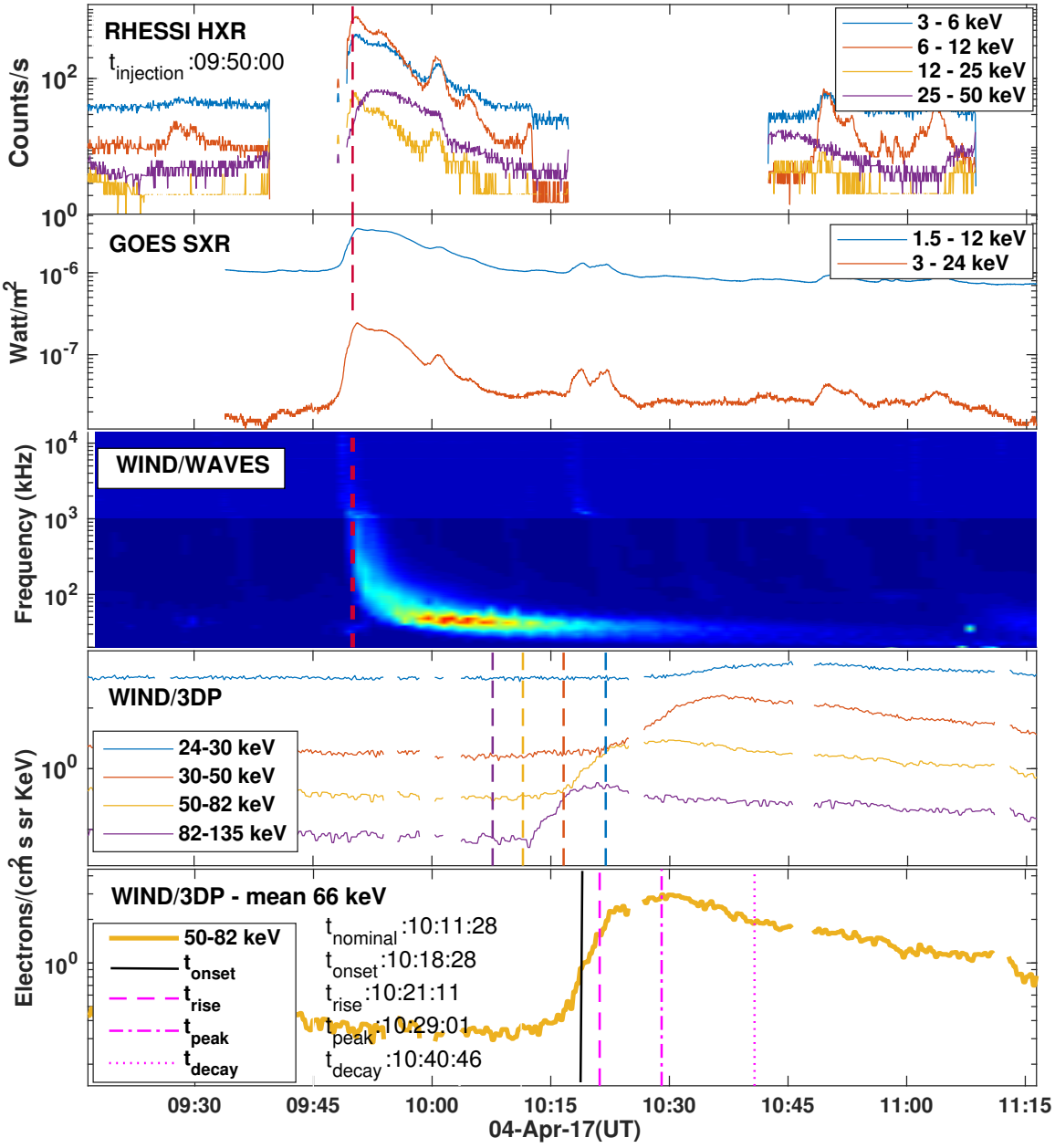
RHESSI HXR
t_injection :09:50:00
Counts/s
3 - 6 keV
6 - 12 keV
12 - 25 keV
25 - 50 keV
GOES SXR
Watt/m2
1.5 - 12 keV
3 - 24 keV
WIND/WAVES
Frequency (kHz)
WIND/3DP
24-30 keV
30-50 keV
50-82 keV
82-135 keV
Electrons/(cm2 s sr KeV)
WIND/3DP - mean 66 keV
50-82 keV
t_onset
t_rise
t_peak
t_decay
t_nominal :10:11:28
t_onset :10:18:28
t_rise :10:21:11
t_peak :10:29:01
t_decay :10:40:46
09:30
09:45
10:00
10:15
10:30
10:45
11:00
11:15
04-Apr-17(UT)

Chapter 5

Summary and Future work

5.1 Summary

The motivation for this thesis was to understand the role particle acceleration plays in the heating of the solar corona and how the accelerated particles released into the interplanetary medium (SEPs) might get affected by transport effects. Understanding the transport effects on the SEPs is important to decouple source acceleration effects and to answer the critical question - 'Does the SEP population of electron and the HXR electrons come from the same parent population?'.

Chapter 2 investigates small electron acceleration episodes in the solar corona with no temporal and spatial correspondence to big flares or CMEs, with the aim of understanding particle acceleration characteristics. The emphasis on small events is important since coronal heating is thought to be mostly due to small energy release events(microflares and nanoflares) as bigger events are far and few. Using spectral analysis of HXR producing electrons and the electrons detected near 1 AU we estimated the number of electrons and the energy in electrons in the solar corona and at 1AU. We found that the number of escaping electrons(N_{esc}) can be comparable in number to electrons producing HXR emission(N_{hxr}).We find that the ratio between these two quantities(N_{esc}/N_{hxr}) is much higher compared to larger flares. In Chapter 3 we studied type I noise storm bursts using the high temporal resolution data from NRH. Type I bursts might be one of the most direct signatures of the non-thermal electrons that are present in the solar corona. Our goal was to estimate the energetics of these bursts using a model-independent generic second-order Fermi acceleration mechanism, developed by Subramanian and Becker (2004). An earlier study had done imaging analysis on the same noise storms used in our study and achieved the most resolved imaging of type I noise storms (Mercier et al., 2015). This enabled us to get accurate source size information. We showed that the energy contained in these individual noise storm burst is of the order of $10^{21} - 10^{24}$

ergs s^{-1}. Chapter 4 concerns about the effects of transport on SEP particles. Using data from HXR observations and in-situ SEP measurements, we intended to test whether the HXR producing electrons has any correlation with the electrons later detected at 1AU. This is an important question, which can give clues into particle acceleration in solar flares of which little is understood. We compared the characteristics of the detected SEPs with the source characteristics such as location, spectral analysis, and interplanetary magnetic field conditions.

5.2 Future Work

5.2.1 Investigating deviations from standard flare model

The standard model of flare(also known as CSHKP model) describes the temporal evolution of an eruptive flare. Magnetic reconnection happens higher in the corona. This marks the impulsive phase of flare where the accelerated particles stream down through the denser chromosphere indicated by the sharp rise in HXR intensity. Modulations in HXR flux up-to 90% is also observed. Around this time the radio spectrum shows the appearance of coronal type III bursts which signify particles streaming through the corona from the acceleration site. If the particles get access to open magnetic field lines the type III bursts are observed in kHz range as well. As the non-thermal electrons mostly deposit their energy in the chromospheric foot-points, they heat the surrounding plasma. This forces the plasma along the magnetic loops, which ultimately cools down emitting thermal bremsstrahlung(SXR). This is reflected in the Neupert effect, where the time integral of the non-thermal emission matches the evolution of SXR emission (Benz, 2017; Fletcher et al., 2011).

In Chapter 2 we studied events which showed this eruptive flaring phase but did not have any associations with CMEs or big flares. We note that some of these events show deviations from these standard flare model sequence of temporal evolution. Four events(26 June,27 June and two events on 25 December 2004) show very little enhancement of SXR flux. Also, the two events that occurred on 25 December does not demonstrate the Neupert effect. The acceleration of particles in the solar flare is not very well understood. It has been observed that the number of electrons required to produce the observed HXR emission required the participation of most of the electrons present at the acceleration site. However, we are not aware of any acceleration mechanisms that could efficiently accelerate these many numbers of electrons. This is known as the number problem (Aschwanden et al., 2002). An often hypothesized solution is one in which there is a constant influx of electrons to replace the accelerated electrons which results in the modulation of the observed HXR flux. We

do not see such kind of modulation in any of our events. This signifies that detailed 3D radiative MHD simulations, that can self-consistently give observable signatures due these small magnetic perturbations are needed.

Most of the energy content generated in the flare is radiated away in the EUV wavelengths. In our study, we have only used Hard X-ray and radio data. To better understand the dynamics of these events, it is important to do imaging studies in multiple wavelengths. Curiously all of our events happened in the year 2004. The only imaging telescope available for that time period is the Extreme ultraviolet Imaging Telescope(EIT) aboard SOHO. In a future study, we intend to use EUV wavelength data as well as search for events that occurred in the SDO era(post-2010) to enable such analysis. Also with focusing HXR instruments such as FOXSI and Nu-STAR, more sensitive observations of such small events highlighted in our study is possible and this might throw more light into the physics powering their particle acceleration.

5.2.2 Survey of Type I noise storms

Type I noise storms as described in Chapter 3 are examples of small electron acceleration episodes in the solar corona. In the chapter, we studied four events specifically because of the availability of both high spatial and temporal information about them. Our results show that the energy output of a typical burst is around $10^{21} - 10^{24}$ $ergs\ s^{-1}$. This closely resembles the energy output of nanoflares. This suggests a more comprehensive statistical study of such events is a necessity. One major factor impending such studies is lack of instruments which could simultaneously image the noise storm at high spatial resolution and then record the spectra at high temporal and frequency resolution.

LOFAR4SW is an upcoming international project making use of the unique capabilities of LOFAR telescope (van Haarlem et al., 2013). LOFAR4SW will design and upgrade both the hardware and software to use LOFAR for cutting edge space weather science. One of the stated scientific goals of LOFAR4SW is to acquire full solar Stokes dynamic spectra in the frequency range 10-300 Mhz with a time resolution of 0.01 s and frequency resolution of 5 kHz. This is an order of magnitude upgrade over NRH facility, whose data that we used in Chapter 3. LOFAR4SW will also be able to provide full disk solar imaging across a frequency range of 10-300 Mhz with a time resolution of 0.01 s and spatial resolution <30 arcsec. For comparison, the smallest core size attained using the combined observations of GMRT and NRH was 31 arcsec. LOFAR4SW is scheduled to start observing campaign in 2020. A detailed survey of type I noise storms will be greatly benefited by the availability of this data.

5.2.3 Simulation of SEP transport

We characterized the SEPs using their arrival times and their time-intensity profile shape. The arrival times were calculated by estimating the difference in arrival times in comparison to the nominal Parker spiral length during the time of transport. To quantify the shape of the time-intensity profile, we defined a quantity known as the symmetricity ratio, which is the ratio of the rising time difference and decay time difference in reference to the peak time. Since all our events showed near-simultaneous onset of HXR and type III signatures, we have ruled out the possibility of delayed injection. Then the question beckon as to what processes during the transport phase delays the arrival of particles at 1AU. One popular model, to study the interplanetary transport of electrons is the focused transport model with pitch angle scattering. We briefly mention the model below.

SEP particles experience near collisionless travel through the interplanetary space. The collisions between SEP particles and particles constituting the Solar wind is also far and few. The SEP particles stream along the interplanetary magnetic field(IMF) as described in Chapter 4. The IMF field can be modelled as an Archimedean spiral(Parker, 1958) with a smooth average field component which has turbulent fluctuations overlayed on top of it. However due to sparsity of observations and the length scale involved, it is impossible to completely map the trajectories of energetic particles from the Sun to the observation point. The quantity measured by the particle detectors onboard space instruments is the intensity of charged particles as a function of time, energy and direction of incidence (generally related to the local direction of the magnetic field) in a given point of the heliosphere where the spacecraft is located. We aim to understand how transport along IMF affects the solar energetic particles and quantify how the transport phase results in the delay of particle arrival at 1AU. Below we present some preliminary results from our studies which point to possible directions to probe to understand transport effects on SEPs.

The motion along the IMF can be separated into two parts - the motion of the guiding centre of the particle orbit and the gyration of the particle around it. In the scatter free transport conditions as assumed, the gyratory motion of the particles along the smooth IMF field line gets averaged out. Thus the motion of the guiding centre represents the translational motion of the particle along the IMF averaged over many gyrations. The turbulent fluctuations along the IMF result in the particle undergoing pitch angle scattering. The particle pitch-angle cosine, μ, is defined as the cosine of the angle made between the particle velocity and the magnetic field vector; it is given by

$$\mu = \hat{B}.\hat{v} \tag{5.1}$$

The focussed transport equation which describes particle propagation along the field line with is given by (Roelof, 1969):

$$\frac{\partial f}{\partial t} + v\mu\frac{\partial f}{\partial x} + \frac{v(1-\mu^2)}{2L_z}\frac{\partial f}{\partial \mu} = \frac{\partial}{\partial \mu}\left[D_{\mu\mu}\frac{\partial f}{\partial \mu}\right] \tag{5.2}$$

where $f = f(v,\mu,z,t)$ is the electron phase space density (or 'distribution function'), and t and v are time and electron velocity, respectively. The distance along the field line is given by z, and the cosine of the electron's pitch angle is given by μ.

In the above equation, the second term on the left-hand side describes the advective motion of particles along the magnetic field lines, the third term on the left-hand side describes the focusing of particles as the magnetic field strength scale off and the term on the right-hand side accounts for the effect of magnetic fluctuations which results in pitch angle scattering of particles. The particle speed, v, remains constant in this model, in which the magnetic field is assumed to be static. The focussing effect results in the collimation of the particles as it nears 1 AU. The focussing term in the above equation takes care of this. It is assumed that the interplanetary magnetic fields decrease as $B(z) \propto z^{-2}$. The length scale over which this change occurs is given by:

$$L(z) = \frac{-B(z)}{(dB/dz)} = \frac{z}{2} \tag{5.3}$$

We assume a pitch-angle dependent scattering model, with minimum at $\mu = 0$ (Jokipii, 1966).The power spectrum of fluctuations is represented by a powerlaw of the form:

$$P(k) \propto k^{-q} \tag{5.4}$$

where k is the wavenumber parallel to the magnetic field and q is the spectral slope of the magnetic field power spectrum, then the pitch angle diffusion coefficient is of the form

$$D_{\mu\mu} = \frac{\nu}{2}(1-\mu^2) \tag{5.5}$$

where ν is the scattering frequency, with the form,

$$\nu(\mu) = \nu_o|\mu|^{q-1} \tag{5.6}$$

with $\nu_o = 6v/[2\lambda_{||}(4-q)(2-q)]$, where v is the velocity of the particles and $\lambda_{||}$ is the mean free path along the magnetic field line. The scattering is isotropic or in other words the strength of the scattering is independent of the pitch-angle of the particles when q=1. Then

Eq5.5 becomes,

$$D_{\mu\mu} = \frac{1}{2}\frac{v}{\lambda_{||}}(1-\mu^2) \tag{5.7}$$

We take the mean free path with an added dependence on electron's position from the sun and electron's velocity.

$$\lambda_{||}(z) = \lambda_o\left(\frac{z_+ - z}{z_o}\right)^{\alpha}\left(\frac{v}{v_o}\right)^{\eta} \tag{5.8}$$

Here λ_o is the mean free path of the electrons near the earth, and z_o is the location point of the satellite in units of AU. α is a parameter chosen to give the best fit to the observed data. v_o is the velocity of the lowest energetic particles corresponding to 27 KeV. η is the parameter chosen such that the simulations match the observations.

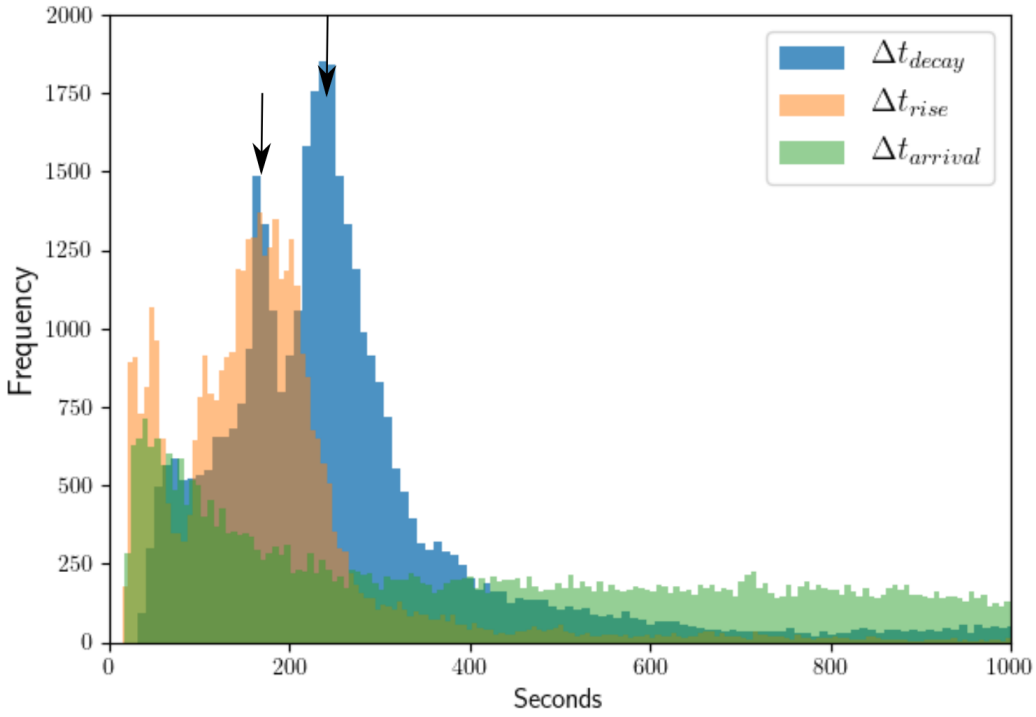

Fig. 5.1 Figure shows the histograms plot of the three quantities $\Delta t_{arrival}$,Δt_{rise},Δt_{decay} for the simulated lightcurves. The Δt_{decay} shows two peaks indicating that the simulation was successful in capturing the symmetric and long tail nature of the SEPs. This figure might be compared with Fig4.5 which shows the same quantity for real SEPs. The green histogram shows $\Delta t_{arrival}$ times. We see a distribution with long uniform tail suggesting that the simulation is capable of producing different delay times solely via pitch angle scattering. The first peak corresponds to scenarios where the parameters didn't cause any scattering.

Using the methods derived by Gardiner (1985) and used by MacKinnon and Craig (1991); Dröge et al. (2014), the transport equation can be transformed into equivalent stochastic differential equations which can be iteratively solved in a Monte-Carlo setting to determinie the evolution of a pseudo particle's position and pitch angle at each time step:

$$z_{i+1} = z_i + \mu_i v \Delta t \tag{5.9}$$

$$\mu_{i+1} = \mu_i + \left(\frac{dD_{\mu\mu,i}}{d\mu} + \frac{v(1-\mu_i^2)}{2L_{z,i}} \right) \Delta t + \sqrt{2D_{\mu\mu,i}\Delta t}\,\xi \tag{5.10}$$

Substituting for $D_{\mu\mu,i}$ from eq5.5, we get,

$$\mu_{i+1} = \mu_i - \mu_i f_s \Delta t + (1-\mu_i^2)\frac{v}{(z_i/2)}\Delta t + \sqrt{(1-\mu_i^2) f_s \Delta t}\,\xi \tag{5.11}$$

Here $f_s = v/\lambda_{||}$.The subscript i denotes the simulation time-step, and $\xi \in$ N(0, 1) represents a random variable drawn from a normally distributed pool of mean 0, and variance 1.

There are five free parameters in our simulation- viz, 1) the mean free path of the electrons near Earth, λ_0 2) the power-law index of spatial coordinates, α 3) the power-law index of velocity term, η 4) the bias term added to the coordinates,z_+ and 5) the magnetic fluctuation power-law index, q. We initiated Monte-Carlo simulation runs with varying values of these parameters. The parameter values where updates in a grid search manner, with λ_0 values between [0.015,1.2] AU , α values between [0.05,2.2], η values between [0.0,2.5] and q values between [1.01,1.9]. For z_+ we chose [2.5e13,5.5e13,7.5e13,9.5e13]. The total number of independent simulations that resulted out of this process $\sim$ 21000. Similar to observed SEP events, as described in Chapter 4, we characterize the simulated SEP time-intensity profile using the three quantities - $\Delta t_{arrival}$,Δt_{rise},Δt_{decay}. A histogram plot of Δt_{rise} and Δt_{decay} and their ratio, is plotted in Fig5.1. Of all the five free parameters in our model, we found the magnetic fluctuation powerlaw index q to be the most sensitive in affecting the shape of the time-intensity profile of the simulated SEPs.This is shown in Fig5.2.

We see a very sensitive dependence on the parameter q, regarding the overall SEP time-intensity profile characteristics. Two bands corresponding to q=1.0 (blue markers) and q>1.1 (red markers) is filled by a small variation of q>1.0 and q<1.1.

As a future extension of our work, we would like to infer the injection histories of the detected SEPs by fitting with our simulated model lightcurves. Propagation of SEP particles is influenced both by the source acceleration characteristics and the turbulent magnetic field affecting its transport. The Monte-Carlo method we have used enables us to track the time history of all the individual test particles. Using this information, we can quantify

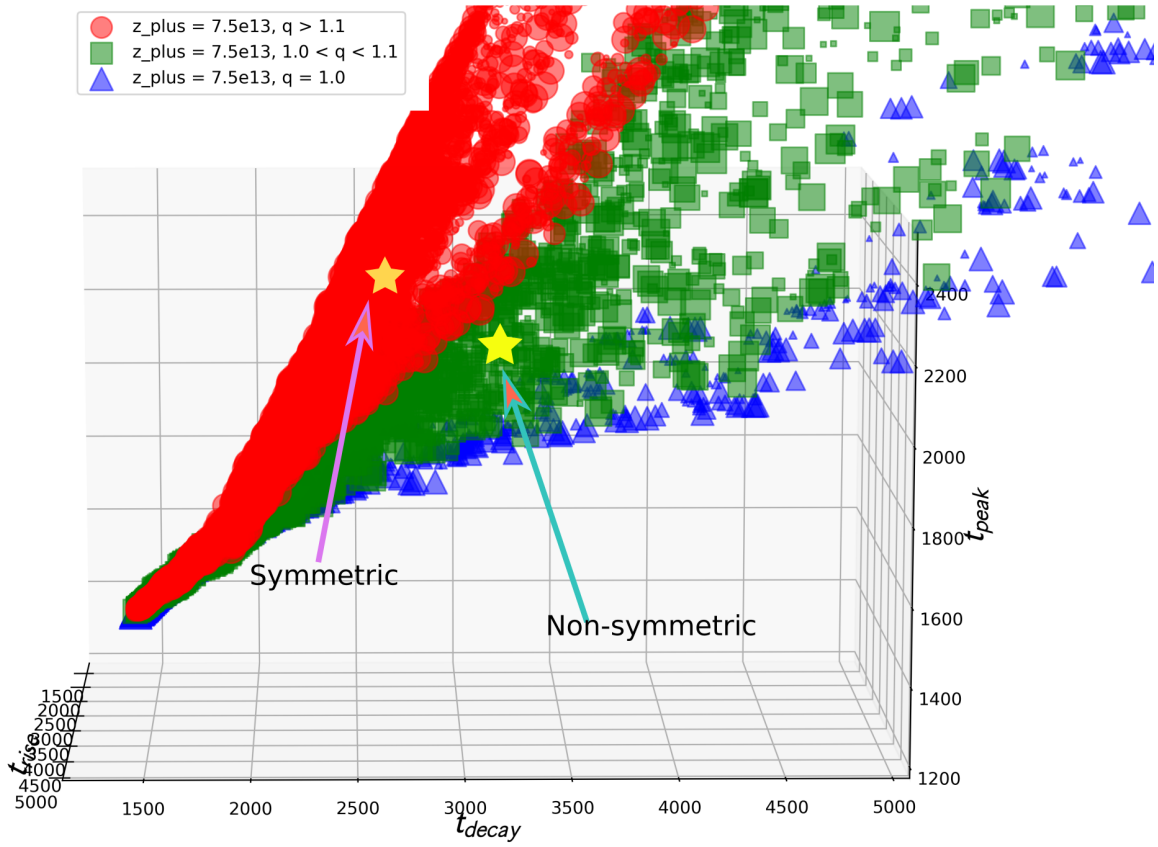

Fig. 5.2 3D scatterplot of the the three quantities t_{rise},t_{peak} and t_{decay}. In this figure, we have fixed the free parameter z_+=7.5e13, while all the other parameters are allowed to vary. The three coloured markers correspond to the different ranges of q.The red circles represent q>1.1, the green squares represent q between range [1.0,1.1]. The blue triangles represent the isotropic regime of q=1.0. The two yellow stars correspond the averaged case of symmetric and non-symmetric SEPs (thick black line in Fig 4.6). Thus the simulation is able to simulate both symmetric and non-symmetric SEP lightcurves.

the angular distribution of the particles (PADs)in reference to the alignment of the local magnetic field. At the simulation stage, no prior assumption about the source,Q, is assumed. We inject a delta distribution of test particles, corresponding to mean energy of 3DP SST detectors and the response of the transport process on it is observed near Earth. To deduct the injection profile and match it with the observed SEP near the spacecraft, we will employ the SEPinversion technique described in Agueda et al. (2008, 2012). This will help to understand if the observed spectrum changes(Fig 4.12) and the resulting symmetricity can be established in a statistically significant manner. In our modelling approach, we have only used a 1.2 AU length straight magnetic field line for transporting the test particles. However, as described in detail in Chapter 4, the IMF line is curved , and often we see the particles not following

the nominal field line. We will investigate whether actual field line characteristics that the particles travelled has any effect on the resulting time-intensity profile of the particles by modifying our magnetic field line model to include curvature and drift. There are approaches which model this magnetic field lines in a Monte-Carlo based methods (Pommois et al., 1999, 2002). There are also approaches which make use of advanced computational techniques to solve the transport equation, which can also be implemented into our approach (Dunzlaff et al., 2015).

The power law index of the magnetic field fluctuations, calculated in-situ using ACE SWEPAM data was found to be in the range of [-0.89,-2.3] with an average around -1.66 (Borovsky, 2012). In our simulation model, we find a spectral index of q = -1.3$\pm$0.1 fits the time-intensity profile of symmetric events and a spectral index of q = -1.07$\pm$0.02 fits non-symmetric events. This fit was done using only the observed intensities without employing PAD information. The degeneracies in estimating the best-fit parameters can be mitigated by constraining the simulated SEP lightcurves with the time-intensity profile information of the actual SEPs as well as the PAD information of the observed SEPs. We intend to model our magnetic field fluctuations using data of the actual interplanetary magnetic field conditions the SEP transport phase to access the influence on the time-intensity profile and PAD of the observed SEP.

The data from Parker Solar Probe mission will be available to the scientific community by the end of 2019. Parker Solar Probe(PSP) mission is humanities first visit its star. One of the major scientific goals of the mission is to explore the mechanisms that accelerate and transport energetic particles (Fox et al., 2016). PSP will spend close to 2100 hours inside of 30 $R_{\odot}$ and will be able to detect SEP particles as they start their journey to interplanetary space. Since any resultant signatures on the SEP electrons at this stage will be mostly from the source acceleration properties, we will be able to decouple the acceleration effects from those of transport effects. The data from this mission will help to validate or invalidate our findings regarding the sensitive dependence of the magnetic field fluctuation, spectral index, q in deciding the time-intensity profile characteristics of the detected SEPs.

References

N. Agueda, R. Vainio, D. Lario, and B. Sanahuja. Injection and Interplanetary Transport of Near-Relativistic Electrons: Modeling the Impulsive Event on 2000 May 1. ApJ, 675: 1601–1613, March 2008. doi: 10.1086/527527.

N. Agueda, R. Vainio, and B. Sanahuja. A Database of >20 keV Electron Green's Functions of Interplanetary Transport at 1 AU. ApJS, 202:18, October 2012. doi: 10.1088/0067-0049/202/2/18.

A. Anastasiadis. Acceleration of solar energetic particles: the case of solar flares. *Journal of Atmospheric and Solar-Terrestrial Physics*, 64:481–488, March 2002. doi: 10.1016/S1364-6826(02)00003-2.

A. Anastasiadis and L. Vlahos. Particle acceleration in an evolving active region by an ensemble of shock waves. *Astrophysical Journal*, 428:819–826, June 1994. doi: 10.1086/174290.

Benz Arnold O. *Plasma Astrophysics*. Astrophysics and Space Science Library. Springer Netherlands, 1993. ISBN 9789401049153.

Kaspar Arzner and Loukas Vlahos. Particle acceleration in multiple dissipation regions. *The Astrophysical Journal*, 605(1):L69–L72, mar 2004. doi: 10.1086/392506. URL http://dx.doi.org/10.1086/392506.

M. Aschwanden and A. A. van Ballegooijen. The Minimum Energy Principle Applied to Parker's Coronal Braiding and Nanoflaring Scenario'. In *Catalyzing Solar Connections*, volume 195 of *IAU Symposium*, page 52, Nov 2018.

M. J. Aschwanden. *Physics of the Solar Corona. An Introduction with Problems and Solutions (2nd edition)*. December 2004.

M. J. Aschwanden and S. L. Freeland. Automated Solar Flare Statistics in Soft X-Rays over 37 Years of GOES Observations: The Invariance of Self-organized Criticality during Three Solar Cycles. *The Astrophysical Journal*, 754:112, August 2012. doi: 10.1088/0004-637X/754/2/112.

M. J. Aschwanden, T. D. Tarbell, R. W. Nightingale, C. J. Schrijver, A. Title, C. C. Kankelborg, P. Martens, and H. P. Warren. Time Variability of the "Quiet" Sun Observed with TRACE. II. Physical Parameters, Temperature Evolution, and Energetics of Extreme-Ultraviolet Nanoflares. *The Astrophysical Journal*, 535:1047–1065, June 2000. doi: 10.1086/308867.

References

M. J. Aschwanden, D. Alexander, T. Metcalf, and N. Nitta. The Electron Number Problem Revisited with RHESSI Flare Observations. In *American Astronomical Society Meeting Abstracts #200*, volume 34 of *Bulletin of the American Astronomical Society*, page 776, May 2002.

Markus J. Aschwanden. GeV particle acceleration in solar flares and ground level enhancement (GLE) events. *Space Science Reviews*, 171(1-4):3–21, feb 2012. doi: 10.1007/s11214-011-9865-x. URL http://dx.doi.org/10.1007/s11214-011-9865-x.

Markus J. Aschwanden, Amir Caspi, Christina M. S. Cohen, Gordon Holman, Ju Jing, Matthieu Kretzschmar, Eduard P. Kontar, James M. McTiernan, Richard A. Mewaldt, Aidan O'Flannagain, Ian G. Richardson, Daniel Ryan, Harry P. Warren, and Yan Xu. Global energetics of solar flares. v. energy closure in flares and coronal mass ejections. *The Astrophysical Journal*, 836(1):17, feb 2017. doi: 10.3847/1538-4357/836/1/17. URL http://dx.doi.org/10.3847/1538-4357/836/1/17.

W. T. Barnes, P. J. Cargill, and S. J. Bradshaw. INFERENCE OF HEATING PROPERTIES FROM "HOT" NON-FLARING PLASMAS IN ACTIVE REGION CORES. i. SINGLE NANOFLARES. *The Astrophysical Journal*, 829(1):31, sep 2016. doi: 10.3847/0004-637x/829/1/31. URL http://dx.doi.org/10.3847/0004-637X/829/1/31.

Samuel D. Tun Beltran, S. Cutchin, and S. White. A new look at type-III bursts and their use as coronal diagnostics. *Solar Physics*, 290(9):2423–2437, sep 2015. doi: 10.1007/s11207-015-0760-6. URL http://dx.doi.org/10.1007/s11207-015-0760-6.

S. G. Benka and G. D. Holman. A thermal/nonthermal model for solar microwave bursts. *The Astrophysical Journal*, 391:854–864, June 1992. doi: 10.1086/171394.

S. G. Benka and G. D. Holman. A thermal/nonthermal model for solar hard X-ray bursts. *The Astrophysical Journal*, 435:469–481, November 1994. doi: 10.1086/174829.

R.D. Bentley, K.-L. Klein, L. van Driel-Gesztelyi, P. Démoulin, G. Trottet, P. Tassetto, and G. Marty. *Solar Physics*, 193(1/2):227–245, 2000. doi: https://doi.org/10.1023/A:1005218007132. URL https://doi.org/10.1023/A:1005218007132.

Arnold O Benz. Flare observations. *Living reviews in solar physics*, 14(1):2, 2017.

Joseph E Borovsky. The velocity and magnetic field fluctuations of the solar wind at 1 au: Statistical analysis of fourier spectra and correlations with plasma properties. *Journal of Geophysical Research: Space Physics*, 117(A5), 2012.

John C. Brown. The deduction of energy spectra of non-thermal electrons in flares from the observed dynamic spectra of hard x-ray bursts. *Solar Physics*, 18(3):489–502, Jul 1971. ISSN 1573-093X. doi: 10.1007/BF00149070. URL https://doi.org/10.1007/BF00149070.

L Burlaga, E Sittler, F Mariani, and arid R Schwenn. Magnetic loop behind an interplanetary shock: Voyager, helios, and imp 8 observations. *Journal of Geophysical Research: Space Physics*, 86(A8):6673–6684, 1981.

A. Buttighoffer. Solar electron beams associated with radio type III. *Astronomy and Astrophysics*, 335:295–302, Jul 1998.

I. Cairns, D. Oberoi, J. Morgan, T. Bastian, S. Bhatnagar, M. Bisi, L. Benkevitch, J. Bowman, A. Donea, O. Giersch, B. Jackson, G. L. Chat, L. Golub, K. Hariharan, D. Herne, J. Kasper, J. Kennewell, C. Lonsdale, V. Lobzin, L. Matthews, A. Mohan, J. Padmanabhan, V. Pankratius, M. Pick, P. Subramanian, R. Ramesh, J. Raymond, K. Reeves, A. Rogers, R. Sharma, S. Tingay, S. Tremblay, D. Tripathi, D. Webb, S. White, and Z. B. Z. Abidin. MWA Observations of Solar Radio Bursts and the Quiet Sun. MWA Proposal id.2017A-06, January 2017.

H. V. Cane, R. E. McGuire, and T. T. von Rosenvinge. Two Classes of Solar Energetic Particle Events Associated with Impulsive and Long-Duration Soft X-Ray Flares. *The Astrophysical Journal*, 301:448, Feb 1986. doi: 10.1086/163913.

HV Cane. Near-relativistic solar electrons and type iii radio bursts. *The Astrophysical Journal*, 598(2):1403, 2003.

HV Cane and WC Erickson. Energetic particle propagation in the inner heliosphere as deduced from low-frequency (< 100 khz) observations of type iii radio bursts. *Journal of Geophysical Research: Space Physics*, 108(A5), 2003.

HV Cane, RA Mewaldt, CMS Cohen, and TT Von Rosenvinge. Role of flares and shocks in determining solar energetic particle abundances. *Journal of Geophysical Research: Space Physics*, 111(A6), 2006.

H. Carmichael. A Process for Flares. *NASA Special Publication*, 50:451, 1964.

Benjamin D. G. Chandran and Jason L. Maron. Thermal conduction and particle transport in strong magnetohydrodynamic turbulence, with application to galaxy cluster plasmas. *The Astrophysical Journal*, 602(1):170–180, feb 2004. doi: 10.1086/380897.

I. M. Chertok, S. Kahler, H. Aurass, and A. A. Gnezdilov. Sharp Decreases of Solar Metric Radio Storm Emission. *Solar Physics*, 202:337–354, September 2001. doi: 10.1023/A:1012211412695.

E. W. Cliver. A Revised Classification Scheme for Solar Energetic Particle Events. *Central European Astrophysical Bulletin*, 33:253–270, Jan 2009.

E. W. Cliver, S. W. Kahler, M. A. Shea, and D. F. Smart. Injection onsets of 2 GeV protons, 1 MeV electrons, and 100 keV electrons in solar cosmic ray flares. ApJ, 260:362–370, Sep 1982. doi: 10.1086/160261.

N. B. Crosby, M. J. Aschwanden, and B. R. Dennis. Frequency distributions and correlations of solar X-ray flare parameters. *Solar Physics*, 143:275–299, February 1993. doi: 10.1007/BF00646488.

J. T. Dahlin, J. F. Drake, and M. Swisdak. Electron acceleration in three-dimensional magnetic reconnection with a guide field. *Physics of Plasmas*, 22(10):100704, oct 2015. doi: 10.1063/1.4933212. URL http://dx.doi.org/10.1063/1.4933212.

D. W. Datlowe and R. P. Lin. Evidence for thin-target x-ray emission in a small solar flare on 26 February 1972. *Solar Physics*, 32(2):459–468, oct 1973. doi: 10.1007/BF00154958. URL http://dx.doi.org/10.1007/BF00154958.

G. Del Zanna, G. Aulanier, K.-L. Klein, and T. Török. A single picture for solar coronal outflows and radio noise storms. *Astronomy and Astrophysics*, 526:A137, February 2011. doi: 10.1051/0004-6361/201015231.

J.-P. Delaboudinière, G. E. Artzner, J. Brunaud, A. H. Gabriel, J. F. Hochedez, F. Millier, X. Y. Song, B. Au, K. P. Dere, R. A. Howard, R. Kreplin, D. J. Michels, J. D. Moses, J. M. Defise, C. Jamar, P. Rochus, J. P. Chauvineau, J. P. Marioge, R. C. Catura, J. R. Lemen, L. Shing, R. A. Stern, J. B. Gurman, W. M. Neupert, A. Maucherat, F. Clette, P. Cugnon, and E. L. van Dessel. EIT: Extreme-Ultraviolet Imaging Telescope for the SOHO Mission. *Solar Physics*, 162:291–312, December 1995. doi: 10.1007/BF00733432.

P. Dmitruk and D. O. Gómez. Turbulent Coronal Heating and the Distribution of Nanoflares. *The Astrophysical Journal Letters*, 484:L83–L86, July 1997. doi: 10.1086/310760.

H Dreicer. Electron and ion runaway in a fully ionized gas. ii. *Physical review*, 117(2):329, 1960.

Hz Dreicer. Electron and ion runaway in a fully ionized gas. i. *Physical Review*, 115(2):238, 1959.

W. Dröge, Y. Y. Kartavykh, N. Dresing, B. Heber, and A. Klassen. Wide longitudinal distribution of interplanetary electrons following the 7 February 2010 solar event: Observations and transport modeling. *Journal of Geophysical Research (Space Physics)*, 119: 6074–6094, August 2014. doi: 10.1002/2014JA019933.

P Dunzlaff, RD Strauss, and MS Potgieter. Solving parker's transport equation with stochastic differential equations on gpus. *Computer Physics Communications*, 192:156–165, 2015.

G. Einaudi and M. Velli. The distribution of flares, statistics of magnetohydrodynamic turbulence and coronal heating. *Physics of Plasmas*, 6:4146–4153, November 1999. doi: 10.1063/1.873679.

E. O. Elgaroy. *Solar Noise Storms*. Elsevier Science, 1976. URL http://www.ebook.de/de/product/23272706/e_o_elgaroy_solar_noise_storms.html.

R. E. Ergun, D. Larson, R. P. Lin, J. P. McFadden, C. W. Carlson, K. A. Anderson, L. Muschietti, M. McCarthy, G. K. Parks, H. Reme, J. M. Bosqued, C. D'Uston, T. R. Sanderson, K. P. Wenzel, Michael Kaiser, R. P. Lepping, S. D. Bale, Paul Kellogg, and J. L. Bougeret. Wind spacecraft observations of solar impulsive electron events associated with solar type iii radio bursts. *The Astrophysical Journal*, 503(1):435–445, Aug 1998. doi: 10.1086/305954.

Gregory D. Fleishman, Eduard P. Kontar, Gelu M. Nita, and Dale E. Gary. A COLD, TENUOUS SOLAR FLARE: ACCELERATION WITHOUT HEATING. *The Astrophysical Journal*, 731(1):L19, mar 2011. doi: 10.1088/2041-8205/731/1/L19. URL http://dx.doi.org/10.1088/2041-8205/731/1/L19.

Gregory D. Fleishman, Valentin D. Pal'shin, Natalia Meshalkina, Alexandra L. Lysenko, Larisa K. Kashapova, and Alexander T. Altyntsev. A COLD FLARE WITH DELAYED HEATING. *The Astrophysical Journal*, 822(2):71, may 2016. doi: 10.3847/0004-637X/822/2/71. URL http://dx.doi.org/10.3847/0004-637X/822/2/71.

Lyndsay Fletcher, Brian R Dennis, Hugh S Hudson, Sam Krucker, Ken Phillips, Astrid Veronig, Marina Battaglia, Laura Bone, Amir Caspi, Qingrong Chen, et al. An observational overview of solar flares. *Space science reviews*, 159(1-4):19, 2011.

NJ Fox, MC Velli, SD Bale, R Decker, A Driesman, RA Howard, Justin C Kasper, J Kinnison, M Kusterer, D Lario, et al. The solar probe plus mission: Humanity's first visit to our star. *Space Science Reviews*, 204(1-4):7–48, 2016.

Crispin Gardiner. *Stochastic Methods*. Springer-Verlag Berlin Heidelberg, 1985.

John T Gosling. The solar flare myth. *Journal of Geophysical Research: Space Physics*, 98 (A11):18937–18949, 1993.

G. A. Graham, I. J. Rae, C. J. Owen, and A. P. Walsh. Investigating the Effect of IMF Path Length on Pitch-angle Scattering of Strahl within 1 au. *The Astrophysical Journal*, 855:40, March 2018. doi: 10.3847/1538-4357/aaaf1b.

Dennis K Haggerty and Edmond C Roelof. Impulsive near-relativistic solar electron events: Delayed injection with respect to solar electromagnetic emission. *The Astrophysical Journal*, 579(2):841, 2002.

B. N. Handy, L. W. Acton, C. C. Kankelborg, C. J. Wolfson, D. J. Akin, M. E. Bruner, R. Caravalho, R. C. Catura, R. Chevalier, D. W. Duncan, C. G. Edwards, C. N. Feinstein, S. L. Freeland, F. M. Friedlaender, C. H. Hoffmann, N. E. Hurlburt, B. K. Jurcevich, N. L. Katz, G. A. Kelly, J. R. Lemen, M. Levay, R. W. Lindgren, D. P. Mathur, S. B. Meyer, S. J. Morrison, M. D. Morrison, R. W. Nightingale, T. P. Pope, R. A. Rehse, C. J. Schrijver, R. A. Shine, L. Shing, K. T. Strong, T. D. Tarbell, A. M. Title, D. D. Torgerson, L. Golub, J. A. Bookbinder, D. Caldwell, P. N. Cheimets, W. N. Davis, E. E. Deluca, R. A. McMullen, H. P. Warren, D. Amato, R. Fisher, H. Maldonado, and C. Parkinson. The transition region and coronal explorer. *Solar Physics*, 187:229–260, July 1999. doi: 10.1023/A:1005166902804.

I. G. Hannah, S. Christe, S. Krucker, G. J. Hurford, H. S. Hudson, and R. P. Lin. RHESSI microflare statistics. II. x-ray imaging, spectroscopy, and energy distributions. *The Astrophysical Journal*, 677(1):704–718, apr 2008. doi: 10.1086/529012. URL http://dx.doi.org/10.1086/529012.

I. G. Hannah, H. S. Hudson, M. Battaglia, S. Christe, J. Kašparová, S. Krucker, M. R. Kundu, and A. Veronig. Microflares and the Statistics of X-ray Flares. *Space Science Reviews*, 159:263–300, September 2011. doi: 10.1007/s11214-010-9705-4.

K. Harvey and J. Harvey. Observations of Moving Magnetic Features near Sunspots. *Solar Physics*, 28:61–71, January 1973. doi: 10.1007/BF00152912.

J. S. Hey, S. J. Parsons, and J. W. Philips. Fluctuations in cosmic radiation at radio-frequencies. *Nature*, 158(4007):234–234, aug 1946. doi: doi:10.1038/158234a0.

J. Heyvaerts and E. R. Priest. Coronal heating by phase-mixed shear Alfven waves. *Astronomy & Astrophysics*, 117:220–234, January 1983.

T Hirayama. Theoretical model of flares and prominences. *Solar Physics*, 34(2):323–338, 1974.

G. D. Holman. Acceleration of runaway electrons and Joule heating in solar flares. *The Astrophysical Journal*, 293:584–594, June 1985. doi: 10.1086/163263.

G. D. Holman, M. J. Aschwanden, H. Aurass, M. Battaglia, P. C. Grigis, E. P. Kontar, W. Liu, P. Saint-Hilaire, and V. V. Zharkova. Implications of x-ray observations for electron acceleration and propagation in solar flares. *Space Science Reviews*, 159(1-4): 107–166, aug 2011. doi: 10.1007/s11214-010-9680-9. URL http://dx.doi.org/10.1007/s11214-010-9680-9.

Gordon D. Holman. DC Electric Field Acceleration of Ions in Solar Flares. *The Astrophysical Journal*, 452:451, Oct 1995. doi: 10.1086/176316.

H. S. Hudson. Solar flares, microflares, nanoflares, and coronal heating. *Solar Physics*, 133 (2):357–369, jun 1991. doi: http://dx.doi.org/10.1007/BF00149894. URL http://dx.doi.org/10.1007/BF00149894.

Shinnosuke Ishikawa, Lindsay Glesener, Säm Krucker, Steven Christe, Juan Camilo Buitrago-Casas, Noriyuki Narukage, and Juliana Vievering. Detection of nanoflare-heated plasma in the solar corona by the FOXSI-2 sounding rocket. *Nature Astronomy*, 1(11):771–774, oct 2017. doi: 10.1038/s41550-017-0269-z.

K. Iwai, S. Masuda, Y. Miyoshi, F. Tsuchiya, A. Morioka, and H. Misawa. PEAK FLUX DISTRIBUTIONS OF SOLAR RADIO TYPE-i BURSTS FROM HIGHLY RESOLVED SPECTRAL OBSERVATIONS. *The Astrophysical Journal*, 768(1):L2, apr 2013. doi: 10.1088/2041-8205/768/1/l2.

K. Iwai, Y. Miyoshi, S. Masuda, F. Tsuchiya, A. Morioka, and H. Misawa. SPECTRAL STRUCTURES AND THEIR GENERATION MECHANISMS FOR SOLAR RADIO TYPE-i BURSTS. *The Astrophysical Journal*, 789(1):4, jun 2014. doi: 10.1088/0004-637x/789/1/4.

T. James and P. Subramanian. Energetics of small electron acceleration episodes in the solar corona from radio noise storm observations. *Monthly Notices of the Royal Astronomical Society*, 479:1603–1611, September 2018. doi: 10.1093/mnras/sty1216.

Tomin James, Prasad Subramanian, and Eduard P Kontar. Small electron acceleration episodes in the solar corona. *Monthly Notices of the Royal Astronomical Society*, 471 (1):89–99, jun 2017. doi: https://doi.org/10.1093/mnras/stx1460. URL https://doi.org/10.1093/mnras/stx1460.

J. R. Jokipii. Cosmic-Ray Propagation. I. Charged Particles in a Random Magnetic Field. ApJ, 146:480, November 1966. doi: 10.1086/148912.

V. Joulin, E. Buchlin, J. Solomon, and C. Guennou. Energetic characterisation and statistics of solar coronal brightenings. *Astronomy & Astrophysics*, 591:A148, jul 2016. doi: 10.1051/0004-6361/201526254. URL http://dx.doi.org/10.1051/0004-6361/201526254.

S. Kahler. Injection profiles of solar energetic particles as functions of coronal mass ejection heights. *The Astrophysical Journal*, 428:837–842, June 1994. doi: 10.1086/174292.

S. W. Kahler. Solar flares and coronal mass ejections. *Annual Review of Astron and Astrophys*, 30:113–141, 1992. doi: 10.1146/annurev.aa.30.090192.000553.

S. W. Kahler. Characteristic Times of Gradual Solar Energetic Particle Events and Their Dependence on Associated Coronal Mass Ejection Properties. *The Astrophysical Journal*, 628:1014–1022, August 2005. doi: 10.1086/431194.

S. W. Kahler, N. R. Sheeley, Jr., R. A. Howard, D. J. Michels, M. J. Koomen, R. E. McGuire, T. T. von Rosenvinge, and D. V. Reames. Associations between coronal mass ejections and solar energetic proton events. J. Geophys. Res., 89:9683–9693, November 1984. doi: 10.1029/JA089iA11p09683.

SW Kahler, EW Cliver, AJ Tylka, and WF Dietrich. A comparison of ground level event e/p and fe/o ratios with associated solar flare and cme characteristics. *Space science reviews*, 171(1-4):121–139, 2012.

M.-B. Kallenrode. Current views on impulsive and gradual solar energetic particle events. *Journal of Physics G Nuclear Physics*, 29:965–981, May 2003.

M.-B. Kallenrode, G. Wibberenz, and S. Hucke. Propagation conditions of relativistic electrons in the inner heliosphere. *The Astrophysical Journal*, 394:351–356, July 1992. doi: 10.1086/171587.

May-Britt Kallenrode. *Space physics: an introduction to plasmas and particles in the heliosphere and magnetospheres*. Springer Science & Business Media, 2013.

Alain Kerdraon and Jean-Marc Delouis. The nançay radioheliograph. In *Coronal Physics from Radio and Space Observations*, volume 483, page 192, 1997.

K.-L. Klein. *Long-duration non thermal energy release in flares and outside flares*, pages 55–74. Springer Berlin Heidelberg, 1995. doi: 10.1007/3-540-59109-5_42. URL https://doi.org/10.1007/3-540-59109-5_42.

K.-L. Klein. Suprathermal Electrons in Non-flaring Active Regions (Invited review). In C. E. Alissandrakis and B. Schmieder, editors, *Three-Dimensional Structure of Solar Active Regions*, volume 155 of *Astronomical Society of the Pacific Conference Series*, page 182, 1998.

Karl-Ludwig Klein and Silvia Dalla. Acceleration and propagation of solar energetic particles. *Space Science Reviews*, 212(3-4):1107–1136, jul 2017. doi: https://doi.org/10.1007/s11214-017-0382-4. URL https://doi.org/10.1007/s11214-017-0382-4.

LW Klein and LF Burlaga. Interplanetary magnetic clouds at 1 au. *Journal of Geophysical Research: Space Physics*, 87(A2):613–624, 1982.

J. A. Klimchuk. Key aspects of coronal heating. *Philosophical Transactions of the Royal Society A: Mathematical, Physical and Engineering Sciences*, 373(2042):20140256–20140256, apr 2015. doi: 10.1098/rsta.2014.0256. URL http://dx.doi.org/10.1098/rsta.2014.0256.

J. A. Klimchuk and P. J. Cargill. Spectroscopic diagnostics of nanoflare-heated loops. *The Astrophysical Journal*, 553(1):440–448, may 2001. doi: https://doi.org/10.1086/320666. URL https://doi.org/10.1086/320666.

K. J. Knizhnik, V. M. Uritsky, J. A. Klimchuk, and C. R. DeVore. Power-Law Statistics Of Driven Reconnection In The Magnetically Closed Corona. *ArXiv e-prints*, January 2018.

K. Kobayashi, J. Cirtain, A. R. Winebarger, K. Korreck, L. Golub, R. W. Walsh, B. De Pontieu, C. DeForest, A. Title, S. Kuzin, S. Savage, D. Beabout, B. Beabout, W. Podgorski, D. Caldwell, K. McCracken, M. Ordway, H. Bergner, R. Gates, S. McKillop, P. Cheimets, S. Platt, N. Mitchell, and D. Windt. The High-Resolution Coronal Imager (Hi-C). *Solar Physics*, 289:4393–4412, November 2014. doi: 10.1007/s11207-014-0544-4.

E. P. Kontar, J. C. Brown, A. G. Emslie, W. Hajdas, G. D. Holman, G. J. Hurford, J. Kašparová, P. C. V. Mallik, A. M. Massone, M. L. McConnell, M. Piana, M. Prato, E. J. Schmahl, and E. Suarez-Garcia. Deducing electron properties from hard x-ray observations. *Space Science Reviews*, 159(1-4):301–355, aug 2011. doi: 10.1007/s11214-011-9804-x. URL http://dx.doi.org/10.1007/s11214-011-9804-x.

E. P. Kontar, J. E. Perez, L. K. Harra, A. A. Kuznetsov, A. G. Emslie, N. L. S. Jeffrey, N. H. Bian, and B. R. Dennis. Turbulent kinetic energy in the energy balance of a solar flare. 2017. URL http://arxiv.org/pdf/1703.02392v1.

R. A. Kopp and G. W. Pneuman. Magnetic reconnection in the corona and the loop prominence phenomenon. *Solar Physics*, 50:85–98, October 1976. doi: 10.1007/BF00206193.

A. Kouloumvakos, A. Nindos, E. Valtonen, C. E. Alissandrakis, O. Malandraki, P. Tsitsipis, A. Kontogeorgos, X. Moussas, and A. Hillaris. Properties of solar energetic particle events inferred from their associated radio emission. *Astronomy and Astrophysics*, 580:A80, August 2015. doi: 10.1051/0004-6361/201424397.

S. Krucker, E. P. Kontar, S. Christe, and R. P. Lin. Solar Flare Electron Spectra at the Sun and near the Earth. *Astrophysical Journal Letters*, 663(2):L109–L112, July 2007. doi: 10.1086/519373. URL http://dx.doi.org/10.1086/519373.

Sam Krucker, Davin E. Larson, Robert P. Lin, and Barbara J. Thompson. On the origin of impulsive electron events observed at 1 AU. *The Astrophysical Journal*, 519(2):864–875, jul 1999. doi: 10.1086/307415. URL http://dx.doi.org/10.1086/307415.

V. Krupar, M. Maksimovic, O. Santolik, E. P. Kontar, B. Cecconi, S. Hoang, O. Kruparova, J. Soucek, H. Reid, and A. Zaslavsky. Statistical survey of type III radio bursts at long wavelengths observed by the solar TErrestrial RElations observatory (STEREO)/waves instruments: Radio flux density variations with frequency. *Solar Physics*, 289(8):3121–3135, apr 2014. doi: 10.1007/s11207-014-0522-x. URL http://dx.doi.org/10.1007/s11207-014-0522-x.

V. Krupar, E. P. Kontar, J. Soucek, O. Santolik, M. Maksimovic, and O. Kruparova. On the speed and acceleration of electron beams triggering interplanetary type III radio bursts. *Astronomy & Astrophysics*, 580:A137, aug 2015. doi: 10.1051/0004-6361/201425308. URL http://dx.doi.org/10.1051/0004-6361/201425308.

T. Kudoh and K. Shibata. Alfvén Wave Model of Spicules and Coronal Heating. *The Astrophysical Journal*, 514:493–505, March 1999. doi: 10.1086/306930.

Sanjay Kumar and R. Bhattacharyya. Continuous development of current sheets near and away from magnetic nulls. *Physics of Plasmas*, 23(4):044501, apr 2016a. doi: 10.1063/1.4945634. URL https://doi.org/10.1063/1.4945634.

Sanjay Kumar and R. Bhattacharyya. Continuous development of current sheets near and away from magnetic nulls. *Physics of Plasmas*, 23(4):044501, apr 2016b. doi: 10.1063/1.4945634. URL http://doi.org/10.1063/1.4945634.

Sanjay Kumar, R. Bhattacharyya, and P. K. Smolarkiewicz. Formation of magnetic discontinuities through viscous relaxation. *Physics of Plasmas*, 21(5):052904, may 2014. doi: 10.1063/1.4878955. URL https://doi.org/10.1063/1.4878955.

Sanjay Kumar, R. Bhattacharyya, and P. K. Smolarkiewicz. On the role of topological complexity in spontaneous development of current sheets. *Physics of Plasmas*, 22(8): 082903, aug 2015. doi: 10.1063/1.4928883. URL http://dx.doi.org/10.1063/1.4928883.

M.R Kundu. *Solar Radio Astronomy*. John Wiley & Sons Inc, 1965.

I. Lange and S. E. Forbush. Further note on the effect on cosmic-ray intensity of the magnetic storm of March 1, 1942. *Terrestrial Magnetism and Atmospheric Electricity (Journal of Geophysical Research)*, 47:331, 1942. doi: 10.1029/TE047i004p00331.

M. Laurenza, E. W. Cliver, J. Hewitt, M. Storini, A. G. Ling, C. C. Balch, and M. L. Kaiser. A technique for short-term warning of solar energetic particle events based on flare location, flare size, and evidence of particle escape. *Space Weather*, 7:S04008, April 2009. doi: 10.1029/2007SW000379.

K. D. Leka and G. Barnes. Photospheric Magnetic Field Properties of Flaring versus Flare-quiet Active Regions. IV. A Statistically Significant Sample. *The Astrophysical Journal*, 656:1173–1186, February 2007. doi: 10.1086/510282.

J. R. Lemen, A. M. Title, D. J. Akin, P. F. Boerner, C. Chou, J. F. Drake, D. W. Duncan, C. G. Edwards, F. M. Friedlaender, G. F. Heyman, N. E. Hurlburt, N. L. Katz, G. D. Kushner, M. Levay, R. W. Lindgren, D. P. Mathur, E. L. McFeaters, S. Mitchell, R. A. Rehse, C. J. Schrijver, L. A. Springer, R. A. Stern, T. D. Tarbell, J.-P. Wuelser, C. J. Wolfson, C. Yanari, J. A. Bookbinder, P. N. Cheimets, D. Caldwell, E. E. Deluca, R. Gates, L. Golub, S. Park, W. A. Podgorski, R. I. Bush, P. H. Scherrer, M. A. Gummin, P. Smith, G. Auker, P. Jerram, P. Pool, R. Soufli, D. L. Windt, S. Beardsley, M. Clapp, J. Lang, and N. Waltham. The Atmospheric Imaging Assembly (AIA) on the Solar Dynamics Observatory (SDO). *Solar Physics*, 275:17–40, January 2012. doi: 10.1007/s11207-011-9776-8.

R. P. Lepping, M. H. Acũna, L. F. Burlaga, W. M. Farrell, J. A. Slavin, K. H. Schatten, F. Mariani, N. F. Ness, F. M. Neubauer, Y. C. Whang, J. B. Byrnes, R. S. Kennon, P. V. Panetta, J. Scheifele, and E. M. Worley. The Wind Magnetic Field Investigation. *Space science reviews*, 71(1-4):207–229, Feb 1995. doi: 10.1007/BF00751330.

C. Y. Li, Y. Chen, B. Wang, G. P. Ruan, S. W. Feng, G. H. Du, and X. L. Kong. EUV and magnetic activities associated with type-i solar radio bursts. *Solar Physics*, 292(6), jun 2017. doi: https://doi.org/10.1007/s11207-017-1108-1. URL https://doi.org/10.1007/s11207-017-1108-1.

E.M. Lifshitz, L.P. Pitaevskii, J.B. Sykes, and R.N. Franklin. *Physical Kinetics*. Course of theoretical physics. Elsevier Science, 1995. ISBN 9780750626354. URL https://books.google.co.in/books?id=h7LgAAAAMAAJ.

R. P. Lin. The Emission and Propagation of 40 keV Solar Flare Electrons. I: The Relationship of 40 keV Electron to Energetic Proton and Relativistic Electron Emission by the Sun. *Solar Physics*, 12:266–303, May 1970. doi: 10.1007/BF00227122.

R. P. Lin and H. S. Hudson. 10 100 keV electron acceleration and emission from solar flares. *Solar Physics*, 17(2):412–435, April 1971. doi: 10.1007/BF00150045. URL http://dx.doi.org/10.1007/BF00150045.

R. P. Lin, D. W. Potter, D. A. Gurnett, and F. L. Scarf. Energetic electrons and plasma waves associated with a solar type iii radio burst. *The Astrophysical Journal*, 251:364–373, December 1981. doi: 10.1086/159471.

R. P. Lin, P. T. Feffer, and R. A. Schwartz. Solar Hard X-Ray Bursts and Electron Acceleration Down to 8 keV. *The Astrophysical Journal Letters*, 557:L125–L128, August 2001. doi: 10.1086/323270.

R.P. Lin. Non-relativistic solar electrons. *Space Science Reviews*, 16(1-2), 1974. doi: 10.1007/bf00240886. URL http://dx.doi.org/10.1007/BF00240886.

RP Lin. Wind observations of suprathermal electrons in the interplanetary medium. In *The Advanced Composition Explorer Mission*, pages 61–78. Springer, 1998.

Y. E. Litvinenko and B. V. Somov. Relativistic acceleration of protons in reconnecting current sheets of solar flares. *Solar Physics*, 158:317–330, May 1995. doi: 10.1007/BF00795666.

Yuri E. Litvinenko. Electron acceleration by strong DC electric fields in extragalactic jets. *Astronomy and Astrophysics*, 349:685–690, Sep 1999.

E. T. Lu and R. J. Hamilton. Avalanches and the distribution of solar flares. *The Astrophysical Journal Letters*, 380:L89–L92, October 1991. doi: 10.1086/186180.

E. T. Lu, R. J. Hamilton, J. M. McTiernan, and K. R. Bromund. Solar flares and avalanches in driven dissipative systems. *The Astrophysical Journal*, 412:841–852, August 1993. doi: 10.1086/172966.

Q. Y. Luo, F. S. Wei, and X. S. Feng. Electron acceleration by lower hybrid turbulence in solar flares. *The Astrophysical Journal*, 584(1):497–508, feb 2003. doi: 10.1086/345618.

A. L. MacKinnon and I. J. D. Craig. Stochastic simulation of fast particle diffusive transport. A&A, 251:693–699, November 1991.

P. C. H. Martens. The generation of proton beams in two-ribbon flares. *The Astrophyscial Journal Letters*, 330:L131–L133, July 1988. doi: 10.1086/185220.

P. C. H. Martens and A. Young. Neutral Beams in Two-Ribbon Flares and in the Geomagnetic Tail. *The Astrophyscial Journal Letters*, 73:333, Jun 1990. doi: 10.1086/191469.

Stephen Mason. Galileo's scientific discoveries, cosmological confrontations, and the aftermath. *History of Science*, 40(4):377–406, 2002. doi: 10.1177/007327530204000401. URL https://doi.org/10.1177/007327530204000401.

S. Masson, P. Démoulin, S. Dasso, and K.-L. Klein. The interplanetary magnetic structure that guides solar relativistic particles. A&A, 538:A32, February 2012. doi: 10.1051/0004-6361/201118145.

S. Masuda, T. Kosugi, H. Hara, S. Tsuneta, and Y. Ogawara. A loop-top hard X-ray source in a compact solar flare as evidence for magnetic reconnection. *Nature*, 371:495–497, October 1994. doi: 10.1038/371495a0.

W. H. Matthaeus, G. P. Zank, S. Oughton, D. J. Mullan, and P. Dmitruk. Coronal Heating by Magnetohydrodynamic Turbulence Driven by Reflected Low-Frequency Waves. *The Astrophysical Journal Letters*, 523:L93–L96, September 1999. doi: 10.1086/312259.

P. S. McIntosh. The classification of sunspot groups. *Solar Physics*, 125:251–267, February 1990. doi: 10.1007/BF00158405.

Charles Meegan. GLAST GRB Observations and Capabilities. In *37th COSPAR Scientific Assembly*, volume 37, page 1988, Jan 2008.

D. B. Melrose. *Plasma astrophysics: Nonthermal processes in diffuse magnetized plasmas. Volume 1 - The emission, absorption and transfer of waves in plasmas*. 1980a.

D. B. Melrose. *Plasma astrophysics: Nonthermal processes in diffuse magnetized plasmas. Volume 2 - Astrophysical applications*. 1980b.

C. Mercier and G. Trottet. Coronal radio bursts: A signature of nanoflares? *The Astrophysical Journal*, 474(1):L65–L68, jan 1997. doi: https://doi.org/10.1086/310422. URL https://doi.org/10.1086/310422.

C. Mercier, P. Subramanian, A. Kerdraon, M. Pick, S. Ananthakrishnan, and P. Janardhan. Combining visibilities from the giant meterwave radio telescope and the nancay radio heliograph. *Astronomy & Astrophysics*, 447(3):1189–1201, feb 2006. doi: 10.1051/0004-6361:20053621. URL https://doi.org/10.1051/0004-6361:20053621.

C. Mercier, P. Subramanian, G. Chambe, and P. Janardhan. The structure of solar radio noise storms. *Astronomy & Astrophysics*, 576:A136, apr 2015. doi: http://dx.doi.org/10.1051/0004-6361/201321064. URL http://dx.doi.org/10.1051/0004-6361/201321064.

J. A. Miller. Particle Acceleration in Solar Flares. In P. C. H. Martens, S. Tsuruta, and M. A. Weber, editors, *Highly Energetic Physical Processes and Mechanisms for Emission from Astrophysical Plasmas*, volume 195 of *IAU Symposium*, page 277, May 2000.

James A. Miller, T. N. Larosa, and R. L. Moore. Stochastic electron acceleration by cascading fast mode waves in impulsive solar flares. *The Astrophysical Journal*, 461:445, apr 1996. doi: 10.1086/177072.

James A. Miller, Peter J. Cargill, A. Gordon Emslie, Gordon D. Holman, Brian R. Dennis, T. N. LaRosa, Robert M. Winglee, Stephen G. Benka, and S. Tsuneta. Critical issues for understanding particle acceleration in impulsive solar flares. *Journal of Geophysical Research*, 102(A7):14631, 1997. doi: 10.1029/97ja00976. URL http://dx.doi.org/10.1029/97JA00976.

W. W. Morgan, P. C. Keenan, and E. Kellman. *An atlas of stellar spectra, with an outline of spectral classification*. 1943.

R. J. Morton and J. A. McLaughlin. High-resolution Observations of Active Region Moss and its Dynamics. *The Astrophysical Journal*, 789:105, July 2014. doi: 10.1088/0004-637X/789/2/105.

Werner M Neupert. Comparison of solar x-ray line emission with microwave emission during flares. *The Astrophysical Journal*, 153:L59, 1968.

L. Ofman. Wave Modeling of the Solar Wind. *Living Reviews in Solar Physics*, 7:4, October 2010. doi: 10.12942/lrsp-2010-4.

K. W. Ogilvie, D. J. Chornay, R. J. Fritzenreiter, F. Hunsaker, J. Keller, J. Lobell, G. Miller, J. D. Scudder, Jr. Sittler, E. C., R. B. Torbert, D. Bodet, G. Needell, A. J. Lazarus, J. T. Steinberg, J. H. Tappan, A. Mavretic, and E. Gergin. SWE, A Comprehensive Plasma Instrument for the Wind Spacecraft. *Space science reviews*, 71(1-4):55–77, Feb 1995. doi: 10.1007/BF00751326.

M. Oka, S. Ishikawa, P. Saint-Hilaire, S. Krucker, and R. P. Lin. Kappa Distribution Model for Hard X-Ray Coronal Sources of Solar Flares. *The Astrophysical Journal*, 764(1): 6, February 2013. doi: 10.1088/0004-637X/764/1/6. URL http://dx.doi.org/10.1088/0004-637X/764/1/6.

Mathew J Owens and Robert J Forsyth. The heliospheric magnetic field. *Living Reviews in Solar Physics*, 10(1):5, 2013.

E. N. Parker. Dynamics of the Interplanetary Gas and Magnetic Fields. *The Astrophysical Journal*, 128:664, November 1958. doi: 10.1086/146579.

E. N. Parker. Direct coronal heating from dissipation of magnetic field. In *NASA Conference Publication*, volume 228 of *NASA Conference Publication*, November 1983.

E. N. Parker. The Rapid Dissipation of Stellar Magnetic Fields and the Production of X-Ray Coronas. In C. de Jager and B. Chen, editors, *Solar Physics and Interplanetary Travelling Phenomena*, page 925, 1985.

E. N. Parker. Small-scale energy storage and release as the cause of the stellar X-ray corona. In G. Athay and D. S. Spicer, editors, *NASA Conference Publication*, volume 2483 of *NASA Conference Publication*, September 1987.

E. N. Parker. Nanoflares and the solar x-ray corona. *The Astrophysical Journal*, 330:474, jul 1988. doi: 10.1086/166485. URL http://dx.doi.org/10.1086/166485.

C. E. Parnell and P. E. Jupp. Statistical Analysis of the Energy Distribution of Nanoflares in the Quiet Sun. *The Astrophysical Journal*, 529:554–569, January 2000. doi: 10.1086/308271.

V. Petrosian and T. Q. Donaghy. On the Spatial Distribution of Hard X-Rays from Solar Flare Loops. *The Astrophysical Journal*, 527:945–957, December 1999. doi: 10.1086/308133.

Theophilos Pisokas, Loukas Vlahos, and Heinz Isliker. Synergy of stochastic and systematic energization of plasmas during turbulent reconnection. *The Astrophysical Journal*, 852(2): 64, jan 2018. doi: 10.3847/1538-4357/aaa1e0.

P. Pommois, P. Veltri, and G. Zimbardo. Transport of Magnetic Field Lines in the Solar Wind Magnetic Turbulence and Influence on Particle Propagation to High Heliographic Latitudes. In A. Wilson and et al., editors, *Magnetic Fields and Solar Processes*, volume 9 of *ESA Special Publication*, page 1115, Dec 1999.

P. Pommois, P. Veltri, and G. Zimbardo. Magnetic field line turbulent diffusion and propagation of solar energetic particles. In Huguette Sawaya-Lacoste, editor, *Solspa 2001, Proceedings of the Second Solar Cycle and Space Weather Euroconference*, volume 477 of *ESA Special Publication*, pages 305–308, Mar 2002.

D. W. Potter, R. P. Lin, and K. A. Anderson. Impulsive 2-10 keV solar electron events not associated with flares. *The Astrophysical Journal*, 236:L97, mar 1980. doi: 10.1086/183206. URL http://dx.doi.org/10.1086/183206.

V. S. Ptuskin. Cosmic-Ray Acceleration by Long-Wave Turbulence. *Soviet Astronomy Letters*, 14:255, March 1988.

BR Ragot. Lengths of wandering magnetic field lines in the turbulent solar wind. *The Astrophysical Journal*, 653(2):1493, 2006.

R. Ramesh, K. Sasikumar Raja, C. Kathiravan, and A. Satya Narayanan. LOW-FREQUENCY RADIO OBSERVATIONS OF PICOFLARE CATEGORY ENERGY RELEASES IN THE SOLAR ATMOSPHERE. *The Astrophysical Journal*, 762(2):89, dec 2012. doi: https://doi.org/10.1088/0004-637X/762/2/89. URL https://doi.org/10.1088/0004-637X/762/2/89.

A. F. Rappazzo, M. Velli, G. Einaudi, and R. B. Dahlburg. Coronal Heating, Weak MHD Turbulence, and Scaling Laws. *The Astrophysical Journal Letters*, 657:L47–L51, March 2007. doi: 10.1086/512975.

D. V. Reames. Acceleration of energetic particles by shock waves from large solar flares. *The Astrophysical Journal Letters*, 358:L63–L67, August 1990. doi: 10.1086/185780.

Donald V Reames. Solar energetic particles: A paradigm shift. *Reviews of Geophysics*, 33 (S1):585–589, 1995.

Donald V Reames. Energetic particles and the structure of coronal mass ejections. *GEOPHYSICAL MONOGRAPH-AMERICAN GEOPHYSICAL UNION*, 99:217–226, 1997.

Donald V Reames. Solar energetic particles: Sampling coronal abundances. *Space Science Reviews*, 85(1-2):327–340, 1998.

Donald V. Reames. Particle acceleration at the Sun and in the heliosphere. *Space Science Reviews*, 90:413–491, Oct 1999. doi: 10.1023/A:1005105831781.

Donald V Reames. The two sources of solar energetic particles. *Space Science Reviews*, 175 (1-4):53–92, 2013.

References

IG Richardson and HV Cane. Near-earth interplanetary coronal mass ejections during solar cycle 23 (1996–2009): Catalog and summary of properties. *Solar Physics*, 264(1):189–237, 2010.

E. C. Roelof. Propagation of Solar Cosmic Rays in the Interplanetary Magnetic Field. In H. Ögelman and J. R. Wayland, editors, *Lectures in High-Energy Astrophysics*, page 111, 1969.

R. Rosner, W. H. Tucker, and G. S. Vaiana. Dynamics of the quiescent solar corona. *The Astrophysical Journal*, 220:643–645, March 1978. doi: 10.1086/155949.

P. Saint-Hilaire, N. Vilmer, and A. Kerdraon. A DECADE OF SOLAR TYPE III RADIO BURSTS OBSERVED BY THE NANçAY RADIOHELIOGRAPH 1998-2008. *The Astrophysical Journal*, 762(1):60, dec 2012. doi: 10.1088/0004-637X/762/1/60. URL http://dx.doi.org/10.1088/0004-637X/762/1/60.

J. T. Schmelz, V. L. Kashyap, S. H. Saar, B. R. Dennis, P. C. Grigis, L. Lin, E. E. De Luca, G. D. Holman, L. Golub, and M. A. Weber. Some Like It Hot: Coronal Heating Observations from Hinode X-ray Telescope and RHESSI. *The Astrophysical Journal*, 704: 863–869, October 2009. doi: 10.1088/0004-637X/704/1/863.

S. Serio, G. Peres, G. S. Vaiana, L. Golub, and R. Rosner. Closed coronal structures. II - Generalized hydrostatic model. *The Astrophysical Journal*, 243:288–300, January 1981. doi: 10.1086/158597.

R. Sharma, D. Oberoi, A. Suresh, and M. Arjunwadkar. Quantifying weak non-thermal meterwave solar emission using non-imaging techniques. In D. Banerjee, J. Jiang, K. Kusano, and S. Solanki, editors, *IAU Symposium*, volume 340 of *IAU Symposium*, pages 181–182, February 2018. doi: 10.1017/S1743921318002004.

N. R. Sheeley, Jr. The Evolution of the Photospheric Network. *Solar Physics*, 9:347–357, October 1969. doi: 10.1007/BF02391657.

T. Shimizu. Energetics and Occurrence Rate of Active-Region Transient Brightenings and Implications for the Heating of the Active-Region Corona. *Publications of the ASJ*, 47: 251–263, April 1995.

G. M. Simnett. Electron acceleration in the corona. *Solar Physics*, 229(2):213–226, jul 2005. doi: 10.1007/s11207-005-5619-9. URL http://dx.doi.org/10.1007/s11207-005-5619-9.

D. S. Spicer. Magnetic Energy Storage and Convension in the Solar Atmosphere. *Space Science Reviews]*, 31(4):351–435, Dec 1982. doi: 10.1007/BF00171370.

D. S. Spicer, A. O. Benz, and J. D. Huba. Solar type I noise storms and newly emerging magnetic flux. *Astronomy & Astrophysics*, 105:221–228, January 1982.

P. A. Sturrock. Model of the High-Energy Phase of Solar Flares. *Nature*, 211:695–697, August 1966. doi: 10.1038/211695a0.

P. A. Sturrock. *Plasma Physics, An Introduction to the Theory of Astrophysical, Geophysical and Laboratory Plasmas*. 1994.

Prasad Subramanian and Peter A. Becker. Noise-storm continua: Power estimates for electron acceleration. *Solar Physics*, 225(1):91–103, nov 2004. doi: https://doi.org/10.1007/s11207-004-3256-3. URL https://doi.org/10.1007/s11207-004-3256-3.

Prasad Subramanian and Peter A. Becker. Further constraints on electron acceleration in solar noise storms. *Solar Physics*, 237(1):185–200, aug 2006. doi: 10.1007/s11207-006-0084-7. URL 10.1007/s11207-006-0084-7.

A. Suresh, R. Sharma, D. Oberoi, S. B. Das, V. Pankratius, B. Timar, C. J. Lonsdale, J. D. Bowman, F. Briggs, R. J. Cappallo, B. E. Corey, A. A. Deshpande, D. Emrich, R. Goeke, L. J. Greenhill, B. J. Hazelton, M. Johnston-Hollitt, D. L. Kaplan, J. C. Kasper, E. Kratzenberg, M. J. Lynch, S. R. McWhirter, D. A. Mitchell, M. F. Morales, E. Morgan, S. M. Ord, T. Prabu, A. E. E. Rogers, A. Roshi, N. Udaya Shankar, K. S. Srivani, R. Subrahmanyan, S. J. Tingay, M. Waterson, R. B. Wayth, R. L. Webster, A. R. Whitney, A. Williams, and C. L. Williams. Wavelet-based characterization of small-scale solar emission features at low radio frequencies. *The Astrophysical Jour*, 843(1):19, jun 2017. doi: https://doi.org/10.3847/1538-4357/aa774a. URL https://doi.org/10.3847/1538-4357/aa774a.

B. Swalwell, S. Dalla, and R. W. Walsh. Solar Energetic Particle Forecasting Algorithms and Associated False Alarms. *Solar Physics*, 292(11):173, Nov 2017. doi: 10.1007/s11207-017-1196-y.

P. Testa, B. De Pontieu, J. Allred, M. Carlsson, F. Reale, A. Daw, V. Hansteen, J. Martinez-Sykora, W. Liu, E. E. DeLuca, L. Golub, S. McKillop, K. Reeves, S. Saar, H. Tian, J. Lemen, A. Title, P. Boerner, N. Hurlburt, T. D. Tarbell, J. P. Wuelser, L. Kleint, C. Kankelborg, and S. Jaeggli. Evidence of nonthermal particles in coronal loops heated impulsively by nanoflares. *Science*, 346(6207):1255724–1255724, oct 2014. doi: 10.1126/science.1255724.

Paola Testa, Bart De Pontieu, Juan Martínez-Sykora, Ed DeLuca, Viggo Hansteen, Jonathan Cirtain, Amy Winebarger, Leon Golub, Ken Kobayashi, Kelly Korreck, Sergey Kuzin, Robert Walsh, Craig DeForest, Alan Title, and Mark Weber. OBSERVING CORONAL NANOFLARES IN ACTIVE REGION MOSS. *The Astrophysical Journal*, 770(1):L1, may 2013. doi: 10.1088/2041-8205/770/1/l1. URL http://dx.doi.org/10.1088/2041-8205/770/1/L1.

Durgesh Tripathi, Helen E. Mason, and James A. Klimchuk. EVIDENCE OF IMPULSIVE HEATING IN ACTIVE REGION CORE LOOPS. *The Astrophysical Journal*, 723(1):713–718, oct 2010. doi: https://doi.org/10.1088/0004-637X/723/1/713. URL https://doi.org/10.1088/0004-637X/723/1/713.

V. M. Uritsky and J. M. Davila. Spatiotemporal Organization of Energy Release Events in the Quiet Solar Corona. *The Astrophysical Journal*, 795:15, November 2014. doi: 10.1088/0004-637X/795/1/15.

M'aP van Haarlem, MW Wise, AW Gunst, George Heald, JP McKean, JWT Hessels, AG De Bruyn, Ronald Nijboer, John Swinbank, Richard Fallows, et al. Lofar: The low-frequency array. *Astronomy & astrophysics*, 556:A2, 2013.

References

N. Vilmer. Solar flares and energetic particles. *Philosophical Transactions of the Royal Society A: Mathematical, Physical and Engineering Sciences*, 370(1970):3241–3268, jun 2012. doi: 10.1098/rsta.2012.0104. URL http://dx.doi.org/10.1098/rsta.2012.0104.

L Vlahos, ME Machado, R Ramaty, RJ Murphy, C Allisandrakis, T Bai, D Batchelor, AO Benz, E Chupp, D Ellison, et al. Phenomena associated with mildly relativistic electrons. In *Energetic Phenomena on the Sun*, pages 2–2, 1986.

Loukas Vlahos, Theophilos Pisokas, Heinz Isliker, Vassilis Tsiolis, and Anastasios Anastasiadis. PARTICLE ACCELERATION AND HEATING BY TURBULENT RECONNECTION. *ApJ*, 827(1):L3, aug 2016. doi: 10.3847/2041-8205/827/1/L3. URL http://dx.doi.org/10.3847/2041-8205/827/1/L3.

Andreas von Kienlin, Charles A. Meegan, Giselher G. Lichti, Narayana P. Bhat, Michael S. Briggs, Valerie Connaughton, Roland Diehl, Gerald J. Fishman, Jochen Greiner, Andrew S. Hoover, R. M. Kippen, Chryssa Kouveliotou, William S. Paciesas, Robert D. Preece, Volker Schönfelder, Helmut Steinle, and Robert B. Wilson. The GLAST burst monitor. In Günther Hasinger and Martin J. L. Turner, editors, *Proceedings of the SPIE*, volume 5488 of *Society of Photo-Optical Instrumentation Engineers (SPIE) Conference Series*, pages 763–770, Oct 2004. doi: 10.1117/12.552913.

H. P. Warren and A. D. Warshall. Temperature and Density Measurements in a Quiet Coronal Streamer. *The Astrophysical Journal*, 571:999–1007, June 2002. doi: 10.1086/340069.

D. G. Wentzel. Coronal heating by Alfven waves. II. *Solar Physics*, 50:343–360, December 1976. doi: 10.1007/BF00155297.

M. E. Wiedenbeck, G. M. Mason, C. M. S. Cohen, N. V. Nitta, R. Gómez-Herrero, and D. K. Haggerty. Observations of Solar Energetic Particles from ^{3}He-rich Events over a Wide Range of Heliographic Longitude. ApJ, 762:54, January 2013. doi: 10.1088/0004-637X/762/1/54.

J. P. Wild, S. F. Smerd, and A. A. Weiss. Solar Bursts. *Annual Review of Astronomy and Astrophysics*, 1:291, Jan 1963a. doi: 10.1146/annurev.aa.01.090163.001451.

J. P. Wild, S. F. Smerd, and A. A. Weiss. Solar Bursts. *Annual Reviews in Astronomy and Astrophysics*, 1:291, 1963b. doi: 10.1146/annurev.aa.01.090163.001451.

G. L. Withbroe and R. W. Noyes. Mass and energy flow in the solar chromosphere and corona. *Annual Reviews in Astronomy and Astrophysics*, 15:363–387, 1977. doi: 10.1146/annurev.aa.15.090177.002051.

C. S. Wu. A fast Fermi process - Energetic electrons accelerated by a nearly perpendicular bow shock. *Journal of Geological Research*, 89:8857–8862, October 1984. doi: 10.1029/JA089iA10p08857.

D. M. Zarro, J. T. Mariska, and B. R. Dennis. Testing the DC-Electric Field Model in a Solar Flare Observed by YOHKOH and the Compton Gamma-Ray Observatory. *The Astrophysical Journal*, 440:888, February 1995. doi: 10.1086/175327.

V. V. Zharkova, K. Arzner, A. O. Benz, P. Browning, C. Dauphin, A. G. Emslie, L. Fletcher, E. P. Kontar, G. Mann, M. Onofri, V. Petrosian, R. Turkmani, N. Vilmer, and L. Vlahos. Recent advances in understanding particle acceleration processes in solar flares. *Space Science Reviews*, 159(1-4):357–420, jul 2011. doi: 10.1007/s11214-011-9803-y. URL http://dx.doi.org/10.1007/s11214-011-9803-y.

M. Zombeck. *Handbook of Space Astronomy and Astrophysics: Third Edition*. Cambridge University Press, 2007.

C. Zwaan. On the Appearance of Magnetic Flux in the Solar Photosphere. *Solar Physics*, 60: 213–240, December 1978. doi: 10.1007/BF00156523.

C. Zwaan. The emergence of magnetic flux. *Solar Physics*, 100:397–414, October 1985. doi: 10.1007/BF00158438.